Alma Mater Studiorum – Università di Bologna

DOTTORATO DI RICERCA IN

SCIENZE DELLA TERRA

Ciclo XXVII

Settore Concorsuale di afferenza: 04/A1

Settore Scientifico disciplinare: GEO/07

A 300 million year-long history.

The metamorphic evolution of the Northern Apennine Variscan basement

Presentata da

Deborah Lo Pò

Coordinatore Dottorato

Prof. Jo Hilaire Agnes De Waele

Relatore

Dott. Roberto Braga

Esame finale anno 2015

ABSTRACT

Collision zones are the loci on the Earth where large portions of continental crust of different ages and origin are processed at different depths and temperatures. For these reasons, the exhumed slices of continental crust that is commonly found in collisional orogens record the overprinting relations between different stages of metamorphic (re)crystallization and deformation. Metamorphic petrologists investigate chemical and structural variations from the outcrop to the micron scale in an effort to better understand the petrogenetic processes occurring in collision zones.

The Variscan basement of Northern Apennines (Northern Italy) is an example of a continental crust portion affected by a complex polymetamorphic evolution.

The thesis investigates the metamorphic evolution of this basement occurring in the Cerreto Pass, in the bedrock reached by the Pontremoli well, and in the Pisani Mountains. The study comprised fieldwork in the Cerreto Pass, sampling, petrography and microstructural analysis, determination of the bulk rock and mineral composition, thermodynamic modelling, conventional mineral-mineral geothermobarometry, monazite chemical dating and Ar/Ar dating of muscovite.

The selected samples from the Cerreto Pass are mylonitic micaschist with a white mica + chlorite ± biotite mylonitic foliation wrapping around plagioclase, quartz and garnet porphyroblasts. Mg-rich prekinematic white mica and fish-shaped white mica are also present. The samples from the Pontremoli well are medium grained micaschist with a white mica and chlorite schistose fabric surrounding garnet porphyroblasts. Coronitic microstructures around inherited monazite grains in this rock consist of concentric shells of apatite + Th-silicate, allanite and epidote. Phyllites overlying the micaschist were also studied: they consist of a white mica and chlorite schistosity partially obliterating a previous foliation. The studied samples from the Pisani Mountains are chloritoid-bearing phyllites with abundant hematite bands and disseminated grains.

In late Carboniferous the Cerreto micaschists underwent a high-pressure event at 430-480°C and 11-13.5 kbar, probably due to the Variscan thickening stage. Some similarities occur between the Variscan evolution in Northern Apennines and that described for other fragments of the Southern Variscan belt, as suggested by previous petrological works on the Variscan basement of Northern Apennines.

The Pontremoli samples, by contrast, record a different metamorphic history. Detrital monazite yields U-Th-Pb chemical ages of 294 ± 5 Ma, interpreted as a late-Variscan thermal stage unrelated to the reconstructed metamorphic evolution. The Pontremoli micaschist experienced a prograde evolution at 500-600°C and 5-7 kbar, followed by a pressure peak at 520°C at 8 kbar and then a nearly isothermal cooling to 500°C at 2 kbar. The overall anticlockwise shape of the *P-T-D* path is different from the available metamorphic histories of the pre-Mesozoic basement of the Northern Apennines, and may be due to the post-Variscan shear zone tectonics or to the Alpine orogeny.

A shearing stage affected the Cerreto mylonite at 190.7 ± 1.3 Ma (Ar/Ar isotopic age of Na-rich mylonitic muscovite) and was accompanied by a strong ductile deformation at 450-500°C and 6-7.5 kbar. This age suggests that the exhumation of the Cerreto mylonite took place during the rifting stage of the Adria margin before the opening of the Ligurian-Piedmont ocean.

The high-pressure greenschist-facies conditions (475 °C and 9-10 kbar) preserved in the chloritoid-bearing phyllites from the Pisani Mountains indicate that, from the late Oligocene onwards, the Northern Appenine basement attained similar *P-T* conditions as the overlying metasediments (Verrucano).

As a whole the results on the Cerreto, Pontremoli and Pisani Mountains samples allowed to reconstruct a long-lasting metamorphic history straddling the Variscan and Alpine orogenesis.

The study of the Variscan basement of Northern Apennines allowed also to contribute to a better understanding of some general petrological issues generally found in low- to medium-grade metapelites from orogenic settings.

(i) Middle-grade mylonitic micaschist usually contains zoned minerals (e.g. garnet and white mica) in different microstructural sites. With suitable samples it is possible to reconstruct a *P-T-D* path as much complete as possible by combining microstructural analysis and thermodynamic modelling. Prekinematic white mica may preserve Mg-rich cores related to the pre-peak stage. Mn-poor garnet rim records the peak metamorphism. Na-rich mylonitic white mica, the XFe of chlorite and the late mineral assemblage may constrain the retrograde stage.

(ii) Metapelites and particularly orthogneiss may contain coronitic microstructures of apatite + Th-silicate, allanite and epidote around unstable monazite grains. In general, it is still not clear what are the *P-T* variations responsible for the

development of this kind of corona. In the Pontremoli micaschist, chemistry and microstructure of Th-rich monazite relics surrounded by an apatite-allanite-epidote coronitic microstructure suggest that monazite mineral was inherited and underwent partial dissolution and replacement by REE-accessory minerals at fluid-present peak metamorphic conditions. Element partitioning between garnet and accessory minerals and a detailed microstructural study on garnet inclusion mineralogy (which comprises xenotime in the garnet core, allanite in the outer core and epidote in the rim) allowed to link the crystallization of REE-minerals to the garnet growth in order to reconstruct the reaction history. The replacement of inherited monazite by apatite, allanite and epidote occurred during a prograde evolution at 500-600°C and 5-7 kbar.

(iii) Fish-shaped white mica is not always a (prekinematic) mica-fish. Observed at high-magnification BSE images it may consist of several white mica grains defining a fish-shaped asymmetric foliation boudin formed during a mylonitic stage. Hence, the asymmetric foliation boudin is a suitable microstructure to obtain geochronological information about the shearing stage (190.7 ± 1.3 Ma in the Cerreto mylonite case study). Differently from the asymmetric foliation boudins, mylonitic foliation may include relics of earlier events as evidenced by the ages of 374 and 315 Ma related to the Variscan orogenic cycle.

(iv) Thermodynamic modelling is an useful tool to constrain the *P-T* conditions experienced by a metamorphic rock. However inadequate assumption (e.g. neglecting important components as C, O_2) may result calculation that reproduces neither the observed mineral assemblage nor the measured mineral compositions. The effects of different Fe_2O_3 bulk contents were investigated on the calculated phase equilibria of low-temperature/intermediate-pressure metasedimentary rocks from the Pisani Mountains. Thermodynamic modelling of a chloritoid-bearing hematite-rich metasedimentary rock fails to reproduce the observed mineral compositions when the bulk Fe_2O_3 is neglected or determined through titration. The mismatch between observed and computed mineral compositions and assemblage is resolved by tuning the effective ferric iron content by *P-X*Fe_2O_3 diagrams. The introduction of ferric iron affects the stability of the main rock-forming silicates that often yield important thermobaric information.

CONTENTS

A TIME TRAVEL

THROUGH THE EVOLUTION OF THE

VARISCAN BASEMENT OF NORTHERN APENNINES

Chapter 1

A TIME TRAVEL THROUGH

THE EVOLUTION OF THE VARISCAN BASEMENT OF NORTHERN APENNINES

1.1 INTRODUCTION

Collision zones are those areas of the Earth where orogenic belts form. They are regions of fundamental petrogenetic processes related to the growth and consumption of lithosphere. The transformations that submersed rocks undergo during the collision are also linked to the long-term biogeochemical cycle of elements (C-O-H-N) that affects life development (Evans, 2011). The study of metamorphic rocks is thus fundamental to investigate the processes occurring throughout the collision. In principle, metamorphic minerals and microstructures may record different stages of the orogenic events: when a crustal slab undergoes below the overhanging plate margin the values of Pressure-Temperature (*P-T*) increase (prograde metamorphism); then rocks reach peak conditions (maximum temperature); finally the exhumation of the buried rocks is related to a *P-T* decrease (retrograde metamorphism). In practice, the last stages of metamorphism are better preserved whereas the record of the prograde metamorphism is not commonly recognizable. One challenge is indeed to reconstruct complete metamorphic evolutions comprising also pre-peak stages. Then **the task of metamorphic petrologists is to decipher the information and estimate the physical and chemical conditions during the metamorphic evolution**. The *P-T-t-D-X* (Pressure-Temperature-time-Deformation-composition) path experienced by metamorphic rocks provides fundamental constrains for the geodynamic models.

In the study of collisional basement metamorphic petrology has to face some first-order problems:

1. Textural ad chemical modifications occurring during the retrograde evolution hamper the reconstruction of the prograde metamorphic history.

2. Difficulties also arise when the petrologic record has to be correlated with age determinations derived from major and accessory minerals. **Monazite** is one of the main accessory minerals useful for obtaining geochronological information. Therefore much effort is dedicated to connect monazite U-Th-Pb chemical or isotopic ages with *P-T* constraints obtained from mineral assemblages. A

Figure of the previous page: River "Canale dell'Acqua Torbida" in the Cerreto Pass. The Variscan basement outcrops are in river slope on the left.

common approach relies on the Y partitioning between garnet and monazite (Vance *et al.*, 2003; Williams *et al.*, 2007), but it requires that monazite grows during metamorphic evolution. However, clear breakdown microstructures of monazite testify that monazite can also be consumed during metamorphic evolution (Janots *et al.*, 2006; Rasmussen & Muhling, 2007) and the link between monazite and *P-T* sensitive minerals becomes more complicated. The breakdown reactions of monazite have been observed but their thermobaric conditions are still debated.

3. Another key mineral in metamorphic petrology is **potassic white mica**, because it is a fabric-forming major mineral, *P-T* sensitive, and also useful for geochronologic purpose. However potassic white mica occurring in different microstructural positions can provide complex age patterns at thin section scale.

4. In calculating the thermobaric conditions by thermodynamic modelling (i.e., using pseudosections), specific problems are: (i) inadequate assumption (neglecting important components as C, CO_2, O_2, considering H_2O in excess, indeterminateness in the fluid activity); (ii) uncertainty related to the solid-solutions models and the thermodynamic dataset; (iii) selection of a reliable representative chemical system; (iv) errors in the effective bulk composition used as input for the calculation of the pseudosection.

The thesis aims to propose innovative approaches to tackle some of the above-mentioned petrological questions. They are:

1. how to reconstruct a complete polyphase *P-T-D* path comprising pre-peak stages through the combination of thermodynamic modelling and microstructural analysis **(chapter 2);**

2. how to relate geothermobarometry and geochronology when monazite is inherited. The topic deals also with estimating the *P-T* conditions of the reactions involving monazite breakdown in medium-grade metapelites **(chapter 3)**;

3. investigating the type of geochronological record provided by potassic white mica in different mylonitic microstructures (e.g. mylonitic foliation and asymmetric foliation boudins; **chapter 4)**;

4. exploring the influence of ferric iron on phase assemblages and composition in greenschist-facies metamorphic rocks **(chapter 5)**.

In summary, the application of modern petrological methods allowed to **investigate the potentialities and limits of the research advancements in the study of collisional basements.**

1.2 THE NORTHERN APENNINES

The Northern Apennines are an example of collisional orogen that involved both Mesozoic-Tertiary sedimentary sequence and Variscan basement. While the Alpine tectono-metamorphic history of the Triassic Verrucano Group, a metasedimentary sequence tectonically stacked onto the Variscan basement, is well-known (Theye *et al*, 1997; Giorgetti *et al*, 1998; Jolivet *et al*, 1998; Franceschelli & Memmi, 1999; Franceschelli *et al*, 2004), **the state of knowledge on the Variscan basement is poor and modern studies applying advanced petrologic methodologies lack.** The difficulties to study the Variscan basement of Northern Apennines arise from (i) poor exposure of scattered outcrops and (ii) a strong Alpine overprint on Variscan features (Franceschelli *et al.*, 2004). For these reasons, the Variscan *P-T-t* path is less constrained than the Alpine evolution or, when *P-T* data are available (Bertini *et al.*, 1994; Molli *et al.*, 2002), the reconstructed history refers to the late, exhumation-related stages.

This **knowledge gap** attracted our interest and one of the outcome of this research is to provide better constraints on the pre-Alpine *P-T-t* path and compare the obtained new paths with others retrieved from several Mediterranean Variscan basements.

Since in Southern Tuscany the thermometamorphism related to the emplacement of Pliocene-Quaternary granitoids has obliterated the earlier stages (Elter & Pandeli, 1990; Franceschini, 1998; Musumeci *et al.*, 2002; Pandeli *et al.*, 2005; Musumeci *et al.*, 2011), only the Variscan basement outcropping in Northern Tuscany and Liguria was selected. The occurrences are Punta Bianca, Cerreto Pass, Pontremoli 1 well, Apuane Alps and Pisani Mountains (Fig. 1.1).

In order to obtain useful *P-T* information through thermodynamic modelling, the investigation was limited to medium-grade metasediments, which contain suitable low-variance parageneses. For this reason the greenschist-facies Variscan basement in Apuane Alps and Punta Bianca could not be analysed with the above method. The hematite-rich chloritoid-bearing phyllites from the Monti Pisani, and the garnet micaschist samples from the Cerreto Pass and the Pontremoli well resulted suitable for a study involving phase diagram calculations (see below). The rocks sampled in those

three areas recorded different stages of the metamorphic evolution, so it was possible to combine all the information to reconstruct **a long-lasting metamorphic history**.

The thesis is indeed a time travel through the evolution of the Variscan basements of Northern Apennines, from the first recognizable metamorphic signature of Variscan times to the Alpine metamorphic overprint. The results reveal, for the first time in the study of these basements, a complex history between the Variscan and the Alpine orogenic cycles.

Therefore, this research deals with the following regional goals:

1. to unravel the Variscan tectono-metamorphic history including the pre-peak, peak and exhumation conditions and establish possible correlations with other circum-Mediterranean Variscan basements **(chapter 2);**

2. to outline the metamorphic history between the Variscan and the Alpine orogeneses **(chapter 3)**;

3. to constrain the age of the shearing event in the Cerreto mylonites **(chapter 4);**

4. to determine the peak conditions of the Alpine metamorphism **(chapter 5)**.

Although the results of this research line contribute to a better understanding of the metamorphic evolution of the Variscan basement of Northern Apennines, open regional questions still remains and are reported in "Conclusions" **(chapter 6)**.

1.2.1 Geological framework

In Italy fragments of Variscan basement (Fig. 1.2) occurs in the Alps, in the Corsica-Sardinia block, in the Calabria-Peloritani orogen and in Northern Apennines (Boriani *et al.*, 2003).

The Variscan basement of Northern Apennines is the less studied among these fragments. Differently from the Alps, Corsica-Sardinia and the Calabrian-Peloritan orogen, small extent and scattered exposures characterize the Variscan basement of Northern Apennines. Furthermore only few petrological data are available for this basement (Molli *et al.*, 2002; Franceschelli *et al.*, 2004).

The Northern Apennines (Figg. 1.3a, b) are a thrust and fold belt formed during the E-ward collision between the Corsica-Sardinia block (Europe) and the Adria microplate (Africa) during the last 30 Ma (Vai & Martini, 2001; Molli, 2008). They consist of oceanic (Liguride Units) and continental (Tuscan Units and Tuscan Metamorphic Units) domains. Each unit is overlain by neogenic successions, outcropping especially in South Tuscany.
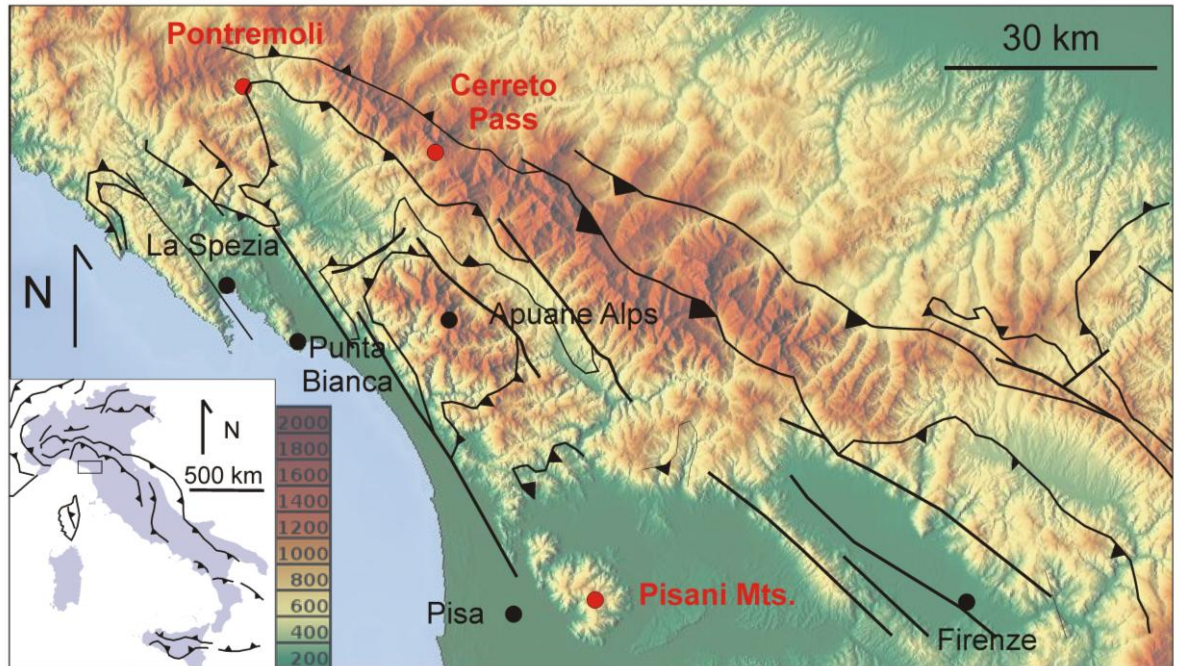
Figure 1.1 Localization of Pontremoli, Cerreto Pass and Pisani Mountains (in red) in the relief map of Northern Apennines (Google Maps). The main thrusts in Italy are from Patacca & Scandone (1989), while the tectonic setting of Northern Apennines is from Bigi *et al.* (1983) and Molli (2008).

The tectonic units are (from top to bottom; Elter, 1975; Fig. 1.4a):

- ➢ the Epiligurian wedge-top sediments
- ➢ Liguride Units: ophiolites from the Jurassic Ligurian-Piedmontese ocean;
- ➢ Tuscan Units: low-grade metamorphic or sedimentary sequences deposited in late Triassic-Tertiary derived above the Adria crust;
- ➢ Tuscan Metamorphic Units: metamorphic sequence representing the Adria continental crust, consisting of a Variscan pre-Carboniferous basement and Late Carboniferous-Oligocene metasedimentary rocks;
- ➢ basement and sedimentary rocks deriving from the Umbro-Marchigian and the Padan domains.
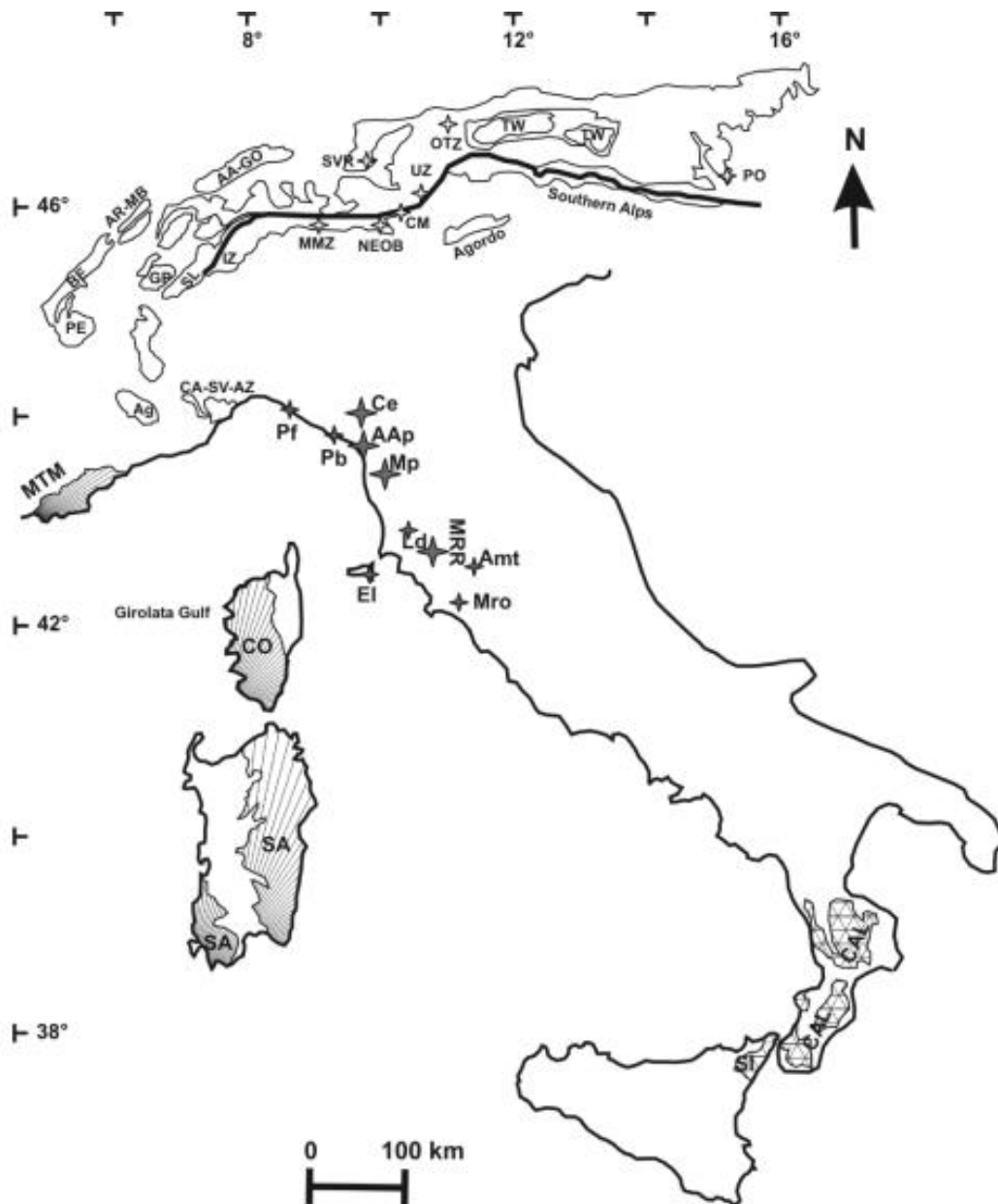
Figure 1.2 Distribution of the Variscan Massifs in Italy (from Padovano *et al.*, 2012, modified from Vai, 2001). See the following page for further details. Alps (white areas): CA-SV-AZ, Calizzano-Savona-Arenzano M.; Ag, Argentera M.; PE, Pelvoux M.; BE, Belledonne M.; GP, Gran Paradiso M.; AR-MB, Aiguilles Rouges-Mont Blanc M.; SL, Sesia Lanzo Zone; IZ, Ivrea Zone; AA-GO, Aar-Gotthard M.; MMZ, Monte Muggio Zone; NEOB, North-East Orobic Basement; SVR, Silvretta Thrust Sheet; UZ, Ulten Zone; CM, Cima Mezzana; OTZ, Oetzal Zone; TW, Tauern Window; PO, Pohorje M.; Northern Apennines (grey areas): Pf, Neogenic Portofino Conglomerates; Ce, Cerreto area; Pb, Punta Bianca; AAp, Apuan Alps; Mp, Monti Pisani; Ld, Larderello / Travale geothermal fields; MRR, Monticiano-Roccastrada Ridge; Amt, Amiata geothermal field; Mro, Monti Romani; El, Eastern Elba Island. A areas filled with oblique lines: MTM, Maures–Tanneron M.; CO, Corsica M.; SA, Sardinia M. Areas filled with triangles: SI, Sicily (Peloritani M.); CAL, Calabria (Aspromonte, Sila, Serre M.). Thick black line: Insubric Line.
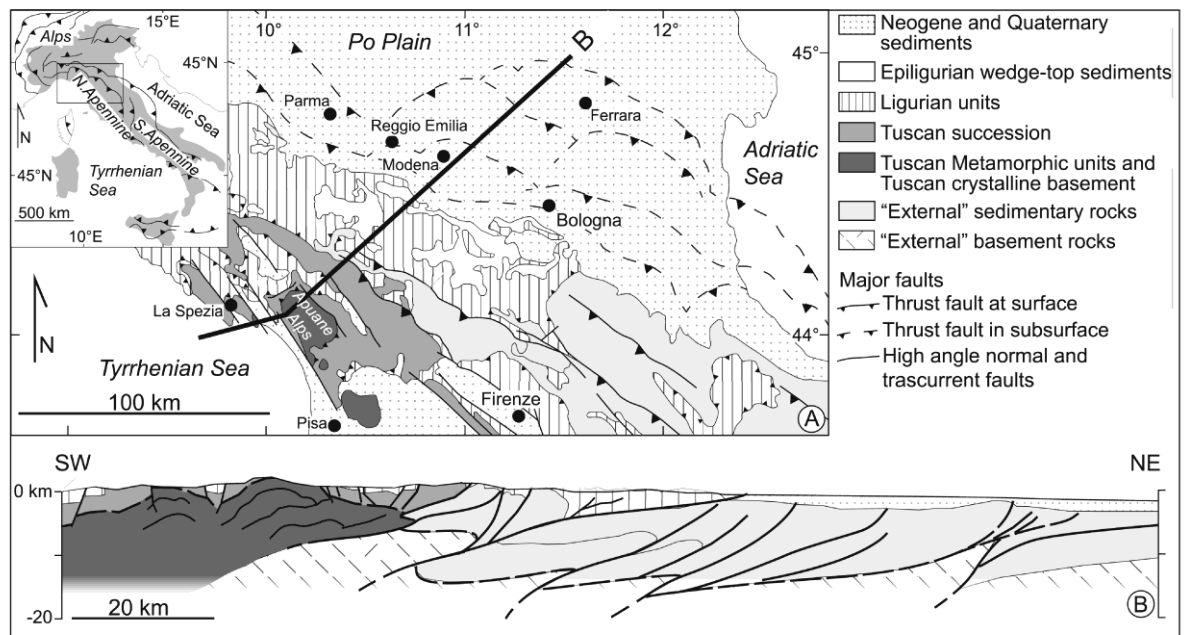
Figure 1.3 Northern Apennine setting (modified from Clemenzi *et al.*, 2014 and Molli, 2008): (a) tectonic map of the Northern Apennines; (b) cross-section.

The Variscan basement outcrops in Punta Bianca, Apuan Alps, Pisani Mountains, the Monticiano-Roccastrada Ridge, eastern Elba Island, Romani Mountains, and was also found in the subsurface of the Larderello-Travale geothermal region and of the Pontremoli area.

Regional correlations among the different Variscan basement occurrences are difficult, because of the scarcity and bad-quality of the outcrops and the strong Alpine overprint (Pandeli *et al.*, 1994).

This basement shows evidence of a pre-Alpine metamorphism, which has been ascribed to the collisional stages of the Variscan Orogeny (Conti *et al.* 1993), preserved as relics because of the strong Alpine metamorphism superposition (Franceschelli *et al.*, 2004).

In the Larderello subsurface (Southern Tuscany), the Variscan basement consists of three different units (from top to bottom; Bertini *et al.*, 2006; Fig. 1.3b):

➢ Phyllitic and quartzitic complex (greenschist-facies Variscan metamorphism and Alpine overprinting; Pandeli *et al.*, 2005);

➢ Micaschist complex (Variscan metamorphism and Alpine overprinting; Pandeli *et al.*, 2005);

➢ Gneiss complex (Variscan metamorphism at P = 7 kbar at T=500-600°C; Bertini *et al.*, 1994).

Pandeli *et al.* (2005) correlate the rocks from the Cerreto Pass and the Pontremoli to the Micaschist Complex, and the metasediments from the Pisani Mountains to the Phyllitic and quartzitic complex.

Chapter 2, 3, 4 contains specific geological frameworks and tectonic maps of the selected study areas: the readers are referred to the corresponding chapters.
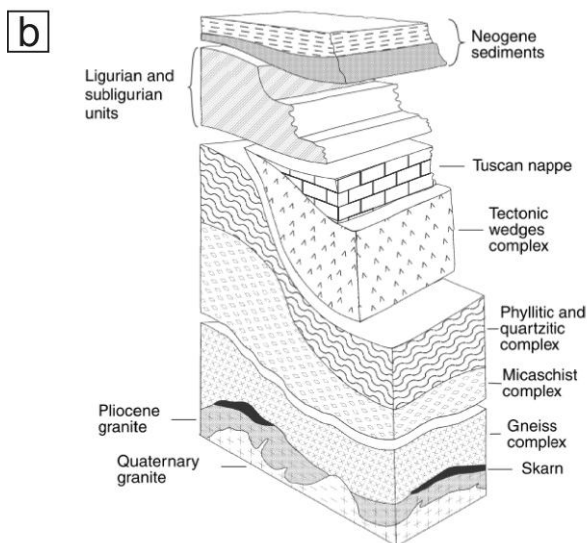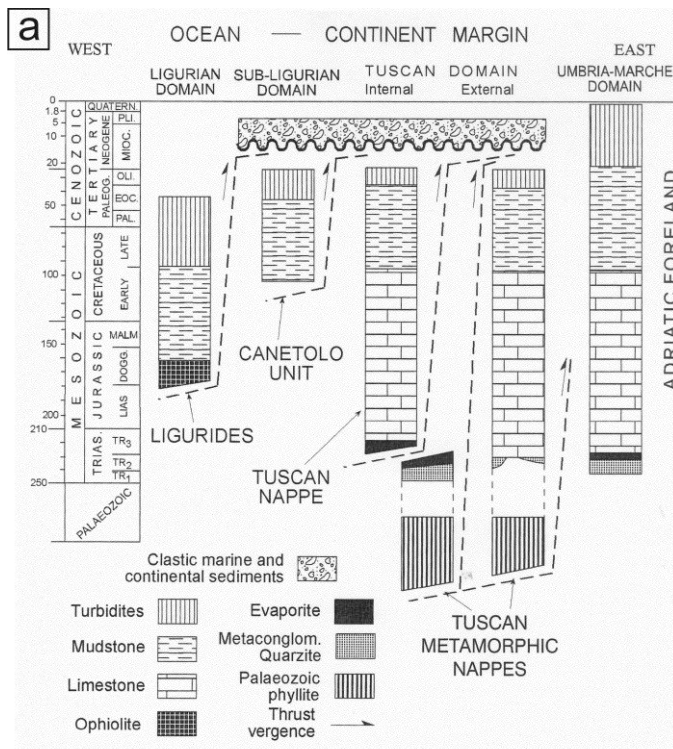
Figure 1.4 Tectonic setting of Northern Apennines: (a) relationships among the tectono-stratigraphic units in Northern Apennines (from Vai & Martini, 2001); (b) metamorphic units in the Variscan basement beneath the Larderello geothermal field (from Bertini *et al.*, 2006).

1.2.2 History of research on the Northern Apennine Variscan basement

In the '60s-70s Variscan metamorphism was envisaged in the Pre-Triassic sequences of Northern Apennines (**Borsi et al., 1966; Rau & Tongiorgi, 1974; Cocozza et al., 1974; Vai, 1978**). **Rau & Tongiorgi (1966, 1974)** studied the field relationships and the stratigraphy of the Paleozoic succession in the Pisani Mountains: they recognized both Variscan ("Formazione delle Filladi e Quarziti listate di Buti") and post-Variscan units ("Formazioni degli Scisti di San Lorenzo" and "Conglomerati e Brecce d'Asciano"). The Variscan unit was overlain by a discordance formed in Late Carboniferous. The Rb-Sr age determination on bulk-rock from the Monti Pisani phyllites of **Borsi et al. (1967)** revealed 275 ± 12 Ma. Only few years later, **Del Moro et al. (1982)** dated with the Ar-Ar method a muscovite associated with andalusite in the Micaschist Complex from the Larderello subsurface. The obtained age of 285 ± 11 Ma has been interpreted as a late-Variscan thermal stage. The first reconstructions related to the Variscan basement were published in late '70-early '80 (**Vai, 1978; Bagnoli et al., 1979; Tongiorgi & Bagnoli, 1981**). The studies adopted basically a biostratigraphic approach and correlation with the metamorphic evolution of Sardinia. The paper by **Kligfield et al. (1986)** is a milestone in the research history of Northern Apennines. They performed K-Ar and ^{40}Ar-^{39}Ar on potassic white mica separates of Paleozoic to Oligocene metasedimentary rocks present from the Alpi Apuane. The mixed ages obtained in the Variscan basement suggested the overprinting of the Alpine events on the Variscan metamorphism. The age interval of 27-10 Ma was attributed to the Alpine evolution. **Rau (1990)** for the first time attempted to reconstruct the evolution of the Variscan basement from Late Paleozoic to Mid Triassic on the basis of the analysis of post-Variscan sedimentary basins. **Conti et al. (1991a)** proposed the first complete framework of the Variscan and Alpine events. They assert that all the Paleozoic units in Northern Apennines show a low-grade Alpine metamorphism and only some of them contain greenschist- or amphibolites-facies Variscan relics. In particular, **Conti et al. (1991b, 1993)** outlined the superposition of the Alpine events on the Variscan structures in the Apuane Alps. A new reappraisal of the geodynamic evolution affecting the Variscan basement is provided by **Rau (1993)**. After the Variscan collision (Late Carboniferous) the Variscan chain underwent transcurrent dextral megashear zones accompanied by alternating transpessive and trastensive tectonics. These shear zones caused the fragmentation of the Variscan belt and the formation of shallow marine basins. In Permian and Lower-Triassic times the transcurrent tectonics continued. In Middle- and Upper-Triassic the

extension prevailed, leading to the definitive separation of the Tuscan Variscan basement from the "stable" Europe. The Tuscan Variscan basement became indeed a passive margin of the Adria promontory (Rau, 1993). **Bertini *et al.* (1994)** proposed some *P-T* estimates for the Variscan metamorphism for the Gneiss Complex in the Larderello subsurface. **Pandeli *et al.* (1994)** proposed a revised stratigraphy of the Paleozoic stratigraphic sequences in Northern Apennines. A study on the ore deposits in the Variscan basement from the Apuane Alps is given by **Dini *et al.* (1995, 2001)**. **Franceschini (1998)** attributed the low-pressure high-temperature metamorphism in the Larderello subsurface to the Pliocene-Quaternary thermometamorphism. **Molli *et al.* (2002)** analysed the major and trace elements composition of the amphibolites from the Cerreto Pass. Their data support an Enriched-type MORB derivation for the amphibolites protolith. Classical thermobarometry on the same samples indicate an initial medium-pressure amphibolites stage followed by a greenschist-facies metamorphism. They also performed Ar-Ar dating on horneblende separates, obtaining a Variscan age (312-328 Ma) for the metamorphism affecting the amphibolites. The geological features of the Larderello geothermal field are reported in **Batini *et al.* (2003)** and **Bertini *et al.* (2006).** A review of the knowledge on the Variscan and Alpine events in Northern Apennines was published by **Franceschelli et al. (2004)**. **Elter & Pandeli (2005)** assessed a common evolution among the Maures Massif, Corsica-Sardinia Block, Northern Apennines from Early Carboniferous to the Late Carboniferous-Early Permian. The Authors suggested that the Posada Valley Zone of Sardinia might continue in the Tuscan Variscan basement. **Pandeli *et al.* (2005)** focussed on the Micaschist Complex and the Gneiss Complex of the Larderello area, proposing correlations with the Cerreto and Pontremoli Variscan basement. The high temperature-low pressure metamorphism in the Larderello subsurface was outlined by **Rossetti *et al.* (2008). Leoni *et al.* (2009)** estimated the *P-T* conditions of the metamorphism affecting the tectonic units outcropping in the Pisani Mountains. **Musumeci *et al.* (2011)** performed U-Pb dating on detrital zircon and ^{40}Ar-^{39}Ar dating on metamorphic muscovite from the Variscan basement in the Elba Island. A correlation of the exhumation history of the Variscan basement outcropping in the Alps, the Corsica-Sardinia-Maures-Tanneron Massif, the Calabria-Peloritani Orogen, and the Northern Apennines is also provided by **Padovano *et al.* (2012)**. They found similarities corroborating the thesis that those massifs belonged to the same basement

until Late Carboniferous time, when a regional dextral strike–slip shear zone (the East Variscan Shear Zone) led to their segmentation.

1.3   METHODS

The study is primary petrological, carried out through fieldwork in key outcrops, detailed petrography, determination of the mineral and rock compositions, geothermobarometry and geochronology.

A brief description of the used methods is presented below. In-depth accounts of the methods are reported in the following chapters dealing with the different case studies.

1.3.1. Fieldwork

A bibliographic research anticipated the fieldwork in order to select the most appropriate sites. The fieldwork regarded the Variscan basement in the Cerreto Pass, the only site with significant rock exposures. A geological survey allowed to determine the main structural and petrographic features of the mylonitic micaschist and amphibolite, the geometric relationships between the Variscan basement and the enclosing Triassic evaporites and the sampling of representative micaschist. One of the results of the fieldwork activity was the creation of a geological map reporting the existing outcrops of the Variscan basement. 34 samples were collected. Sampling was also carried on the hematite-rich phyllites from the Pisani Mountains (5 samples). Professor Molli (University of Pisa) and Professor Alessandra Montanini (University of Parma) kindly provided the micaschist recovered from the cuttings of the Pontremoli commercial well (8 samples) and some samples from the Cerreto Pass.

1.3.2 Petrography

Petrographic observations were carried out with a polarising optical microscope and the scanning electron microscope Philips 515B at the Dipartimento di Scienze Biologiche, Geologiche ed Ambientali (Università di Bologna). Additional observations with a Jeol JSM-6500F thermal Field emission scanning microscopy at INGV (Rome) were achieved.

Petrographic characterization and microstructural analysis were always performed on each sample to reconstruct the deformation and blastesis sequences and the metamorphic-deformation relationships. The porphyroblast-matrix geometric relations were particularly useful for this purpose.

1.3.3 Mineral and rock compositions

Mineral chemistry was determined through a CAMECA SX100 electron microprobe equipped with five wavelength dispersive spectrometers at the Institut für Mineralogie und Kristallchemie (Universität Stuttgart). X-ray maps of minerals were acquired to inspect the spatial distribution of selected major and trace elements. Point analyses were accurately chosen on the basis of their microstructural position. Compositional diagrams were then constructed to recognize compositional trends and variations. Rock compositions (major elements) were obtained by XRF analyses on pressed powder pellets using the Philips PW1480 and the Axios-Panalytical spectrometers at the Department of Biological, Geological and Environmental Sciences, Bologna University or by calculating the bulk-rock using mineral modes and compositions.

1.3.4 Geothermobarometry

Geothermobarometry is the branch of metamorphic petrology that permits the estimation of the *P-T* conditions of formation of metamorphic assemblages. The so-called conventional methods (e.g. mineral-mineral elemental exchange and/or net transfer reactions) have been recently replaced by thermodynamic modelling for calculating phase diagrams. *P-T* pseudosection (Connolly and Petrini, 2002; Powell and Holland, 2008) are isochemical phase diagram showing the stable paragenesis at different thermobaric condition for a fixed rock composition. Thermodynamic modelling allows also to calculate isothermal Pressure-Composition (*P-X*) diagrams or isobaric Temperature-Composition (*T-X* diagram), where the chemistry of the rock is a variable. This can be useful when dealing with metasomatic rocks and the composition of the fluid has to be known.

Another variable considered in metamorphic petrology is the time (t) of metamorphism. Through geochronological methods we can obtain the age of different stages in the metamorphic evolution and reconstruct *P-T-X-t* path. If the tectono-metamorphic sequence has been established through microstructural analysis, then the thermobaric and chemical constrains can be connected with deformation (*D*), thus defining *P-T-X-t-D* path. The usage of pseudosections (Williams & Jercinovic, 2012) has benefited from the improvement of the thermodynamic dataset (Berman, 1988; Holland & Powell, 1998), from the implementation of software that easily calculate phase diagrams (Connolly, 2005) and from the development of new activity-models for minerals (Holland & Powell, 1998; 2011). With pseudosections it is possible to predict the

evolution of the mineral assemblages and compositions during *P-T-X* variations (forward modelling). Another potentiality of the pseudosections is the possibility to quantify the variations in the *P-T-X* space of many rock properties, such as the mineral modes and compositions (isopleths), thermodynamic parameters, sound- and seismic-wave velocities. This PhD work often employs compositional isopleths, that are lines in a phase diagram indicating the calculated stable composition of a solid solution mineral, eventually changing with pressure and temperatures. By comparing the observed and computed mineralogy we are able to identify some thermobaric and chemical constraints and thus define a *P-T-X* path. Differently from the classical geotermobarometry that gives only one point (± uncertainties) within the *P-T* space, pseudosections report all the possible parageneses that can be generated with a given composition in a specific *P-T* window. Mineral assemblages that were stable in the earlier phases of the metamorphic evolution can be detected, even if they are no more present in the observed rock sample.

Medium-grade metapelites are suitable for the thermodynamic modelling approach because of their reactivity in response to relatively small changes in pressure and temperature or fluid composition and because reliable solid solution models are available (Spear, 1993; Massonne, in press).

In order to obtain *P-T* estimates during the PhD activity thermodynamic modelling was preferentially performed, accompanied by classical geothermobarometry when necessary.

1.3.5 Geochronology

The absolute dating of tectono-metamorphic events in crystalline basements relies on the measurement of elements and/or isotopes originated from the natural decay of U, Th and K included in minerals lattice. We used two geochronological techniques in order to achieve the ages of different stages of the metamorphic evolution: *in situ* U-Th-Pb chemical dating of monazite and Ar-Ar isotopic dating of potassic white mica.

Monazite (lanthanum-cerium light rare earth elements phosphate) is a mineral of geochronological interest for understanding metamorphic processes (Kelly *et al.*, 2006). It contains Th and U at a level detectable by the electron microprobe (Montel *et al.*, 1996), so it is possible to analyze tiny monazite microdomains directly on polished thin sections, thus preserving their textural position (William & Jercinovic, 2002). Furthermore monazite contains virtually no common Pb, so all the Pb analysed derives

from the Th and U decay. Before dating, the monazite has to be chemically and microstructurally characterized in order to establish if it is metamorphic or inherited and to link monazite to the reconstructed metamorphic history.

Potassic white mica can be dated by the ^{40}Ar-^{39}Ar method that derives from the K-Ar dating. It is based on the decay of K to Ar (McDougall & Harrison, 1999). Through some extraction techniques (e.g. laser) it is possible to analyse the ^{40}Ar, that is generated by the K decay, and the ^{39}Ar, induced by the irradiation of K-bearing minerals in a nuclear reactor. This method permits to obtain age mapping of minerals in rock chips at high spatial resolution (50-100 µm; Di Vincenzo, 2004). Potassic white mica is not only a suitable mineral for ^{40}Ar-^{39}Ar dating. Since the composition of potassic white mica changes in response to P-T variations, this mineral can provide also petrological information. Thus, potassic white mica is one of the main minerals that allows to link petrology and geochronology.

1.3.6 Linking geothermobarometry and geochronology

The connection between petrological and textural evolution with the age dating is not a trivial problem (Vance *et al.*, 2003). Even if zircon and monazite (tipical minerals targeted for age dating work) can supply very precise ages, it is not easy to interpret when these minerals (re)crystallize in relation to the evolution of major minerals that define P-T-D history. This is because understanding when accessory phases grow with respect to changing pressure and temperature and melt/rock composition is still limited (Kelsey *et al.*, 2008). If our capabilities to perform forward modelling of the main rock-forming minerals (garnet, micas, feldspar, Al_2SiO_5…) has been increasing since the evolution of more realistic solid solutions models (Holland & Powell, 1998), the forward modeling of dateable accessory minerals is hampered by the lack of thermodynamic data both for accessory minerals as well as for trace-element bearing end-members of major minerals (YAG garnet, for example; Pyle & Spear, 2000).

Vance *et al.* (2003) suggest potential solutions to solve the problematic link between petrological and chronometric data. The use of "the-inclusion-is-older-than-the-host" textural criteria still constitutes the favorite approach to resolve the relative chronology between major and accessory minerals. This approach, however, is hampered by a number of factors reviewed by Langone *et al.* (2011). Another method to infer a relative chronology between dateable and major minerals is the analysis of trace element distribution between major and accessory minerals. The Y partitioning between garnet

and monazite or the Heavy Rare Earth Elements (HREE) distribution between garnet and zircon/monazite are common tools to asses when these accessory phases grew with respect to *P-T* sensitive equilibria involving garnet. Another approach is linking an accessory phase to a specific reaction involving major rock-forming minerals, so a metamorphic mineral growth event can be dated. All approaches mentioned above require textural and/or chemical connection between geochronometers and geothermobaromers. Only few thermodynamic modelling involving phosphates have been performed (Janots *et al*, 2007; Spear & Pyle, 2010). However, the poor availability of activity models for accessory minerals doesn't always permit to use thermodynamic modelling to obtain the *P-T* conditions of the reactions between accessory minerals. An alternative way is to link the growth of accessory minerals to the crystallization of *P-T* sensitive major minerals through chemical an microstructural constraints (Gieré *et al*, 2011; see chapter 3).

1.4 CHAPTER OVERVIEW

The chapters are chronologically ordered according to the age of the investigated metamorphic stage.

Chapter 2 proposes an integration between classical microstructural analyses and thermodynamic modelling in the Cerreto micaschist. Themodynamic modelling comprises phase diagrams calculation and garnet isopleths thermobarometry. This approach aims to reconstruct *P-T-D* path as much complete as possible for the Variscan collision and exhumation. A comparison between the obtained *P-T* path and the thermobaric trajectories proposed for other Variscan basement of the circum-Mediterranean area is presented.

Chapter 3 focuses on the post-Variscan evolution in the Pontremoli micaschist recovered from the cuttings of the Pontremoli 1 commercial well (Agip; Anelli *et al*, 1994). Coronitic microstructures around monazite grains in this rock consist of apatite surrounded by allanite and an epidote rim. The chemistry and microstructure of the 294 ± 8 Ma old Th-rich monazite grains suggest that the monazite was inherited and underwent partial dissolution at peak metamorphic conditions. Element partitioning between garnet and accessory minerals and a detailed microstructural study on garnet inclusion mineralogy allowed us to link the crystallization of REE-minerals to the garnet growth. An anticlockwise *P-T* path was reconstructed taking into account the effect of garnet fractionation on bulk-rock composition. The obtained *P-T* path

postdates 296 ± 6 Ma and results different from the available metamorphic histories of the pre-Mesozoic basement of the Northern Apennines.

Chapter 4 reports a combined microstructural-geochronological study on the shearing fabric in the Cerreto mylonites. This is the first attempt of determining the age of the shearing stage after the Variscan peak in the in the Variscan basement of Northern Apennines. The issue of linking petrology and geochronology has been faced by dating a fabric-forming mineral, which is potassic white mica, through *in situ* and step-heating laserprobe Ar-Ar method. The study provides a comparison of the age distribution in mylonitc foliation and in asymmetric foliation boudins and a possible interpretation of the mylonitic ages.

Chapter 5 concerns the Alpine peak metamorphism in the chloritoid-bearing hematite-rich phyllites from the Pisani Mountains. This study investigates also the effects of different Fe_2O_3 bulk contents on the calculated phase equilibria of low-temperature/intermediate-pressure metasedimentary rocks. Thermodynamic modelling within the $MnO–Na_2O–K_2O–FeO–MgO–Al_2O_3–SiO_2–H_2O–TiO_2–O$ (MnNKFMASHTO) chemical system fails to reproduce the observed mineral compositions when the bulk Fe_2O_3 is determined through titration. The mismatch between observed and computed mineral compositions and assemblage is resolved by tuning the effective ferric iron content by P-$X$$Fe_2O_3$ diagrams. The introduction of ferric iron affects the stability of the main rock-forming silicates that often yield important thermobaric information. The use of P-T-$X$$Fe_2O_3$ phase diagrams provided chemical and thermobaric constrains about the Alpine peak conditions.

Chapter 6 presents the general conclusions. The main findings and the open questions are reported.

1.5 PUBLISHED PARTS

This thesis comprises three papers prepared for the submission to international journals. A fourth paper (chapter 4) has been already published and it has been reported unchanged into the thesis. Only the lay-out and the figure positions has been rearranged. The pubblication is:

> **Lo Pò D.** & Braga R. (2014). Influence of ferric iron on phase equilibria in greenschist-facies assemblages: the hematite-rich metasedimentary rocks from the Monti Pisani (Northern Apennines). *Journal of Metamorphic Geology*, 32, 371-387.

Participation at international and national conferences was accompanied by oral or poster presentations of some results of my PhD research. The corresponding abstract are:

Lo Pò D., Braga R., Theye T., Massonne H.-J., Montanini A., and Molli G. (2014). Linking the formation of coronitic microstructures around monazite to the growth of garnet in the Pontremoli well metapelites (Northern Apennines, Italy). *Rend. Online Soc. Geol. It.*, Suppl. n. 1 Vol. 31., p. 474. [Oral presentation at the SGI-SIMP Conference 2014]

Lo Pò D. & Braga R., (2013). Quantifying Effective Ferric Iron Content in Hematite-Rich Metapelites Through Phase Equilibria Modelling. *Mineralogical Magazine*, 77(5) 1640. [Oral presentation at the Goldschimdt 2013]

Lo Pò D., Braga R., Montanini A., and Molli G. (2012). Tectono-metamorphic evolution of medium-grade metapelites of the Northern Apennine Paleozoic Basement inferred from quantitative modeling of microstructures. *European Mineralogical Conference* Vol. 1, EMC2012-394-2. [Poster at the European Mineralogical Conference 2012]

1.6 REFERENCES

Anelli, L., Gorza, M., Pieri, M. & Riva, M., 1994. Surface well data in the Northern Apennines (Italy). *Memorie della Società Geologica Italiana,* **48**, 461-471.

Bagnoli, G., Gianelli, G., Puxeddu, M., Rau, A. &, Tongiorgi, M., 1979. A tentative stratigraphic reconstruction of the Tuscan Paleozoic basement. *Memorie della Società Geologica Italiana,***20**, 99–116.

Batini, F., Brogi, A., Lazzarotto, A., Lotta, D. & Pandeli, E., 2003. Geological features of the Larderello-Travale and Mt. Amiata geothermal areas (southern Tuscany, Italy). *Episodes,* **26**, 239-244.

Berman, R.G., 1988. Internally consistent thermodynamic data for minerals in the system $N_2O–K_2O–CaO–MgO–FeO–Fe_2O_3–Al_2O_3–SiO_2–TiO_2–H_2O–CO_2$. *Journal of Petrology,* **29**, 445–522.

Bertini, G., Elter, F.M. & Talarico, F., 1994. Evidenze di una fase estensionale pre-triassica nel complesso degli gneiss nell'area geotermica di Larderello (Toscana meridionale). *Studi Geologici. Camerti*, Vol. spec., **1**, 129–137.

Bertini, G., Casini, M., Gianelli, G. & Pandeli, E., 2006. Geological structure of a long-living geothermal system, Larderello, Italy. *Terra Nova,* **18**, 163-169.

Bigi, G., Castellarin, A., Coli, M., Dal Piaz, G. V., Sartori, R., Scandone, P. & Vai, G. B. 1990. Structural model of Italy. In: Progetto Geodinamica, SELCA, Firenze.

Boriani, A., Sassi, F.P. & Sassi, R., 2003. The basement complexes in Italy, with special regards to those exposed in the Alps: a review. *Episodes,* **26**, 186-192.

Borsi, S., Ferrara, G., Rau, A. & Tongiorgi, M., 1967. Determinazioni col metodo Rb/Sr delle filladi e quarziti listate di Buti (Monti Pisani). *Atti della Società toscana di scienze naturali, Memorie, Serie A,* **73**, 632-646.

Clemenzi, L., Molli, G., Storti, F., Muchez, P., Swennen, R. & Torelli, L., 2014. Extensional deformation structures within a convergent orogen: The Val di Lima low-angle normal fault system (Northern Apennines, Italy). *Journal of Structural Geology,* **66**, 205-222.

Cocozza, A., Jacobacci, R., Nardi, I. & Salvadori, I., 1974. Schema stratigrafico-strutturale del Massico Sardo-Corso e minerogenesi della *Memorie della Società Geologica Italiana,* **13**, 85–186.

Connolly, J. A. D., 2005. Computation of phase equilibria by linear programming: a tool for geodynamic modeling and its application to subduction zone decarbonation. *Earth and Planetary Science Letters,* **236**, 524-541.

Connolly, J.A.D. & Petrini, K., 2002. An automated strategy for calculation of phase diagram sections and retrieval of rock properties as a function of physical conditions. *Journal of Metamorphic Geology,* **20**, 697–708.

Conti, P., Costantini, A., Decandia, F.A, Elter, F.M., Gattiglio, M., Lazzarotto, A., Meccheri, M., Pandeli, E., Rau, A., Sandrelli, F., Tongiorgi, M. & Di Pisa, A., 1991a. Structural frame of the Tuscan Paleozoic: a review. *Bollettino Della Società Geologica Italiana,* **110**, 523–541.

Conti, P., Gattiglio, M. & Meccheri, M., 1991b. The overprint of the Alpine tectono-metamorphic evolution on the Hercynian orogen: an example from the Apuane Alps (Northern Apennines, Italy). *Tectonophysics,* **191**, 335–346

Conti, P., Di Pisa, A., Gattiglio, M. & Meccheri, M., 1993. The Pre-Alpine Basement in the Alpi Apuane (Northern Apennines, Italy). In Von Raumer, J. F., Neubauer, F., (eds), Pre-Mesozoic geology in the Alps. Springer Verlag, pp. 609-621.

Del Moro, A., Puxeddu, M., Radicati di Brozolo, F. & Villa, I.M., 1982. Rb-Sr and K-Ar Ages on Minerals at Temperatures of 3000-400° C from Deep Wells in the Larderello Geothermal Field (Italy). *Contributions to Mineralogy and Petrology,* **81**, 340-349.

Di Vincenzo, G., 2004. ^{40}Ar-^{39}Ar dating by laser probe: implications for the interpretation of K-Ar ages. *Atti dei Convegni Lincei,* **206**, 37-60.

Dini, A., Benvenuti, M., Lattanzi, P. & Tanelli, G., 1995. Mineral assemblages in the Hg–Zn–(Fe)–S system at Levigliani, Tuscany, Italy. *European Journal of Mineralogy,* **7**, 417-427.

Dini, A., Benvenuti, M., Costagliola, P. & Lattanzi, P., 2001. Mercury deposits in metamorphic settings: the example of Levigliani and Ripa mines, Apuane Alps (Tuscany, Italy). *Ore Geology Reviews,* **18**, 149-167.

Elter, P., 1975. L'ensemble ligure. *Bulletin de la Societe Geologique de France,* **17**, 984-997.

Elter, M. & Pandeli, E., 1990. Alpine and Hercynian orogenic phases in the basement rocks of the Northern Apennines (Larderello geothermal field, Southern Tuscany, Italy). *Eclogae Geologicae Helveticae,* **83**, 241-264.

Elter, F.M. & Pandeli, E., 2005. Structural-metamorphic correlations between three Variscan segments in Southern Europe: Maures Massif (France), Corsica (France)-Sardinia (Italy), and Northern Appennines (Italy). In The Southern

Variscan Belt, *Journal of the Virtual Explorer*, Carosi, R., Dias, R., Iacopini, D., Rosenbaum, G. (eds). Electronic Edition, ISSN 1441–8142, 19, Paper 1.

Evans, K., 2011. Metamorphic carbon fluxes: how much and how fast? *Geology,* **39**, 95-96.

Franceschelli, M. & Memmi I., 1999. Zoning of chloritoid from kyanite-facies metapsammites, Alpi Apuane, Italy. *Mineralogical Magazine,* **63**, 105–110.

Franceschelli, M., Gianelli, G., Pandeli, E. & Puxeddu, M., 2004. Variscan and Alpine metamorphic events in the northern Apennines (Italy): a review. *Periodico di Mineralogia*, **73**, 43-56.

Franceschini, F., 1998. Evidence of an extensive Pliocene-Quaternary contact metamorphism in Southern Tuscany. *Memorie della Società Geologica Italiana,* **52**, 479-492.

Gieré, R., Rumble, D.R., Gunther, D., Connolly, J.A.D. & Caddick, M.J., 2011. Correlation of Growth and Breakdown of Major and Accessory Minerals in Metapelites from Campolungo, Central Alps. *Journal of Petrology,* **52**, 2293-2334.

Giorgetti, G., Goffé, B., Memmi, I. & Nieto, F., 1998. Metamorphic evolution of Verrucano metasediments in Northern Apennines: new petrological constraints. *European Journal of Mineralogy,* **9**, 859-873.

Holland, T.J.B. & Powell, R., 1998. An internally consistent thermodynamic data set for phases of petrological interest. *Journal of Metamorphic Geology,* **16**, 309–343.

Holland, T. J. B. & Powell, R., 2011. An improved and extended internally consistent thermodynamic dataset for phases of petrological interest, involving a new equation of state for solids. *Journal of Metamorphic Geology,* **29**, 333-383.

Janots, E., Negro, F., Brunet, F., Goffé, B., Engi, M. & Bouybaouene, M. L., 2006. Evolution of the REE mineralogy in HP–LT metapelites of the Sebtide complex, Rif, Morocco: monazite stability and geochronology. *Lithos,* **87**, 214–234.

Janots, E., Brunet, F., Goffé, B., Poinssot, C., Burchard, M. & Cemic, L., 2007. Thermochemistry of monazite-(La) and dissakisite-(La): implications for monazite and allanite stability in metapelites. *Contributions to Mineralogy and Petrology,* **154**, 1–14.

Jolivet, L., Faccenna, C., Goffè, B., Mattei, M., Rossetti, F., Brunet, C., Storti, F., Funiciello, R., Cadet, J.P., D'Agostino, N. & Parra, T., 1998. Midcrustal shear

zones in postorogenic extension: example from the northern Tyrrenian Sea. *Journal of Geophysical Research,* **103**, 12123–12160.

Kelly, N. M., Clarke, G. L. & Harley, S. L., 2006. Monazite behaviour and age significance in poly-metamorphic high-grade terrains: a case study from the western Musgrave Block, central Australia. *Lithos,* **88**, 100-134.

Kelsey, D. E., Clark, C. & Hand, M., 2008. Thermobarometric modelling of zircon and monazite growth in melt-bearing systems: Examples using model metapelitic and metapsammitic granulites. *Journal of Metamorphic Geology,* **26**, 199-212.

Kligfield, R., Hunziker, J, Dallmeyer, R.D. & Schamel, S. 1986. Dating of deformational phases using K-Ar and ^{40}Ar/^{39}Ar techniques: results from the Northern Apennines. *Journal of Structural Geology,* **8**, 781-798.

Langone, A., Braga, R., Massonne, H.-J. & Tiepolo, M., 2011. Preservation of old (prograde metamorphic) U-Th-Pb ages in unshielded monazite from the high-pressure paragneisses of the Variscan Ulten Zone (Italy). *Lithos,* **127**, 68-85.

Leoni, L., Montomoli, C. & Carosi R., 2009. Il metamorfismo delle unità tettoniche dei Monti Pisani (Appennino Settentrionale). *Atti della Società toscana di scienze naturali, Memorie, Serie A,* **114**, 61-73.

Massonne, H.-J., 2014. Wealth of P-T-t information in medium-high grade metapelites: example from the Jubrique Unit of the Betic Cordillera, S Spain. *Lithos,* **208-209**,137-152.

McDougall, I. & Harrison, T. M., 1999. Geochronology and Thermochronology by the ^{40}Ar/^{39}Ar Method. Oxford University Press, pp. 269.

Molli, G., 2008. Northern Apennine–Corsica orogenic system: an updated overview. *Geological Society, London, Special Publications,* **298**, 413-442.

Molli, G., Montanini, A. & Frank W., 2002. MORB-derived Varisican amphibolites in the Northern Apennine Basement: the Cerreto metamorphic slices (Tuscan-Emilian Apennine, NW Italy). *Ofioliti,* **27**, 17-30.

Montel, J.-M., Foret, S., Veschambre, M., Nicollet, C. & Provost, A., 1996. Electron microprobe dating of monazite. *Chemical Geology,* **131**, 37-53.

Musumeci G., Bocini L. & Corsi R., 2002. Alpine tectonothermal evolution of the Tuscan Metamorphic Complex in the Larderello geothermal field (northern Apennines, Italy). Journal of the Geological Society, London, **159**, 443-456.

Musumeci, G., Mazzarini, F., Tiepolo, M. & Di Vincenzo, G., 2011. U-Pb and ^{40}Ar-^{39}Ar geochronology of Palaeozoic units in the northern Apennines: determining

protolith age and alpine evolution using the Calamita Schist and Ortano Porphyroid. *Geological Journal, 46*, 288-310.

Padovano, M., Elter, F. M., Pandeli, E. & Franceschelli, M., 2012. The East Variscan Shear Zone: new insights into its role in the Late Carboniferous collision in southern Europe. *International Geology Review, 54*, 957-970.

Pandeli, E., Gianelli, G., Puxeddu, M. & Elter, F. M., 1994. The Paleozoic basement of the Northern Apennines: stratigraphy, tectono-metamorphic-sedimentary evolution and Alpine hydrothermal processes. *Memorie della Società Geologica Italiana, 48*, 627-654.

Pandeli E., Gianelli G. & Morelli M., 2005. The crystalline units of the middle-upper crust of the Larderello geothermal region (southern Tuscany, Italy): new data for their classification and tectono-metamorphic evolution.). *Bollettino Società Geologica Italiana volume spec*iale, **3**, 139-155.

Patacca, E. & Scandone, P., 1989. Post-Tortonian mountain building in the Apennines: the role of the passive sinking of a relic lithospheric slab. In *The Lithosphere in Italy: Advances in Earth Science Research*, eds. A. Boriani, M. Bonafede, G. B. Piccardo and G. B. Vai, Vol. 80, 157-176. Accademia Nazionale dei Lincei, Rome.

Powell, R. & Holland, T.J.B., 2008. On thermobarometry. *Journal of Metamorphic Geology*, **26**, 155-179.

Pyle, J.M. & Spear, F.S., 2000. An empirical garnet (YAG) ± xenotime thermometer. *Contributions to Mineralogy and Petrology,* **138**, 51–58.

Rasmussen, B. & Muhling, J.R., 2007. Monazite begets monazite: evidence for the dissolution of detrital monazite and reprecipitation of syntectonic monazite during low-grade regional metamorphism. *Contributions to Mineralogy and Petrology,* **154**, 675–689.

Rau, A., 1990. Evolution of the Tuscan domain between the Upper Carboniferous and the Middle Triassic: a new hypothesis. *Bollettino Società Geologica Italiana,* **109**, 231-238.

Rau, A., 1993. Il Paleozoico toscano: da segmento della catena Varisica sud-europea a margine passivo alpidico peri-adriatico. *Memorie della Società Geologica Italiana, 49*, 325-334.

Rau, A., M. & Tongiorgi, M., 1966. Considerazioni preliminari sulla geologia della parte meridionale dei Monti Pisani (versante SW). *Memorie della Società Geologica Italiana, 5*, 300-314.

Rau, A. & Tongiorgi, M., 1974. La geologia dei Monti Pisani a Sud-Est della Valle del Guappero. *Memorie della Società Geologica Italiana, 13*, 227-408.

Rossetti, F., Balsamo, F. & Villa, I. M., Bouybaouenne, M., Faccenna, C., Funiciello, R., 2008. Pliocene–Pleistocene HT–LP metamorphism during multiple granitic intrusions in the southern branch of the Larderello geothermal field (southern Tuscany, Italy). *Journal of the Geological Society, 165*, 247-262.

Spear, F.S. & Pyle, J. M., 2010. Theoretical modeling of monazite growth in a low-Ca metapelite. *Chemical Geology, 273*, 111-119.

Spear, F.S., 1993. Metamorphic phase equilibria and pressure-temperature-time paths. Mineralogical society of America, Washington D.C., pp.799.

Theye, T., Reinhardt, J., Goffé, B., Jolivet, L. & Brunet, C. 1997. Ferro and magnesiocarpholite from Mt. Argentario (Italy): first evidence for high-pressure metamorphism of the metasedimentary Verrucano sequence, and significance for P-T path reconstruction. *European Journal of Mineralogy, 9*, 859-873.

Tongiorgi, M. & Bagnoli, G., 1981. Stratigraphie du socle paléozoïque de la bordure continentale de l'Apennin septentrional (Italie centrale). *Bulletin de la Societe Geologique de France, 4*, 319-323.

Vai, G. B., 2001. Basement and early (pre-Alpine) history. In *Anatomy of an orogen: The Apennines and adjacent Mediterranean basins* (pp. 121-150). Springer Netherlands.

Vai, G.B., 1978. Tentative correlation of Paleozoic rocks, Italian Peninsula and Islands, *Oest. Akad. Wiss. Schrift. Erdw. Kom. 3*, 313–329.

Vai, G.B. & Martini, I.P., 2001. Anatomy of an Orogen: the Apennines and Adjacent Mediterranean Basins, Kluwer Academic Publishers, pp. 632.

Vance, D., Müller, W. & Villa, I.M., 2003. Geochronology: linking the isotopic record with petrology and textures - an introduction. In Vance, D., Midller, W., Villa, I. M. (eds) 2003. Geochronology: Linking the Isotopic Record with Petrology and Textures. *Geological Society, London, Special Publications, 220*, 1-24.

Williams, M.L. & Jercinovic, M.J., 2012. Tectonic interpretation of metamorphic tectonites: integrating compositional mapping, microstructural analysis and in situ monazite dating. *Journal of Metamorphic Geology, 30*, 739-752.

Williams, M. L., Jercinovic, M. J. & Hetherington, C. J., 2007. Microprobe monazite geochronology: understanding geologic processes by integrating composition and chronology. *Annual Review of Earth and Planetary Sciences,* **35**, 137-175.

Insights into the Variscan orogeny:

The tectono-metamorphic evolution of the Cerreto micaschist

CHAPTER 2

INSIGHTS INTO THE VARISCAN OROGENY:

THE TECTONO-METAMORPHIC EVOLUTION OF THE CERRETO MICASCHIST

2.1 INTRODUCTION

Medium-grade mylonitic metapelite can preserve several textural domains related to different stages of the tectono-metamorphic evolution. Sometimes even mineral assemblages formed during prograde-metamorphism are not totally obliterated. A detailed microstructural analysis is the essential basis to link the mineral assemblage (effect of the metamorphism) with the fabric (effect of the deformation) and thus to reconstruct the tectono-metamorphic evolution (Passchier & Trouw, 2005). Then thermodynamic modelling allows to associate Pressure and Temperature constrains for each microstructure and metamorphic stage by comparing the observed mineral assemblages and compositions in distinct microstructural positions with the computed ones in *P-T* phase diagrams (Powell & Holland, 2008). Therefore thermodynamic modelling coupled with a detailed microstructural analysis is a powerful tool to reconstruct Pressure-Temperature-Deformation paths (Williams & Jercinovic, 2012).

A combined microstructural-petrological study on the micaschist from the Cerreto Pass provides new *P-T* constraints for the recognized metamorphic-deformational phases. The studied samples belong to the Northern Apennines Variscan basement, a remnant of the southern segment of the Variscan chain now reworked within the northern Apennines nappe stack. Classical geothermobarometry has already been applied on this crustal sector (Molli *et al.*, 2002). However, pseudosections are a better approach for quantifying the Pressure-Temperature variations during the metamorphic evolution since they report all the possible paragenesis along a path (Powell and Holland, 2008). Even if the Cerreto micaschist exhibit a strong mylonitic fabric, relics of the earlier stages were recognized and used to constrain the prekinematic history. In particular the pre-peak stage, never constrained before, points to a thickening process at middle crustal depths during the Variscan collision with the burial of this crustal sector up to 45 km depth. The peak stage, attained at 600°C, was followed by exhumation along

ductile shear zones. The strong deformation in this stage is responsible for the well developed mylonitic fabric.

2.2 GEOLOGICAL FRAMEWORK

The Northern Apennines are an Alpine orogenetic belt generated after the collision between Europe (the Sardinia-Corsica block) and Africa (the Adria microplate) from Oligocene times (Vai & Martini, 2001).

The Northern Apennine nappe-pile edifice consists of oceanic and continental units (from top to bottom): (1) Liguride Units: ophiolitic rocks derived from a branch of the Western Tethys ocean; (2) Tuscan Unit: a continental Triassic-Tertiary sedimentary sequence unaffected by the Alpine metamorphism; (3) Tuscan Metamorphic Units: Variscan basement with its Triassic-Oligocene cover, belonging to the Adria-derived continental sequence and affected by the Alpine metamorphism.

The Variscan basement (Franceschelli *et al.*, 2004) is present in scattered outcrops in the Cerreto Pass (Fig. 2.1a), in the Tuscan Metamorphic Ridge in the subsurface of the Larderello and Pontremoli areas (Fig. 2.1b). The Cerreto metamorphic rocks represent the northernmost occurrence of the Northern Apennines Variscan basement. They consist of mylonitic micaschist with minor lenses of mafic amphibolite. Some micaschist contain garnet porphyroclasts while others exhibit a strong mylonitic fabric, accompanied by retrogression of garnet to chlorite. The main foliation in amphibolite was dated at 312-328 Ma by Ar-Ar on hornblende
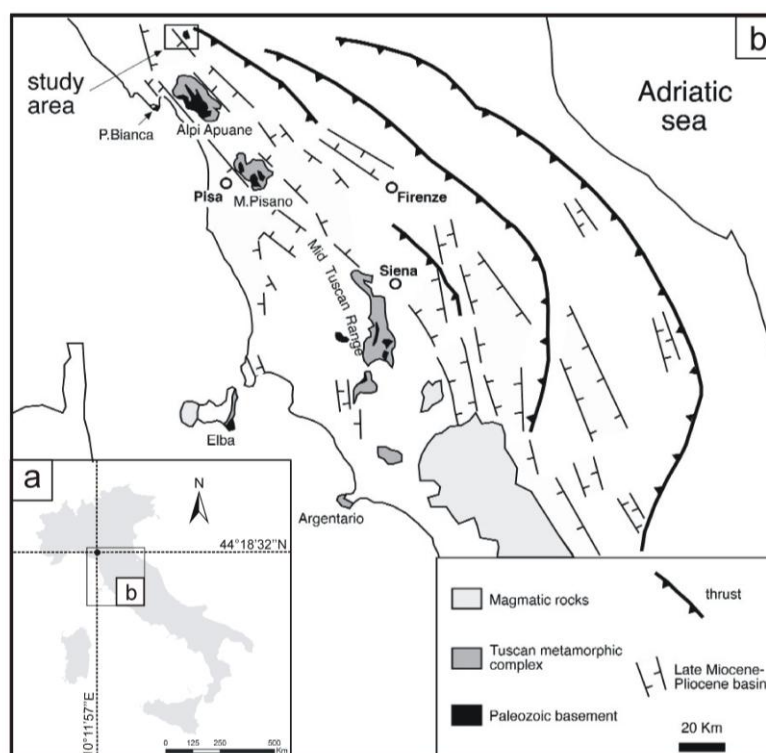
Figure 2.1 Regional geological framework of the study area (Molli et al., 2002): (a) location of the Cerreto outcrop; (b) distribution of the Paleozoic basement in the Northern Apennines with the sampling site.

separates (Molli *et al.*, 2002) and formed at 630°C and 8.5 kbar. This confirms that the Cerreto metamorphic rocks were involved in the collisional stage of the Southern Europe Variscides (Molli *et al.*, 2002).The mylonitic retrograde stage likely occurred in a post-collision setting at 530°C and 4-5 kbar (Molli *et al.*, 2002).

2.3 ANALYTICAL METHODS

Petrographic observation and microstructural analysis were performed with a polarising optical microscope and a scanning electron microscope Philips 515B at the Dipartimento di Scienze Biologiche, Geologiche ed Ambientali (Università di Bologna). Mineral chemistry was acquired using a CAMECA SX100 electron microprobe (EMP) equipped with five wavelength dispersive (WDS) spectrometers at the Institut für Mineralogie und Kristallchemie (Universität Stuttgart). Na, Mg, Al, Si, K, Ca, Ti, Mn, Fe, Ba were analysed in potassic white mica, chlorite, biotite, garnet, plagioclase at acceleration voltage 15 kV and primary electric current 10-15 nA. Counting times for each element element were 20 s at the peak and the background. Mg, Al, Si, Ca, Ti, Mn, Fe, Cr were analysed in garnet at acceleration voltage 15 kV and primary electric current 15 nA. Synthetic and natural minerals and pure oxides were used as standards. The PaP correction procedure was applied. X-ray maps for Fe, Mn, Mg, Ca in garnet were acquired with a counting time of 50 ms and a step width of 6 μm. Acceleration voltage and electric current are 15 kV and 70 nA, respectively. Fe, Mg, Ti, Na X-ray maps in potassic white mica were acquired using a counting time of 100 ms, a step width of 1 μm, an acceleration voltage of 15 kV and a current of 30 nA. Structural formulae for potassic white mica, chlorite, garnet, plagioclase, biotite were calculated with CalcMin program (Brandelik, 2009), while X-ray map images were elaborated with XMap software (Bernhardt *et al.,* 1995).

The bulk-rock composition was determined through WD-XRF analysis on pressed powder pellets using a Philips PW1480 and an Axios-Panalytical spectrometers at the Department of Biological, Geological and Environmental Sciences, Bologna University. Loss on ignition (L.O.I.) was obtained with standard gravimetric procedures, after heating the powder at 950 °C for 12 h.

2.4 PETROGRAPHY

The Micaschist Complex from the Cerreto Pass consists of mylonitic micaschist with pre-kinematic microstructures (Fig 2.2a, b, c, d) and a shearing fabric (Fig. 2.2e, f, g, h). Ultramylonitic levels cut occasionally the mylonitic foliation.

Two samples were studied in detail: PC1 which is a garnet-free micaschist showing a well developed mylonitic foliation, and CER8 which is a garnet-bearing micaschist already described in Molli *et al.* (2002).

PC1 shows quartz porphyroclasts and mica-fishes wrapped by a fine-grained potassic white mica-chlorite mylonitic foliation. The quartz porphyroclasts host chlorite and potassic white mica inclusions.

Large polygonized quartz crystals surrounded by quartz subgrains with suturated grain boundaries form bands (Fig. 2g). The mylonitic foliation is locally crenulated (Fig. 2.2f) or associated with C'-shear bands. Asymmetric foliation boudins consisting of potassic white mica aggregates are also present. Garnet is totally pseudomorphosed by chlorite. Plagioclase grains are poorly present in the mylonitic foliation. Ilmenite, rutile, titanite, allanite, epidote, pyrite, tourmaline, apatite and zircon are the accessory minerals. Ilmenite is xenoblastic and forms also fish-shaped crystals and boudins (Fig. 2.2d). It contains inclusions of biotite. Titanite forms crystals parallel to the mylonitic foliation. An ilmenite crystal, with a rutile core and titanite rim is observed (Fig. 2.2h). Allanite cores are surrounded by epidote rims. In this section an epidote-albite vein is also present.

Figure 2.2 (next page) Petrographic features of the Cerreto micashist: (a) σ-type quartz mantled-porphyroclast (CER8; crossed polars photomicrograph); (b) biotite inclusions in a plagioclase porphyroclast (CER8; crossed polars photomicrograph); (c) fractured and partially retrogressed garnet porphyroclast (CER8; crossed polars photomicrograph); (d) mica-fish and ilmenite-fish (PC1; BSE image); (e) C'-type shear bands (CER8; photomicrograph with plane polarized light); (f) hinge of a fold in the mylonitic foliation (PC1; BSE image); (g) oblique foliation constitutes by aligned quartz subgrains with suturated grain boundaries (CER8; crossed polars photomicrograph); (h) rutile core in an ilmenite crystal surrounded by titanite rim (PC1; BSE image). Abbreviations of minerals: Pl = plagioclase, Bt = biotite, Ms = K white mica, Ilm = ilmenite, Rt = rutile, Ttn = titanite.
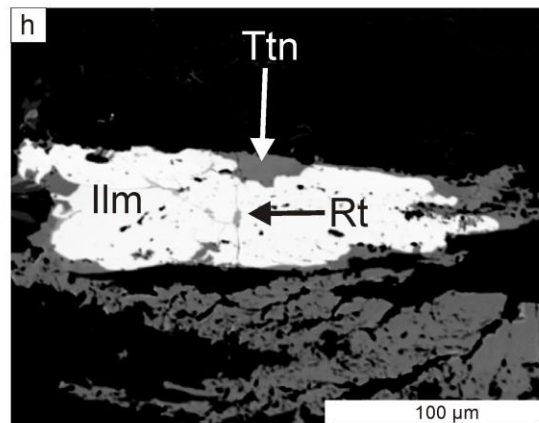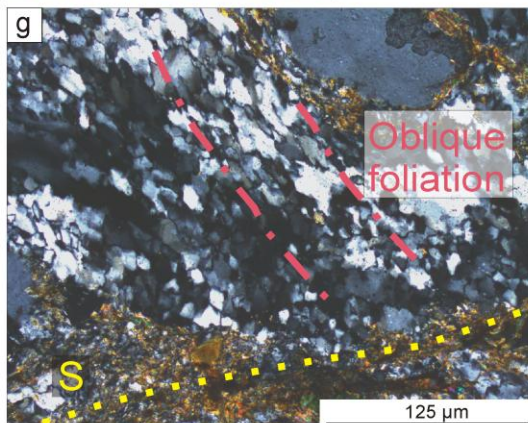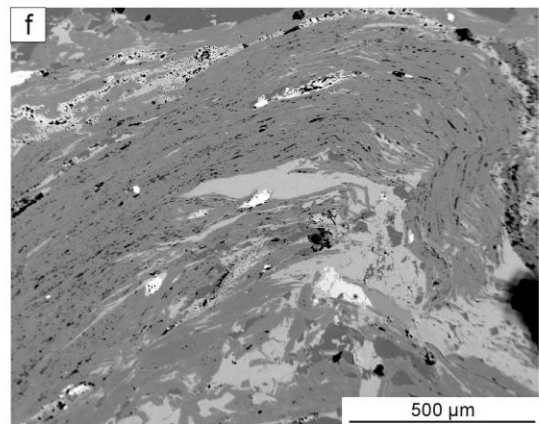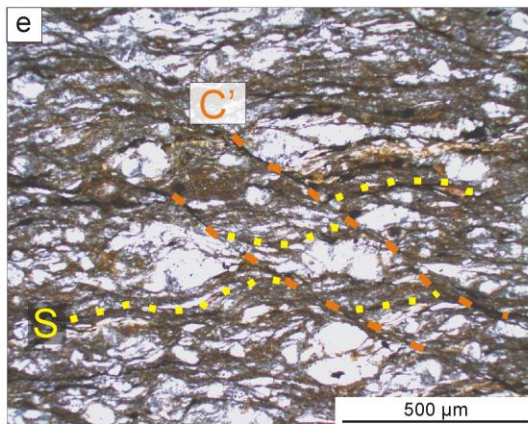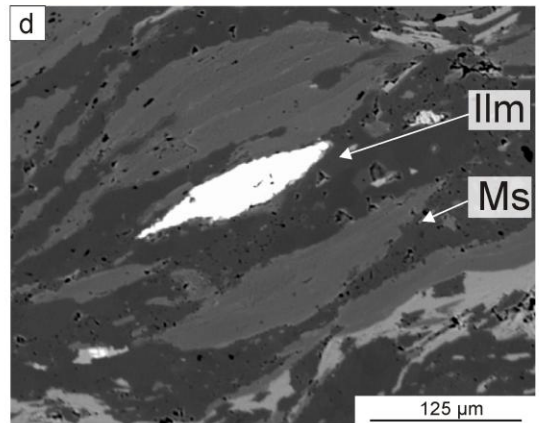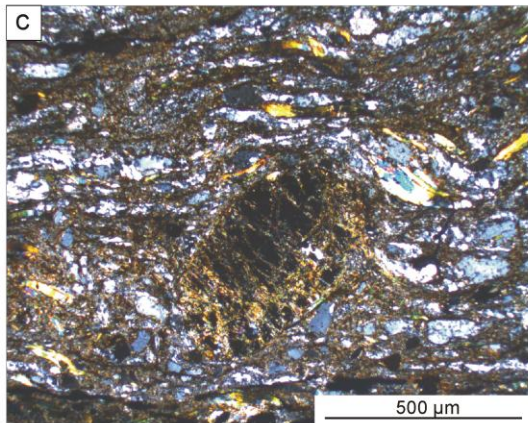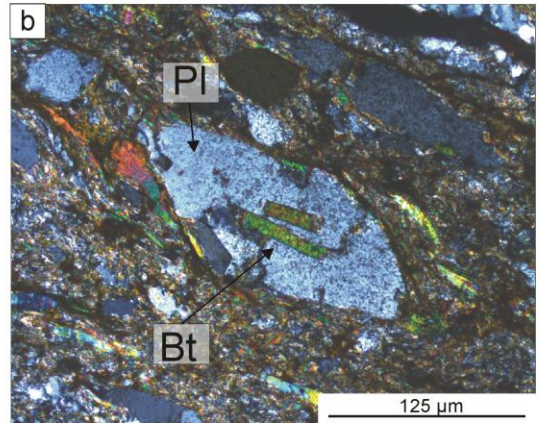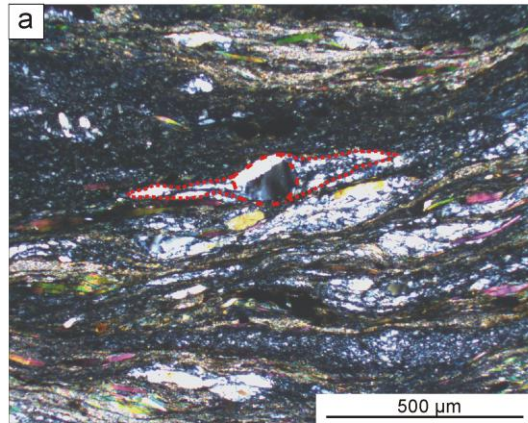
CER8 contains a fine-grained potassic white mica-biotite-chlorite mylonitic foliation (Fig. 2.2e) and pre-kinematic crystals, consisting of mica fishes and quartz, plagioclase and garnet porphyroclasts (Fig. 2.2a, c). Ilmenite, rutile, epidote, allanite, zircon, tourmaline, titanite, chalcopyrite, pyrite, microcline and apatite are accessory minerals. Biotite fishes host plagioclase and zircon inclusions (Fig. 2.2b). Plagioclase porphyroclasts contain inclusions of biotite, apatite and rutile. Garnet porphyroclasts are fractured and partly retrogressed to chlorite (Fig. 2.2c). Ilmenite, quartz and zircon are enclosed in garnet. Recrystallized quartz grains define an oblique foliation (Fig. 2.2g). Rutile cores with ilmenite rims and ilmenite boudins have been observed in both garnet rim and matrix. Epidote and allanite are present both in the mylonitic foliation and in ultramylonitic levels associated with fine-grained chlorite.

2.5 MINERAL AND ROCK COMPOSITION

PC1

Prekinematic potassic white mica has Mg-rich cores and Na-rich rims (Fig. 2.3a, b). The Mg-rich prekinematic potassic white mica has Si=3.17-3.30 apfu, Mg=0.14-0.22 apfu and Na=0.04-0.06 apfu. Na/(Na+K) is 0.04-0.06. The Na-rich prekinematic potassic white mica contains Si=3.03-3.13 apfu, Mg=0.05-0.08 apfu, Na=0.15.0.27 apfu and Na/(Na+K)=0.05-0.27. Potassic white mica lying along the mylonitic foliation has a more variable composition: Si ranges from 3.06 to 3.19 apfu, Mg is 0.06-0.23 apfu, Na is 0.02-0.10 apfu and Na/(Na+K) is 0.02-0.10 (Fig. 2.4a, b, c, d; Tab. 2.1). Chlorite has Si=5.15-5.93 apfu, Al^{IV} =2.07-2.85 apfu, Al^{VI} =2.21-3.34 apfu and Fe/(Fe+Mg)=0.50-0.60 (Tab. 2.1). Feldspar grains are albite ($Ab_{94-99}An_{0-5}Or_{0-4}$) and contain K- feldspar exsolutions ($Ab_{0-1}An_{2-5}Or_{95-97}$). The bulk-composition (Tab. 2.3) is similar to PAAS (Post-Archean Australian Shale; Taylor & McLennan, 1985) and UCC (Upper Continental Crust; McLennan, 2001), excepting for CaO, which is depleted in PC1. In the Fe_2O_3/K_2O *vs* SiO_2/Al_2O_3 diagram (Herron, 1988) the composition of PC1 plots in the wacke-shale boundary.

Table 2.1 Mineral compositions of potassic white mica, chlorite and feldspar in PC1. The formula of potassic white mica is calculated assuming 42- (Ca+ Ba) valencies and 4 H. Fe^{3+} is stoichiometric-estimated considering $Fe^{3+} = 42 -$ sum of the valencies (Si, Ti, Cr, Al, Mn, Mg, Fe)-Ba-Ca. The structural formula of chlorite is calculated on the basis of 28 oxygen and neglecting Na and Ca. Chlorite is assumed as completely idratated, with 16 H. The structural formula of plagioclase is based on 8 oxygen.

K-white mica									
	Prekinematic Mg-rich core			Prekinematic Na-rich rim			Mylonitic foliation		
Point analyses	Ms11_4	Ms11_5	Ms11_6	Ms08_1	Ms9_2	Ms9_3	Ms10_01	Ms10_02	Ms10_03
SiO_2	50.13	49.69	50.62	46.40	47.05	46.38	46.39	45.55	45.10
TiO_2	0.30	0.33	0.38	0.14	0.46	0.40	0.37	0.36	0.31
Al_2O_3	31.45	31.33	30.95	34.78	35.45	36.15	33.85	34.50	34.12
FeO	1.64	1.43	1.66	2.15	1.09	0.98	1.87	1.33	1.69
Fe_2O_3	n.c.	n.c.	n.c.	n.c.	n.c.	n.c.	n.c.	n.c.	n.c.
MnO	0.05	n.d.	n.d.	n.d.	n.d.	n.d.	0.04	n.d.	n.d.
MgO	2.04	1.94	2.30	1.10	0.87	0.72	1.19	0.78	0.95
CaO	0.04	0.03	0.01	n.d.	0.03	0.01	0.02	0.01	0.01
Na_2O	0.42	0.39	0.39	0.35	0.92	0.91	0.33	0.43	0.33
K_2O	10.56	10.76	10.46	10.94	10.56	10.35	10.65	10.93	10.60
BaO	0.19	0.20	0.15	0.35	0.24	0.27	0.34	0.25	0.32
Total	96.82	96.11	96.91	96.20	96.67	96.18	95.04	94.13	93.44
Si	3.274	3.274	3.295	3.085	3.094	3.060	3.112	3.088	3.079
Al^{IV}	0.726	0.726	0.705	0.915	0.906	0.940	0.888	0.912	0.921
Ti	0.015	0.016	0.019	0.007	0.023	0.020	0.019	0.018	0.016
Al^{VI}	1.695	1.707	1.668	1.810	1.841	1.870	1.787	1.844	1.823
Fe^{2+}	0.089	0.079	0.090	0.120	0.060	0.054	0.105	0.075	0.096
Fe^{3+}	n.c.	n.c.	n.c.	n.c.	n.c.	n.c.	n.c.	n.c.	n.c.
Mn	0.003	n.c.	n.c.	n.c.	n.c.	n.c.	0.002	n.c.	n.c.
Mg	0.199	0.191	0.223	0.109	0.085	0.071	0.119	0.079	0.097
Ca	0.003	0.002	0.001	n.c.	0.002	0.001	0.001	0.001	0.001
Ba	0.005	0.005	0.004	0.009	0.006	0.007	0.009	0.007	0.009
Na	0.054	0.050	0.049	0.045	0.117	0.117	0.043	0.056	0.044
K	0.880	0.905	0.869	0.927	0.886	0.871	0.912	0.945	0.923

Table 2.1 continued

| Point analyses | Chlorite | | | | Feldspar | | | | |
| | Mylonitic foliation | | | | Mylonitic foliation | | | Within plagioclase | |
	Chl06_02	Chl06_03	Chl06_04	Chl06_05	Pl01	Pl06_10	Pl03	Kfs03	Kfs04
SiO_2	24.20	24.41	23.93	25.67	68.03	68.27	67.94	64.39	65.00
TiO_2	0.06	0.06	0.07	0.07	0.07	0.00	0.10	0.00	0.00
Al_2O_3	22.05	22.06	22.07	21.85	20.71	20.05	20.97	18.52	18.30
FeO^{tot}	28.85	28.88	28.87	28.49					
Fe_2O_3					0.45	0.09	0.31	0.27	0.28
MnO	0.21	0.23	0.23	0.26					
MgO	12.55	12.89	12.52	12.20	n.d.	n.d	0.03	n.d	0.01
CaO					0.84	0.67	1.11	0.02	n.d
Na_2O					11.67	11.59	11.55	0.54	0.31
K_2O					0.10	0.07	0.11	16.54	16.39
BaO					0.00	0.00	0.00	0.33	0.17
Total	87.91	88.53	87.69	88.54	101.88	100.73	102.12	100.61	100.45
Si	5.193	5.199	5.154	5.432	2.933	2.967	2.923	2.977	2.997
Ti	0.010	0.010	0.011	0.011	0.002	0.000	0.003	0.000	0.000
Al	5.576	5.536	5.603	5.449	1.052	1.027	1.063	1.009	0.994
Fe^{3+}					0.014	0.003	0.010	0.010	0.010
Fe^{tot}	5.178	5.143	5.201	5.042					
Mn	0.037	0.041	0.042	0.047					
Mg	4.015	4.093	4.022	3.850					
Ca					0.039	0.031	0.051	0.001	n.c.
Na					0.976	0.977	0.963	0.048	0.027
K					0.006	0.004	0.006	0.975	0.964
Ba					n.c.	n.c.	n.c.	n.c.	n.c.
An					0.038	0.031	0.050	0.007	0.003
Ab					0.956	0.966	0.944	0.047	0.027
Or					0.006	0.004	0.006	0.947	0.969

CER8

Pre-kinematic potassic white mica shows compositional variations: the core is characterised by higher contents of Ti, Fe and Mg, while the rim is richer in Na (Tab. 2.2). Specifically, the core contains Si=3.12-3.22 apfu, Fe=0.11-0.14 apfu, Mg=0.18-0.24 apfu, Ti=0.04-0.06 apfu, Na=0.09-0.12 apfu, while the rims have Si=3.05-3.12 apfu, Fe=0.06-0.10 apfu, Mg=0.07-0.13 apfu, Ti=0.03-0.04 apfu, Na=0.03-0.13 apfu. Potassic white mica along the mylonitic foliation is characterized by scattered compositions, with Si=3.04-3.13 apfu, Fe=0.03-0.14 apfu, Mg=0.11-0.25 apfu, Ti=0.02-0.06 apfu, Na=0.03-0.06 apfu. Pre-kinematic biotite has XFe=0.48-0.52. XFe in mylonitic biotite is 0.52-0.57. Biotite deriving from garnet retrocession has Si=2.79-2.92 apfu and XFe=0.51-0.55. Mylonitic chlorite contains Si=5.30-5.35 apfu, Al^{IV} =2.65-2.70 apfu, Al^{VI} =2.61-2.75 apfu and XFe=0.47-0.48. Plagioclase included into mica-fishes ($Ab_{77-83}An_{16-22}Or_1$) and porphyroclasts ($Ab_{72-86}An_{14-27}Or_{0-3}$) are oligoclase. Microcline porphyroclasts in the matrix ($Ab_{1-9}An_{0-2}Or_{90-98}$) are also observed. Garnet shows a prograde growth zoning (Fig. 2.3c, d), ranging from $Alm_{62}Grs_{20}Prp_9Sps_8$ in the core to $Alm_{68}Grs_{18}Prp_{12}Sps_2$ in the rim (Fig. 2.4d; Tab. 2.2). The bulk-composition of

CER8 (Tab. 2.3) normalized to PAAS and UCC shows a depletion in MnO and CaO and an enrichment in MgO. The CER8 micaschist derives from a wacke-shale protolith according to the Fe_2O_3/K_2O vs SiO_2/Al_2O_3 diagram (Herron, 1988).

Table 2.2 Structural formulae of potassic white mica and garnet in CER8. The structural formula of potassic white mica is calculated assuming 42- (Ca+ Ba) valencies and 4 H. Fe^{3+} is stoichiometric-estimated considering $Fe^{3+} = 42$ – sum of the valencies (Si, Ti, Cr, Al, Mn, Mg, Fe)-Ba-Ca. The garnet formula is normalized on 8 cations. Fe^{3+} is equal to 4 – Al.

K-white mica									
	Prekinematic core			Prekinematic rim			Mylonitic foliation		
Point analyses	Ms13_08	Ms16	Ms17	Ms04	Ms01_09	Ms01_10	Ms20	Ms90fm	Ms97fm
SiO_2	47.82	47.83	48.19	46.58	46.43	46.71	46.04	45.97	46.08
TiO_2	0.92	1.04	0.98	0.56	0.53	0.67	0.56	0.49	0.58
Al_2O_3	32.43	33.00	33.07	35.08	35.44	34.94	34.34	33.45	32.38
FeO	1.90	1.71	1.58	1.39	1.38	1.43	2.02	2.38	2.19
Fe_2O_3	n.c.	n.c.	n.c.	n.c.	n.c.	n.c.	n.c.	n.c.	n.c.
MnO	0.01	n.d.	n.d.	0.01	n.d.	0.02	0.01	0.05	0.02
MgO	1.75	1.63	1.48	1.08	0.94	1.02	1.23	1.55	1.62
CaO	0.03	0.03	0.00	n.d.	n.d.	n.d.	n.d.	0.05	0.13
Na_2O	0.72	0.88	0.71	0.98	0.98	0.98	0.36	0.27	0.33
K_2O	9.94	9.84	10.19	9.83	10.05	10.08	10.62	10.35	10.49
BaO	0.86	0.83	0.83	1.00	0.97	0.93	1.20	1.26	1.35
Total	96.37	96.79	97.03	96.50	96.72	96.75	96.38	95.81	95.18
Si	3.167	3.150	3.166	3.080	3.069	3.086	3.076	3.091	3.131
Al^{IV}	0.833	0.850	0.834	0.920	0.931	0.914	0.924	0.909	0.869
Ti	0.046	0.052	0.048	0.028	0.027	0.033	0.028	0.025	0.030
Al^{VI}	1.698	1.712	1.726	1.814	1.829	1.807	1.780	1.742	1.724
Fe^{2+}	0.105	0.094	0.087	0.077	0.076	0.079	0.113	0.134	0.124
Fe^{3+}	n.c.	n.c.	n.c.	n.c.	n.c.	n.c.	n.c.	n.c.	n.c.
Mn	0.001	n.c.	n.c.	0.001	n.c.	0.001	0.001	0.003	0.001
Mg	0.173	0.160	0.145	0.106	0.092	0.100	0.123	0.156	0.164
Ca	0.002	0.002	0.000	0.000	n.c.	n.c.	n.c.	0.004	0.009
Ba	0.022	0.021	0.021	0.026	0.025	0.024	0.031	0.033	0.036
Na	0.093	0.113	0.090	0.125	0.126	0.125	0.047	0.035	0.044
K	0.839	0.827	0.854	0.829	0.847	0.849	0.905	0.888	0.910

Table 2.2 continued

Garnet									
		inner core			outer core			rim	
Point analyses	Grt10	Grt11	Grt16	Grt21	Grt24	Grt25	Grt27	Grt28	Grt29
SiO_2	36.92	37.17	36.42	36.17	35.53	36.18	36.40	36.83	36.85
TiO_2	0.27	0.27	0.28	0.11	0.09	0.10	0.13	0.13	0.12
Al_2O_3	21.40	21.27	20.99	21.21	21.06	21.19	21.29	21.42	21.32
Cr_2O_3	0.02	0.03	0.02	0.02	0.02	n.d.	0.02	0.01	0.02
Fe_2O_3	0.23	0.68	0.92	0.55	0.71	0.65	0.28	0.49	0.35
FeO	28.43	28.72	28.60	30.24	30.55	30.56	31.35	31.28	31.12
MnO	3.77	3.83	3.28	2.24	1.48	1.21	0.87	0.88	0.86
MgO	2.39	2.45	2.63	2.96	2.92	2.99	2.74	2.99	2.99
CaO	7.00	6.89	6.97	6.08	6.39	6.63	6.41	6.52	6.38
Na_2O	0.04	0.05	0.04	0.02	0.02	0.03	0.04	0.04	0.04
Total	100.46	101.35	100.15	99.59	98.79	99.54	99.52	100.58	100.05
Si	5.812	5.809	5.725	5.691	5.603	5.682	5.750	5.752	5.800
Ti	0.032	0.031	0.034	0.013	0.011	0.012	0.015	0.015	0.014
Al	3.971	3.917	3.889	3.932	3.914	3.923	3.965	3.942	3.956
Cr	0.002	0.003	0.003	0.003	0.002	n.c.	0.002	0.001	0.003
Fe^{3+}	0.027	0.080	0.109	0.065	0.084	0.077	0.033	0.058	0.042
Fe^{2+}	3.743	3.754	3.760	3.979	4.028	4.014	4.141	4.084	4.097
Mn	0.503	0.507	0.437	0.298	0.198	0.161	0.116	0.116	0.115
Mg	0.560	0.570	0.616	0.693	0.687	0.700	0.645	0.697	0.701
Ca	1.180	1.154	1.175	1.024	1.080	1.115	1.085	1.091	1.076
Na	0.013	0.015	0.012	0.005	0.007	0.010	0.013	0.012	0.011
Grs	0.20	0.19	0.20	0.17	0.18	0.19	0.18	0.18	0.18
Prp	0.09	0.10	0.10	0.12	0.11	0.12	0.11	0.12	0.12
Alm	0.62	0.63	0.63	0.66	0.67	0.67	0.69	0.68	0.68
Sps	0.08	0.08	0.07	0.05	0.03	0.03	0.02	0.02	0.02

Table 2.3 Bulk-rock composition of PC1 and CER8 determined through WD-XRF analysis and modified for thermodynamic modelling.

	XRF		Thermodynamic modelling	
	PC1	CER8	PC1	CER8
	wt. %	wt. %	wt. %	wt. %
SiO_2	67.74	63.29	70.53	65.48
TiO_2	0.85	0.90	0.89	0.93
Al_2O_3	16.90	14.47	17.60	14.97
Fe_2O_3	4.61	7.44	-	-
FeO	-	-	4.32	6.92
MnO	0.05	0.10	0.06	0.10
MgO	1.53	3.97	1.59	4.11
CaO	0.75	1.61	0.53	1.39
Na_2O	1.59	3.12	1.66	3.23
K_2O	2.71	2.77	2.83	2.87
P_2O_5	0.18	0.20	-	-
L.O.I.	3.08	2.13	in excess	in excess
Total	100.00	100.00	100.00	100.00
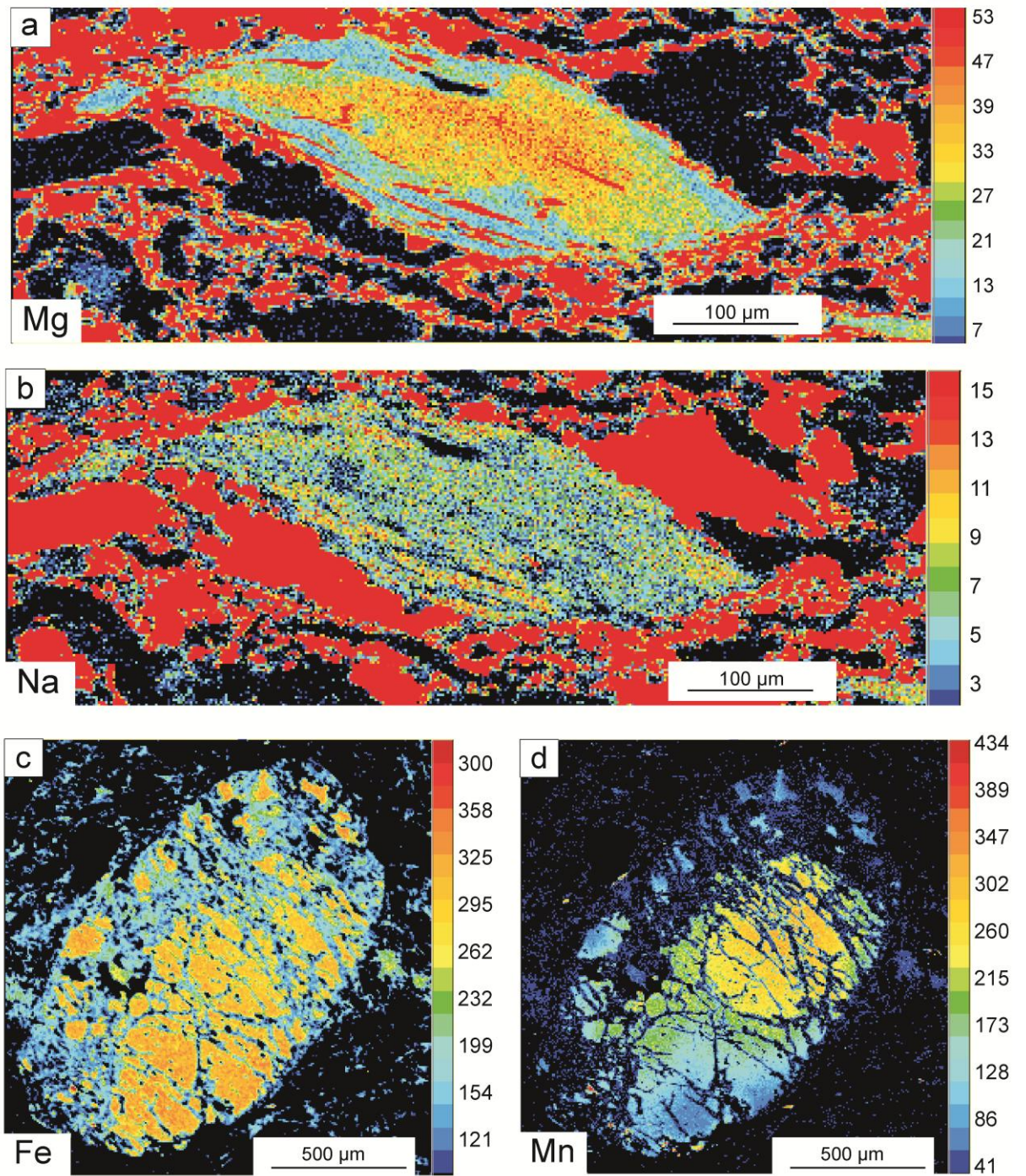
Figure 2.3 X-ray maps of potassic white mica in PC1 and garnet in CER8: (a) Mg distribution in potassic white mica; (b) Na distribution in potassic white mica; (c) Fe distribution in garnet; (d) Mn distribution in garnet. The colour code scales is related to the counts X-ray radiation per time unit.
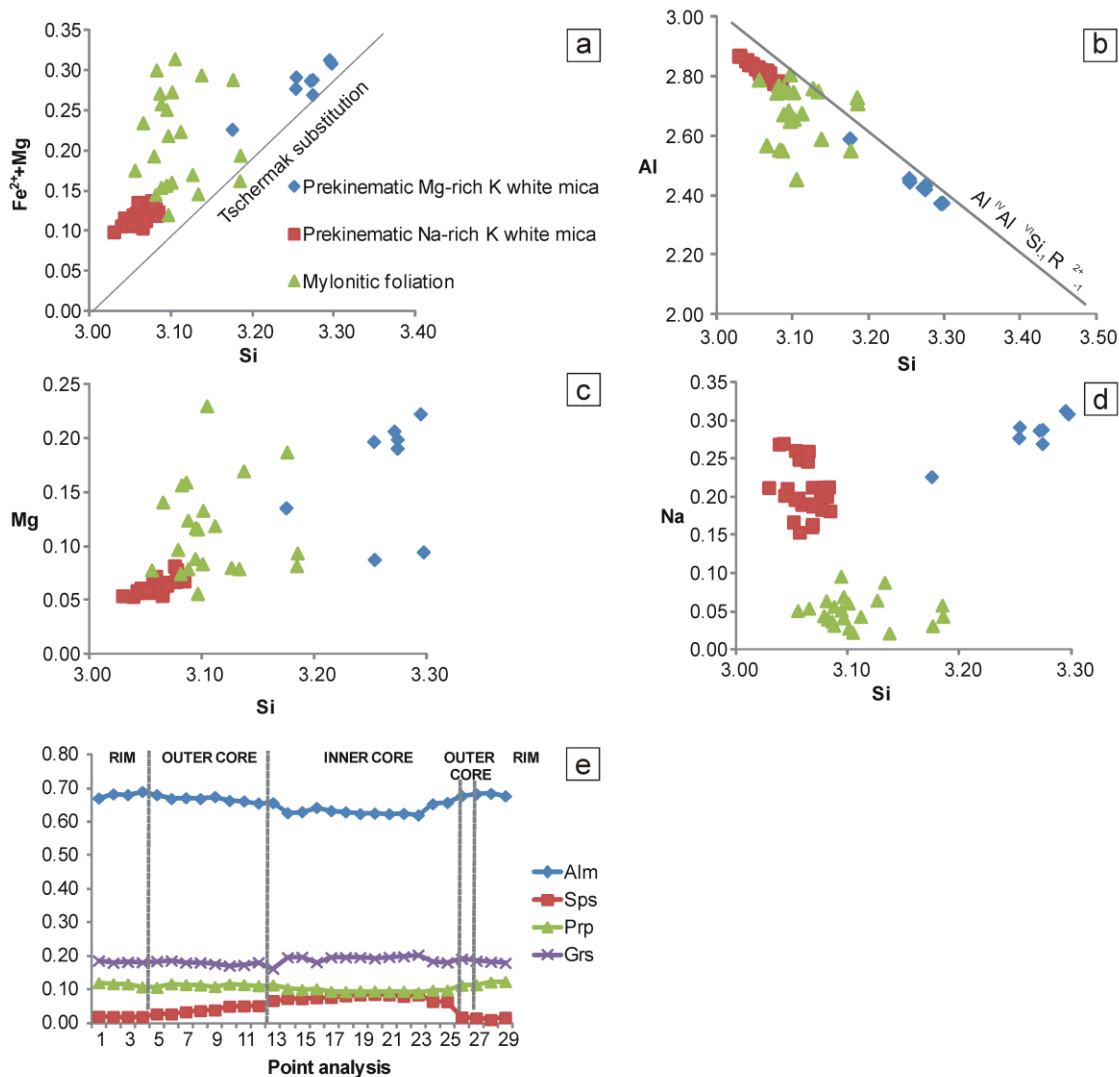
Figure 2.4 Compositional diagrams for potassic white mica in PC1 and garnet in CER8: (a) Fe^{2+}+Mg *vs.* Si in potassic white mica; (b) Mg *vs.* Al in potassic white mica; (c) Mg *vs.* Si in potassic white mica; (d) Na *vs.* Si in potassic white mica; (e) compositional profile along garnet.

2.6 GEOTHERMOBAROMETRY

2.6.1 Phase diagram calculation

Thermodynamic modelling was performed in the MnCKNFMASHT system with Perple_X package (Connolly, 1990; Connolly & Petrini, 2002). Mn was considered in the system because it has the effect of shifting garnet-in curve to lower pressures and temperatures (Thompson, 1957; Albee, 1965; Spear & Cheney, 1989; Mahar e*t al.,* 1997; Tinkham *et al.,* 2001). Ti was also considered to include the Ti-bearing minerals in the parageneses. Iron was assumed as totally ferrous because of the lack of ferric-iron minerals and of the negligible stochiometric amount in major minerals. The

thermodynamic dataset of Holland & Powell (1998, with the 2002 upgrade) and the compensated Redlich Kwong (CORK) fluid equation of state by Holland & Powell (1991, 1998) were used. SiO_2 and H_2O were considered in excess. We used the following solid solution models: Pheng(HP) for K-white mica (Holland & Powell, 1998; the maximum paragonite content has been set to 50 mol.%), Mica(M) for Na-Ca-white mica (Massonne, 2010; the maximum muscovite content has been set to 50 mol.%), Gt(HP) for garnet (Holland & Powell, 1998), TiBio(HP) for biotite (Powell & Holland, 1999), Chl(HP) for chlorite (Holland *et al.*, 1998), feldspar for plagioclase (Fuhrman & Lindsley, 1988), Kf for microcline-albite solid solutions (Waldbaum & Thompson, 1968), St(HP) for staurolite (Holland & Powell, 1998), hCrd for cordierite and IlGkPy for ilmenite (ideal models; http://www.perplex.ethz.ch/PerpleX_solution_model_glossary.html). Pure phases are titanite, rutile, zoisite, lawsonite, sillimanite, kyanite and andalusite. We performed thermodynamic modelling for the garnet-free micaschist (PC1; *P-T* pseudosection) and the garnet-bearing micaschist (CER8; garnet isopleths thermobarometry).

2.6.2 *P-T* pseudosection

The *P-T* pseudosection was calculated using the XRF bulk-rock composition of PC1 (Fig. 2.5). CaO was calculated excluding the Ca contained in apatite (Tab. 2.3). The considered *P-T* range is 350-600°C and 2-15 kbar. K-white mica is stable in the entire *P-T* grid. Na-Ca-white mica out-curve is above 400°C-2 kbar and 600°C-5 kbar. Chlorite breaks down at temperatures exceeding 600°C. Biotite appear at temperatures higher than 500°C. Garnet stability is above 400°C at P>12 kbar and above 550°C at P>4 kbar. Staurolite is stable in a narrow *PT* range around 600°C and 6 kbar. Plagioclase-in curve is at temperatures higher than 400°C at 2 kbar and 650°C at 15 kbar. K-feldspar occurs below 9 kbar and 500°C. Lawsonite appears in the low-temperature high-pressure corner. Zoisite is present at 500°C at 7-9 kbar and 450°C at14 kbar. Rutile is not stable at pressures below 9 kbar for temperatures higher than 450°C. Ilmenite coexists with rutile at temperature equal to 450°C for pressures below 9 kbar and at pressures equal to 9 kbar for temperatures higher than 450 °C. Ilmenite then replaces rutile at temperatures higher than 450°C for pressures below 9 kbar. Titanite-out curve is at 400°C-2 kbar and 500°C-12 kbar. The Si content in K-white mica increases with pressure reaching 3.39 apfu. XFe=Fe/(Fe+Mg) in chlorite decreases from 0.62 with increasing temperature (Fig. 2.5c). The maximum measured Si content (3.30

apfu) and the Na/(Na+K) ratio (0.04) of the prekinematic Mg-rich potassic white mica plots at 455°C and 12 kbar in the paragenetic field chlorite-K white mica-garnet-Na white mica-titanite-rutile-quartz (Fig. 2.6). Considering 2σ-errors in the range of 5% for the temperature estimate and 10% in the pressure value (Massonne, 2013), the previous isopleth intersection plot at about 430-480°C and 11.0-13.5 kbar. The peak stage cannot be constrained with PC1, because garnet is completely retrogressed to chlorite. The retrograde evolution was constrained in pseudosection1. The intersection among the Si content in mylonitic potassic white mica (3.06-3.19), the XFe of mylonitic chlorite (0.50-0.60) and the titanite-bearing assemblages plot at 450-500°C and 6.0-7.5 kbar in the paragenetic field chlorite + potassic white mica + sodic white mica + plagioclase + ilmenite + titanite ± rutile (Fig. 2.6), in agreement with the observed paragenesis. Garnet-out curve is crossed, in agreement with the petrographic observations.
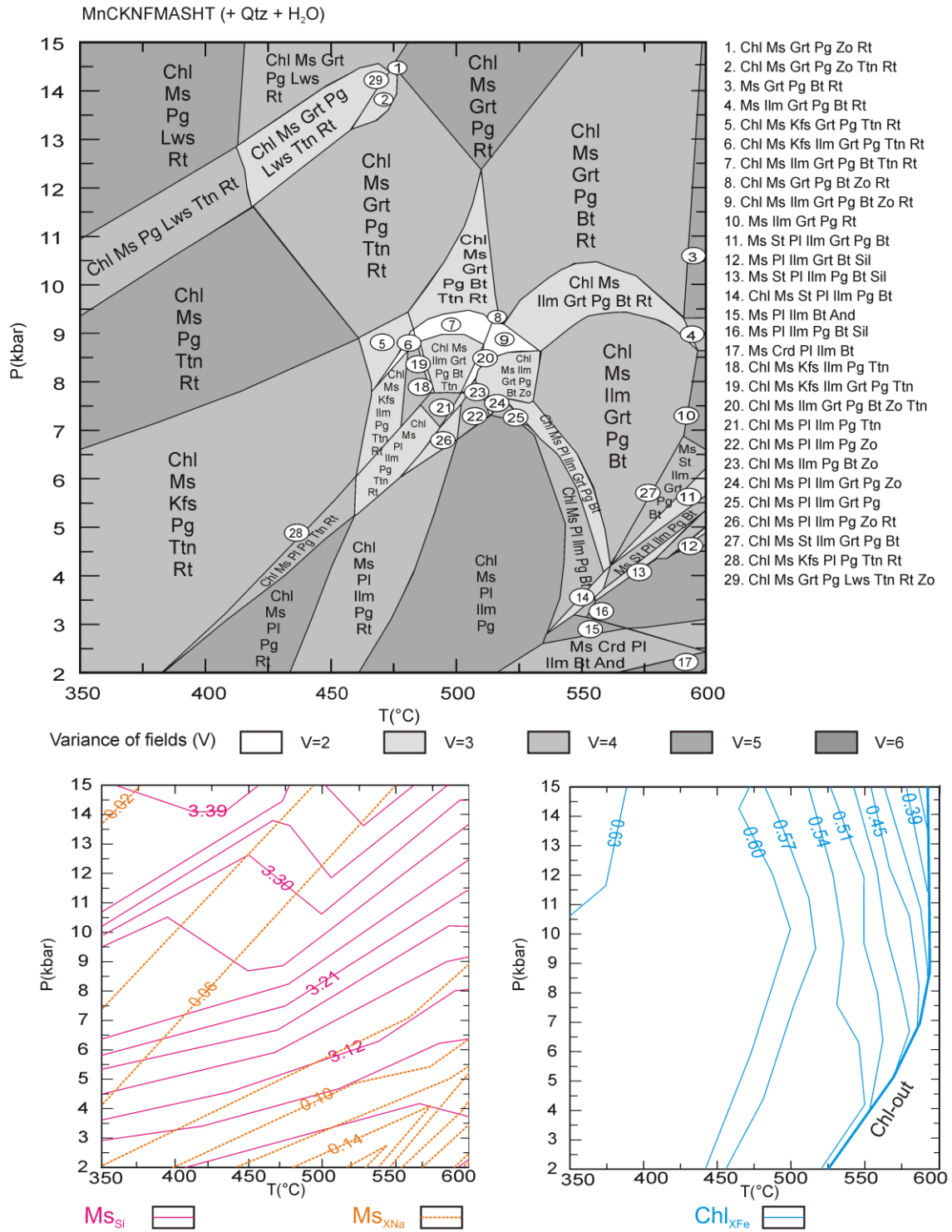
Figure 2.5 *P-T* pseudosection for PC1 with potassic white mica and chlorite isopleths. Abbreviations: Ms = potassic white mica (muscovite/phengite), Pg = sodic white mica, Chl = chlorite, Kfs = alkali-feldspar, Pl = plagioclase, Grt = garnet, Bt = biotite, St = staurolite, And = andalusite, Crd = cordierite, Ilm = ilmenite, Rt = rutile, Ttn = titanite, Lws = lawsonite, Zo = zoisite.
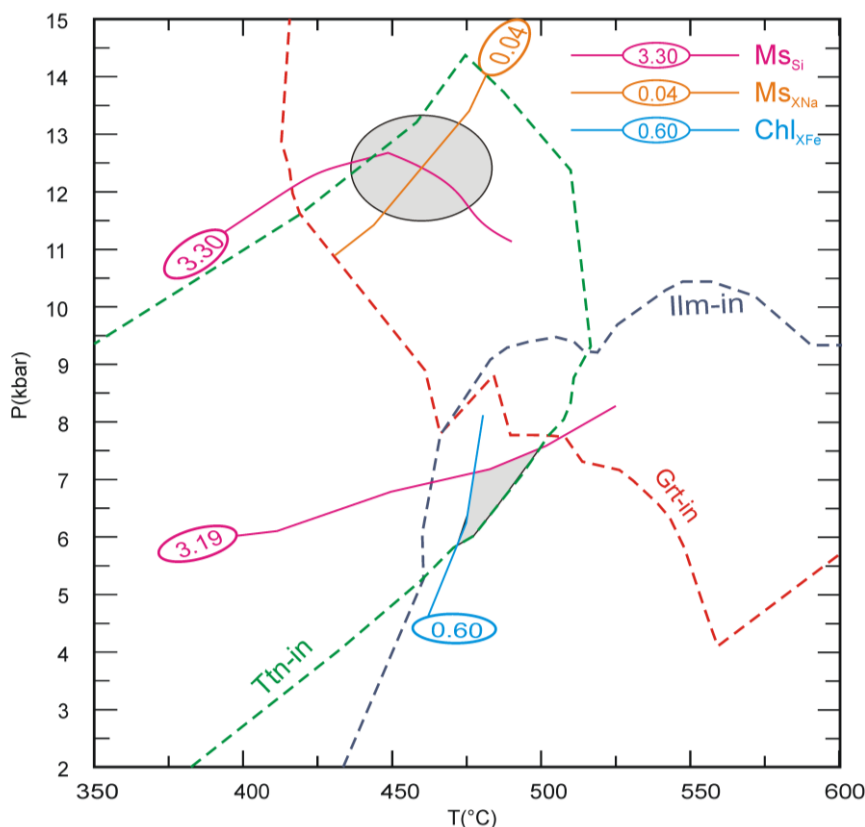
Figure 2.6 Potassic white mica isopleths constraining the pre-peak stage (grey circle) and potassic white mica and chlorite isopleths constraining the mylonitic stage in PC1 (grey triangle). The ilmenite-in curve, garnet-in curve and titanite-in curve are also reported.

2.6.3 Garnet isopleths geothermobarometry

In order to constrain the peak conditions, we applied garnet isopleths geothermobarometry for the garnet-bearing micaschist (CER8). XRF-bulk composition, corrected excluding the Ca and P in apatite (Tab. 2.3), and the same parameters of the pseudosection1 were used. The considered *P-T* range is 350-600°C and 2-10 kbar (Fig. 2.7). Garnet-in curve is at around 8 kbar in the range 350-550°C, while garnet is stable at pressures superior than 3 kbar for temperature higher than 550°C. Almandine increases reaching 70 mol. % with increasing temperature. Grossular increases from 70 mol. % towards low-temperature and high-pressures. Spessartine has its peak (24 mol. %) at 500°C and 7.5 kbar, then it decreases either down-temperature and up-temperature. Pyrope variation is also mainly controlled by temperature reaching the maximum value of 15 mol. % at 600°C. Garnet mode increases up to 4 vol. % with growing temperatures and pressures. The observed garnet core composition ($Alm_{62}Grs_{20}Prp_9Sps_8$) plots in a narrow area at 550-575°C and 8-9 kbar. The almandine, grossular and pyrope isopleths ($Alm_{68}Grs_{18}Prp_{12}$) of the garnet rim constrain the peak metamorphism at 580-600°C and 9-10 kbar. Considering the error associated with the

isopleths geothermobarometry (Massonne, 2013), garnet core and garnet rim *P-T* estimations overlap. No fractionation effect could be considered because the garnet mode in CER8 is low (< 1 %).
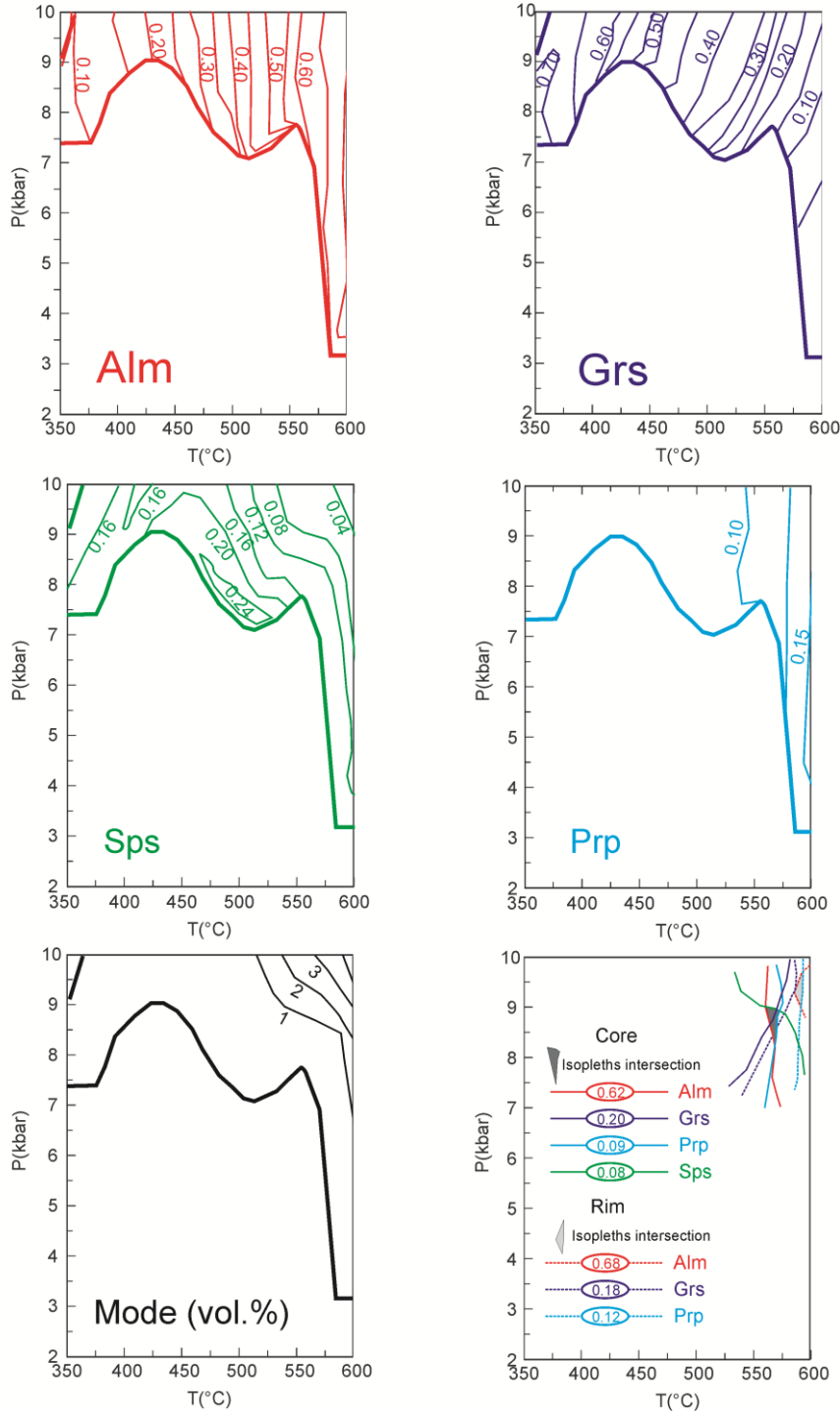
Figure 2.7 Calculated almandine, grossular, spessartine and pyrope isopleths and the mode variations in CER8. The garnet core isopleths intersection and the garnet rim isopleths intersection is also reported.

2.7 DISCUSSION

2.7.1 *P-T-D* path

Thermodynamic modelling combined with microstructural analysis allowed us to reconstruct a clockwise *P-T* path for the micaschist belonging to the Variscan basement in the Cerreto Pas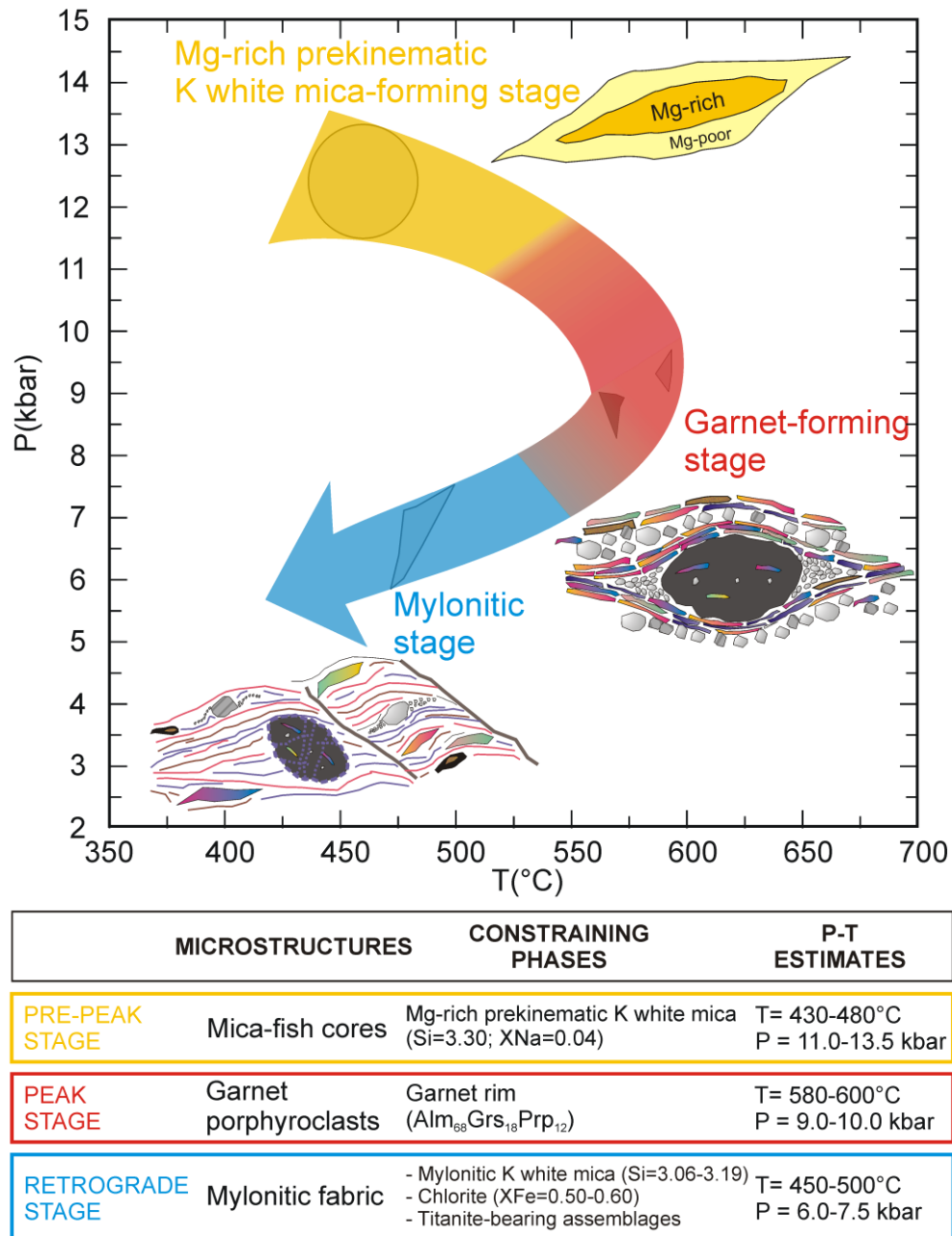s (Fig. 2.8). High-Si Mg-rich potassic white mica relics in deformed potassic white mica grains constrains the pre-peak stage at 430-480°C and 11.0-13.5 kbar. The rim of garnet porphyroclasts crystallized during the metamorphism peak, consisting of 580-600°C and 9-10 kbar. The mylonitic stage is represented by potassic white mica and chlorite along the mylonitic foliation and by the titanite-ilmenite transition in PC1. This stage occurred at 450-500°C and 6.0-7.5 kbar. The shearing event is also responsible for the development of the well-developed mylonitic fabric (mylonitic foliation, shear bands, asymmetric foliations boudins, quartz oblique foliation, deformed prekinematic crystals). The evolution of the calculated mineral assemblages in PC1 along the *P-T-D* path is shown in Fig. 2.9. The diagram displays the variation of the cumulative mineral modes with temperature and pressure: from 430°C-13-5 kbar (pre-peak stage), passing through 600°C-10 kbar (peak stage), to 450°C-6 kbar (retrograde stage). The pre-peak stage generated a quartz-potassic white mica-sodic white mica-chlorite paragenesis. Garnet porphyroclast may have started to crystallize in this stage. Accessory minerals were rutile and titanite. Increasing temperature and decreasing the pressure towards the peak conditions, titanite breaks down and rutile became the only Ti-bearing phase. Garnet abundance grows and when biotite appears, chlorite and potassic white mica amount fall down. At peak conditions chlorite disappears and the paragenesis is quartz-sodic white mica-potassic white mica-biotite-garnet-rutile. Then the retrograde stage starts: rutile is replaced by ilmenite and garnet begins to be replaced by chlorite and potassic white mica. At 520°C garnet breaks down and plagioclase crystallizes. The modal amount of chlorite and potassic white mica increases by 5 and 10 vol. %, respectively. On the contrary, paragonite looses 10 vol. %. Ilmenite is partly replaced by titanite, in agreement with the observed titanite rims around ilmenite crystals. At 475°C Ca-poor plagioclase disappears in favour of K-feldspar and titanite. The calculated retrograde assemblage potassic white mica-chlorite-quartz-titanite-K-feldspar assemblage at 500-450°C is concordant with the observed mylonitic paragenesis. The only apparent discrepancy between observed and calculated mineral assemblages is sodic white mica. Sodic white mica was never observed in the selected sample with optical and scanning electronic microscopes.

However, high-magnification observations with a field emission scanning microscopy on another micaschist from the Cerreto Pass reveal the existence of fine-grained sodic white mica flakes (wide 10-50 μm and thick few μm) intergrown with potassic white mica (see Chapter 4). It is indeed reasonable that sodic white mica is present also in PC1.

	MICROSTRUCTURES	CONSTRAINING PHASES	P-T ESTIMATES
PRE-PEAK STAGE	Mica-fish cores	Mg-rich prekinematic K white mica (Si=3.30; XNa=0.04)	T= 430-480°C P = 11.0-13.5 kbar
PEAK STAGE	Garnet porphyroclasts	Garnet rim ($Alm_{68}Grs_{18}Prp_{12}$)	T= 580-600°C P = 9.0-10.0 kbar
RETROGRADE STAGE	Mylonitic fabric	- Mylonitic K white mica (Si=3.06-3.19) - Chlorite (XFe=0.50-0.60) - Titanite-bearing assemblages	T= 450-500°C P = 6.0-7.5 kbar

Figure 2.8 *P-T-D* path for the Cerreto micaschist. The table contains a summary of the tectono-metamorphic evolution, with the microstructures, the constraining phases and the corresponding *P-T* estimates.
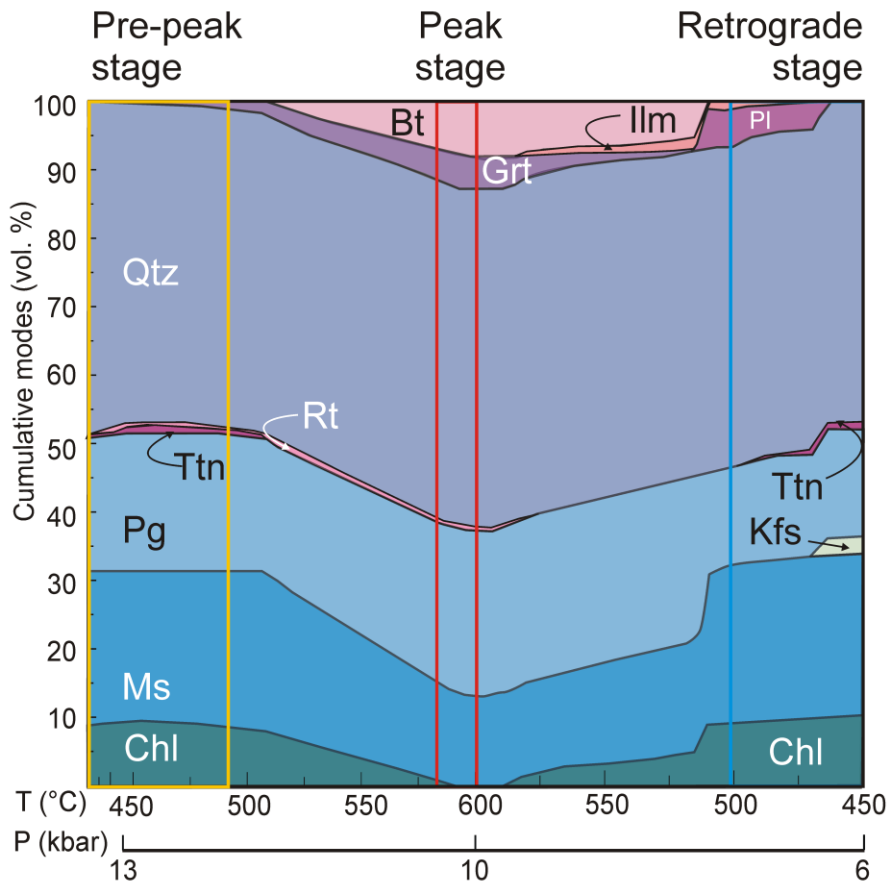
Figure 2.9 Calculated evolution of the mineral modes along the *P-T* path.

2.7.2 Tectonic implications

The obtained *P-T-D* path suggests that the Cerreto micaschist experienced a polyphasic metamorphism during the Variscan orogeny. The initial high-pressure stage may testify the burial at middle-crustal depths during the collision-related thickening of the crust. The temperature peak followed the pressure peak, and this may suggest that the heating subsequent to the thermal equilibration occurred when the exhumation had already begun. The retrograde stage, accompanied by a strong mylonitic deformation, is probably related to an exhumation process along ductile shear zones.

Only two *P-T* paths are available for the Variscan basement of Northern Apennine (Bertini *et al.*, 1994). The Cerreto metamorphic rocks have been correlated with the Micaschist Complex of the Larderello subsurface (Pandeli *et al.*, 2005). The Variscan basement in the Larderello subsurface has been divided into three tectonic units (Batini *et al.*, 2003; Bertini *et al.*, 2006):

    - Phyllitic–Quartzitic Complex: low-grade metasedimentse and metabasite levels, overprinted by the Alpine metamorphism and correlated with the

Variscan succession in the Apuane Alps, in the Monti Pisani and in Punta Bianca;

- Micaschist Complex: two-mica garnet-bearing albite micaschist with minor amphibolite deriving from OFB (Ocean Floor Basalts), affected by a polymetamorphism during the Variscan and Alpine orogenesis;

- Gneiss Complex: muscovite-biotite gneisses with orthogneiss, OFB amphibolite layers and calc-silicate rocks, affected only by the Variscan metamorphism.

Bertini *et al.* (1994) reconstructed the thermobaric history of the Gneiss Complex in the Larderello subsurface through classical geothermobarometry and the stability fields of staurolite, muscovite, andalusite and cordierite. The pre-Alpine history shows a peak metamorphism at 500-600°C and 7 kbar, followed by an isothermal decompression at 500-600°C and 2-3.5 kbar. The Authors interpreted the obtained *P-T* path as related to a fast tectonic exhumation after the Variscan collision. The retrograde stage is different from our reconstruction that proposes a gradient of 40°C kbar^{-1}. The Larderello Gneiss Complex and the Cerreto micaschist metamorphic evolutions result remarkably different. This difference can be explained by considering the Cerreto micaschist and the Larderello Gneiss Complex as basement slices belonging to different paleogeographic domains.

Molli *et al.* (2002) investigated the metamorphic evolution of the Micaschist Complex in the Cerreto Pass. They didn't constrain the pre-peak stage with geothermobarometry, however they envisaged an early metamorphic event in garnet-amphibolite or eclogitic facies Using classical thermobarometry the peak conditions were constrained at 650°C and 8 kbar for the amphibolite and 630°C and 8.5 kbar for the micaschist. Ar-Ar dating on amphibole separates from undeformed and unretrogressed amphibolite gives Variscan ages (328-312 Ma) for the pre-mylonitic stage(s). The micaschist are associated with amphibolite and they show the same microstructural features (e.g. prekinematic relics and mylonitic fabric). Since they share a common metamorphic evolution from at least the peak conditions, the age determination of the amphibolite regards also the garnet-forming stage in the micaschist. According to Molli *et al.* (2002), the retrograde stage occurred at 530°C and 4-5 kbar for the amphibolite. The trajectory by Molli *et al.* (2002) is shifted by 50°C up in the temperature for the peak conditions and by 1 kbar down in the pressure for the retrograde stage with respect to the new *P-T* path. Nevertheless the overall shape of the two *P-T* trajectories is similar

and point to a common peak and exhumation history for the amphibolite and metapelites. The differences in the *P-T* estimates may be due to the use of different geothermobarometric methods (classical geothermobarometry *vs.* pseudosections), the improvements of the thermodynamic data and solutions models for minerals during the last decade (Holland & Powell, 1998), and a lack of uncertainties estimations in the *P-T* calculations of Molli *et al.* (2002). Besides, the peak conditions in the micaschist have been estimated using the garnet rim composition with the higher almandine value. However, since garnet breakdown is intensive, the highest values of almandine could have been lost. As a consequence, higher temperatures in peak conditions cannot be ruled out. The application of thermodynamic modelling on amphibolite can resolve the question.

After the collision stage, the Variscan chain was dismembered in several segments in the interval 330-300 Ma by strike-slip shear zones (e.g. East Variscan Shear Zone; Padovano *et al.,* 2012). The pre-Carboniferous rocks of Northern Apennines have been ascribed to the Southern part of the Variscan belt, as like the Austroalpine basement of the Eastern Alps, Corsica-Sardinia, the Calabrian-Peloritan orogen and the Kabylies (Bagnoli *et al.*, 1979; Vai & Cocozza, 1986, Vai & Martini, 2001; Elter *et al.*, 2004; Elter & Pandeli, 2005). The correlation among these basements relies on stratigraphic and structural similarities. In particular the greenschist-facies metamorphic rocks outcropping in the Apuane Alps show stratigraphic and metamorphic similarities with the External Nappe units of Sardinia (Conti *et al.*, 1991; Pandeli *et al.*, 1994). A correlation based on the metamorphic evolution has been discussed in Elter & Pandeli (2005) and Padovano *et al.* (2012). We selected the *P-T* paths reported by those Authors with the following criteria: (i) metapelitic rocks; (ii) medium-grade peak conditions; (iii) peak conditions occurring at about 330 Ma. We could compared only our retrograde *P-T* path to those trajectories (Fig. 2.10), because only our reconstruction and that of Angì *et al.* (2010) are the only ones providing information about pre-peak conditions (pressures higher than 10 kbar). For pressures below 10 kbar, analogies arise for the peak conditions and exhumation histories among the Cerreto micaschist, the Giuncana area (northwest sector of the Sardinia Massif; Ricci, 1992; Franceschelli *et al.*, 2005; Cruciani *et al.*, 2008), and the Posada Valley Area mylonites (Sardinia, Elter *et al.*, 1999; Elter & Pandeli, 2005). On the contrary, the sillimanite-bearing gneisses of the Pohorje Massif (Austroalpine basement of the Eastern Alps; Thöni, 2002), the Mammola Paragneiss Complex (Serre Massif; Angì *et al.,* 2010), and the ilmenite-

garnet-bearing metapelite of the Mandanici Unit (Peloritani Mountains; Fiannacca *et al.,* 2012) show quite different peak temperature estimates. The peak conditions occurred for all the considered *P-T* paths at 9-10 kbar.

Thus, our *P-T-D* path show similarities with the metamorphic evolution of other segments of the Southern Europe Variscides, especially those outcropping in Sardinia. Some microstructures in the Cerreto Pass micaschist (e.g. book shelf sliding plagioclase and boudins) and the regional framework suggest that the mylonitic event could develop in a strike-slip tectonics with extensional kynematics (Elter & Pandeli, 2005).
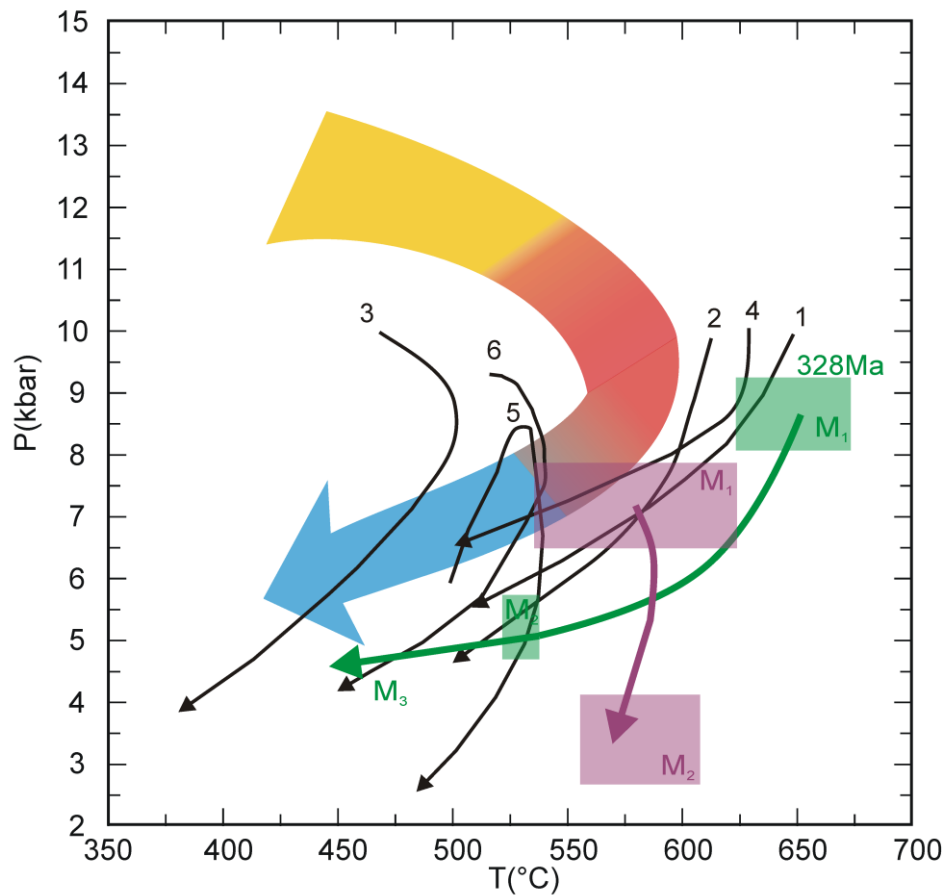
Figure 2.10 Comparison of the obtained P-T path (yellow to blue arrow) with the thermobaric trajectories proposed for some Variscan segments in the circum-Mediterranean area: violet arrows and boxes for the Larderello Gneiss Complex (Northern Apennines; Bertini et al., 1994); green arrows and boxes for the Cerreto amphibolite (Northern Apennines; Molli et al., 2002); 1. Pohorje Massif (Eastern Alps); 2. Giuncana area (Sardinia); 3. Internal Nappe Zone (Sardinia); 4. Posada Valley Area (Sardinia); 5. Mammola Paragneiss Complex (Serre Massif); 6. Mandanici Unit (Fiannacca et al., 2012). See the text for references.

2.8 CONCLUSIONS

This contribution proposes a new reconstruction of the metamorphic evolution for the micaschist outcropping in the Cerreto Pass. These rocks represent a remnant of the Variscan basement, reworked into the Northern Apennine belt by the Alpine tectonics.

For the first time thermodynamic modelling (*P-T* pseudosections and garnet isopleths geothermobarometry) was performed on the Cerreto metamorphic rocks in order to constrain the pressure-temperature evolution. Although a strong retrogression affected the micaschist, prekinematic relics were preserved, thus even the prograde path was defined.

The Cerreto micaschist record a clockwise Pressure-Temperature path consisting of

> ➢ a prograde stage, occurring at high-pressure conditions (T=430-480°C; P=11-13.5 kbar) during the Variscan thickening;

> ➢ a temperature peak (600 °C at 9-10 kbar) that postdates the pressure peak;

> ➢ a retrograde stage at T = 450-500°C and P = 6-7.5 kbar, likely related with the exhumation of Variscan crust along ductile shear zones in a strike-slip tectonic framework.

Comparison with the *P-T* paths of the Variscan basement in Easter Alps, Sardinia and the Calabrian-Peloritan orogen reveals similarities in the metamorphic evolution. On the contrary, the Gneiss Complex in Larderello shows a different *P-T* path.

2.9 REFERENCES

Albee, A.L., 1965. A petrogenetic grid for the Fe-Mg silicates of pelitio schists. *American Journal of Science,* **263**, 512-536.

Angì, G., Cirrincione, R., Fazio, E., Fiannacca, P., Ortolano, G. & Pezzino, A., 2010. Metamorphic evolution of preserved Hercynian crustal section in the Serre Massif (Calabria–Peloritani Orogen, southern Italy). *Lithos,* **115**, 237-262.

Bagnoli, G., Gianelli, G., Puxeddu, M., Rau, A., Squarci, P. & Tongiorgi, M., 1979. A tentative stratigraphic reconstruction of the Tuscan Paleozoic *basement. Memorie Società Geologica Italiana,* **20**, 99-116.

Batini, F., Brogi, A., Lazzarotto, A., Lotta, D. & Pandeli, E., 2003. Geological features of the Larderello-Travale and Mt. Amiata geothermal areas (southern Tuscany, Italy). *Episodes,* **26**, 239-244.

Bernhardt, H.-J, Massonne, H.-J., Reinecke, T., Reinhardt, J. & Willner, A., 1995. Digital element distribution maps, an aid for petrological investigations. Berichte der Deutschen Mineralogischen Gesellschaft, *Beihefte zum European Journal of Mineralogy,* **7**, 28.

Bertini, G., Elter, F.M. & Talarico, F., 1994. Evidenze di una fase estensionale pre-triassica nel complesso degli gneiss nell'area geotermica di Larderello (Toscana meridionale). *Studi Geologici Camerti, Volume speciale,* **1**, 129-137.

Bertini, G., Casini, M., Gianelli, G. & Pandeli, E., 2006. Geological structure of a long-living geothermal system, Larderello, Italy. *Terra Nova,* **18**, 163-169.

Brandelik, A., 2009. CALCMIN – an EXCEL^{TM} Visual Basic application for calculating mineral structural formulae from electron microprobe analyses. *Computers & Geosciences,* **35**, 1540–1551.

Connolly, J.A.D., 1990. Multivariable phase diagrams: an algorithm based on generalized thermodynamics. *American Journal of Science,* **290**,666–718.

Connolly, J.A.D. & Petrini, K., 2002. An automated strategy for calculation of phase diagram sections and retrieval of rock properties as a function of physical conditions. *Journal of Metamorphic Geology,* **20**, 697–708.

Conti, P., Costantini, A., Decandia, F.A., Elter, F.M., Gattiglio, M., Lazzarotto, A., Meccheri, M., Pandeli, E., Rau, A., Sandrelli, F., Tongiorgi, M. & Di Pisa, A., 1991. Structural frame of the Tuscan Palaeozoic: a review. *Bollettino Societa Geologica Italiana*, **100**, 523–541.

Cruciani, G., Franceschelli, M., Elter, F. M., Puxeddu, M. & Utzeri, D., 2008. Petrogenesis of Al–silicate-bearing trondhjemitic migmatites from NE Sardinia, Italy. *Lithos,* **102**, 554-574.

Elter, F.M. & Pandeli, E., 2005. Structural-metamorphic correlations between three Variscan segments in Southern Europe: Maures Massif (France), Corsica (France)-Sardinia (Italy), and Northern Appennines (Italy). In The Southern Variscan Belt, *Journal of the Virtual Explorer*, Carosi, R., Dias, R., Iacopini, D., Rosenbaum, G. (eds). Electronic Edition, ISSN 1441–8142, 19, Paper 1.

Elter, F.M., Faure, M., Ghezzo, C. & Corsi, B., 1999. Late Hercynian shear zones in northeastern Sardinia (Italy). *Géologie de la France,* **2**, 3-16.

Elter, F.M., Corsi, B., Cricca, P. & Muzio, G., 2004. The south-western Alpine foreland: correlation between two sectors of the Variscan chain belonging to "stable Europe": Sardinia-Corsica and the Maures Massif (south-eastern France). *Geodinamica Acta,* **17**, 31-40.

Fiannacca, P., Lo Pò, D., Ortolano, G., Cirrincione, R. & Pezzino, A., 2012. Thermodynamic modeling assisted by multivariate statistical image analysis as a tool for unraveling metamorphic P-T-d evolution: an example from ilmenite-garnet-bearing metapelite of the Peloritani Mountains, Southern Italy. *Mineralogy and Petrology,* **106**, 151 – 171.

Franceschelli, M., Gianelli, G., Pandeli, E. & Puxeddu, M., 2004. Variscan and Alpine metamorphic events in the northern Apennines (Italy): a review. *Periodico di Mineralogia*, **73**, 43-56.

Franceschelli, M., Puxeddu, M. & Cruciani, G., 2005. Variscan metamorphism in Sardinia, Italy: review and discussion. In The Southern Variscan Belt, *Journal of the Virtual Explorer*, Carosi, R., Dias, R., Iacopini, D., Rosenbaum, G. (eds). Electronic Edition, ISSN 1441–8142, 19, Paper 2.

Fuhrman, M.L. & Lindsley, D.H., 1988. Ternary-Feldspar Modeling and Thermometry. *American Mineralogist,* **73**, 201-215.

Herron, M.M., 1988. Geochemical classification of terrigenous sands and shales from core and log data. *Journal of Sedimentary Petrology,* **58**, 820–829.

Holland, T.J.B. & Powell, R., 1991. A compensated-Redlich-Kwong (CORK) equation for volumes and fugacities of CO_2 and H_2O in the range 1 bar to 50 kbar and 100–1600 °C. *Contributions to Mineralogy and Petrology,* **109**, 265–273.

Holland, T.J.B. & Powell, R., 1998. An internally consistent thermodynamic data set for phases of petrological interest. *Journal of Metamorphic Geology,* **16**, 309–343.

Holland, T., Baker, J. & Powell, R., 1998. Mixing properties and activity-composition relationships of chlorites in the system MgO-FeO-Al_2O_3-SiO_2-H_2O. *European Journal of Mineralogy,* **10**, 395-406.

Mahar, E.M., Baker, J.M., Powell, R., Holland, T.J.B. & Howell, N., 1997. The effect of Mn on mineral stability in metapelites. *Journal of Metamorphic Geology,* **15**, 223-238.

Massonne, H.-J., 2010. Phase relations and dehydration behaviour of calcareous sediments at very-low to low grade metamorphic conditions. *Periodico di Mineralogia,* **79**, 2, 21-43.

Massonne, H.-J., 2013. Constructing the pressure–temperature path of ultrahigh-pressure rocks. *Elements,* **9**, 267-272.

McLennan, S.M., 2001. Relationships between the trace element composition of sedimentary rocks and upper continental crust. *Geochemistry, Geophysics, Geosystems,* **2**, 1-24.

Molli, G., Montanini, A. & Frank W., 2002. MORB-derived Varisican amphibolites in the Northern Apennine Basement: the Cerreto metamorphic slices (Tuscan-Emilian Apennine, NW Italy). *Ofioliti,* **27**, 17-30.

Padovano, M., Elter, F. M., Pandeli, E. & Franceschelli, M., 2012. The East Variscan Shear Zone: new insights into its role in the Late Carboniferous collision in southern Europe. *International Geology Review,* **54**, 957-970.

Pandeli, E., Gianelli, G., Puxeddu, M. & Elter, F.M., 1994. The Paleozoic basement of the Northern Apennines: stratigraphy, tectono-metamorphic evolution and Alpine hydrothermal processes. *Memorie della Società Geologica Italiana, 48*, 627-654.

Passchier, C.W. & Trouw, R.A.J., 2005. Microtectonics (Second edition). Springer-Verlag, Berlin, pp. 366.

Powell R. & Holland, T.J.B., 1999. Relating formulations of the thermodynamics of mineral solid solutions: Activity modeling of pyroxenes, amphiboles, and micas. *American Mineralogist,* **84**, 1-14.

Powell, R. & Holland, T.J.B., 2008. On thermobarometry. *Journal of Metamorphic Geology*, **26**, 155-179.

Ricci, C.A., 1992. From crustal thickening to exhumation: petrological, structural and geochronological records in the crystalline basement of Northern Sardinia, in Carmignani, L., and Sassi, F.P., eds., Contribution to the Geology of Italy with special regards to the Paleozoic basements: IGCP, v. 276, Siena (Italy), Newsletter, 5, p. 187–197. Spear & Cheney 1989.

Taylor, S.R. & McLennan, S.M., 1985. The continental crust: its composition and evolution. Blackwell, Oxford, pp. 312.

Thompson, J.B., 1957. The graphical analysis of mineral assemblages in pelitic schists. *Am Mineral* **42**, 842-858.

Thöni, M., 2002, Sm–Nd isotope systematics in garnet from different lithologies (Eastern Alps): Age results, and an evaluation of potential problems for garnet Sm–Nd chronometry: Chemical *Geology,* **185**, 255-281.

Tinkham, D.K., Zuluaga, C.A. & Stowell, H.H., 2001. Metapelitic phase equilibria modeling in MnNCKFMASH: the effect of variable Al_2O_3 and MgO/(MgO + FeO) on mineral stability. *Geological Materials Research,* **3**, 1-42.

Vai, G.B. & Martini, I.P., 2001. Anatomy of an Orogen: the Apennines and Adjacent Mediterranean Basins, Kluwer Academic Publishers, pp. 632.

Waldbaum, D.R. & Thompson, J.B. Jr. 1968. Mixing properties of sanidine crystalline solutions: II. Calculations based on volume data. *American Mineralogist,* **53**, 2000-2017.

Williams, M.L. & Jercinovic, M.J., 2012. Tectonic interpretation of metamorphic tectonites: integrating compositional mapping, microstructural analysis and in situ monazite dating. *Journal of Metamorphic Geology,* **30**, 739-752.

A NEW *P-T-t* PATH FOR THE

post-Variscan history:

LINKING MONAZITE AND GARNET IN THE

Pontremoli metapelites

A NEW *P-T-t* PATH FOR THE POST-VARISCAN HISTORY:
LINKING MONAZITE AND GARNET IN THE PONTREMOLI METAPELITES

3.1 INTRODUCTION

The linkage between accessory minerals rich in rare-earth elements (REE) and major rock-forming phases plays a crucial role in deciphering metamorphic and tectonic processes (Vance *et al.,* 2003). Monazite is one of the main REE-accessory minerals useful for obtaining geochronological information on a wide range of Ca-poor crustal rocks. Therefore much effort is dedicated to connect monazite U-Th-Pb chemical or isotopic ages with pressure (*P*)-temperature (*T*) constraints obtained from mineral assemblages, which can be modelled by thermodynamically-based phase diagrams. In low-medium grade pelitic and felsic compositions, monazite usually occurs as inherited grains and/or authigenic metamorphic crystals. Along a prograde metamorphic path monazite can be progressively consumed by the formation of other REE-accessory minerals like allanite (Wing *et al.*, 2003; Janots *et al.*, 2008). However, Williams *et al.* (2007 and references therein) reported the resumption of monazite growth at the staurolite-in/garnet-out isograd (~550°C). The phase relations described above are complicated by the textural and compositional evidence. During low-grade regional metamorphism (< 400°C) metamorphic monazite may form after the dissolution of precursor (inherited) monazite (Janots *et al.*, 2006; Rasmussen & Muhling, 2007). Inherited and (new) metamorphic monazite may therefore potentially coexist under greenschist-lower amphibolite facies conditions. In these cases, efforts are required to discriminate between inherited monazite, unrelated to the metamorphic assemblages, and metamorphic monazite that can actually provide meaningful age constraints. Even when low-grade monazite and inherited monazite can be distinguished, it is not simple to relate a monazite age to *P-T* conditions obtained from rock-forming minerals. A common approach relies on the Y partitioning between garnet and monazite (Vance *et al.*, 2003; Williams *et al.*, 2007), but it requires that monazite grew together with garnet during metamorphic evolution. However, clear breakdown microstructures of monazite

testify that monazite can be consumed during prograde metamorphic evolution (Janots *et al.*, 2006; Rasmussen & Muhling, 2007) and the linkage between monazite and *P-T* sensitive minerals becomes more complicated. In such a case a possible approach is the connection of the products of the monazite breakdown to the crystallization of *P-T* sensitive major minerals (e.g. garnet) through chemical and microstructural constraints (Gieré *et al.*, 2011).

Here we present a study where inherited, and partially decomposed, monazite has been recognized in garnet-micaschist from the basement beneath Pontremoli, Northern Apennines (Fig. 3.1). The early Permian monazite age presented here provides a lower age limit for the metamorphic history of the Northern Apennine basement. Careful considerations of garnet chemical zoning (major and selected trace elements), garnet mineral inclusions (including xenotime), monazite breakdown products and phase diagram modelling permit to link the reaction history among accessory minerals with the *P-T* evolution of garnet. We propose a previously unrecognized *P-T* path for the post-Variscan history of pre-Mesozoic basement reworked within the Apennines orogenic structures.

3.2 GEOLOGICAL FRAMEWORK AND SAMPLE PROVENANCE

The Northern Apennines are an orogenic belt formed during the collision between the Corsica-Sardinia block and the Adria microplate in Oligocene-Miocene times. In the Northern Apennines, slices of Variscan basement belonging to the distal Adria (i.e. palaeo-Africa) margin can be observed in tectonic windows below the Mesozoic-Tertiary sedimentary sequences (Tuscan Units) that are tectonically overlain by the ophiolite-bearing Ligurian units (Vai & Martini, 2001 and reference therein).

The Variscan basement of the Northern Apennines occurs in few outcrops (Cerreto Pass, Punta Bianca and in the so-called Tuscan Metamorphic Ridge) and in the Larderello and Pontremoli subsurface (Figs. 3.1a, b). The upper 1.5 km of the Variscan basement underlying the sediments of the Larderello geothermal system (Pandeli *et al.*, 2005) istraditionally subdivided into three tectonic units (from top to bottom): (i) Phyllitic-Quartzitic Complex; (ii) Micaschist Complex; (iii) Gneiss Complex (Elter & Pandeli, 1990; Bertini *et al.*, 1994). The Gneiss Complex and the Micaschist Complex were also affected by a thermometamorphism related to the emplacement of Pliocene-Quaternary granites.

The Variscan basement in the Pontremoli subsurface has been correlated to the Micaschist Complex of the Larderello geothermal field (Pandeli *et al.*, 2005). This Complex underwent a low-medium grade regional Variscan metamorphism, followed by a thermo-metamorphic stage at 285 Ma. An Alpine greenschist-facies polyphase metamorphism overprinted the earlier stages (Franceschini, 1998; Pandeli *et al.*, 2005; Musumeci *et al.*, 2011). Differently from the Micaschist Complex of Larderello, the Variscan basement under Pontremoli was not involved in a contact metamorphism induced by the Pliocene-Quaternary igneous activity (Pandeli *et al.*, 2005).

The Pontremoli 1 well intercepted the Variscan basement within the 3059-3520 m depth range (Anelli *et al.*, 1994). SamplesAG6, AG6a, and 3118 come from 3117-3118 m depth (core 6) and are fine-grained rocks with a single planar schistosity consisting of alternating white mica-chlorite quartz-albite-calcite layers. Samples AG7 and Pontremoli 7 were taken from 3422 m depth (core 7) whereas the samples AG8 and Pontremoli8 belong to the stratigraphically deepest core 8 and are representative of the basement at 3519-3520 m depth. Samples AG7, Pontremoli7, AG8 and Pontremoli 8 were studied in detail because of the presence of garnet.
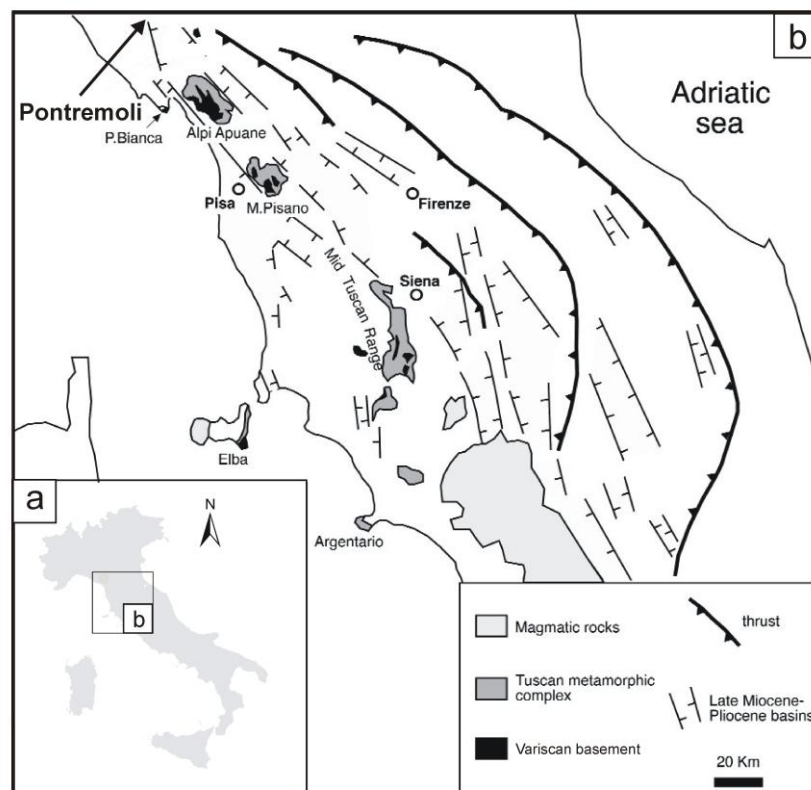
Figure 3.1 Geological framework.
(a) location of the Pontremoli well;
(b) distribution of the Variscan basement in Northern Apennines.

3.3 PETROGRAPHY

The investigated samples (AG7, Pontremoli7, AG8 and Pontremoli 8) show a medium grain size and a schistose fabric with white mica and chlorite wrapping around garnet porphyroblasts (Fig. 3.2a), which contain inclusions of a variety of minerals such as ilmenite, xenotime, allanite, epidote and pyrite. Chlorite and white mica aggregates with a decussate fabric were also observed in late microfolds (Fig. 3.2b). Quartz and poikilitic plagioclase are the other main minerals. Plagioclase crystals host K-feldspar and white mica inclusions. Chlorite, white mica, plagioclase and quartz occur in pressure shadows around the garnet porphyroblasts. Fractures in garnet are filled with chlorite and white mica. The accessory minerals are ilmenite, rutile, zircon, pyrite, tourmaline, monazite, apatite, thorite, allanite, epidote, xenotime, and zircon.

Ilmenite inclusions within garnet define an internal schistosity, which is discontinuous to the external one. Euhedral ilmenite crystals in the matrix are oriented parallel to the schistosity. Rutile cores in matrix ilmenite and K-feldspar inclusions in plagioclase occur. Allanite is also present in the matrix and forms aggregates of anhedral grains. Irregular xenotime grains with corroded rims occur only in the garnet inner core.

The microstructural analysis permits to reconstruct the following metamorphic evolution. Rutile and K-feldspar may represent the remnants of an earlier assemblage. The transition from rutile to ilmenite predates the garnet forming stage, because no rutile but ilmenite has been observed in the garnet inner core. The internal schistosity of ilmenite in garnet represents the relics of a former schistosity (Fig. 3.2c). The crystallisation of garnet porphyroblasts overprints and entraps this schistosity. During garnet growth, white mica-chlorite-ilmenite-external schistosity and quartz and plagioclase re-crystallized. The growth of chlorite and white mica with decussate structure postdates the external schistosity formation. Potassic white mica and chlorite crystallization as replacement products of garnet rims and plagioclase growth in the matrix may be related to a late metamorphic stage.

Pontremoli 7 was studied in more detail because it contains reaction microstructures due to the breakdown of monazite grains (Fig. 3.2d; see "Coronitic microstructure around monazite"). This sample was thus considered suitable to infer the reaction history among REE-minerals.
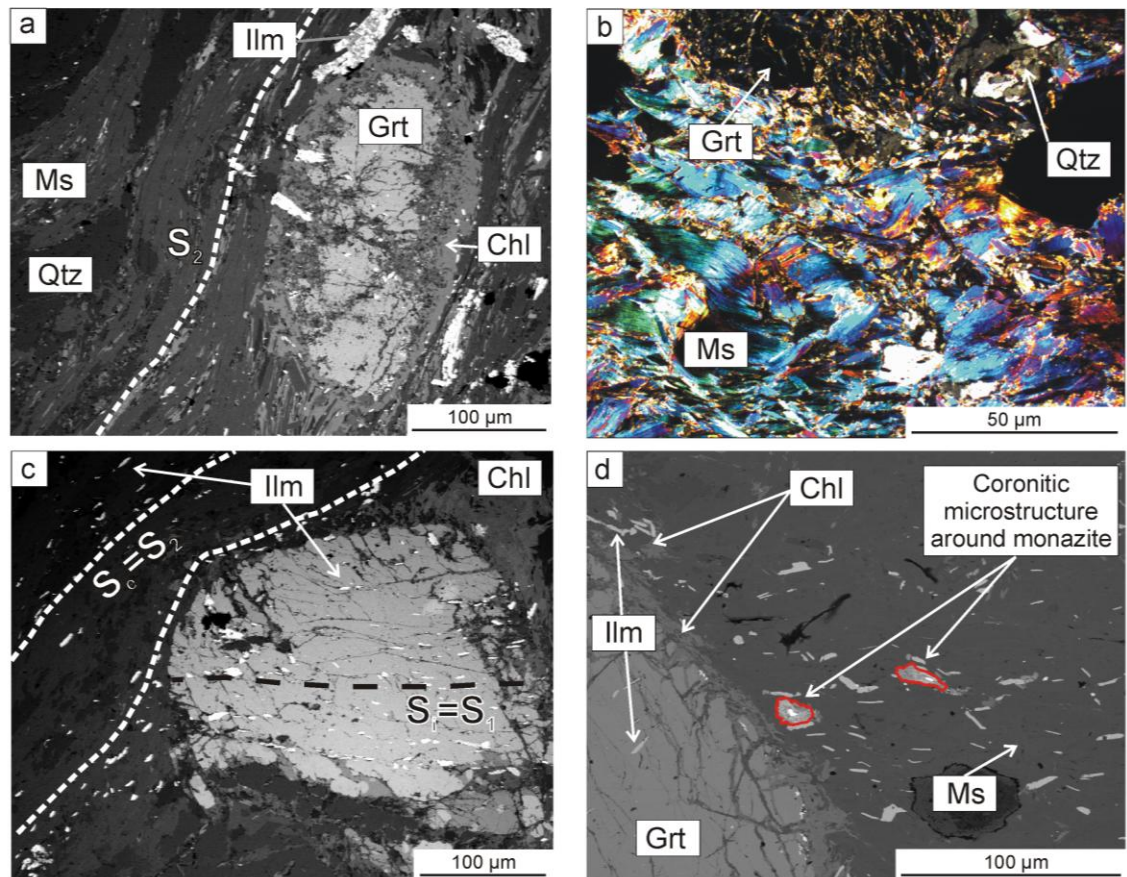
Figure 3.2 Main petrographic features of the Pontremoli metamorphic rocks. (a) potassic white mica and chlorite foliation surrounding a garnet porphyroblast (sample AG7, BSE image); (b) potassic white mica with decussate structure (sample Pontremoli 7, crossed polars photomicrograph); (c) relationships between S_1 and S_2 (sample Pontremoli 8, BSE image); (d) microstructure representing the replacement of monazite in the matrix (sample Pontremoli 7, BSE image). Mineral abbreviations: Grt = garnet, Qtz = quartz, Chl = chlorite, Ms = K white mica, Ilm = ilmenite.

3.3.1 Coronitic microstructure around monazite

A detailed microstructural study on REE-accessory minerals was carried on with a scanning electron microscope Philips 515B with an EDAX energy-dispersive system (EDS) at the Dipartimento di Scienze Biologiche, Geologiche ed Ambientali (Università di Bologna). Analytical conditions were 15 kV and 30 nA for the qualitative analyses of minerals.

Monazite in Pontremoli 7 is surrounded by a complex, polymineralic corona microstructure consisting of apatite + Th-silicate, allanite and epidote (Fig. 3.3). This microstructure, which was previously described from amphibolite-facies orthogneisses by Finger *et al.* (1998) and interpreted as the result of monazite-consuming reactions, is associated with every monazite grain observed within the Pontremoli 7 micaschist. The microstructure has a maximum width of 200 μm and may occur at two microstructural

sites: (1) in the rock matrix surrounded by potassic white mica lamellae (Figs. 3.3a, c), or (2) included in the white mica + chlorite aggregate partially replacing garnet (Fig. 3.3 d, e). When the microstructure is elongated, the elongation is parallel to the schistosity (Fig. 3.3c).

Monazite crystals show lobate rims with a maximum size of 60 µm. The surrounding **apatite** is 10 µm thick. It contains tiny inclusions of Th-silicate, characterised by its brightness in back-scattered electron (BSE) images and confirmed by qualitative EDS analyses. This corona has sharp protrusions into the allanite corona. In places apatite grains grade into the allanite corona and apatite and Th-silicate can be found also in the allanite coronas. The **allanite** corona has a width of c. 10 µm. It shows an irregular internal structure discernable by different grey tones in BSE images. The allanite corona has a greater width (100 µm) when the coronitic microstructures occur within the replaced garnet rims: in this case only relics of monazite and apatite are present. The thickness of the **epidote** corona ranges from few µm adjacent to ilmenite crystals to 30 µm in white-mica matrix. Single epidote crystals close to the corona were also observed.

Microstructural site: matrix

Microstructural site: retrocessed garnet rim

Figure 3.3 BSE images and schematic representations of the coronitic microstructure involving monazite. Abbreviations: Grt = garnet, Chl = chlorite, Ms = K white mica, Ilm = ilmenite, Zrc = zircon, Ep = epidote, Aln = allanite, Py = pyrite, Ap = apatite, Mnz = monazite, Pl = plagioclase.
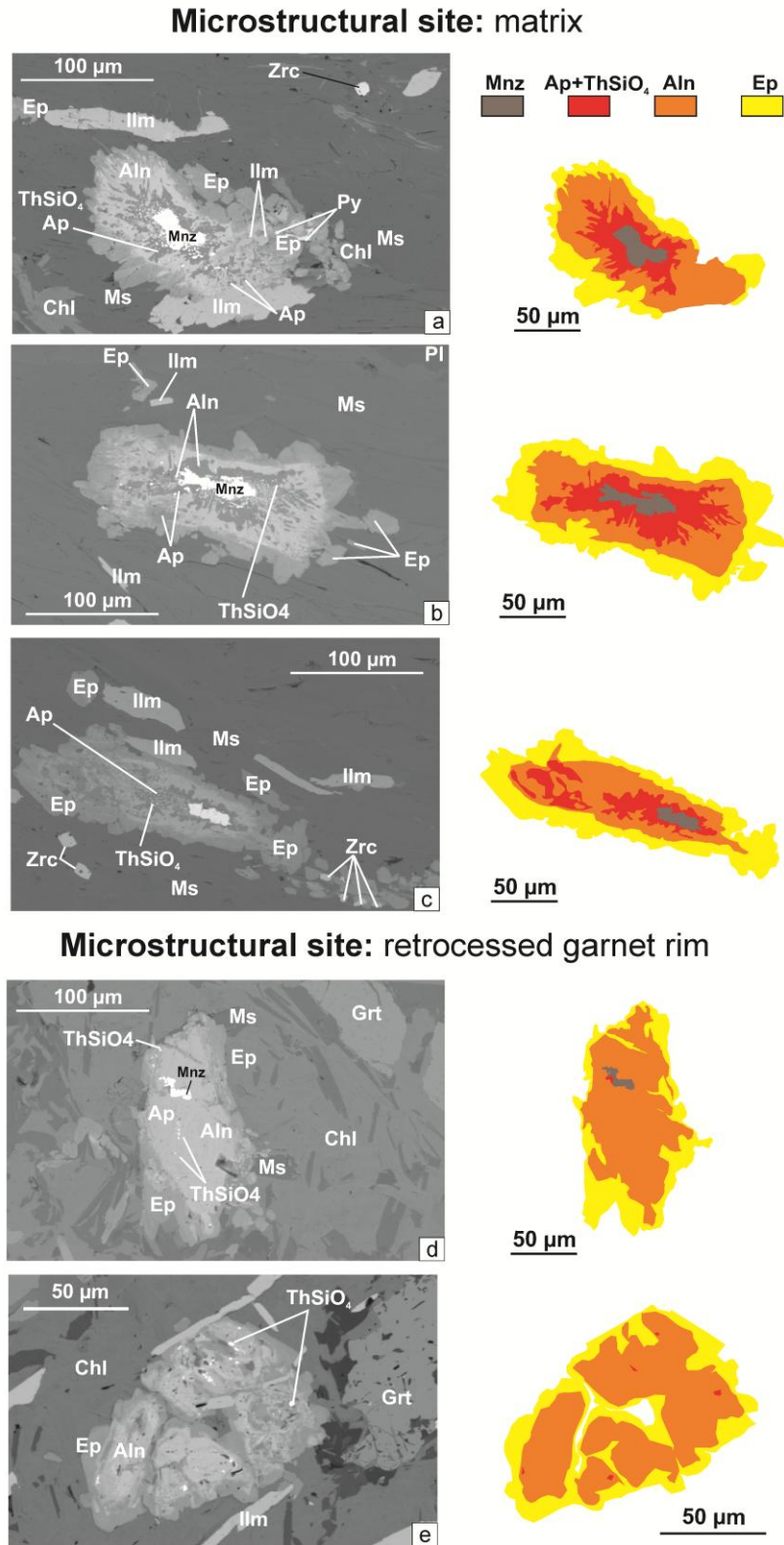
3.4 MINERAL CHEMISTRY

The chemical compositions of white mica, chlorite, garnet, plagioclase, monazite were determined at the Institut für Mineralogie und Kristallchemie (Universität Stuttgart) using a CAMECA SX100 electron microprobe (EMP) equipped with five wavelength dispersive (WD) spectrometers. Sodium, Mg, Al, Si, K, Ca, Ti, Mn, Fe, Ba were analysed in white mica, chlorite, garnet, plagioclase employing an acceleration voltage of 15 kV and 10 or 15 nA beam current. Counting times for each element element were 20 s at the peak and the background. Analytical errors of this standard method were reported by Massonne (2012). Magnesium, Al, Si, Ca, Ti, Mn, Fe, P, Y, Dy, Er, Yb were also analysed in garnet at an acceleration voltage of 20 kV and a beam current of 100 nA. Detection limits for trace elements were 400 ppm for Yb, 400 ppm for Er, 900 ppm for Dy, 120 ppm for Y, 45 ppm for P. Sulphur, U, Th, Pb, Ca, Y, La, Ce, P, Si, Nd, Gd, Dy, Sm, and Pr were determined to analyse and date monazite, using an acceleration voltage of 20 kV and a beam current of 150 nA. Standards for all EMP analyses were synthetic and natural minerals and pure oxides. The PaP correction procedure was applied. X-ray maps for Fe, Mn, Mg, Ca in garnet were acquired with a counting time of 50 ms per step, a step width of 15 μm, and 15 kV and 70 nA as acceleration voltage and electric current, respectively. Yttrium maps were also acquired using a counting time of 180 ms and a beam current of 150 nA. A counting time of 100 ms, a step width of 1 μm, an acceleration voltage of 15 kV and a current of 30 nA were the conditions for the Fe, Mg, Ti, Na X-ray maps of potassic white mica. Structural formulae for potassic white mica, chlorite, garnet, plagioclase, were calculated with the CalcMin program (Brandelik, 2009). Monazite analyses were recalculated with the MinCalc program (Bernhardt, 2010).

Garnet porphyroblasts in Pontremoli7 show a growth zoning with an increase of the almandine (Alm) and pyrope (Prp) components and a decrease of the spessartine (Sps) component from the inner core to the outermost rim (Figs. 3.4a and 3.5a-c). The grossular (Grs) component only decreases from the outer core towards the outermost rim. Typical compositions are $Alm_{72}Sps_{12}Grs_{11}Prp_4$ in the inner core and $Alm_{85}Prp_{11}Grs_3Sps_0$ at the outermost rim (Tab. 3.1). The P content in the inner core is low (below the detection limit). In the outer core and rimwards, P increases reaching a maximum of 180 ppm (Fig. 3.4b). Garnet also shows a clear zoning profile of Y, Dy, Er, Yb: these elements are concentrated only in the inner core of the porphyroblasts, whereas their amounts drop below the detection limit of our EMP analyses (see above)

in both the outer core and the rim. In the inner core average values for Y, Dy, Er, and Yb are 5520 ppm, 1050 ppm, 900 ppm, and 1020 ppm, respectively.

Potassic white mica occurring along the schistosity and as late-stage aggregates with decussate structure consists of Na-rich cores (average Na=0.57 atoms per formula unit (apfu), which is based on 22 oxygen; average Mg=0.15 apfu) and Mg-rich rims (average Na=0.29 apfu; average Mg=0.23 apfu; Figs. 3.4c, e). Small lamellae of Mg-rich potassic white mica also occur in the recrystallized areas (maximal bending areas of late microfolds). The Na-rich potassic white mica has a Si content ranging from 6.04 to 6.20 apfu and $Fe^{2+} + Mg = 0.19$-0.40 apfu; the Mg-rich potassic white mica is characterized by Si = 6.04-6.38 apfu and $Fe^{2+} + Mg = 0.19$-0.60 apfu; potassic white mica in the garnet rim has Si = 6.06-6.39 apfu and $Fe^{2+} + Mg = 0.27$-0.64 apfu (Tab. 3.2). X-ray maps of potassic white mica are displayed in Fig. 3.5.

Chlorite in different microstructural sites shows limited chemical variations. $XFe=Fe^{2+}/(Fe^{2+}+Mg)$ is 0.60-0.63 for chlorite along the schistosity, 0.56-0.62 for crystals with decussate structure, 0.57-0.63 for chlorite surrounding garnet (Tab. 3.3).

Plagioclase compositions range from $Ab_{89-92}An_{8-10}Or_0$ in the core to $Ab_{98-99}An_{1-2}Or_{0-2}$ in the rim (Tab. 3.4). Plagioclase aggregates located in the garnet pressure shadows consist of homogeneous albite crystals ($Ab_{99}An_1Or_0$).

Monazite grains show no systematic chemical zoning and no chemical variations between core and rim. Nevertheless, ThO_2 contents vary between 3.2 and 10.9 wt.%, most analyses clustering between 6-8 wt.% ThO_2. UO_2 contents are in the range 0.0-0.5 wt.%, clustering around 0.3-0.5 wt.%. PbO amounts to 0.01-0.15 wt.% clustering at 0.09-0.15 wt.%. Y_2O_3 contents are low (0.01-0.4 wt.%) and the majority of the analyses gave Y < 1300 ppm. Chemical dating of monazite was performed following the approach of Montel *et al.* (1996). Detailed analytical conditions as well as comparisons of the applied EMP dating method with more precise SHRIMP and TIMS dating results on the same samples were presented by Massonne (2014). We analysed 29 point analyses in 4 monazite grains. The derived ages of 25 analyses cluster between 250 and 361 Ma with a weighted average of 294.2 ± 4.6 Ma (average 2σ error of the single dates; MSWD = 8.6; Tab. 3.5, Fig. 3.6, see Appendix 2 for the complete dataset). We obtained also seven younger ages (from 92 to 250 Ma), which were often obtained at the monazite rims.

Table 3.1 Mineral composition of garnet normalized on 8 cations. Fe^{3+} is equal to 4 – Al.

| Garnet	rim			outer core			inner core		
Point analyses	gt1_01a	gt1_01b	gt1_01c	gt1_04	gt1_05	gt1_05b	gt1_09b	gt1_10a	gt1_11b
wt. %									
SiO_2	35.69	35.82	35.35	35.46	35.44	35.30	35.13	34.77	34.95
Al_2O_3	21.02	21.35	21.05	21.16	21.03	21.02	20.65	20.78	20.77
Fe_2O_3	3.04	3.00	3.39	3.81	3.61	3.88	2.73	2.98	2.71
TiO_2	0.06	0.05	0.05	0.08	0.08	0.07	0.07	0.06	0.07
FeO	36.00	36.02	35.61	33.37	33.18	31.69	29.90	29.41	29.55
MnO	0.10	0.15	0.28	1.31	1.59	2.44	4.86	4.96	5.16
MgO	2.51	2.13	2.02	1.44	1.36	1.24	1.08	1.06	1.04
CaO	1.73	2.30	2.22	4.10	4.10	4.64	4.15	4.15	4.08
P_2O_5	0.03	0.02	0.01	0.02	0.01	0.02	b.d.l.	b.d.l.	b.d.l.
Y_2O_3	b.d.l.	b.d.l.	0.06	b.d.l.	b.d.l.	b.d.l.	0.77	0.80	0.85
Dy_2O_3	b.d.l.	b.d.l.	0.07	b.d.l.	0.04	b.d.l.	0.09	0.08	0.11
Er_2O_3	b.d.l.	b.d.l.	b.d.l.	b.d.l.	b.d.l.	b.d.l.	0.13	0.14	0.12
Yb_2O_3	b.d.l.	b.d.l.	b.d.l.	b.d.l.	b.d.l.	b.d.l.	0.13	0.11	0.15
Total	100.20	100.89	100.13	100.78	100.44	100.29	99.67	99.29	99.58
ppm									
P	150.13	89.90	59.79	89.90	40.15	69.83	n.c.	n.c.	n.c.
Ti	350.11	320.14	309.95	470.02	490.40	399.87	390.28	369.90	429.85
Y	n.c.	n.c.	449.63	n.c.	n.c.	n.c.	6039.66	6319.99	6720.01
Dy	n.c.	n.c.	589.87	n.c.	n.c.	n.c.	750.19	659.57	980.21
Er	n.c.	n.c.	n.c.	n.c.	n.c.	n.c.	1129.85	1190.19	1089.63
Yb	n.c.	n.c.	n.c.	n.c.	n.c.	n.c.	1112.32	961.84	1282.72
apfu									
Si	2.895	2.889	2.879	2.868	2.877	2.869	2.889	2.871	2.879
P	0.002	0.001	0.001	0.001	0.001	0.001	0.000	0.000	n.c.
Al^{IV}	0.105	0.111	0.121	0.132	0.123	0.131	0.111	0.129	0.121
Al^{VI}	1.905	1.917	1.900	1.885	1.890	1.882	1.891	1.893	1.896
Fe^{3+}	0.186	0.182	0.208	0.232	0.220	0.238	0.169	0.185	0.168
Fe^{2+}	2.442	2.429	2.426	2.257	2.253	2.154	2.057	2.031	2.036
Mn	0.007	0.010	0.019	0.090	0.110	0.168	0.338	0.347	0.360
Mg	0.304	0.257	0.245	0.174	0.164	0.150	0.132	0.130	0.128
Ca	0.150	0.199	0.194	0.356	0.357	0.404	0.366	0.367	0.360

Table 3.2 Structural formulae of potassic white mica calculated on the basis of 22 oxygen. Fe^{3+} is stoichiometric-estimated considering $Fe^{3+} = 42$ – sum of the valences (Si, Ti, Cr, Al, Mn, Mg, Fe)-Ba-Ca.
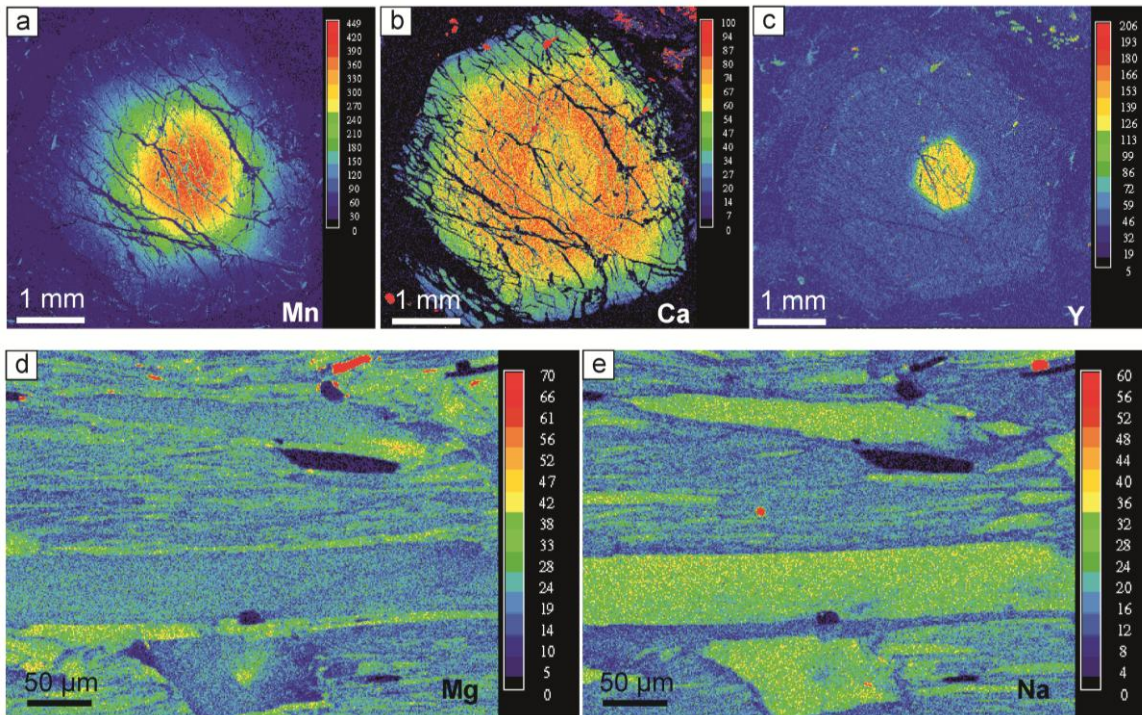
K-white mica								
	Schistosity				Decussate structure			
	Na-rich core		Mg-rich rim		Na-rich core		Mg-rich rim	
Point analyses	Ms01_03	Ms01_02	Ms24	Ms25	Ms45_05	Ms45_06	Ms44_01	Ms44_02
SiO_2	46.35	46.25	47.79	47.44	45.76	45.58	46.76	46.59
TiO_2	0.52	0.53	0.45	0.50	0.38	0.40	0.36	0.31
Al_2O_3	35.91	35.82	32.06	32.12	36.23	36.28	32.93	32.83
FeO	1.05	1.13	2.22	2.03	0.86	0.82	1.71	1.58
Fe_2O_3	0.00	0.00	0.00	0.00	0.00	0.00	0.00	0.00
MnO	0.00	0.01	0.04	0.00	0.00	0.01	0.02	0.00
MgO	0.87	0.88	1.75	1.54	0.61	0.63	1.29	1.36
CaO	0.01	0.03	0.04	0.00	0.02	0.03	0.00	0.01
Na_2O	2.21	2.28	0.86	0.89	2.22	2.24	0.87	0.72
K_2O	8.21	8.17	10.01	9.97	8.38	8.19	10.08	10.45
BaO	0.14	0.14	0.17	0.20	0.22	0.25	0.17	0.18
Total	95.27	95.23	95.39	94.70	94.68	94.42	94.19	94.04
Si	6.116	6.113	6.375	6.369	6.090	6.077	6.310	6.310
Al^{IV}	1.884	1.887	1.625	1.631	1.910	1.923	1.690	1.690
Al^{VI}	3.702	3.693	3.415	3.452	3.774	3.776	3.546	3.551
Ti	0.052	0.052	0.045	0.050	0.038	0.040	0.036	0.032
Fe^{2+}	0.115	0.125	0.248	0.228	0.096	0.092	0.193	0.179
Fe^{3+}	0.000	0.000	0.000	0.000	0.000	0.000	0.000	0.000
Mn	0.000	0.001	0.005	0.000	0.000	0.001	0.002	0.000
Mg	0.171	0.172	0.348	0.308	0.121	0.125	0.259	0.275
Ca	0.002	0.005	0.005	0.000	0.003	0.005	0.000	0.002
Ba	0.007	0.007	0.009	0.011	0.012	0.013	0.009	0.010
Na	0.566	0.583	0.223	0.233	0.572	0.578	0.228	0.190
K	1.382	1.378	1.704	1.707	1.423	1.392	1.735	1.806

Table 3.2 continued

K-white mica		
	Garnet rim	
Point analyses	Ms46_01	Ms46_02
SiO_2	46.57	46.81
TiO_2	0.24	0.29
Al_2O_3	35.22	33.94
FeO	1.55	1.87
Fe_2O_3	0.00	0.00
MnO	0.03	0.00
MgO	0.85	1.19
CaO	0.02	0.00
Na_2O	0.76	0.81
K_2O	10.07	9.92
BaO	0.24	0.18
Total	95.55	95.00
Si	6.176	6.246
Al^{IV}	1.824	1.754
Al^{VI}	3.681	3.583
Ti	0.024	0.029
Fe^{2+}	0.172	0.208
Fe^{3+}	0.000	0.000
Mn	0.003	0.000
Mg	0.167	0.236
Ca	0.003	0.000
Ba	0.012	0.009
Na	0.196	0.210
K	1.704	1.688
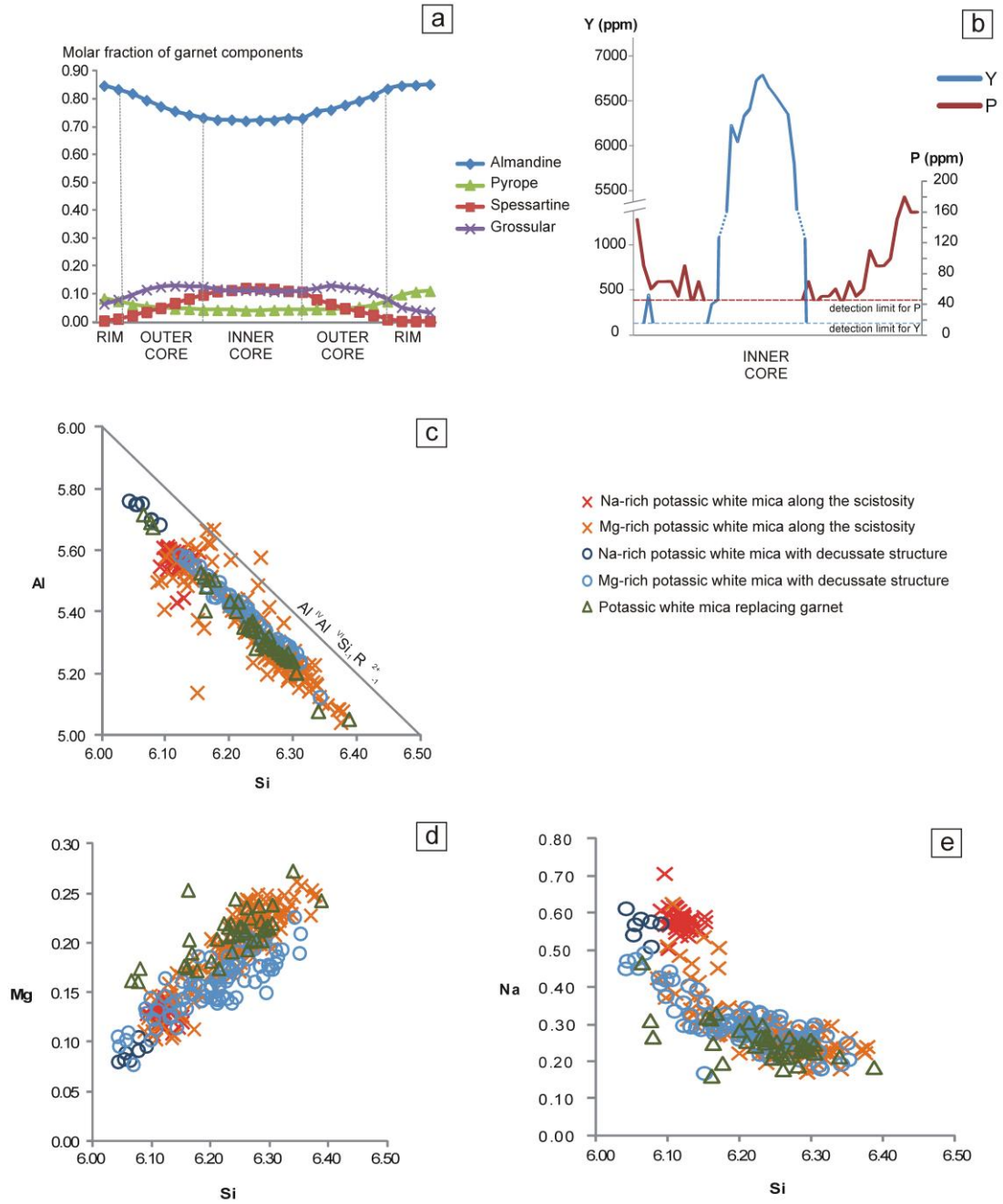
Figure 3.4 Chemical diagrams of garnet and potassic white mica. (a) compositional profile of almandine, spessartine, pyrope and grossular along a garnet transect; (b) Y and P profile along the same transect; (c) Si *vs.* Al plot for potassic white mica in different microstructural positions; (d) Si *vs.* Mg plot for potassic white mica in different microstructural positions (e) Si *vs.* Na for potassic white mica.

Figure 3.5 X-ray maps of garnet and potassic white mica. (a) Mn in garnet; (b) Ca in garnet; (c) Y in garnet; (d) Mg in potassic white mica along the schistosity; (e) Na in potassic white mica along the schistosity.

Table 3.3 Structural formulae of chlorite calculated on the basis of 28 oxygen and the negligence of Na and Ca. Chlorite is assumed to be completely hydrated (16 H).

Chlorite						
	Schistosity		Decussate structure		Garnet rim	
Point analyses	Chl01	Chl02	Chl10	Chl03	Chl07	Chl08
SiO$_2$	23.53	24.22	24.01	24.12	24.05	23.74
TiO$_2$	0.06	0.08	0.07	0.07	0.07	0.04
Al$_2$O$_3$	20.67	21.72	20.95	20.84	21.03	21.86
FeO	31.76	31.26	31.63	30.08	29.51	31.58
MnO	0.18	0.13	0.14	0.10	0.10	0.09
MgO	10.65	11.30	11.26	11.53	12.41	10.57
Total	86.84	88.71	88.07	86.73	87.17	87.89
Si	5.218	5.215	5.232	5.293	5.235	5.175
Al^{IV}	2.782	2.785	2.768	2.707	2.765	2.825
Al^{VI}	2.619	2.726	2.611	2.681	2.631	2.793
Ti	0.010	0.013	0.011	0.011	0.011	0.006
Fe	5.890	5.628	5.763	5.520	5.370	5.758
Mn	0.033	0.023	0.026	0.019	0.019	0.017
Mg	3.519	3.626	3.655	3.770	4.026	3.435

Table 3.4 Structural formulae of plagioclase based on 8 oxygen.

Plagioclase								
	Core			Rim			Garnet pressure shadows	
	Pl02_03	Pl02_04	Pl01_04	Pl01	Pl04	Pl05	Pl07	Pl08
SiO$_2$	66.27	66.60	66.30	68.59	68.74	68.86	68.74	68.76
Al$_2$O$_3$	21.40	21.52	21.32	19.31	19.28	19.30	19.05	19.29
Fe$_2$O$_3$	0.05	0.09	0.10	0.13	b.d.l.	0.04	0.13	0.15
CaO	1.98	2.01	2.20	0.33	0.20	0.15	0.12	0.25
Na$_2$O	10.94	10.91	10.88	11.81	11.86	12.01	12.34	12.08
K$_2$O	0.07	0.05	0.05	0.02	0.02	0.00	0.05	0.03
BaO	b.d.l.	0.02	b.d.l.	b.d.l.	b.d.l.	b.d.l.	b.d.l.	b.d.l.
Total	100.71	101.20	100.86	100.18	100.11	100.36	100.44	100.55
Si	2.894	2.894	2.892	2.994	3.000	2.999	2.998	2.993
Al	1.102	1.102	1.096	0.993	0.992	0.990	0.979	0.990
Fe^{3+}	0.002	0.003	0.003	0.004	n.c.	0.001	0.004	0.005
Ba	n.c.	0.000	n.c.	n.c.	n.c.	n.c.	n.c.	n.c.
Ca	0.093	0.094	0.103	0.015	0.010	0.007	0.006	0.012
Na	0.926	0.919	0.920	1.000	1.004	1.014	1.044	1.019
K	0.004	0.003	0.003	0.001	0.001	0.000	0.003	0.001

Table 3.5 EMP age and mineral chemistry of monazite on the basis of 4 oxygen.

Monazite Point analyses	Mnz04_01	Mnz01_02a	Mnz01_08a	Mnz02_04a	Mnz02_05a	Mnz04_07a	Mnz02_01a	Mnz01_01a
SiO_2	0.58	0.81	0.80	0.91	0.58	0.63	0.49	0.50
P_2O_5	29.34	27.30	26.28	29.80	29.98	30.33	30.51	30.77
SO_3	0.03	0.02	0.04	0.06	0.03	0.02	0.02	0.01
CaO	1.54	1.58	1.78	1.88	1.47	1.51	1.40	1.58
Y_2O_3	0.05	0.09	0.08	0.05	0.01	0.03	0.09	0.10
La_2O_3	14.56	13.42	13.72	13.84	15.39	14.86	14.69	14.67
Ce_2O_3	28.64	27.53	26.80	26.70	29.16	28.70	29.02	29.10
Pr_2O_3	3.05	2.65	2.79	2.93	3.04	3.06	3.09	3.20
Nd_2O_3	11.95	11.48	11.12	11.33	11.63	11.87	12.19	12.26
Sm_2O_3	2.11	2.05	1.97	2.04	1.54	1.90	2.15	2.14
Gd_2O_3	1.54	1.57	1.50	1.46	0.79	1.18	1.59	1.55
Dy_2O_3	0.20	0.27	0.21	0.21	0.11	0.17	0.27	0.27
PbO	0.10	0.13	0.14	0.15	0.11	0.12	0.09	0.10
ThO_2	6.89	9.08	9.62	10.17	7.44	7.69	5.87	5.76
UO_2	0.42	0.48	0.50	0.52	0.42	0.47	0.43	0.43
Total	100.99	98.46	97.35	102.05	101.70	102.55	101.88	102.43
Si	0.023	0.033	0.035	0.022	0.024	0.019	0.031	0.032
P	0.972	0.946	0.972	0.981	0.982	0.991	0.981	0.945
S	0.001	0.001	0.002	0.001	0.001	0.000	0.001	0.001
Ca	0.065	0.069	0.077	0.061	0.062	0.064	0.056	0.066
Y	0.001	0.002	0.001	0.000	0.001	0.002	0.001	0.002
La	0.210	0.203	0.197	0.219	0.210	0.206	0.211	0.210
Ce	0.410	0.413	0.376	0.412	0.402	0.405	0.397	0.415
Pr	0.043	0.040	0.041	0.043	0.043	0.044	0.044	0.043
Nd	0.167	0.168	0.156	0.161	0.162	0.167	0.166	0.172
Sm	0.028	0.029	0.027	0.021	0.025	0.028	0.027	0.028
Gd	0.020	0.021	0.019	0.010	0.015	0.020	0.019	0.021
Dy	0.003	0.004	0.003	0.001	0.002	0.003	0.002	0.003
Pb	0.001	0.001	0.002	0.001	0.001	0.001	0.001	0.001
Th	0.061	0.085	0.089	0.065	0.067	0.050	0.059	0.076
U	0.004	0.004	0.004	0.004	0.004	0.004	0.003	0.004
AGE	289.58	294.37	294.07	293.1	312.09	314.01	294.84	292.09
statistical error	7.21	5.88	5.49	6.81	6.69	8.18	7.68	6.24
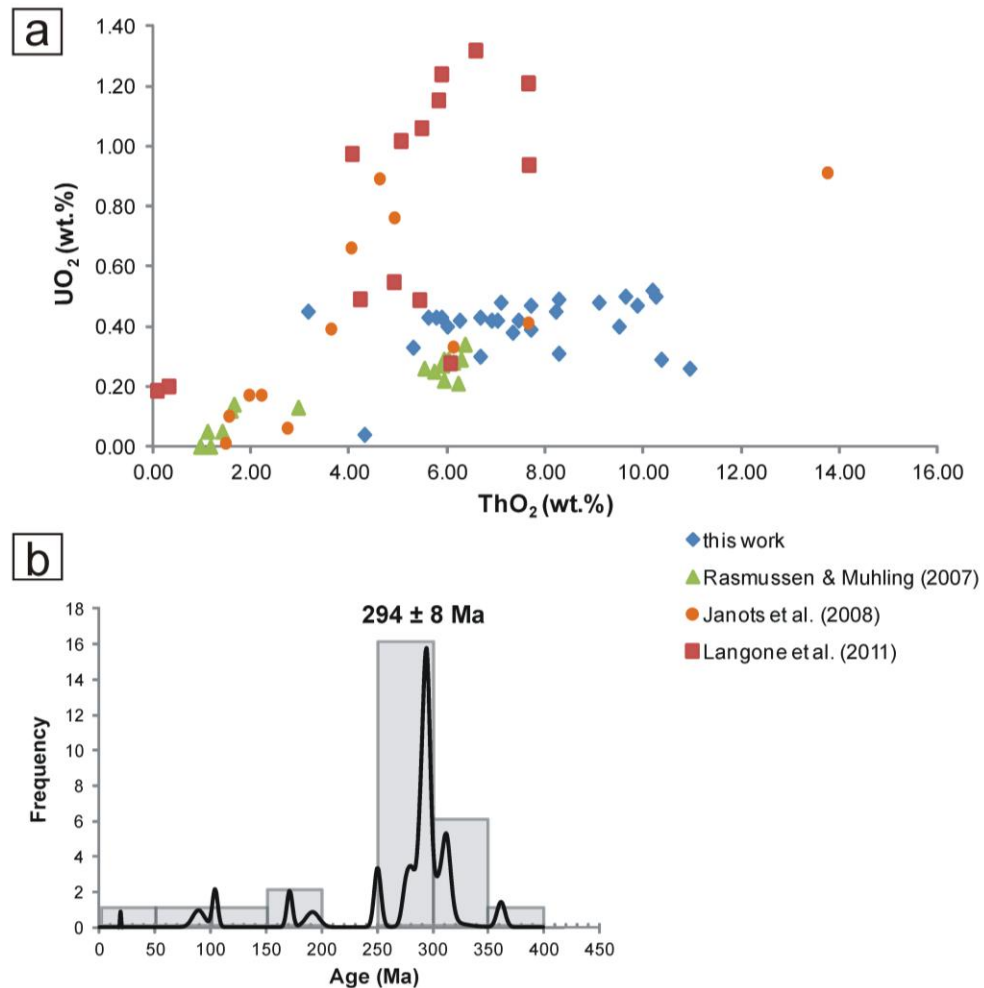
Figure 3.6 Monazite composition and EMP age. (a) UO_2 *vs.* ThO_2 diagram of the monazite analysed in the Pontremoli sample and other monazite occurrences (Rasmussen & Muhling, 2007; Janots *et al.*, 2008; Langone *et al.*, 2011); (b) relative probability plot and histogram of the monazite EMP ages.

3.5 GEOTHERMOBAROMETRY

3.5.1 Calculation of the bulk-rock chemistry

We performed thermodynamic modelling in order to derive the *P-T* path of the Pontremoli sample (Pontremoli7) and, in particular, the thermobaric conditions during the growth of chemically different garnet domains. One of the input parameters to calculate isochemical phase diagrams, so-called pseudosections, is the bulk-rock composition. Because of the limited availability of the cuttings, it was not possible to obtain sufficient material to prepare powders for conventional XRF analyses. Moreover, the presence of zoned garnet required the calculation of different bulk compositions to take into account possible modifications of the effective bulk compositions (Stüwe, 1997) due, for instance, to the shielding of inner garnet zones at late stage metamorphic equilibration. For these reasons, we calculated three different bulk compositions to

model different stages of the metamorphic evolution. The initial, unfractionated bulk-rock chemistry was calculated by combining mineral modes and average mineral compositions (bulk1). We also calculated the bulk composition after the fractionation of the entire garnet core (bulk2) and the whole garnet (bulk3).

As the composition bulk1 includes the entire garnet and the Pontremoli7 thin section represents a garnet-rich area, we averaged the mode of Pontremoli7 and AG7 samples to avoid garnet overestimation. The Pontremoli 7 and AG7 modal compositions were obtained by counting 1000 points for each thin section, using a polarizing optical microscope equipped with a mechanical point-counter. The calculated bulk composition of the selected sample is Ca-poor and Mn-rich compared to the average composition of pelites given by Shaw (1956). Whole-rock Ca and Al amounts normalized to Shaw's (1956) data plot along the reaction line of the monazite to allanite reaction inferred by Wing *et al.* (2003). This agrees with the occurrence of allanite replacing monazite in the studied sample.

The garnet core composition was calculated using mineral chemistry and the garnet core mode. The composition of the garnet core was subtracted from the unfractionated XRF bulk-rock composition (in mol units), obtaining the "bulk2" composition.

We determined the volumes of the garnet core and rim in Pontremoli 7 through image analysis of X-ray maps. To apply this approach the required parameters are composition and density of the unfractionated rock, and composition, volume and density of the fractionated phase. For the digital image analysis of two garnets we applied the JMicroVision 1.2.7 software (http://www.jmicrovision.com/). The garnet core volume resulted in 9 % vol. of the whole rock. The garnet composition taken into account is an average of the inner core and outer core analyses. The density of the garnet inner core (4.15 g cm^{-1}) and density of the bulk-rock (2.91 g cm^{-1}) were obtained from the thermodynamic output in the inner core intersection area. The composition bulk3 was finally calculated excluding the whole garnet by the method outlined above. The resultant compositions are reported in Table 3.6.

Table 3.6 Calculated bulk-rock compositions with garnet (bulk1) and without garnet core (bulk2) and the whole garnet (bulk3).

	unfractioned composition (bulk1)	fractioned compositions	
		garnet inner and outer core fract. (bulk2)	whole garnet fract. (bulk3)
	wt. %	wt. %	wt. %
SiO_2	53.31	57.03	57.85
TiO_2	1.17	1.31	1.36
Al_2O_3	24.22	24.18	24.32
FeO	12.00	8.26	7.13
MnO	0.44	0.03	0.00
MgO	2.56	2.71	2.72
CaO	0.62	0.09	0.00
Na_2O	1.19	1.33	1.38
K_2O	4.49	5.06	5.25

Footnote: To convert vol. % in wt. % we used the densities of minerals reported in Anthony *et al.* (2011). The densities of the minerals that show significant solid solution were calculated through a linear interpolation between the densities of the corresponding end-members.

3.5.2 Phase diagram calculations

Thermodynamic modelling in the $MnO-K_2O-Na_2O-CaO-FeO-MgO-Al_2O_3-SiO_2-H_2O-TiO_2$ system was performed with the PERPLE_X computer package (Connolly 1990; Connolly & Petrini, 2002). Ti was considered to take into account the relationships among Ti-rich minerals (rutile, ilmenite and titanite). Ferric iron was not introduced in the chemical system because of the lack of Fe^{3+}-rich oxides and the negligible stoichiometrically calculated Fe^{3+} content in the major silicates (Lo Pò & Braga, 2014). Neglecting ferric iron implies that the Fe^{3+}-rich minerals (allanite and epidote) cannot be thermodynamically properly modelled. They are represented by Fe-free zoisite. Nevertheless, we think that this simplification is adequate also because of the low modal amounts (< 1 vol. %) of allanite-epidote. The following input parameters were chosen: (a) the thermodynamic dataset of Holland & Powell (1998, with the 2002 upgrade); (b) the compensated Redlich Kwong (CORK) fluid equation of state by Holland & Powell (1991, 1998); (c) SiO_2 and H_2O in excess. The solid solution models used in the thermodynamic modelling were: K-white mica (Holland & Powell, 1998; the maximum paragonite content has been set to 50 mol.%), Na-Ca-white mica (Massonne, 2010; the maximum muscovite content has been set to 50 mol.%), garnet (Holland & Powell, 1998), biotite (Powell & Holland, 1999), chlorite (Holland *et al.*, 1998), plagioclase

(Fuhrman & Lindsley, 1988), K-feldspar (Waldbaum & Thompson, 1968), staurolite (Holland & Powell, 1998) and ilmenite (ideal ilmenite-geikielite-pyrophanite solid solution; http://www.perplex.ethz.ch/PerpleX_solution_model_glossary.html). Pure phases in the calculations were titanite, rutile, zoisite, sillimanite and andalusite.

3.5.3 Prograde path before peak conditions (bulk1)

An isochemical phase diagram was calculated for bulk1 and the *P-T* range 2-15 kbar and 300-600 °C (Fig. 3.7). Potassic white mica is stable throughout the entire *P-T* range. Chlorite and Na-Ca white-mica disappear at temperature higher than 550°C at 3 kbar and 600°C at 6-7 kbar, replaced by staurolite and plagioclase. The garnet-in curve is located at 400°C at 5 kbar to 450°C at 3 kbar. Biotite occurs above 530 °C. The plagioclase-in curve is located below 7 kbar. The *P-T* fields with zoisite terminate between 450°C and 530°C. Ilmenite is replaced by rutile only at relatively low temperatures and high pressures. Titanite-bearing *P-T* fields occur below 450 °C. The paragenetic field containing chlorite + potassic white mica + sodic white mica + ilmenite + rutile + titanite + quartz + K-feldspar plots at 350-400°C and P < 3.5 kbar. Isopleths for molar fractions of garnet related to the garnet inner core $Alm_{72}Sps_{12}Grs_{11}Prp_4$ intersect in a small area at 530 °C and 5.5 kbar within this paragenetic field albeit without sodic white mica. The resulting prograde path runs from 350-400°C and P < 5 kbar to 530 °C and 5.5 kbar, crossing the rutile/ilmenite transition and the garnet-in curve, in agreement with the observed petrographic and microstructural features. The plagioclase-in and zoisite-out curves are also crossed. Corresponding isopleths for the garnet outer core intersect outside the investigated *P-T* range, but this can be due to the negligence of a fractionation effect. The calculated Si content in potassic white mica is 6.14-6.16 apfu in the early paragenesis field, and 6.12-6.14 apfu in the garnet inner core intersection area. Such values are within the observed Si range of the Na-rich potassic white mica (Si=6.04-6.20 apfu). The calculated XFe of chlorite is 0.73 apfu in the early paragenesis field and 0.56-0.69 apfu in the garnet inner core intersection area. The observed XFe of chlorite along the schistosity is 0.56-0.62 apfu.

### 3.5.4 Peak conditions after early garnet fractionation (bulk2)

The composition bulk2 excludes the garnet core. Therefore, only the rim of the garnet was considered for *P-T* estimations. In the *P-T* pseudosection for bulk2 (Fig. 3.8) the

topology is different compared to that of bulk1. Potassic white mica is again stable in the entire *P-T* range, but chlorite occurs only at temperatures below 500°C. Na-Ca-white-mica disappears at temperature higher than 525°C at 2 kbar and 600°C at 5 kbar in the *P-T* pseudosection for bulk2. The staurolite-in curve runs from 530°C at 3 kbar to 600°C at 7 kbar. Ilmenite replaces rutile above 450°C. The *P-T* field of garnet is reduced compared to that of bulk1. The garnet isopleths geothermobarometry defines *P-T* conditions around 575°C and 7 kbar for the rim compositions ($Alm_{83-85}Prp_{7-11}Grs_{3-8}$). These conditions are compatible with the paragenetic fields containing potassic white mica, sodic white mica, chlorite, garnet, ilmenite, biotite, staurolite, and quartz. The *P-T* isopleth for the maximum Si content in Na-rich potassic white mica (6.20 apfu) intersects the garnet compositional isopleths.

MnTiKCNFMASH (+ Qtz + H$_2$O)
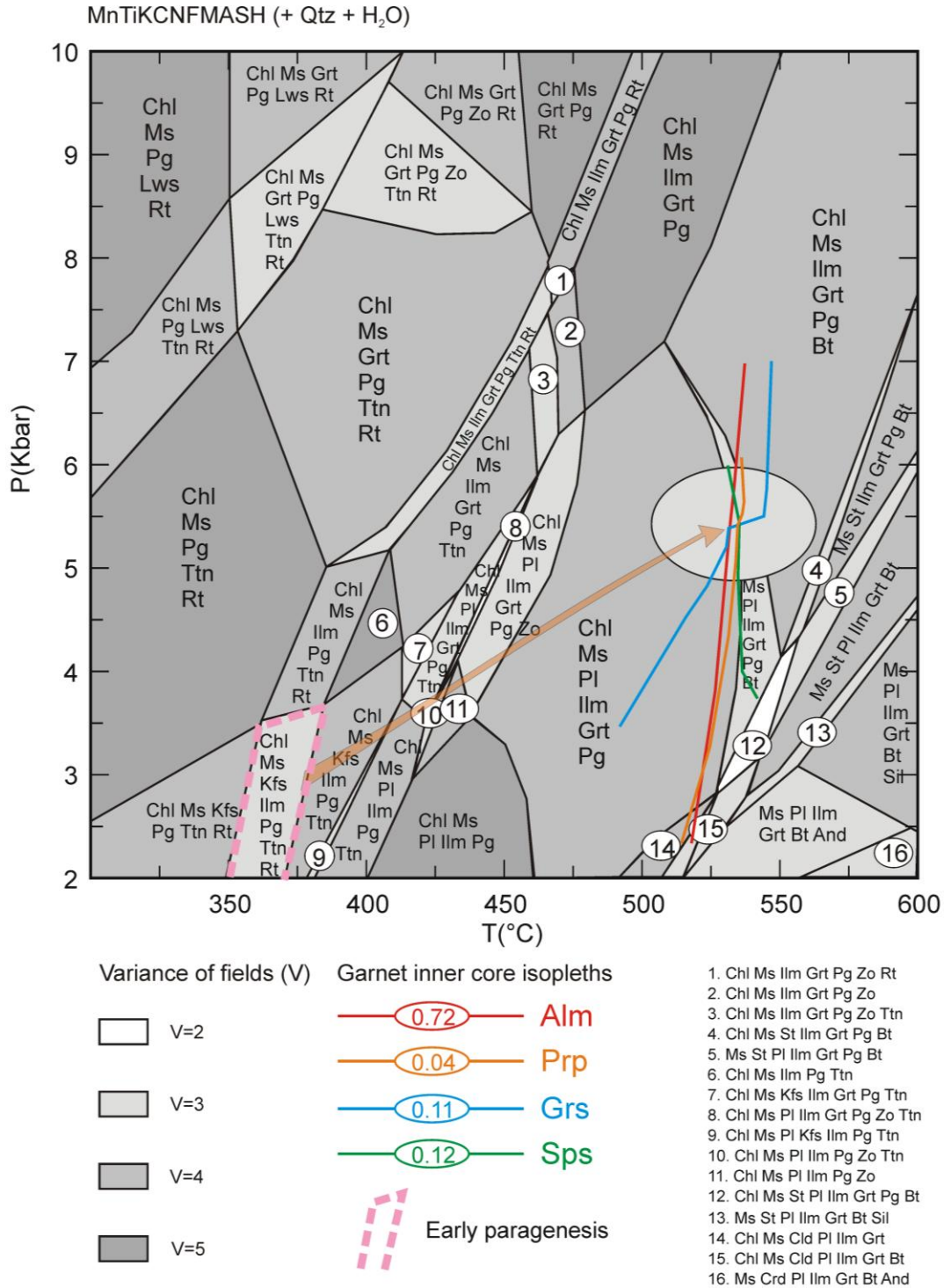
Figure 3.7 *P-T* pseudosection calculated with the unfractionated bulk-composition (bulk1). The dotted area outlines the field corresponding to an early paragenesis and the small triangle is the inner core garnet isopleths area. A *P-T* uncertainty ellipse is also displayed. Abbreviations: Ms = potassic white mica (muscovite/phengite), Pg = sodic white mica, Chl = chlorite, Kfs = alkali-feldspar, Pl = plagioclase, Grt = garnet, Bt = biotite, St = staurolite, And = andalusite, Crd = cordierite, Ilm = ilmenite, Rt = rutile, Ttn = titanite, Lws = lawsonite, Zo = zoisite, Sil = sillimanite, Cld = chloritoid, Ab = albite.
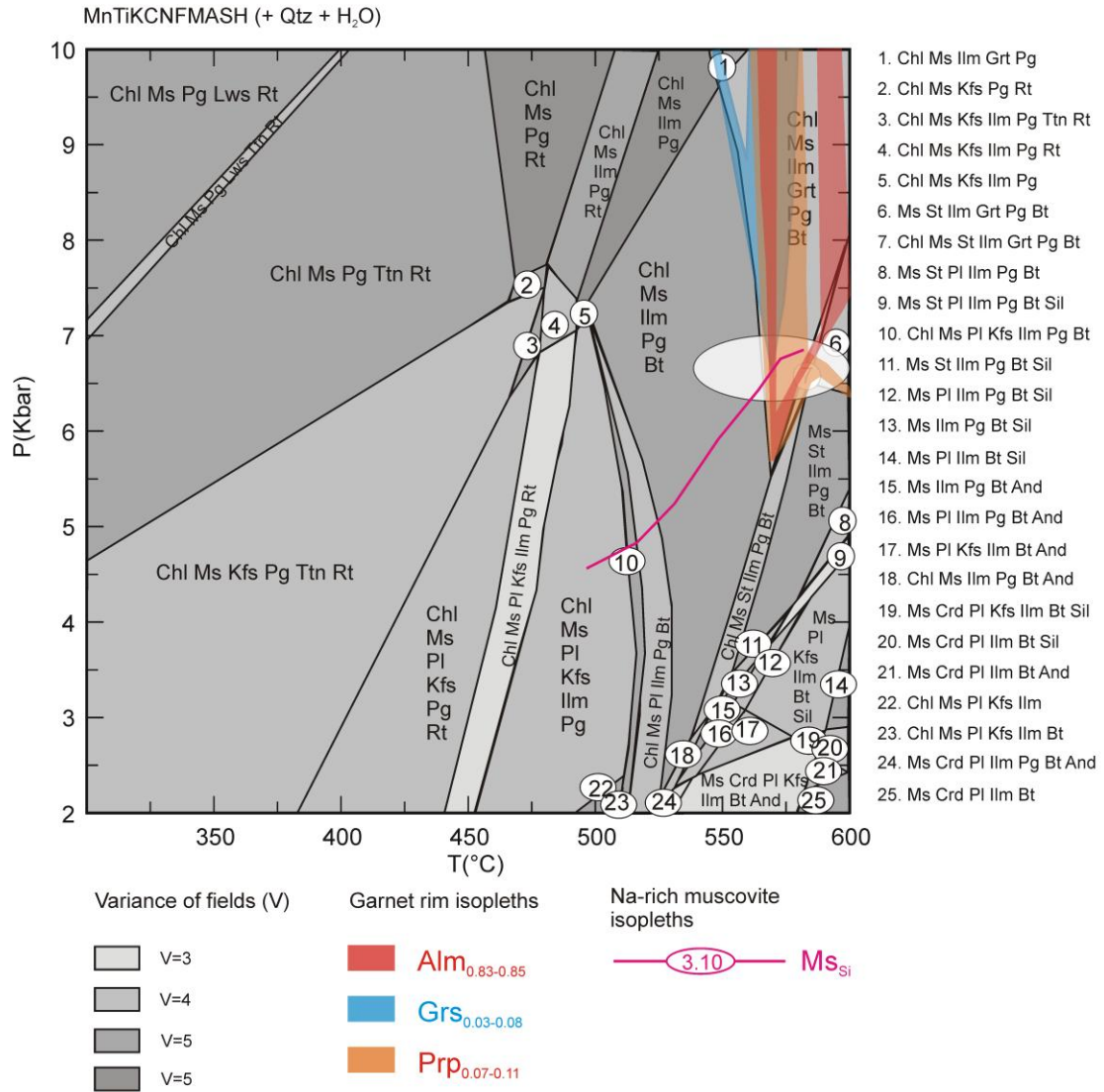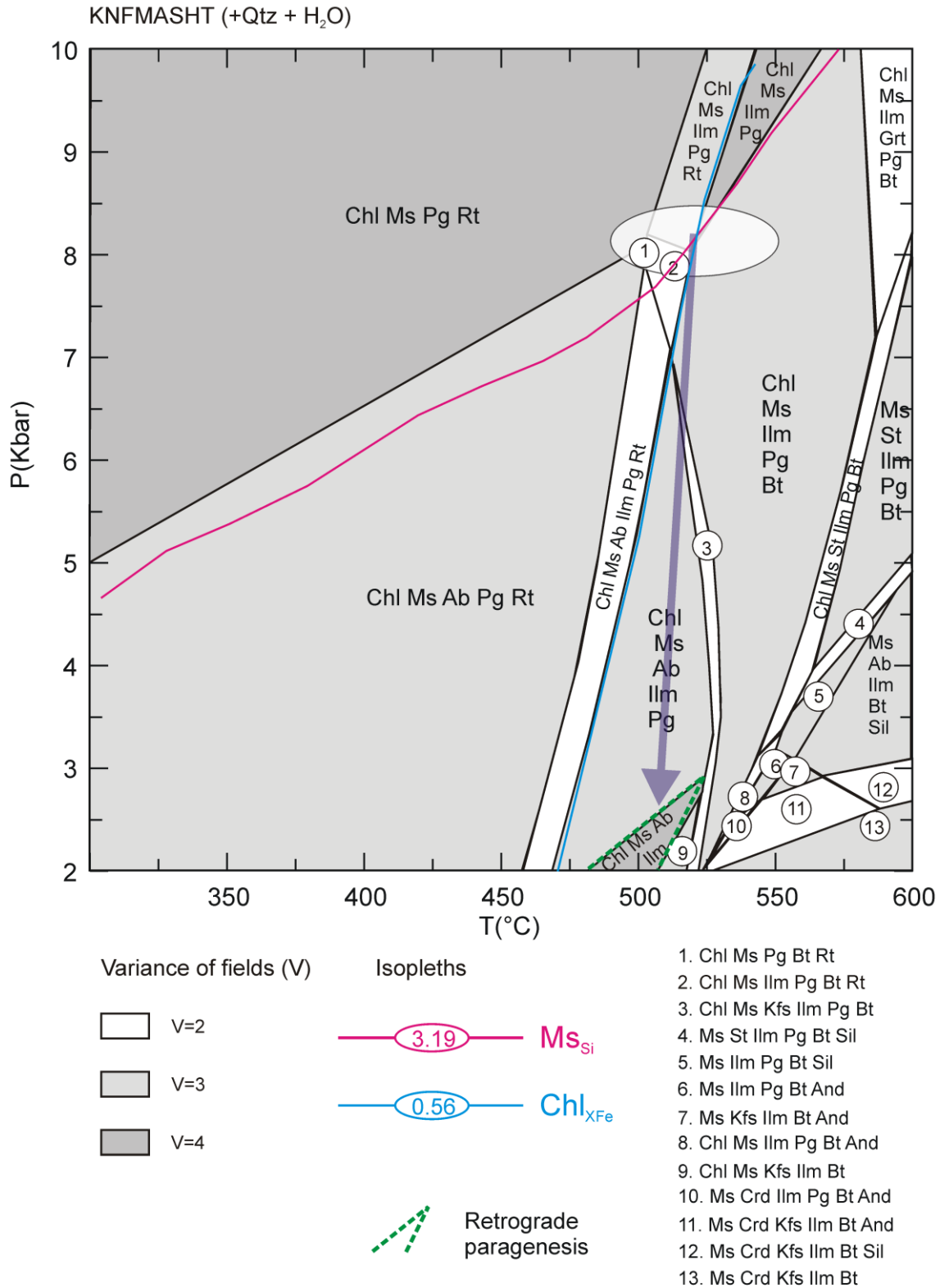
Figure 3.8 *P-T* pseudosection calculated for an effective composition after the fractionation of the garnet core (bulk2). The circle corresponds to the garnet rim composition with a *P-T* uncertainty ellipse. The maximum Si content in the potassic white mica core (Na-rich) is also displayed.

3.5.5 Retrograde path (bulk3)

Since the garnet rim was in equilibrium with the Na-rich core of the potassic white mica crystals, the Mg-rich rims of the potassic white mica in aggregates along the schistosity and with decussate microstructure should have crystallised later together with chlorite in the same microstructural position. Thermodynamic modelling of this stage is based on composition bulk3 excluding the whole garnet (Fig. 3.9). Because no significant Mn and Ca was left, the KNFMASHT chemical subsystem was selected for corresponding calculations. Potassic white mica is again stable in the entire *P-T* range of the pseudosection for bulk3. Na-white mica breaks down above 525°C at 2 kbar and 600°C

at 5 kbar. Chlorite occurs below 550°C. Biotite forms at temperatures of 500°C and more. Staurolite occurs around 550-600°C and above 3 kbar. Albite appears in the range 300-500°C at pressures below 5 and 8 kbar, respectively. At higher temperatures (550-600°C) the maximum pressure for albite occurrence is 5 kbar. The maximum Si content in Mg-rich potassic white mica (6.38 apfu) and the minimum XFe ratio in chlorite (0.56) with decussate structure indicate *P-T* conditions of 520°C and 8 kbar by intersecting isopleths. These conditions are in the paragenetic field potassic white mica + chlorite + ilmenite + sodic white mica + quartz. The lower values of Si in Mg-rich potassic white mica and the observed paragenesis potassic white mica + chlorite + albite + ilmenite + quartz allow to constrain the retrograde evolution passing through T=500°C and P=2 kbar.

KNFMASHT (+Qtz + H₂O)

Figure 3.9 *P-T* pseudosection calculated for an effective composition after the fractionation of the entire garnet (bulk3). Maximum Si content in the potassic white mica rim (Mg-rich) and the minimum XFe in chlorite allow the estimation of the pressure peak. The ellipse represents the *P-T* uncertainty. Retrograde paragenesis is delimitated by the green line.

3.6 DISCUSSION

3.6.1 The identification of inherited monazite in the Pontremoli micaschist

Most of the monazite analyses in the Pontremoli micaschist yielded ThO_2 and UO_2 contents in the range of 6-8 and 0.3-0.5 wt.%, respectively. The ThO_2 and UO_2 contents in low-grade, fluid-derived monazite are generally < 2 wt. % and 0-0.1 wt.%, respectively. These contents are distinct from igneous/high-grade monazite that shows ThO_2 = 3-6 wt.% and UO_2 ~ 0.2-0.3 wt.% (Schandl & Gorton, 2004; Rasmussen & Muhling, 2007; Langone *et al.*, 2011). Thus, high ThO_2 and UO_2 contents identify igneous or medium- to high-grade monazite. Thus, the monazite from Pontremoli micaschist resembles monazite formed at medium-high rather than low-medium grade conditions inferred for the prograde path of the Pontremoli micaschist.

The partitioning of Y between a Y-rich mineral and coexisting garnet is a useful tool to assess the mutual relationships between the two phases. The Y content in the garnet falls from 4550-6800 ppm (inner core) to values close to the detection limit in the outer core and in the rim. The observed Y zoning can be explained with the consumption of a Y-rich phase during the crystallization of the garnet inner core. The low (< 1300 ppm) Y concentration in monazite excludes monazite from being the source of Y for the garnet inner core. The Y and the HREE concentrations in garnet are instead controlled by xenotime consumption because this mineral with resorption features was found only in the garnet inner core. When xenotime was almost completely dissolved and all Y was introduced in the inner garnet core, no significant amounts of Y were available during the growth of the garnet outer core and rim. This is in agreement with the results of Spear & Pyle (2010), who demonstrated that xenotime becomes instable at pressures above 5-6 kbar. Moreover, these authors suggest, through theoretical modelling, that during garnet growth xenotime commonly breaks down and this explain why xenotime is found only in the garnet inner core and not in the matrix. Most of the monazite analyses in the Pontremoli micaschist yielded ThO_2 and UO_2 contents in the range of 6-8 and 0.3-0.5 wt.%, respectively. The ThO_2 and UO_2 contents in low-grade, fluid-derived monazite are generally < 2 wt. % and 0-0.1 wt.%, respectively (Rasmussen & Muhling, 2009). Such low contents are distinct from igneous and high-grade metamorphic monazite that usually shows ThO_2 contents of 3-6 wt.% and UO_2 contents of 0.2-0.3 wt.% (Schandl & Gorton, 2004; Rasmussen & Muhling, 2007; Langone *et al.*, 2011). Thus, the observed high ThO_2 and UO_2 contents point to igneous or medium-

to high-grade monazite in the Pontremoli micaschist and not to the low-medium grade conditions inferred for the prograde path of the Pontremoli micaschist by other methods. The partitioning of Y between a Y-rich mineral and coexisting garnet is a useful tool to assess the mutual relationships between the two phases. The Y content in the garnet falls from 4550-6800 ppm (inner core) to values close to the detection limit in the outer core and in the rim. The observed Y zoning can be explained by the consumption of a Y-rich phase during the crystallization of the garnet inner core. The low (< 1300 ppm) Y concentrations in monazite excludes this mineral from being the source of Y for the garnet inner core. The Y and the HREE concentrations in garnet are instead controlled by consumption of xenotime which shows resorption features and occurs exclusively in the garnet inner core. After xenotime was almost completely dissolved and nearly all Y was introduced in the inner garnet core, no significant amounts of Y were anymore available during the growth of the garnet outer core and rim. This is in agreement with the results of Spear & Pyle (2010), who demonstrated that xenotime becomes instable at pressures above 5-6 kbar. Moreover, these authors suggested, through theoretical modelling, that during garnet growth xenotime commonly breaks down and this explain why xenotime is found only in the garnet inner core and not in the matrix.

3.6.2 *P-T* condition and garnet response to REE-accessory mineral reactions

Textural evidence indicates that the Th-rich monazite became unstable and underwent partial or total dissolution. This process led to the formation of a complex corona made of different REE-minerals. The sequence of these REE-minerals forming the multiple corona microstructure around monazite can be correlated with a change of the kind of mineral inclusions in the garnet porphyroblasts where single allanite crystals are hosted only in the garnet outer core whereas the garnet rim hosts epidote (Figs. 3.3 e, f). The garnet zoning also reflects the order of growth of the different REE-minerals. While the usual Fe, Mn and Mg growth zoning in garnet can be observed, its Ca profile is more complex, with lower values in the inner core than in the outer core (Figs. 3.4a, 3.5b). From the garnet outer core to the rim the Ca content decreases gradually, following the common grossular prograde pattern. Similarly to Ca, also P is low in the garnet inner core and then increases towards the garnet rim. The humps in the Ca profile and the low P content in the garnet inner core may be explained by the contemporary crystallization of apatite in the matrix, replacing the pre-existing monazite.

As inferred by Finger *et al.* (1998) for a similar occurrence in amphibolite-facies

metagranitoids, the original monazite may provide the phosphorous necessary for the apatite growth, since apatite always surrounds monazite (Fig. 3.3). Thorium, previously hosted in monazite, partitions into Th-silicates and apatite in the corresponding corona. The anorthite component in plagioclase and biotite may provide Ca and Fe required for allanite and epidote growth (Finger *et al.*, 1998).

Based on the above considerations, we infer the following correspondence between garnet zoning and the crystallization of the REE-minerals produced during the consumption of the inherited monazite (Fig. 3.10): 1) garnet inner core - crystallization of apatite and Th-silicate, 2) garnet outer core - crystallization of allanite, 3) garnet rim - crystallization of epidote.

If this reconstruction is correct, we can correlate the thermobaric conditions of the garnet growth to the accessory mineral reactions. Since uncertainties involving thermodynamic modelling must be considered, we follow the suggestion by Massonne (2013) who proposed 2σ-errors in the range of 10% and 5% related to the corresponding pressure and temperature estimate, respectively. For this reason we infer that the partial destruction of monazite and the development of the apatite, allanite and epidote coronae occurred presumably at 500-600 °C and 5-7 kbar during the prograde evolution. This assumption is compatible with the Y-Al-garnet (YAG) thermometry (Pyle & Spear, 2000) that yields, for the garnet inner core, an average temperature of 562°C (± 30°C). Interestingly, the *P-T* estimates of several amphibolite-facies metagranitoids with apatite-allanite-epidote coronas around monazite reported in Finger *et al.* (1998) were also metamorphosed in the range of 500–600 °C and 4–7 kbar.

Since monazite predates the garnet, the monazite age of 294 ± 5 Ma must be older than the garnet forming metamorphic stage.
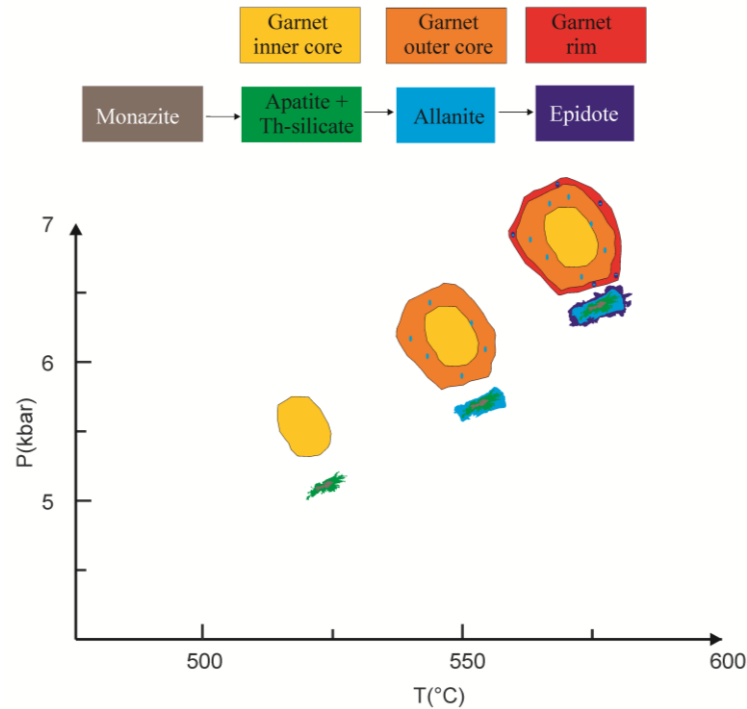
Figure 3.10 *P-T* evolution of the sequence of the REE-minerals related to garnet growth.

3.6.3 The monazite-allanite transition

Previous studies based on natural assemblages (summarised by Tomkins & Pattinson, 2007) indicate that allanite forms from a monazite precursor at the biotite-in isograd. (~ 300-400°C; Spear, 1993). Moreover, the thermodynamic calculations by Janots *et al.* (2007) in the system SiO_2–Al_2O_3–FeO–Fe_2O_3–MgO–CaO–Na_2O–K_2O–P_2O_5–La_2O_3–CO_2–H_2O predict that the reaction of monazite to form allanite starts at temperatures as low as 300°C. The results of our study, however, show that the monazite-allanite transition falls in the 500-600 °C (at 5-7 kbar) range. This discrepancy may be due to (i) the uncertainties regarding the calorimetric data for synthetic monazite(-La), $LaPO_4$, and dissakisite, $CaLaMgAl_2(SiO_4)_3OH$, (ii) the simplification that these end-member phases are good analogues for natural monazite(-Ce) and Fe-allanite(-Ce) (Janots *et al.*, 2007), (iii) the differences in the bulk-rock compositions, especially in the Ca content, considered here (CaO = 0.62 wt. %) and used (0.88 wt. %) by Janots *et al.* (2007). A lower CaO content might favour the stability of monazite over allanite, thus, probably shifting the reaction monazite = allanite to higher temperatures (Foster & Parrish, 2003; Wing *et al.*, 2003). In the diagram $Ca_{sample}/Ca_{Shaw's\ average\ pelite}$ vs. $Al_{sample}/Al_{Shaw's\ average\ pelite}$ for samples from the biotite and garnet zone (Wing *et al.*, 2003), the Pontremoli metapelite plots along the line in which metamorphic allanite and low-grade monazite coexist.

3.6.4 *P-T* path

The derived *P-T* path (Fig. 3.11) starts at 350°C and P < 5 kbar (rutile and K-feldspar bearing paragenesis). The chlorite + potassic white mica + sodic white mica + ilmenite + rutile + titanite + quartz + K-feldspar paragenesis (350-400°C and P < 3.5 kbar) is in agreement with the K-feldspar inclusions in plagioclase and the rutile/ilmenite transition and may represent an early metamorphic stage. At increasing temperature, rutile breaks down and the calculated field chlorite + potassic white mica + ilmenite + sodic white mica + titanite + quartz could correspond to the assemblage that formed the schistosity now represented only by the ilmenite S_i in garnet. With a further increment of temperature the garnet-in curve was crossed, and conditions of 530 °C and 5.5 kbar, obtained by garnet inner core isopleths, were reached. Zoisite and titanite of the prograde path have not been observed in the studied rock sample, however the calculated modes of these phases are less than 2 %. The temperature derived from the garnet inner core isopleths is 130°C higher than the temperatures of the garnet-in curve. This may be due to reaction overstepping or to an imperfect correspondence of the maximum-Mn analysis of garnet and the true Mn-content of the garnet innermost core. The peak conditions of 575°C and 7 kbar (garnet rim and potassic white mica cores) were followed by a stage at higher pressures (520°C and 8 kbar) that stabilized the Mg-rich potassic white mica and chlorite with decussate structure. The retrograde evolution points to T=500°C and P=2 kbar. The lack of biotite at the peak conditions may be due to its complete retrocession to chlorite and potassic white mica during the retrograde evolution. Sodic white mica is always present in the *P-T* pseudosection along the derived path, but distinct crystals have not been observed. Thus, we think that sodic white mica was replaced by potassic white mica and albite during the retrograde evolution. In Fig. 3.12 the main observed and computed parageneses of the pre-peak stage, temperature and pressure peak stages and retrograde stage are displayed.
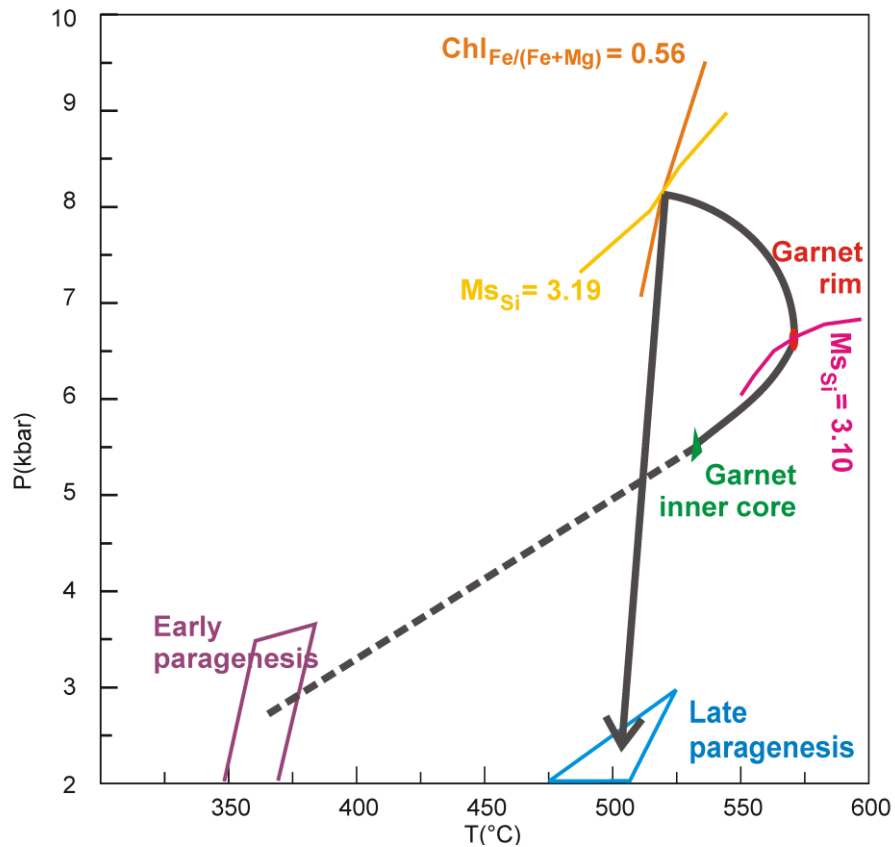
Figure 3.11 Obtained *P-T* path for the selected sample. The anticlockwise trajectory passes through a metamorphic peak at 575°C and 7 kbar, followed by the pressure peak at 8 kbar during the retrograde evolution.

3.6.5 Tectonic consequences

The pre-Oligocene metamorphic record in the late Variscan basement of the Northern Apennines is evident for the Larderello and Pontremoli subsurface basement (Bertini *et al.*, 1994; Pandeli *et al.*, 2005) and for the Cerreto micaschist outcrops (Molli *et al.*, 2002). In the Larderello and Cerreto basements, only retrograde segments of Variscan *P-T* paths (Bertini *et al.*, 1994; Molli *et al.*, 2002) are available with no information on the prograde metamorphic stages. The reconstruction of a complete *P-T* loop for the Pontremoli hidden basement provides important insights into the late- to post-Variscan geodynamic evolution in this sector of the Mediterranean area. In the Pontremoli micaschist, the monazite chemical age of 294 ± 5 Ma obtained here from monazite relics represents a lower age limit for the metamorphic evolution that took place from Early Permian times onwards. The Early Permian monazite age can refer to a medium-high grade metamorphic stage unrelated to the Pontremoli metamorphic history. This age is nearly coeval with the 275-285 Ma Rb/Sr bulk rock age obtained for the Variscan basement outcropping in the Pisani Mountains (Borsi *et al.*, 1967; Ferrara & Tonarini,

1985) and with the 285 ± 11 Ma Rb/Sr age for a muscovite associated with andalusite in a Larderello micaschist (Del Moro *et al.*, 1982), interpreted as a late Variscan thermal stage. The emplacement of plutons, which accompanied the collapse of the Variscan orogen, occurred in late Carboniferous-early Permian times (Mohn *et al.*, 2010 and references therein). The Early Permian magmatism is characterised by intrusions at different crustal levels, from the crust-mantle boundary (e.g. the Braccia Gabbro; Hermann *et al.*, 2001) to low- and mid-crustal (the Ivrea Mafic complex at 288 Ma: Demarchi *et al.*, 1998; Peressini *et al.*, 2007; the Sondalo gabbroic complex at 290 Ma: Tribuzio *et al.*, 1999; Braga *et al.*, 2001; the Collon Gabbro at 284 Ma: Monjoie *et al.*, 2005) and shallow depths (Bocca di Tenda Gabbro at 280-283 Ma, Corsica: Tribuzio *et al.*, 2009; Renna *et al.*, 2013).
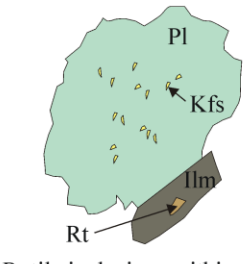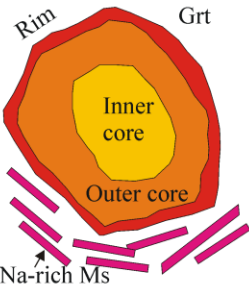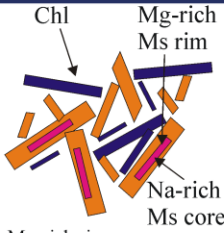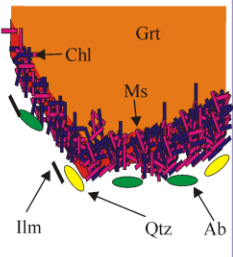
Late-Variscan magmatic activity has been recognized also in the Penninic domain and Internal Massif of the Western Alps (Tilton et *al.*, 1997; Bertrand *et al.*, 2000; Liati *et al.*, 2001; Bertrand *et al.*, 2005; Ring *et al.*, 2005), in the Malenco Unit of the Central Alps (Hermann & Rubatto, 2003), in Sardinia (307-299 Ma; Del Moro *et al.*, 1975; Bralia *et al.*, 1981; Poli *et al.*, 1989), in the Serre Massif in Calabria (Schenk, 1980; Graessner *et al.*, 2000), and in the Betic Cordillera (Zeck & Whitehouse, 1999; Esteban *et al.*, 2011). In the Tuscan Metamophic Units Late-Variscan magmatic bodies have not been found. However, the Liguride Units contain gabbro-derived granulites with a 290 Ma age related to the emplacement of the protoliths: Meli *et al.*, 1996; Montanini & Tribuzio, 2001). The here obtained younger chemical ages in the Pontremoli micaschist (19-250 Ma) may represent mixed ages between late Variscan and Alpine events. As a consequence, more age constraints (e.g. ^{40}Ar-^{39}Ar dating of potassic white mica) are needed to better reconstruct the timing of tectonic events occurred from late-Variscan times onward. Nevertheless, we are able to infer two different sequences of events:

A first scenario considers the reconstructed *P-T* path for the Pontremoli micaschist (counterclockwise segment followed by a nearly isothermal decompression) and its relation to the activity of a regional scale shear zone accommodating transpressive (conterclockwise - T_{max} before P_{max}) to transtensive (near isothermal decompression) deformation (McCann *et al.*, 2006). Transpressive tectonics has been documented in Mid-Permian times (Cadel, 1986; Cadel *et al.*, 1996; Deroin & Bonin, 2003), while several Variscan basement complexes record extensional deformation from very late Carboniferous to Mid Triassic times (e.g. 280-210 Ma in the Ivrea lower crust; Brodie *et al.*, 1989). This frame is in line with regional scale considerations, suggesting the

importance of intracontinental strike-slip tectonics (Arthaud & Matte, 1977; Doglioni 1984; Massari, 1986; Ziegler, 1986; Handy & Zingg, 1991; Schmid, 1993; Matte, 2001), and with the depositional history of Upper Carboniferous-Mid Triassic sediments of the Tuscan Domain (Rau, 1990; Molli, 2002).

The second scenario considers the role of the post-Oligocene evolution of the Northern Apennine chain during the collision of the Sardinia-Corsica block and the Adria margin. Most of the youngest monazite ages obtained here are within the 27-11 Ma age range defined by Ar-Ar dating of white micas from the Alpi Apuane phyllites (Kligfield *et al.*, 1986). These ages were related to underplating of the Adria microplate below the Corsica-Sardinia block and subsequent early exhumation of the Adria continental margin (Fellin *et al.*, 2007; Molli, 2008). In this frame the tectonic loading during the thickening stages may explain the anticlockwise segment of the *P-T* path for the Pontremoli micaschist. This loading was followed by rapid exhumation due to crustal extension connected to the opening of the Tyrrhenian Sea. The uncertainties connected with the analysis of young monazite ages with the EMP and the significant difference between the *P-T* paths of the Pontremoli micaschist and adjacent basement complexes make it difficult to relate the entire metamorphic evolution of the Pontremoli micaschist to late Alpine events.

As a whole, although we cannot definitively rule out the involvement of the Pontremoli micaschist in the Oligocene-Miocene Apennines-related deformation and metamorphism, our favourite scenario relates the Pontremoli basement evolution to a regional scale strike-slip shear zone as part of the South Europe post-Variscan shear belts accommodating lateral displacement between Africa and Europe (Arthaud & Matte, 1977; Doglioni 1984; Massari, 1986; Ziegler, 1986; Handy & Zingg, 1991; Schmid, 1993; Matte, 2001). In this view, the correlation of Pontremoli basement rocks with those of the Micaschist Complex at Larderello (Pandeli *et al.*, 2005) should be reconsidered.

	PRE-PEAK STAGE	PEAK TEMPERATURE STAGE		PEAK PRESSURE STAGE	RETROGRADE STAGE
MICROSTRUCTURES	Rutile inclusions within ilmenite; K-feldspar inclusions within plagioclase	Garnet porphyroblasts and Na-rich cores in potassic white mica		Mg-rich rims around Na-rich-cores in potassic white mica and chlorite with decussate structure. Mg-rich potassic white mica occurs also in the recrystallized areas	Late observed paragenesis
CONSTRAINING PHASES	Garnet-free and rutile- and K-feldspar bearing paragenesis	Garnet composition — INNER CORE: Alm_{72} Sps_{12} Grs_{11} Prp_4	RIM: Alm_{83-85} Grs_{3-8} Prp_{7-11} — Si max in potassic white mica cores=6.20	Si max=6.28 in potassic white mica rims and XFe=0.56 in chlorite	Late paragenesis and low Si content in potassic white mica
COMPUTED ASSEMBLAGE	Ms Chl Pg Ilm Rt Ttn Kfs Qtz	Ms Chl Pg Pl Ilm Grt Qtz	Ms Chl Pg Ilm Grt Bt Qtz	Ms Chl Pg Ilm Qtz	Ms Chl Ab Ilm Qtz
OBSERVED ASSEMBLAGE	Ms Chl Ilm Rt Kfs Qtz	Ms Chl Pl Ilm Grt Qtz	Ms Chl Ilm Grt Qtz	Ms Chl Ilm Qtz	Ms Chl Ab Ilm Qtz
T / P	350 °C < 3.5 kbar	530 °C 5.5 kbar	575 °C 7 kbar	520 °C 8 kbar	500 °C 2-3 kbar

Figure 3.12 Scheme with the main petrographic and chemical constrains and the computed *P-T* conditions.

3.7 CONCLUSIONS

1. Discontinuous variations of Ca and Y in chemical profiles of garnet can be attributed to its growth during apatite crystallization and xenotime breakdown. Thus, garnet compositions is able to record modifications in accessory minerals of mineral assemblages.

2. Coronitic microstructures of accessory minerals and changes of the inclusion mineralogy of garnet provide microstructural evidences of the reaction history. Through garnet isopleths thermobarometry the *P-T* conditions of the reactions among REE-minerals were inferred: the sequence monazite → apatite + Th-silicate → allanite →epidote occurred during prograde metamorphism at 500-600°C and 5-7 kbar.

3. The chemistry and microstructure of the monazite grains suggest that the monazite was inherited and became unstable along the *P-T* path towards peak metamorphic conditions, undergoing partial to total dissolution. Thus the EMP age of 294 ± 5 Ma should be older than the garnet forming metamorphic stage, arguing for a post-Lower Permian metamorphic evolution.

4. The Pontremoli metasediments experienced an anticlockwise *P-T* path: the prograde evolution started at 350°C and P < 5 kbar (rutile and K-feldspar bearing paragenesis and reached the metamorphic peak at 575°C and 7 kbar (garnet rim and potassic white mica cores); the retrograde evolution passed through a higher pressure stage (520°C and 8 kbar), that stabilized the Mg-rich potassic white mica and chlorite with decussate structure, and a late stage at T=500°C and P=2 kbar. The high temperature at medium pressures (~3-7 kbar) of the prograde path was followed by a pressure increase after garnet growth and by a fast tectonic exhumation responsible for the nearly isothermal decompression from 8 to 2 kbar. As a whole this metamorphic history may be related to Permian–Mid Triassic strike-slip zones. In this framework, an early transpression stage was followed by a later transtension predating the Late Triassic to Jurassic extension related to the opening of the Western Tethys (Piccardo *et al.*,1993; Marroni *et al.*, 1998).

3.8 REFERENCES

Anelli, L., Gorza, M., Pieri, M. & Riva, M., 1994. Surface well data in the Northern Apennines (Italy). *Memorie della Società Geologica Italiana,* **48**, 461-471.

Anthony, J.W., Bideaux, R.A., Bladh, K.W. & Nichols, M.C., 2011. Handbook of Mineralogy, Mineralogical Society of America, Chantilly, VA 20151 – 1110, USA. http://www.handbookofmineralogy.org/

Arthaud, F. & Matte, Ph., 1977. Late-Paleozoic strike-slip faulting in southern Europe and northern Africa: result of a right lateral shear zone between the Appalachians and the Urals. *Geological Society of America Bulletin,* **88**, 1305–1320.

Bernhardt, H.-J. 2010. MINCALC-V5, a software tool for mineral analyses data processing.
http://serc.carleton.edu/files/NAGTWorkshops/petrology/min_calc_from_heinz-juergen.pdf

Bertini, G., Elter, F.M. & Talarico, F., 1994. Evidenze di una fase estensionale pre-triassica nel complesso degli gneiss nell'area geotermica di Larderello (Toscana meridionale). *Studi Geologici Camerti, Volume speciale,* **1**, 129-137.

Bertrand, J.-M., Pidgeon, R.T., Leterrier, J., Guillot, F., Gasquet, D. & Gattiglio, M., 2000. SHRIMP and IDTIMS U-Pb zircon ages of the pre-Alpine basement in the Internal Western Alps (Savov and Piemont). *Schweizerische mineralogische und petrographische Mitteilungen,* **80**, 225-248.

Bertrand, J.-M., Paquette, J.L. & Guillot, F., 2005. Permian zircon U-Pb ages in the Gran Paradiso massif: revisiting post-Variscan events in the Western Alps. *Schweizerische mineralogische und petrographische Mitteilungen,* **85**, 15-29.

Borsi, S., Ferrara, G., Rau, A. & Tongiorgi, M., 1967. Determinazioni col metodo Rb/Sr delle filladi e quarziti listate di Buti (Monti Pisani). *Atti della Società toscana di scienze naturali, Memorie, Serie A,* **73**, 632-646.

Braga, R., Giacomini, F., Messiga, B., & Tribuzio, R., 2001. The Sondalo Gabbroic complex (Central Alps, Northern Italy): evidence for emplacement of mantle-derived melts into amphibolite-facies metapelites. *Physics and Chemistry of the Earth, Part A: Solid Earth and Geodes,y* **26**, 333-342.

Bralia, A., Ghezzo, C., Gausparri, G. & Sabatini, G., 1981. Aspetti genetici del batolite sardo-corso. *Rendiconti della Società Italiana di Mineralogia e Petrologia,* **38**, 701-764.

Brandelik, A., 2009. CALCMIN – an EXCEL^{TM} Visual Basic application for calculating mineral structural formulae from electron microprobe analyses. *Computers & Geosciences,* **35**, 1540–1551.

Brodie, K. H., Rutter, E. H. & Rex, D., 1989. On the age of deep crustal extensional faulting in the Ivrea zone, northern Italy. *Geological Society, London, Special Publications,* **45**, 203-210.

Cadel, G., 1986. Geology and Uranium mineralization of the Collio Basin (Central Southern Alps, Italy). *Uranium,* **2**, 215-540.

Cadel, G., Cosi, M., Pennacchioni, G. & Spalla, M.I., 1996. A new map of the Permo-Carboniferous cover and Variscan metamorphic basement in the central Orobic Alps, Southern Alps-Italy: structural and stratigraphical data. *Memorie di Scienze Geologiche Padova,* **48**,1-53.

Connolly, J.A.D., 1990. Multivariable phase diagrams: an algorithm based on generalized thermodynamics. *American Journal of Science,* **290**,666–718.

Connolly, J.A.D. & Petrini, K., 2002. An automated strategy for calculation of phase diagram sections and retrieval of rock properties as a function of physical conditions. *Journal of Metamorphic Geology,* **20**, 697–708.

Del Moro, A., Di Simplicio, P., Ghezzo, C., Guasparri, G., Rita, F. & Sabatini, G., 1975. Radiometric data and intrusive sequenze in the Sardinia batholith. *Neues Jahrbuch für Mineralogie Abhandlungen,* **126**, 28-44.

Del Moro, A., Puxeddu, M., Radicati di Brozolo, F. & Villa, I.M., 1982. Rb-Sr and K-Ar Ages on Minerals at Temperatures of 3000-400° C from Deep Wells in the Larderello Geothermal Field (Italy). *Contributions to Mineralogy and Petrology,* **81**, 340-349.

Demarchi, G., Quick, J., Sinigoi, S. & Mayer, A., 1998. Pressure gradient and original orientation of a lower- crustal intrusion in the Ivrea-Verbano Zone, northern Italy. *Journal of Geology,* **106**, 609-621.

Deroin, J.P. & Bonin, B., 2003.Late Variscan tectonomagmatic activity in Werstern Europe and surrounding areas: the Mid-Permian Episode. In Decandia, F.A., Cassinis, G., Spina A. (Guest eds.), Spec. Proc. on «Late Palaeozoic to Early Mesozoic events of Mediterranean Europe, and additional regional reports», April 30th-May 7th 2001, Siena (Italy). *Bollettino Società Geologica Italiana volume spec*iale, **2**, 169-184.

Doglioni, C., 1984. Tettonica triassica transpressiva nelle Dolomiti. *Giornale di Giologia,* **46**, 47–60.

Elter, F.M. & Pandeli, E., 1990. Alpine and Hercynian orogenic phases in the basement rocks of the Northern Apennines (Larderello geothermal field. Southern Tuscany, Italy). *Eclogae Geologicae Helvetiae,* **83**, 241-264.

Esteban, J.J., Tubía, J.M., Cuevas, J., Vegas, N., Sergeev, S. & Larionov, A., 2011. Peri-Gondwanan provenance of pre-Triassic metamorphic sequences in the western Alpujarride nappes (Betic Cordillera, southern Spain. *Gondwana Research,* **20**, 443-449.

Fellin, M.G., Reiners, P.W., Brandon, M.T., Wuthrich, E., Balestrieri, M.L. & Molli, G., 2007. Thermochronologic evidence for exhumational history of the Alpi Apuane metamorphic core complex, northern Apennines, Italy. *Tectonics,* **26**, TC6015.

Ferrara, G. & Tonarini, S., 1985. Radiometric geochronology in Tuscany: results and problems. *Rendiconti della Società Italiana di Mineralogia e Petrologia,* **40**, 111-124

Finger, F., Broska, I., Roberts., M.P. & Schermaier, A., 1998. Replacement of primary monazite by apatite-allanite-epidote coronas in an amphibolite facies granite gneiss from the eastern Alps. *American Mineralogist,* **83**, 248-258.

Foster, G. & Parrish, R.R., 2003. Metamorphic monazite and the generation of P-T-t paths. In Vance, D., Muller, W., and Villa, I.M., (eds) Geochronology: Linking the Isotopic Record with Petrology and Textures. *Geological Society, Special Publications,* **22**, 25-47.

Franceschini, F., 1998. Evidence of an extensive Pliocene-Quaternary contact metamorphism in Southern Tuscany. *Memorie della Società Geologica Italiana,* **52**, 479-492.

Fuhrman, M.L. & Lindsley, D.H., 1988. Ternary-Feldspar Modeling and Thermometry. *American Mineralogist,* **73**, 201-215.

Gieré, R., Rumble, D.R., Gunther, D., Connolly, J.A.D. & Caddick, M.J., 2011. Correlation of growth and breakdown of major and accessory minerals in metapelites from Campolungo, Central Alps. *Journal of Petrology,* **52**, 2293-2334.

Graessner, T., Schenk, V., Bröcker, M. & Mezger, K., 2000. Geochronological constraints on timing of granitoid magmatism, metamorphism and post-

metamorphic cooling in the Hercynian crustal cross-section of Calabria. *Journal of Metamorphic Geology,* **18**, 409-421.

Handy, M.R. & Zingg, A., 1991. The tectonic and rheological evolution of an attenuated cross section of the continental crust: Ivrea crustal section, southern Alps, north-western Italy and southern Switzerland. *Geological Society of America Bulletin,* **103**, 236–253.

Hermann, J., Müntener, O. & Günther, D., 2001. Differentiation of mafic magma in a continental crust-to-mantle transition zone. *Journal of Petrology,* **42**,189-206.

Hermann, J. & Rubatto, D., 2003. Relating zircon and monazite domains to garnet growth zones: age and duration of granulite facies metamorphism in the Val Malenco lower crust. *Journal of Metamorphic Geology,* **21**, 833-852.

Holland, T.J.B. & Powell, R., 1991. A compensated-Redlich-Kwong (CORK) equation for volumes and fugacities of CO_2 and H_2O in the range 1 bar to 50 kbar and 100–1600 °C. *Contributions to Mineralogy and Petrology,* **109**, 265–273.

Holland, T.J.B. & Powell, R., 1998. An internally consistent thermodynamic data set for phases of petrological interest. *Journal of Metamorphic Geology,* **16**, 309–343.

Holland, T., Baker, J. & Powell, R., 1998. Mixing properties and activity-composition relationships of chlorites in the system $MgO\text{-}FeO\text{-}Al_2O_3\text{-}SiO_2\text{-}H_2O$. *European Journal of Mineralogy,* **10**, 395-406.

Janots, E., Negro, F., Brunet, F., Goffé, B., Engi, M. & Bouybaouene, M.L., 2006. Evolution of the REE mineralogy in HP–LT metapelites of the Sebtide complex, Rif, Morocco: monazite stability and geochronology. *Lithos,* **87**, 214–234.

Janots, E., Brunet, F., Goffé, B., Poinssot, C., Burchard, M. & Cemic, L., 2007. Thermochemistry of monazite-(La) and dissakisite-(La): implications for monazite and allanite stability in metapelites. *Contributions to Mineralogy and Petrology,* **154**, 1–14.

Janots, E., Engi, M., Berger, A., Allaz, J., Schwarz, J.-O. & Spandler, C., 2008. Prograde metamorphic sequence of REE minerals in pelitic rocks of the Central Alps: implications for allanite–monazite–xenotime phase relations from 250 to 610 °C. *Journal of Metamorphic Geology,* **26**, 509–526.

Kligfield, R., Hunziker, J, Dallmeyer, R.D. & Schamel, S. 1986. Dating of deformational phases using K-Ar and $^{40}Ar/^{39}Ar$ techniques: results from the Northern Apennines. *Journal of Structural Geology,* **8**, 781-798.

Langone, A., Braga, R., Massonne, H.-J. & Tiepolo, M., 2011. Preservation of old (prograde metamorphic) U-Th-Pb ages in unshielded monazite from the high-pressure paragneisses of the Variscan Ulten Zone (Italy). *Lithos,* **127**, 68-85.

Liati, A., Gebauer, D., Froitzheim, N. & Fanning, C.M., 2001. U-Pb SHRIMP geochronology of an amphibolitized eclogite and an orthogneiss from the Furgg zone (Western Alps) and implications for its geodynamic evolution. *Schweizerische mineralogische und petrographische Mitteilungen,* **81**, 379-393.

Lo Pò, D. & Braga, R., 2014. Influence of ferric iron on phase equilibria in greenschist facies assemblages: the hematite-rich metasedimentary rocks from the Monti Pisani (Northern Apennines). *Journal of Metamorphic Geology,* **32**, 371-387.

Marroni, M., Molli, G., Montanini, A. & Tribuzio, R., 1998, The association of continental crust rocks with ophiolites (Northern Apennines, Italy): Implications for the continent-ocean transition. *Tectonophysics,* **29**, 43-66.

Massari, F., 1986. Some thoughts on the Permo-Triassic evolution of the South Alpine area (Italy). *Memorie della Società Geologica Italiana,* **34**, 179–188

Massonne, H.-J., 2010. Phase relations and dehydration behaviour of calcareous sediments at very-low to low grade metamorphic conditions. *Periodico di Mineralogia,* **79**, 2, 21-43.

Massonne, H.-J., 2012. Formation of amphibole and clinozoisite-epidote during exhumation of eclogite in a subduction channel. *Journal of Petrology,* **53**, 1969-1998.

Massonne, H.-J., 2013. Constructing the pressure–temperature path of ultrahigh-pressure rocks. *Elements,* **9**, 267-272.

Massonne, H.-J., 2014. Wealth of P-T-t information in medium-high grade metapelites: example from the Jubrique Unit of the Betic Cordillera, S Spain. *Lithos,* **208-209**,137-152.

Matte, P., 2001. The Variscan collage and orogeny (480-290 Ma) and the tectonic definition of the Armorica microplate: a review. *Terra Nova,* **13**, 112-128.

McCann, T., Pascal, C., Timmerman, M.J**.**, Krzywiec, P., López-Gómez, J., Wetzel, A., Krawczyk, C.M., Rieke, H. & Lamarche, J., 2006. Post-Variscan (end Carboniferous – Early Permian) basin evolution in Western and Central Europe. In Gee, D.G. & Stephenson, R.A. (eds.), European Lithosphere Dynamics. *Geological Society of London, Memoirs,* **32**, 355-388.

Meli, S., Montanini, A., Thoni, M. & Frank, W., 1996. Age of mafic granulite blocks from the External Liguride Units (northern Apennine, Italy). *Memorie di Scienze Geologiche Padova,* **48**, 65-72.

Mohn, G., Manatschal, G., Müntener, O., Beltrando, M. & Masini, E., 2010. Unravelling the interaction between tectonic and sedimentary processes during lithospheric thinning in the AlpineTethys margins. *International Journal of Earth Sciences,* **99**, 75–101.

Molli, G., 2002. Field Trip Eastern Liguria/Alpi Apuane. Gordon Research Conference on Rock Deformation. Il Ciocco, Barga, Italy, CNR Report, 58 pp.

Molli, G., 2008. Northern Apennine-Corsica orogenic system: an updated overview. In Siegesmund S, Fugenschuh B, Froitzheim N (eds) Tectonic Aspects of the Alpine-Dinaride-Carpathian System. *Geological Society, Special Publications,* **298**, 413-442.

Molli, G., Montanini, A. & Frank W., 2002. MORB-derived Varisican amphibolites in the Northern Apennine Basement: the Cerreto metamorphic slices (Tuscan-Emilian Apennine, NW Italy). *Ofioliti,* **27**, 17-30.

Monjoie, P., Bussy, F., Lapierre, H. & Pfeifer, H.R., 2005. Modeling of in situ crystallization processes in the Permian mafic layered intrusion of Mont Collon (Dent Blanche nappe, western Alps). *Lithos,* **83**, 317–346.

Montanini, A. & Tribuzio, R., 2001. Gabbro-derived and felsic granulites from the Northern Apennines (Italy): evidence for emplacement of tholeiitic basalts in the post-Variscan lower crust. *Journal of Petrology,* **42**, 2259- 2277.

Montel, J.-M., Foret, S., Veschambre, M., Nicollet, C. & Provost, A., 1996. Electron microprobe dating of monazite. *Chemical Geology,* **131**, 37-53.

Musumeci, G., Mazzarini, F., Tiepolo, M. & Di Vincenzo, G., 2011. U-Pb and [40]Ar-[39]Ar geochronology of Palaeozoic units in the northern Apennines: determining protolith age and alpine evolution using the Calamita Schist and Ortano Porphyroid. *Geological Journal,* **46**, 288-310.

Pandeli, E., Gianelli, G. & Morelli, M., 2005. The cristalline units of the middle-upper crust of the Larderello geothermal region (southern Tuscany, Italy): new data for their classification and tectono-metamorphic evolution. *Bollettino Della Società Geologica Italiana,* **3**, 139-155.

Peressini, G., Quick, J. E., Sinigoi, S., Hofmann, A. W. & Fanning, M., 2007. Duration of a large mafic intrusion and heat transfer in the lower crust: a SHRIMP U–Pb

zircon study in the Ivrea–Verbano Zone (Western Alps, Italy). *Journal of Petrology,* **48**, 1185-1218.

Piccardo, G.B., Rampone, E., Vannucci, R., Shimizu, N., Ottolini, L. & Bottazzi, P., 1993. Mantle processes in the sub-continental lithosphere: the case study of the rifted sp-lherzolites from Zabargad (Red Sea). *European Journal of Mineralogy,* **5**, 1039-1056.

Poli, G., Ghezzo, C. & Conticelli, S., 1989. Geochemistry of granitic rocks from the Hercynian Sardinia-Corsica batholith: implication for magma genesis. *Lithos,* **23**, 247-266.

Powell R. & Holland, T.J.B., 1999. Relating formulations of the thermodynamics of mineral solid solutions: Activity modeling of pyroxenes, amphiboles, and micas. *American Mineralogist,* **84**, 1-14.

Pyle, J.M. & Spear, F.S., 2000. An empirical garnet (YAG) ± xenotime thermometer. *Contributions to Mineralogy and Petrology,* **138**, 51–58.

Rasmussen, B. & Muhling, J.R., 2007. Monazite begets monazite: evidence for the dissolution of detrital monazite and reprecipitation of syntectonic monazite during low-grade regional metamorphism. *Contributions to Mineralogy and Petrology,* **154**, 675–689.

Rasmussen, B. & Muhling, J.R., 2009. Reactions destroying detrital monazite in greenschist-facies sandstones from the Witwatersrand basin, South Africa . *Chemical Geology,* **264**, 311-327.

Rau, A., 1990. Evolution of the Tuscan domain between the Upper Carboniferous and the Middle Triassic: a new hypothesis. *Bollettino Società Geologica Italiana,* **109**, 231-238.

Renna, M.R., Tribuzio, R. & Braga, R., 2013. Petrogenetic relationships between peralkaline rhyolite dykes and mafic rocks in the post-Variscan gabbroic complex from Bocca di Tenda (northern Corsica, France). *Contributions to Mineralogy and Petrology,* **165**, 1073 – 1085.

Ring, U., Collins, A.S. & Kassem, O.K., 2005. U-Pb SHRIMP data on the crystallization age of the Gran Paradiso augengneiss, Italian Western Alps: Further evidence for Permian magmatic activity in the Alps during break-up of Pangea. *Eclogae Geologicae Helvetiae,* **98**, 363-370.

Schandl, E.S. & Gorton, M.P., 2004. A textural and geochemical guide to the identification of hydrothermal monazite: Criteria for selection of samples for

dating epigenetic hydrothermal ore deposits: Economic *Geology and Bulletin of the Society of Economic Geologists,* **99**, 1027–1035.

Shaw, D.M., 1956. Geochemistry of pelitic rocks. Part III. Major elements andgeneral geochemistry. *Geological Society of America Bulletin ,* **67**, 919–934.

Schenk, V., 1980. U-Pb and Rb-Sr radiometric dates and their correlation with metamorphic events in the granulite-facies basement. of the Serre, southern Calabria (Italy). *Contributions to Mineralogy and Petrology,* **73**, 23-38.

Schmid, S., 1993. Ivrea Zone and adjacent southern Alpine basement. In J.F. von Raumer, F. Neubauer (Eds.), *Pre-Mesozoic Geology in the Alps, Springer*, Berlin, 567-584.

Spear, F.S., 1993. Metamorphic phase equilibria and pressure-temperature-time paths. Mineralogical Society of America, Washington D.C., pp. 799.

Spear, F.S. & Pyle, J.M., 2010. Theoretical modeling of monazite growth in a low-Ca metapelite. *Chemical Geology,* **273**, 111-119.

Stüwe, K., 1997. Effective bulk composition change due to cooling: a model predicting complexities in retrograde reaction textures. *Contributions to Mineralogy and Petrology,* **129**, 43–52.

Tilton, G.R., Ames, L., Schertl, H.-P. & Schreyer, W., 1997. Reconnaissance isotopic investigations on rocks of an undeformed granite contact within the coesite-bearing unit of the Dora Maira Massif. *Lithos,* **41**, 25-36.

Tomkins, H.S. & Pattison, D.R.M., 2007. Accessory phase petrogenesis in relation to major phase assemblages in pelites from the Nelson contact aureole, southern British Columbia. *Journal of Metamorphic Geology,* **25**, 401-421.

Tribuzio, R., Thirlwall, M.F. & Messiga, B., 1999. Petrology, mineral and isotope geochemistry of the Sondalo gabbroic complex (Central Alps, Northern Italy): implications for the origin of post-Variscan magmatism. *Contributions to Mineralogy and Petrology,* **136**, 48–62.

Tribuzio, R., Renna, M.R., Braga, R. & Dallai, L., 2009. Petrogenesis of Early Permian olivine-bearing cumulates and associated basalt dykes from Bocca di Tenda (Northern Corsica): implications for post-collisional Variscan evolution. *Chemical Geology,* **259**, 190-203.

Vai, G.B. & Martini, I.P., 2001. Anatomy of an Orogen: the Apennines and Adjacent Mediterranean Basins, Kluwer Academic Publishers, pp. 632.

Vance, D., Müller, W. & Villa, I.M., 2003. Geochronology: linking the isotopic record with petrology and textures - an introduction. In Vance, D., Midller, W., Villa, I. M. (eds) 2003. Geochronology: Linking the Isotopic Record with Petrology and Textures. *Geological Society, London, Special Publications,* **220**, 1-24.

Waldbaum, D.R. & Thompson, J.B. Jr. 1968. Mixing properties of sanidine crystalline solutions: II. Calculations based on volume data. *American Mineralogist,* **53**, 2000-2017.

Williams, M.L., Jercinovic, M.J. & Hetherington, C.J., 2007. Microprobe monazite geochronology: understanding geologic processes by integrating composition and chronology. *Annual Review of Earth and Planetary Sciences,* **35**, 137-175.

Wing, B.A., Ferry, J.M. & Harrison, T.M., 2003. Prograde destruction and formation of monazite and allanite during contact and regional metamorphism of pelites: petrology and geochronology. *Contributions to Mineralogy and Petrology,* **145**, 228-250.

Zeck, H.P. & Whitehouse, M.J., 1999. Hercynian, Pan-African, Proterozoic and Archean ion-microprobe zircon ages for a Betic-Rif core complex, Alpine belt, W Mediterranean–consequences for its PTt path. *Contributions to Mineralogy and Petrology,* **134(2-3)**, 134-149.

Ziegler, P.A., 1986. Geodynamic model for the Paleozoic crustal consolidation of Western and Central Europe. *Tectonophysics,* **126**, 303-328.

DATING THE MYLONITIC STAGE

IN THE CERRETO VARISCAN BASEMENT:

Ar/Ar LASER ANALYSIS OF POTASSIC WHITE MICA IN

ASYMMETRIC FOLIATION BOUDINS

DATING THE MYLONITIC STAGE IN THE CERRETO VARISCAN BASEMENT: AR/AR LASER ANALYSIS OF POTASSIC WHITE MICA IN ASYMMETRIC FOLIATION BOUDINS

4.1 INTRODUCTION

Asymmetric foliation boudins (or foliation-fishes) are polycrystalline aggregates of mica with a sigmoidal shape (Platt & Vissers, 1980; Passchier & Trouw, 2005; Arslan *et al.*, 2008; Fossen, 2010). They occur in strongly foliated mylonitic rocks and are interpreted to develop during the late stages of the mylonitic event responsible for the development of the foliation (Fossen, 2010). The asymmetry creates a monoclinic microstructure, so they are potential kinematic indicators of the sense of shear (Hanmer, 1986; Passchier & Druguet, 2002; Goscombe & Passchier, 2003; Goscombe *et al.*, 2004).

Compared to other fabric elements defined by micas, e.g. porphyroclasts, mylonitic foliation, shear bands, which are useful to reconstruct the relative timing of deformative and metamorphic events, the asymmetric foliation boudins are less studied.

The importance of the correct interpretation of the microstructure is amplified when this microstructure consists of potassic white mica that can be the target of ^{40}Ar/^{39}Ar dating (Faure, 1986; McDougall & Harrison, 1999; Dickin, 1995).

Since mylonitic metapelites contain potassic white mica belonging to distinct fabric elements ^{40}Ar/^{39}Ar dating of potassic white mica is a suitable tool to constrain the age of different stages of the metamorphic evolution. In particular potassic white mica in mylonitic foliation, shear bands and asymmetric boudins is useful to attain information about the age and duration of the shearing stage (Mulch & Costa, 2004; Sanchez *et al.*, 2011).

We present a microstructural and geochronological study on asymmetric foliation boudins occurring in mylonitic micaschist of the Cerreto Pass. These rocks are part of the Variscan basement of the Northern Apennines (Italy). Up to now no data are

---

available for the shearing stage in this crustal sector. $^{40}Ar/^{39}Ar$ dating of white mica in asymmetric foliation boudins and mylonitic foliation reveals a complex pre-Oligocene shearing history associated to the rifting stage that preludes the opening of the Western Tethys.

4.2 GEOLOGICAL FRAMEWORK

The Northern Apennines (Italy) are an Alpine orogenic belt formed during the Oligocene-Miocene collision between the Corsica-Sardinia and the Adria margins (Vai & Martini, 2001).

The Northern Apennine pile consists of three tectonic units (from top to bottom):

- Liguride Units: ophiolites from the Ligurian-Piedmontese ocean;

- Tuscan Units: Mesozoic-Tertiary sedimentary sequences belonging to the continental Adria crust;

- Tuscan Metamorphic Units: Apennine-age metamorphic rocks of the Adria microplate consisting of a Variscan basement and its upper Carboniferous-Tertiary cover.

The Variscan basement outcrops in the Cerreto Pass, Punta Bianca, Tuscan Metamorphic Ridge, Elba Island and it had been drilled also in the Larderello and Pontremoli underground (Fig. 4.1a, b). It shows a polymetamorphism from the Variscan orogenesis to the Alpine one. The Variscan history is best preserved in the Cerreto Pass (metamorphic peak at 550-660°C and 0.8-0.9 GPa; Molli *et al.*, 2002), whereas the Apenninic features can be observed in the Tuscan Metamorphic Units from Alpi Apuane to the Argentario Promontory.

The Variscan basement in the Cerreto Pass consists of medium-grade micaschist and amphibolite, associated with the Calcare cavernoso Formation, a detachment level of Triassic evaporites that allowed thrusting of the Tuscan Unit on the Tuscan Metamorphic Units during the Alpine orogenesis (Vai & Martini, 2001). Mylonitic deformation occurred under amphibolites- and greenschist-facies metamorphism and affected strongly the micaschist structure and composition. Amphibolite bodies, instead, preserve better the pre-shearing history (Molli *et al.*, 2002).

4.2.1 Previous geochronology

Only few radiometric age determinations are available for the Variscan basement of Northern Apennines.

Borsi *et al.* (1967) obtained 275 ± 12 Ma with the Rb/Sr on whole rock method for the Variscan basement outcropping in the Pisani Mountains ("Buti Quartzites and Phyllites Formation"; Schiaffino & Tongiorgi, 1962; Rau & Tongiorgi, 1966; Lo Pò & Braga, 2014). Del Moro *et al.* (1982) used the Rb-Sr and K-Ar methods on biotites, muscovites and horneblende from the Variscan basement in the Larderello subsurface. Their results give a bimodal age distribution of 285 ± 11 and 2.5-3.7 Ma: the former is related to the late Variscan thermal event, whereas the latter is related to the Pliocene magmatism.

K-Ar and ^{40}Ar-^{39}Ar analyses have been carried out on white mica separates from Paleozoic to Oligocene metasedimentary rocks present in the Alpi Apuane basement (Kligfield *et al.*,1986). In particular the ages obtained for the Paleozoic basement (80 to 24 Ma) were explained by partial resetting by Oligocene-Miocene metamorphism and/or excess argon.

Molli *et al.* (2002) performed Ar-Ar dating on two amphibolites samples from the Cerreto Pass: the Ar-Ar ages obtained on hornblende belonging to the main foliation (312 and 328 Ma) were related to the collisional stage of the Variscan orogenesis. Hence the Variscan basement in the Cerreto Pass might represent a remnant of the Southern Europe Variscan belt now included in the Apennine stacks.

Musumeci *et al.* (2011) presented geochronological data on detrital zircon and on metamorphic muscovite respectively from the Ortano Porphyroid and the Calamita Schist, two Palaeozoic metamorphic units outcropping in the eastern Elba Island. U-Pb dating in detrital zircon indicated a Middle-Ordovician magmatic origin (470 and 450 Ma) for the protolith of the porphyroids. Ar-Ar in metamorphic muscovite recorded the Late Miocene contact metamorphism (6 Ma) caused by the Porto Azzurro magmatic body (Musumeci *et al.*, 2011).

The mylonitic foliation in the micaschist and amphibolite from the Cerreto Pass, postdating the amphibolite foliation (312 ± 4 Ma $-$ 328 ± 5 Ma), has never been dated before. In this contribution we present the first determination of the shearing stage age affecting the Variscan basement of Northern Apennines.
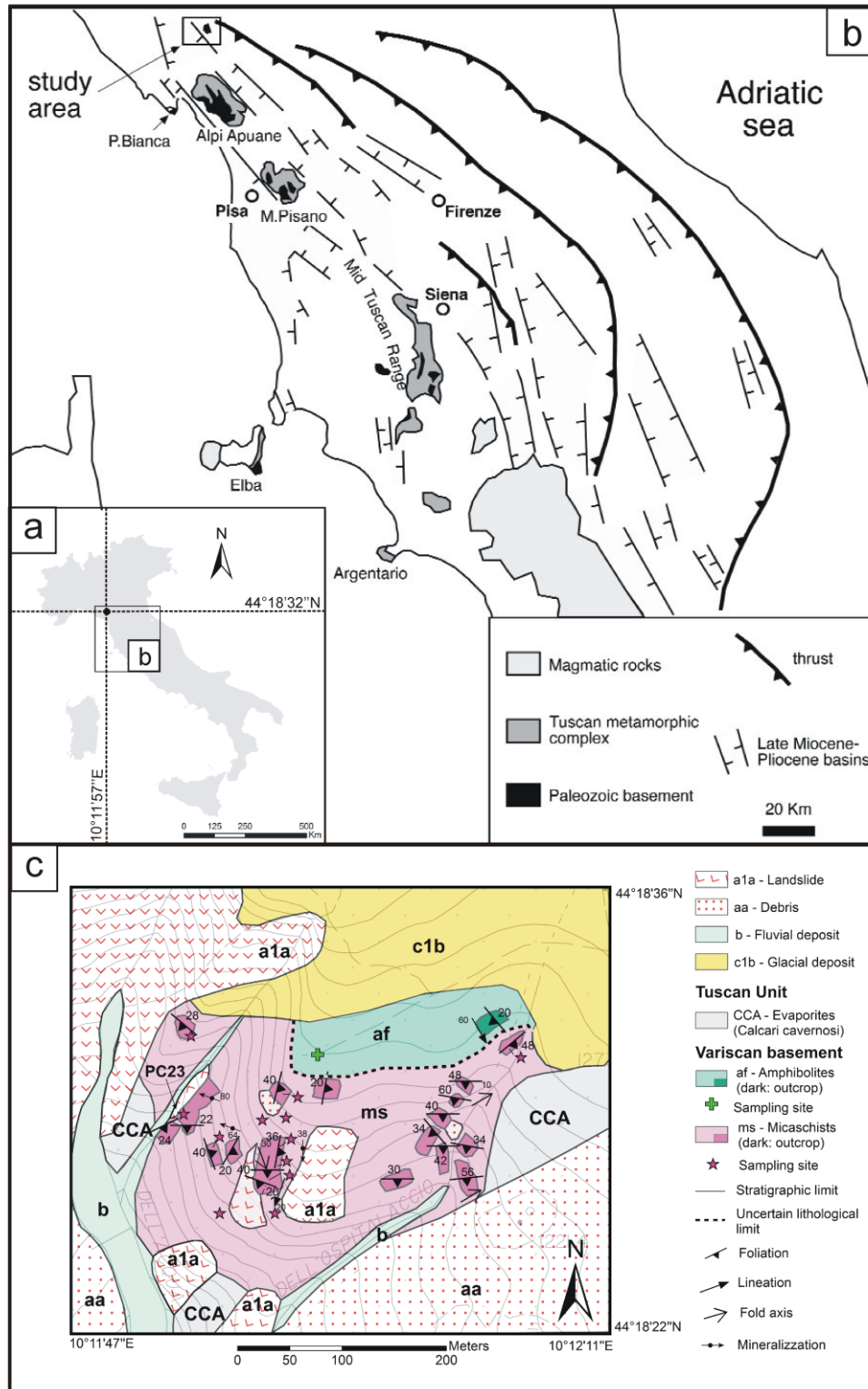
Figure 4.1 Geological framework of the study area: (a) localization of the Cerreto Pass; (b) distribution of the Variscan basement in Northern Apennines; (c) geological map with the Variscan basement outcrops in the Cerreto Pass.

4.3 FIELD DATA

The Variscan basement in the Cerreto Pass is made of mylonitic micaschist and amphibolite (Fig. 4.1c). The micaschist are dominant, whereas the amphibolite outcrop only in the uppermost sector. The contact between micaschist and amphibolite cannot be directly observed because it is covered by debris. Micaschist show in some cases a strong retrogression. Shear bands and mantled porphyroclast commoly indicate a dextral sense of shear. The mean field (mylonitic) foliation dips 180° with an increasing inclination towards east. The stretching lineation in the micaschist sequence has a dip of 200° and an inclination of 20°. Axial surface of anticlinal folds dips about 340° with an inclination of 60° in the easternmost outcrops. Mineralization of pyrite, epidote, K-feldspar, titanite lies on a plane dipping 290° with an inclination of 70°. The whole micaschist-amphibolite complex occurs as a tectonic slice enclosed in Triassic evaporites (Calcare Cavernoso Formation) with a topographic area of about 80,000 m^2.
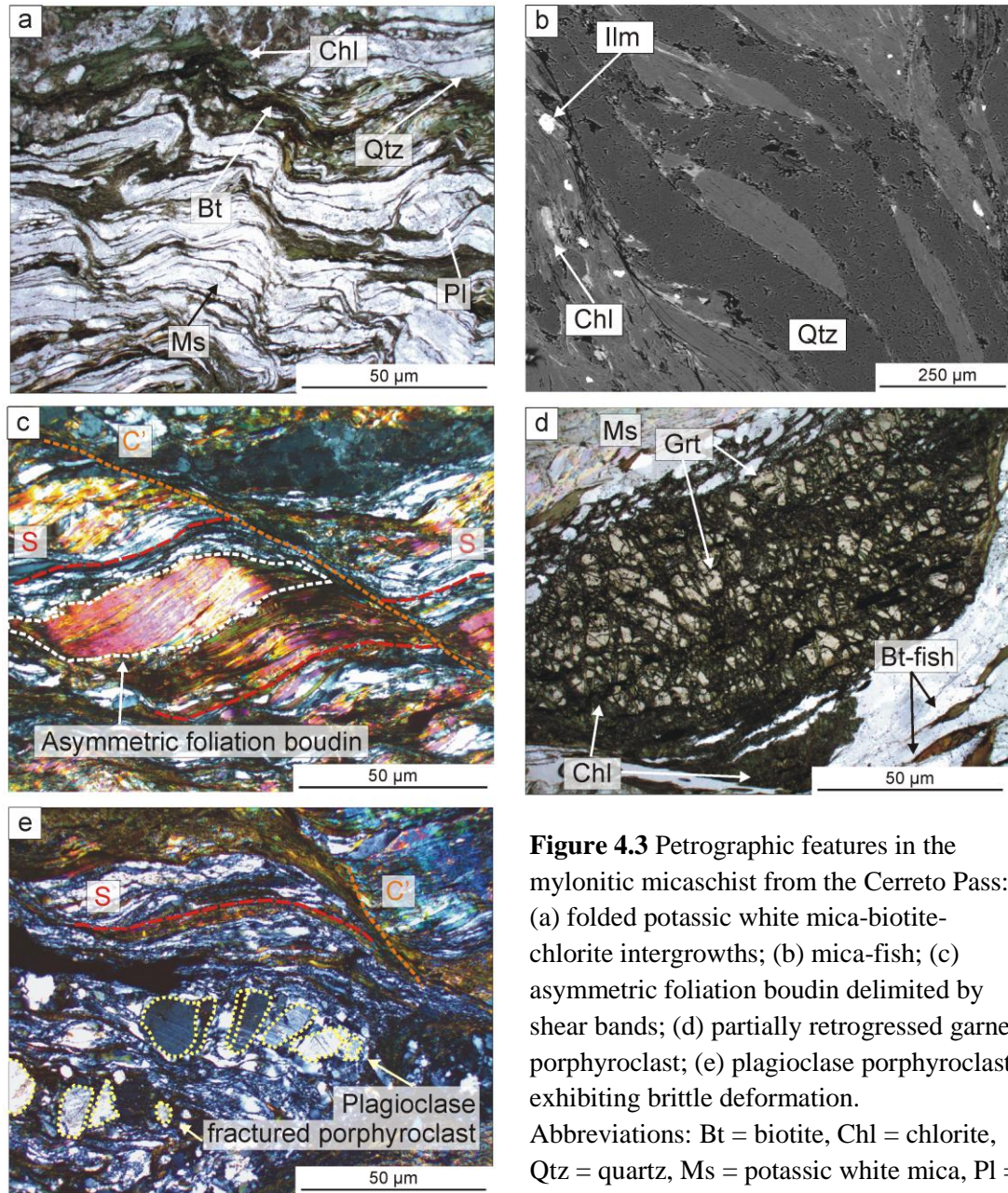
4.4 PETROGRAPHY

Petrographic and microstructural analyses were carried out with a polarising optical microscope and a scanning electron microscope Philips 515B at the Dipartimento di Scienze Biologiche, Geologiche ed Ambientali (Università di Bologna). The samples are micaschist with a well-developed mylonitic foliation wrapping around deformed porphyroclasts. Locally, ultramylonitic levels consisting of fine-grained chlorite, epidote porphyroclasts, albite, quartz, titanite have been observed. These levels overprints the mylonitic foliation and have a different orientation. The samples were cut parallel to the mylonitic lineation and perpendicular to the mylonitic foliation in order to observe in thin sections the microstructures with a monoclinic symmetry. One thin section containing well-developed asymmetric foliation boudins (PC23) was studied in detail. PC23 is a medium-grained micaschist with a mylonitic foliation wrapping around white mica and biotite-fishes, garnet, plagioclase and quartz porphyroclasts. C'-type shear bands are also observed (Fig. 4.2). The mylonitic foliation consists of fine-grained white mica, chlorite and biotite and is usually folded (Fig. 4.3a). Ilmenite, zircon, apatite, rutile, titanite, epidote, tourmaline are the accessory minerals. White mica occurs in mica-fishes (Fig. 4.3b), fine-grained grains along the mylonitic foliation, that in some places form asymmetric foliation boudins (Fig. 4.3c). White mica in the mylonitic foliation is often associated with chlorite and biotite. Flattened garnet porphyroclasts (up to 5 mm in length) are extensively fractured. The fractures are

usually filled by chlorite (Fig. 4.3d) that is particularly abundant at the garnet rims. Ilmenite, quartz and zircon inclusions delineate a discontinuous internal schistosity discordant with respect to the external schistosity (mylonitic foliation). Plagioclase and quartz form flattened porphyroclasts with inclusions of white mica, biotite, rutile and apatite. Book-shelf sliding porphyroclasts of plagioclase and dynamically recrystallized quarz subgrains are also present (Fig. 4.3e). Ilmenite is both into garnet and in the matrix with fractured and bended crystals. Ilmenite crystals with rutile cores occur in the matrix; they host quartz, zircon and apatite inclusions. Titanite was found with irregular grains along the mylonitic foliation. Epidote has an irregular internal structure and contains white mica and chlorite inclusions. It occurs also as inclusions in mica-fishes.

Since the mylonitic foliation is the main schistosity in the selected sample, crystals have been distinguished in prekinematic (mica-fishes, bended potassic white mica, plagioclase, quartz and garnet porphyroclasts) and synkinematic (fine-grained white mica and biotite, chlorite, plagioclase, quartz, ilmenite and titanite along the mylonitc fabric). Crystals along the ultramylonitic levels postdates the mylonitic foliation development.
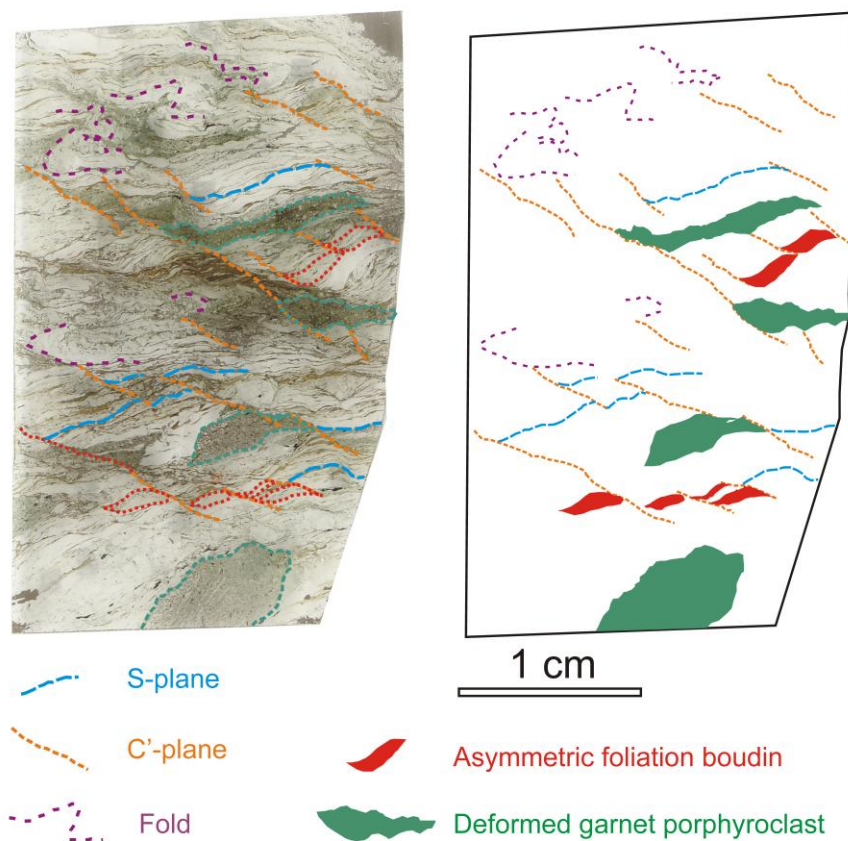
Figure 4.2 Scan and sketch of PC23 thin-section with the main mylonitic microstructures.

Figure 4.3 Petrographic features in the mylonitic micaschist from the Cerreto Pass: (a) folded potassic white mica-biotite-chlorite intergrowths; (b) mica-fish; (c) asymmetric foliation boudin delimited by shear bands; (d) partially retrogressed garnet porphyroclast; (e) plagioclase porphyroclast exhibiting brittle deformation. Abbreviations: Bt = biotite, Chl = chlorite, Qtz = quartz, Ms = potassic white mica, Pl = plagioclase, Grt= garnet.

4.4.1 Asymmetric foliation boudins

In order to investigate the microstructure of the asymmetric foliation boudins, high-magnification images of these microstructures in PC23 were acquired through a Jeol JSM-6500F thermal Field emission scanning microscopy at INGV (Rome), using an acceleration voltage of 10-15 kV and primary electric current 10-15 nA. An EDS microanalyzer allowed to collect semiquantitative analyses of the mineral composition. Following the indications of Fossen (2010) on the descriptive terminology of boudins, width refers to the maximum axis of the boudins in the extension quadrants, and thickness consists of the measure of the axis in the shortening direction. Asymmetric

foliation boudins in the selected sample are characterized by a width of 2-8 mm, a thickness of 0.5-4 mm and an aspect ratio of 2-6. Their area ranges from 1 to 17 mm^2. The majority of the asymmetric foliation boudins is 3 mm wide, 0.7 mm thick and 1 mm^2 extended. The average aspect ratio is 3.5. They have commonly lozenge shape, but also irregular shapes have been observed (Fig. 4.4a). They actually consist of aggregates of potassic white mica crystals with different orientations of the cleavage plains (Fig. 4.4b). The borders among different crystals can be recognized in high-resolution and high-magnification BSE images (Fig. 4.4c), while they cannot be easily distinguished in low-magnification BSE images and X-ray maps. Potassic white mica (bright grey in BSE images) is intimately intergrown with small crystals of sodic white mica (dark grey). The latter usually forms flakes with a width of 10-50 μm and a thickness of few μm (Fig. 4.4d). Chlorite form both intergrowths with potassic white mica,. Furthermore, the stretched rims of the boudins consist of chlorite (Fig. 4.4e). Asymmetric foliation boudins contains ilmenite and minor rutile, apatite, zircon, and epidote. Ilmenite delineates a sort of internal schistosity, with a curvature that increases progressive towards the rim of the boudin and connects continuously with the external schistosity (mylonitic foliation in our case). This is a common features of synkinematic microstructure (Zwart, 1962; Zwart & Calon, 1977, Vernon, 2004). C'-shear bands usually separate adjacent asymmetric foliation boudins.
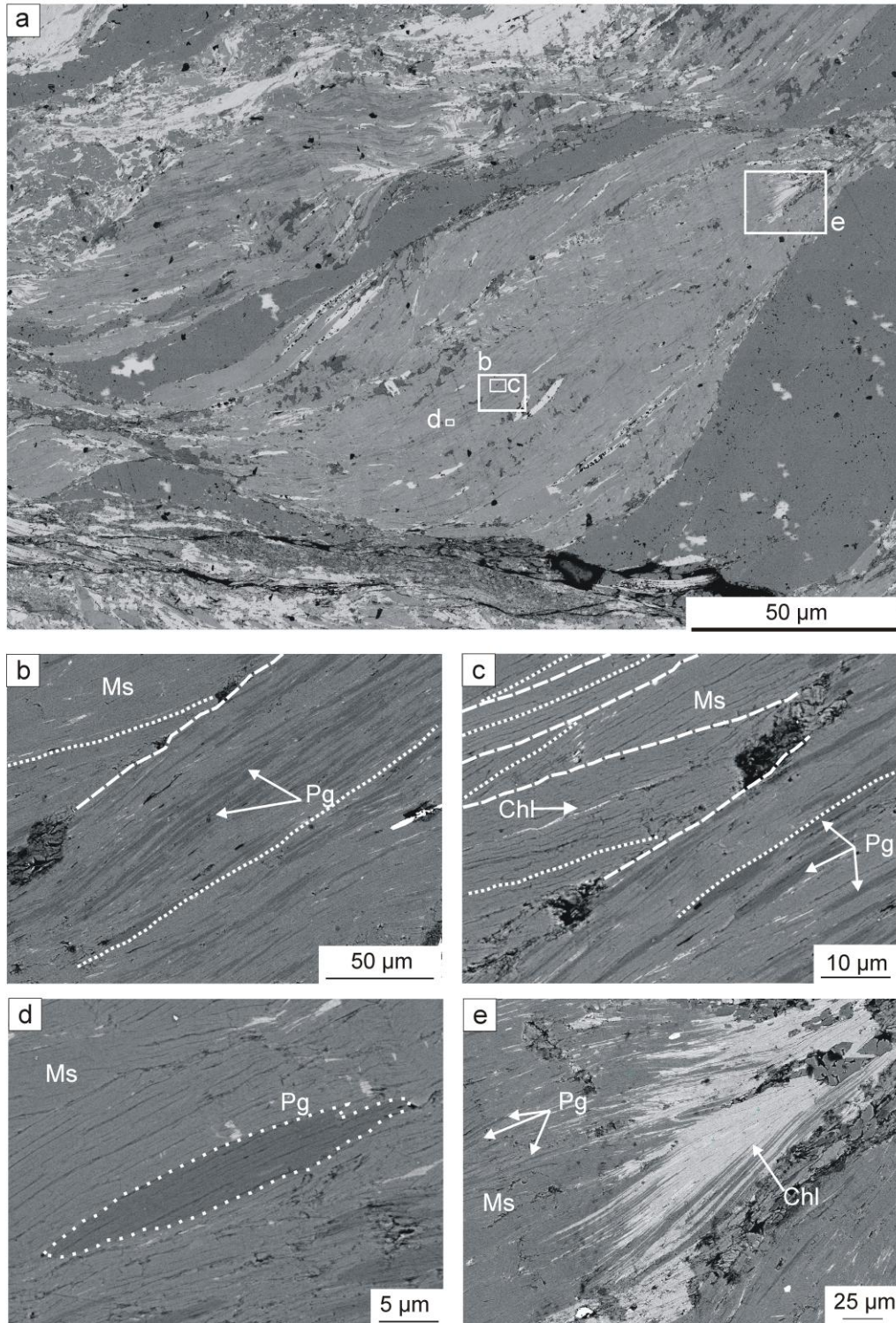
Figure 4.4 Microstructure of an asymmetric foliation boudin: (a) low-magnification complessive view; (b) potassic white mica-sodic white mica intergrowths; (c) several potassic white mica crystals with different orientation of the cleavage plains; (d) 5 µm-wide sodic white mica flake; (e) chlorite tail in the asymmetric boudin rim. The dotted lines indicate the cleavage plains, whereas the dashed lines correspond to the border between two different crystals. Abbreviations: Chl = chlorite, Ms = potassic white mica, Pg = sodic white mica.

4.5 MINERAL CHEMISTRY AND *P-T* ESTIMATES

Mineral chemistry analyses of potassic white mica, chlorite, biotite, garnet, plagioclase were collected through a CAMECA SX100 electron microprobe equipped with five wavelength dispersive spectrometers at the Institut für Mineralogie und Kristallchemie (Universität Stuttgart) with an acceleration voltage of 15 kV, a primary electric current of 10-15 nA and counting times for each element of 20 s at the peak and the background. The elements analysed in potassic white mica, chlorite, biotite, garnet, plagioclase are Na, Mg, Al, Si, K, Ca, Ti, Mn, Fe. Ba was analysed also in white mica and plagioclase. Synthetic and natural minerals and pure oxides were used as standards. The PaP correction procedure was applied. Fe, Mg, Ti, Na X-ray maps in mica-fish and potassic white mica along the mylonitic foliation were collected with a counting time of 100 ms, a step width of 2 μm, an acceleration voltage of 15 kV and a current of 30 nA and were elaborated with XMap software (Bernhardt *et al.*, 1995). Structural formulae were calculated with CalcMin program (Brandelik, 2009). Supplementary Fe, Mg, Ti, Na X-ray maps of potassic white mica in asymmetric foliation boudins were collected with a Jeol JSM-5400 at the University of Bologna using a counting time of 100 ms, a step width of 7 μm, an acceleration voltage of 20 kV and a current of 30 nA.

Potassic white mica shows some chemical variability (Tab. 4.1): mica-fishes have higher contents of Na (0.26-0.55 apfu) and lower contents of Mg (0.08-0.21 apfu) than potassic white mica along the mylonitic foliation (Na=0.04-0.46 apfu; Mg=0.16-0.44 apfu; Fig. 4.5a, b, c); asymmetric foliation boudins show variable composition with Si=6.08-6.38 apfu, Mg=0.10-0.35 apfu, Na=0.09-0.55 apfu (Fig. 4.5e). Na-rich areas can be observed (Fig. 4.5e). Inclusions of potassic white mica in biotite-fishes have Si=6.23-6.32 apfu, Mg=0.17-0.30 apfu, Na=0.32-0.44 apfu (Figs. 4.6a, b). Pre-kinematic **biotite** has Al^{IV} content ranging from 2.38 to 2.56 apfu and $XFe=Fe^{2+}/(Fe^{2+}+Mg)=0.47-0.63$. Mylonitic biotite shows roughly the same composition ($Al^{IV}=2.48-2.62$, $XFe=0.55-0.64$). **Chlorite** lying along the mylonitic foliation has Si=5.10-6.04 apfu and XFe=0.53-0.64; Si and XFe in chlorite deriving from the garnet retrocession are respectively 5.31-5.44 apfu and 0.57-0.60. The composition of **plagioclase** porphyroclasts is $Ab_{79-95}An_{5-21}Or_{0-2}$ in the core and $Ab_{79-89}An_{11-20}Or_{0-1}$ in the rim. **Garnet** shows a slight compositional zonation with an increase of almandine and pyrope and a decrease of grossular and spessartine during crystallization: the composition ranges from $Alm_{66}Grs_{24}Sps_6Prp_5$ in the inner core to $Alm_{73}Grs_{19}Sps_1Prp_7$ in the rim (Tab. 4.2; Fig. 4.6c).

Table 4.1 Microprobe analyses of potassic white mica calculated assuming 42- (Ca+ Ba) valencies and 4 H. Fe^{3+} is stoichiometric-estimated considering $Fe^{3+} = 42$ – sum of the valencies (Si, Ti, Cr, Al, Mn, Mg, Fe)-Ba-Ca.

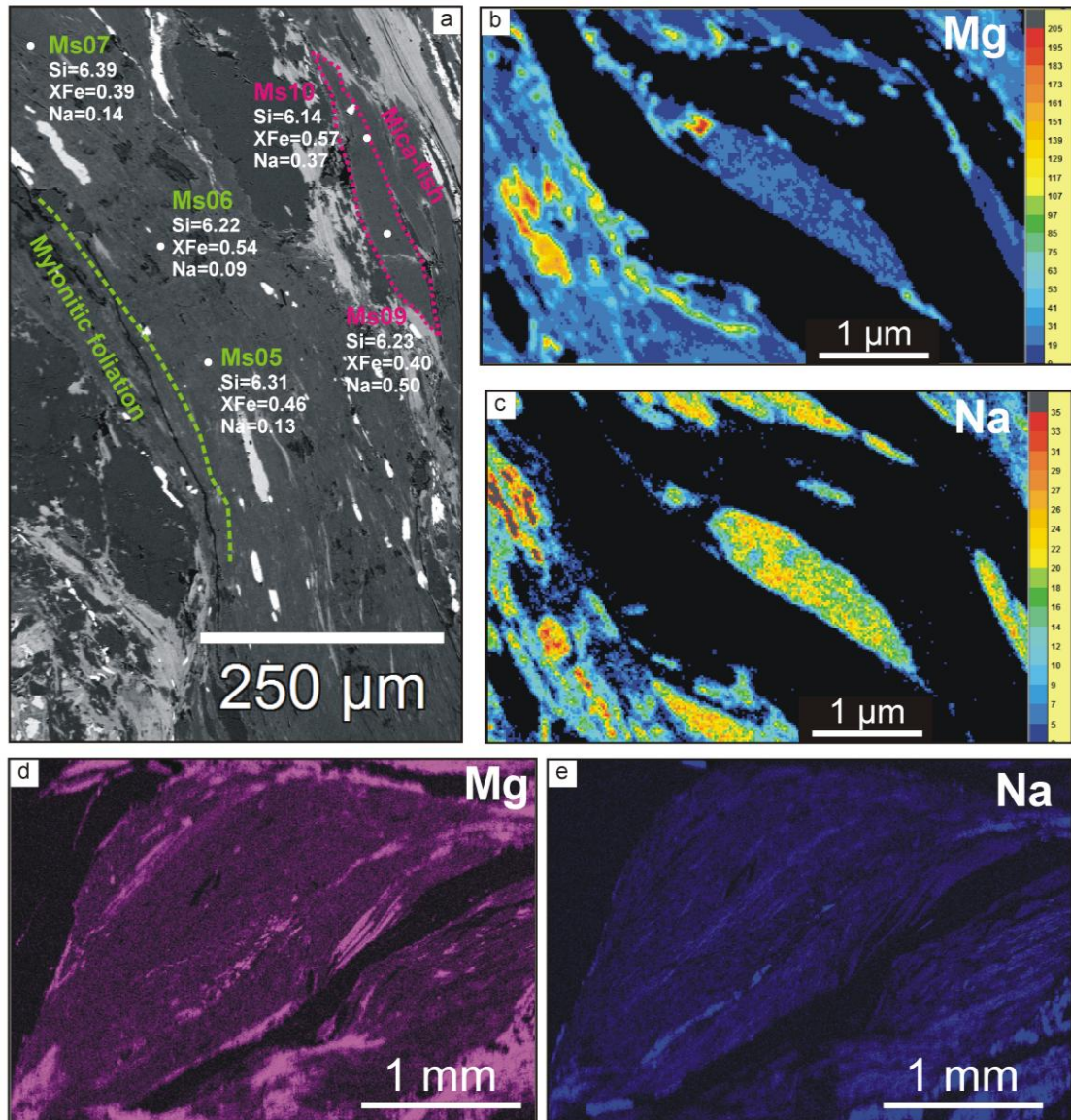| K-white mica												
	inclusions			mica-fishes			mylonitic foliation			asymmetric foliation boudins		
Point analyses	Ms03	Ms04	Ms05	Ms17	Ms18	Ms19	Ms28	Ms30	Ms32	Ms15_01	Ms15_02	Ms15_03
SiO_2	47.83	47.51	47.66	47.21	47.20	47.49	47.31	48.68	48.10	45.49	46.10	46.25
TiO_2	0.52	0.49	0.52	0.37	0.36	0.34	0.23	0.21	0.28	0.27	0.27	0.40
Al_2O_3	34.58	34.24	33.42	35.72	36.27	36.25	34.69	33.56	33.87	36.38	35.12	35.31
FeO	1.54	1.40	1.72	1.14	1.08	1.12	1.28	1.90	1.13	1.25	1.20	1.09
Fe_2O_3	n.c.	n.c.	n.c.	n.c.	n.c.	n.c.	n.c.	n.c.	n.c.	n.c.	n.c.	n.c.
MnO	n.d.	n.d.	n.d.	n.d.	0.01	0.04	n.d.	0.01	n.d.	n.d.	0.02	n.d.
MgO	1.14	1.19	1.49	0.68	0.65	0.50	0.93	1.34	1.20	0.53	0.83	0.79
CaO	0.00	0.03	0.03	0.05	0.06	0.04	0.03	0.08	0.02	0.11	0.01	0.06
Na_2O	1.74	1.68	1.45	1.74	1.87	1.82	0.47	0.39	0.88	1.76	0.64	1.41
K_2O	8.07	8.19	8.40	7.96	7.85	8.20	9.95	10.19	9.44	8.92	10.50	9.16
BaO	0.22	0.21	0.25	0.26	0.24	0.25	0.20	0.07	0.13	0.26	0.20	0.25
Total	95.63	94.94	94.93	95.13	95.59	96.06	95.07	96.42	95.04	94.97	94.87	94.72
Si	6.256	6.266	6.301	6.192	6.159	6.182	6.259	6.366	6.344	6.064	6.168	6.162
Al^{IV}	1.744	1.734	1.699	1.808	1.841	1.818	1.741	1.634	1.656	1.936	1.832	1.838
Al^{VI}	3.586	3.587	3.508	3.715	3.737	3.744	3.668	3.538	3.608	3.779	3.706	3.708
Ti	0.051	0.049	0.052	0.037	0.035	0.034	0.022	0.020	0.027	0.027	0.027	0.040
Fe^{2+}	0.168	0.155	0.190	0.125	0.118	0.122	0.141	0.207	0.124	0.140	0.134	0.121
Fe^{3+}	n.c.	n.c.	n.c.	n.c.	n.c.	n.c.	n.c.	n.c.	n.c.	n.c.	n.c.	n.c.
Mn	n.d.	n.d.	n.d.	n.d.	0.001	0.005	n.d.	0.001	n.d.	n.d.	0.002	n.d.
Mg	0.222	0.234	0.293	0.134	0.125	0.098	0.183	0.260	0.236	0.105	0.166	0.156
Ca	0.000	0.004	0.004	0.006	0.009	0.005	0.004	0.012	0.003	0.015	0.001	0.009
Ba	0.011	0.011	0.013	0.013	0.012	0.013	0.010	0.004	0.007	0.014	0.010	0.013
Na	0.441	0.429	0.372	0.443	0.473	0.460	0.120	0.098	0.226	0.454	0.165	0.365
K	1.347	1.379	1.416	1.331	1.306	1.362	1.679	1.701	1.587	1.517	1.792	1.557

The Si content in mylonitic potassic white mica (average Si=3.11 apfu) can provide information about the pressure range (Massonne & Schreyer, 1987). The application of the geothermometer of Coggon & Holland (2002) and Caddick & Thompson (2008) for the selected Si content yields 3.0-6.6 kbar in the range 450-550°C.

In order to obtain a temperature estimate of the mylonitc event, the deformation-dependent geometry of quartz is used here as temperature microgauges (Passchier & Trouw, 2005 and reference therein). Quartz forms large crystals with undulose extinction, frequently elongated, and aggregates of dynamically recrystallized small grains. A mantle of fine-grained quartz may surround quartz porphyroclasts with deformation lamellae. The deformational mechanism required for these microstructure is the subgrain rotation recrystallization (Stipp *et al.*, 2002). The observed deformation microstructures of quartz develop at 450-550°C (Law *et al.*, 2013; Law, 2014).

These *P-T* estimates are in agreement with the upper greenschist-facies mylonitic mineral assemblage.

Table 4.2 Chemical compositions of biotite, chlorite, plagioclase and garnet. The structural formula of biotite is calculated on the basis of 11 oxygens. The structural formula of chlorite is calculated on the basis of 28 oxygen and neglecting Na and Ca. Chlorite is assumed as completely idratated, with 16 H. The structural formula of plagioclase based on 8 oxygen. The garnet structural formula is of garnet normalized on 8 cations and Fe^{3+} is equal to $4 - Al$.

	Biotite		Chlorite		Plagioclase		Garnet		
	prekinematic	mylonitic foliation	mylonitic foliation	garnet retrocession	core	rim	rim	outer core	inner core
Point analyses	Bt40	Bt61	Chl21	Chl22	Pl02	Pl03	Grt01	Grt08	Grt18
SiO_2	36.74	36.63	24.34	24.73	64.67	63.37	36.71	36.83	36.72
TiO_2	1.57	0.36	0.02	0.04	0.02	0.01	0.07	0.09	0.12
Al_2O_3	18.58	26.32	21.47	21.02	21.81	22.11	21.28	21.54	21.27
Cr_2O_3	n.d.	n.d.	n.d.	n.d.	n.d.	n.d.	0.03	0.03	0.03
FeO^{tot}			29.01	29.93					
Fe_2O_3	n.c.	n.c.			0.05	0.09	0.01	n.d.	0.40
FeO	18.02	18.00					33.18	31.69	29.97
MnO	0.07	0.10	0.24	0.36			0.42	1.07	2.49
MgO	10.50	6.78	12.98	11.98	n.d.	n.d.	1.71	1.33	1.19
CaO	0.17	0.10			3.28	3.99	6.54	7.89	8.46
Na_2O	0.17	0.15			10.10	9.52	0.01	n.d.	0.04
K_2O	8.42	6.40			0.05	0.05			
BaO	0.09	0.03			0.00	0.00			
Total	94.35	94.86	88.06	88.04	99.98	99.14	99.96	100.48	100.68
Si	2.783	2.688	5.223	5.332	2.853	2.825	5.847	5.822	5.785
Ti	0.089	0.020	0.003	0.007	0.000	0.000	0.009	0.011	0.014
Al	1.658	2.276	5.430	5.341	1.134	1.161	3.995	4.013	3.949
Cr	n.c.	n.c.	n.c.	n.c.	n.c.	n.c.	0.003	0.003	0.004
Fe^{3+}	n.c.	n.c.					0.002	0.000	0.047
Fe^{2+}	1.142	1.105					4.420	4.190	3.949
Fe^{tot}			5.206	5.397					
Mn	0.005	0.006	0.044	0.065			0.057	0.144	0.332
Mg	1.186	0.741	4.152	3.850			0.406	0.313	0.280
Ca	0.014	0.008			0.155	0.191	1.115	1.336	1.428
Na	0.026	0.021			0.864	0.823	0.003	0.001	0.011
K	0.814	0.599			0.003	0.003			
Ba	0.003	0.001							

Figure 4.5 Mineral composition of white mica in different microstructural positions: (a) representative analyses of mica-fish (pink) and white mica along the mylonitic foliation (green); (b) Mg X-ray map of a mica-fish (centre) and mylonitic foliation (lower left angle). Note that the mica-fish has less Mg; (c) Na X-ray map of a mica-fish. Note that the mica-fish is richer in Na; (d) Mg X-ray map of an asymmetric foliation boudin; (e) Na X-ray map of an asymmetric foliation boudin.
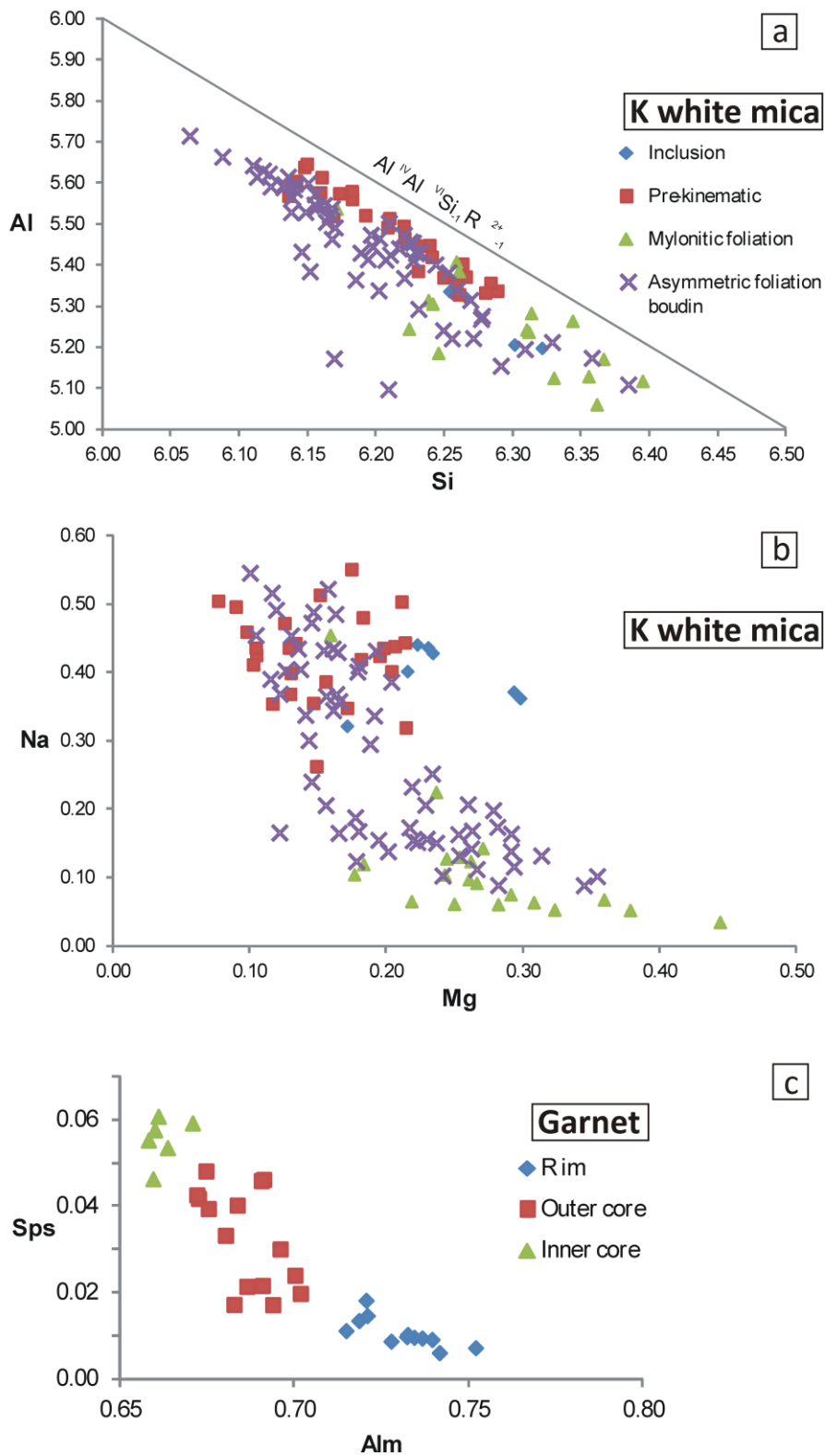
Figure 4.6 Chemical diagram for potassic white mica and garnet: (a) Si *vs.* Al plot for potassic white mica; (b) Mg *vs.* Na plot for potassic white mica; (c) almandine *vs.* spessartine plot for garnet.

4.6 Ar-Ar DATING

^{40}Ar–^{39}Ar data on sample PC23 were performed at IGG–CNR Pisa through *in situ* and step-heating laserprobe analyses. Rock chips (chip A and chip B; diameter ~ 9 mm) were drilled from a polished ≥300 µm-thick section and irradiated for 60 hours along with the fluence monitor Fish Canoyn sanidine (FCs) in the TRIGA reactor at the University of Pavia (Italy). Ages are relative to the Fish Canyon Tuff sanidine (28.03 Ma; Jourdan & Renne, 2007) and were calculated using constants recommended by Steiger & Jäger (1977). In situ laser ^{40}Ar–^{39}Ar analyses were carried using either a continuous wave diode-pumped Nd-YAG infrared (IR) laser (maximum power 20 W) connected to an external computer-controlled shutter and a pulsed Nd-YAG ultraviolet (UV) laser (frequency quadrupled and Q-switched). Multiple (3–4) shots of the IR laser, operating at ~13W and 20 ms, were focused to produce melt pits ~100 µm in diameter. The UV laser, operated at 20 Hz and ~1 mJ per pulse, was focused to ~10 µm and repeatedly rastered by a computer-controlled x–y stage over areas of ~ 0.02 mm^2. ^{40}Ar–^{39}Ar dating was focused on potassic white mica in asymmetric foliation boudins and potassic white mica aligned along the mylonitic foliation. During data acquisition, the sample was observed through a CCD camera coaxial with the laser beam. Incremental heating analysis was performed on a single mica fish (weight 5.1 mg) directly detached from one of the rock chips used for *in situ* analysis. The IR laser beam, homogenized by a beam homogenizer lens which produces a flat power distribution, was defocused to a 2 mm spot size and slowly rastered (at 0.1 mm s^{-1}) by the computer-controlled x–y stage to ensure even heating. Steps were carried out at increasing laser power to complete melting. After cleanup (10 and 15 min), extracted gases were equilibrated via automated valves into a MAP215-50 mass spectrometer equipped with a Balzers SEV217 secondary electron multiplier. Blanks were analyzed every three to four analyses. Data corrected for post-irradiation decay, mass discrimination effects, isotopes derived from interfering neutron reactions and blanks are listed in Tables 4.3 and 4.4. Errors are reported at 2σ and do not include the uncertainty in the J value, which was included in the calculated weighted mean ages or total gas ages. The location of the selected sector for step-heating analysis, the IR laver spots and UV laser pits with the correspondent age is shown in Fig. 4.9.

In chip A, Ar-Ar apparent ages range from 186.6 ± 4.5 Ma to 314.9 ± 8.6 Ma (Fig. 4.7a). The error-weighted mean on the data population of chip A is 189.5 ± 2.8 Ma with a MSWD = 1.38. In chip B, apparent ages ranges between 180.5-374.0 Ma (Fig. 4.7b),

clustering around 191 Ma (error-weighted mean = 191.1 ± 2.0 Ma with MSWD = 1.17). Figures 4.7c, d report the age distribution in asymmetric foliation boudins and along the mylonitic foliation. Step-heating Ar-Ar spectrum is highly discordant (Fig. 8), with a staircase profile especially in low cumulative % of released ^{39}Ar. The apparent ages get systematically old with increasing extraction temperatures. A plateau-like portion can be recognized in the range 178-205 Ma. The total gas is 183.41 ± 1.48 Ma. Considering the data of both chips, the most representative age is 190.7 ± 1.3 Ma with MSWD = 1.3.

**Table 4.3** ^{40}Ar/^{39}Ar in situ analyses: (a) chip A; (b) chip B.

| No.	description	laser	IR # shots / UV (mm^2)	Age (Ma)	±2σ	^{40}Ar* %	Ca/K	±2σ	^{38}Ar$_{Cl}$/^{39}Ar$_K$	±2σ
J=0.005872±0.000047										
Chip A										
92A	asymmetric foliation boudin	UV	200x100	189.1	5.9	92.3	0.11	0.10	0.0012	0.0030
92C	asymmetric foliation boudin	UV	200x100	187.3	4.5	91.5	0.05	0.12	0.0037	0.0026
92D	asymmetric foliation boudin	UV	200x100	226.3	3.1	97.4	0.02	0.05	0.0000	0.0021
92E	asymmetric foliation boudin	UV	200x100	188.6	6.1	99.0	0.03	0.13	0.0022	0.0041
92G	mylonitic foliation	UV	200x100	254	33	92.5	-	-	-	-
92H	asymmetric foliation boudin	UV	200x100	246.3	4.0	99.8	0.00	0.07	0.0001	0.0014
92I	mylonitic foliation	UV	200x100	261.6	3.9	97.8	0.02	0.06	0.0011	0.0021
92L	mylonitic foliation	UV	200x100	246.1	3.7	99.8	0.08	0.06	0.0016	0.0018
92P	mylonitic foliation	IR	3	314.9	8.6	84.3	0.06	0.24	0.0137	0.0034
92Q	mylonitic foliation	IR	3	231	42	89.0	0.10	1.53	0.0143	0.0188
92S	asymmetric foliation boudin	UV	200x100	229.6	2.8	98.7	0.03	0.10	0.0001	0.0012
92T	asymmetric foliation boudin	UV	200x100	192.8	4.0	96.9	0.06	0.13	0.0010	0.0020
92U	asymmetric foliation boudin	UV	200x100	207.9	2.6	97.7	0.04	0.11	0.0023	0.0017
92V	asymmetric foliation boudin	UV	200x100	186.6	4.5	98.1	0.10	0.15	0.0007	0.0019
92W	asymmetric foliation boudin	UV	200x100	192.9	5.7	98.0	-	-	0.0005	0.0014
92X	asymmetric foliation boudin	UV	triangle (b=200, h=400)	250.6	3.0	94.9	0.00	0.11	0.0030	0.0019
92Z	asymmetric foliation boudin	UV	200x100	204.8	3.3	97.9	0.04	0.10	0.0027	0.0017
94A	asymmetric foliation boudin	UV	200x100	209.4	4.4	99.6	0.04	0.15	0.0044	0.0019

No.	description	laser	IR # shots / UV (mm^2)	Age (Ma)	±2σ	^{40}Ar* %	Ca/K	±2σ	^{38}Ar$_{Cl}$/^{39}Ar$_K$	±2σ
J=0.005872±0.000047										
Chip B										
91C	mylonitic foliation	IR	3	189.1	4.0	97.3	0.17	0.12	0.0074	0.0019
91D	mylonitic foliation	IR	3	191.6	1.8	97.3	0.09	0.07	0.0102	0.0012
91E	asymmetric foliation boudin	IR	3	192	30	93.7	0.37	0.79	0.0037	0.0114
91H	mylonitic foliation	IR	4	245.1	6.2	90.2	0.11	0.35	0.0059	0.0040
91I	mylonitic foliation	IR	3	202.4	2.0	94.7	0.17	0.07	0.0086	0.0013
91M	asymmetric foliation boudin	UV	100x100	198	12	96.3	0.07	0.37	0.0047	0.0052
91N	asymmetric foliation boudin	UV	200x100	231.2	3.7	95.5	0.03	0.14	-	-
91Q	asymmetric foliation boudin	UV	200x100	213.4	3.5	95.5	0.084	0.048	0.0017	0.0017
91R	asymmetric foliation boudin	UV	200x100	189.0	4.6	90.0	0.10	0.10	-	-
91S	asymmetric foliation boudin	UV	triangle (b=200, h=200)	188.6	5.4	97.6	0.04	0.20	0.0022	0.0030
91V	mylonitic foliation	IR	3	180	11	97.1	0.04	0.42	0.0006	0.0047
91W	mylonitic foliation	IR	3	374	10	65.5	0.33	0.28	0.0815	0.0045
91X	asymmetric foliation boudin	UV	200x100	190.2	5.2	97.4	0.15	0.17	0.0055	0.0032
91Z	asymmetric foliation boudin	UV	200x100	208.7	2.9	92.9	0.11	0.13	0.0087	0.0023
93A	asymmetric foliation boudin	UV	200x100	193.8	3.4	96.7	0.03	0.11	0.0029	0.0013
93B	asymmetric foliation boudin	UV	triangle (b=140 , h=300)	191.7	3.3	96.7	0.05	0.11	0.0052	0.0018

Table 4.4 $^{40}Ar/^{39}Ar$ step-heating analyses.

No.	laser power (W)	Age (Ma)	±2σ	$^{40}Ar^* \%$	$^{39}Ar_K \%$	Ca/K	±2σ	$^{38}Ar_{Cl}/^{39}Ar_K$	±2σ
100F	0.20	25.4	2.8	36.458	0.186	0.107	0.321	0.029	0.002
100G	0.40	51.66	0.99	74.402	0.874	0.099	0.071	0.032	0.001
100H	0.55	99.14	0.69	80.454	1.628	0.043	0.039	0.020	0.001
100I	0.70	130.13	0.64	91.547	2.599	0.041	0.024	0.013	0.001
100K	0.80	148.82	0.68	94.587	3.316	0.043	0.018	0.009	0.001
100L	0.88	160.48	0.76	96.145	3.692	0.032	0.017	0.007	0.001
100M	0.95	171.44	0.74	96.963	4.692	0.032	0.016	0.005	0.001
100O	1.02	178.90	0.79	97.839	4.397	0.027	0.016	0.003	0.001
100P	1.10	181.82	0.78	97.760	6.564	0.027	0.012	0.004	0.001
100Q	1.17	183.75	0.84	98.040	5.771	0.032	0.013	0.003	0.001
100R	1.25	186.47	0.85	98.324	5.962	0.031	0.013	0.003	0.001
100T	1.32	187.05	0.80	98.596	4.256	0.031	0.016	0.003	0.001
100U	1.40	187.93	0.87	98.498	5.946	0.036	0.015	0.003	0.001
100V	1.50	188.49	0.98	98.444	5.305	0.053	0.015	0.003	0.001
100W	1.60	189.62	0.91	98.402	4.734	0.068	0.017	0.004	0.001
100X	1.70	190.39	0.80	98.483	3.373	0.051	0.021	0.003	0.001
100Y	1.85	191.21	0.79	98.444	4.140	0.076	0.019	0.003	0.001
100Z	1.97	192.19	0.83	98.454	2.894	0.097	0.025	0.003	0.001
101C	2.10	193.22	0.86	98.704	2.149	0.058	0.033	0.003	0.001
101D	2.3	194.0	1.0	98.582	1.792	0.052	0.038	0.002	0.001
101E	2.6	194.55	0.83	98.721	4.600	0.051	0.018	0.003	0.001
101F	2.9	197.14	0.79	98.746	6.973	0.039	0.013	0.002	0.001
101G	3.2	200.46	0.86	98.837	3.387	0.028	0.022	0.002	0.001
101H	3.5	201.74	0.82	98.866	3.075	0.032	0.024	0.002	0.001
101I	3.9	204.59	0.94	98.847	2.363	0.055	0.031	0.002	0.001
101K	4.4	203.4	1.4	98.700	1.454	0.045	0.051	0.002	0.001
101L	5.0	204.5	1.0	98.707	0.858	0.056	0.079	0.001	0.001
101M	6.0	208.15	0.92	98.595	1.253	0.066	0.056	0.002	0.001
101P	7.5	212.2	1.1	98.964	0.886	0.049	0.071	0.002	0.001
101Q	9.0	220.6	1.5	98.816	0.456	0.082	0.149	0.002	0.001
101R	12	224.5	1.4	99.054	0.376	0.117	0.171	0.002	0.001
101T	15	253	11	98.169	0.049	1.020	1.412	0.003	0.005

Figure 4.7 (next page) Ages from *in situ* Ar-Ar dating: (a) ages *vs.* cumulative number of analyses in chip A; (b) ages *vs.* cumulative number of analyses in chip B; (c) relative probability plot considering only the point analyses in asymmetric foliation boudins; (d) relative probability plot with the point analyses along the mylonitic foliation. The relative probability distribution was calculated by the Isoplot/Ex program, v. 3.00 (Ludwig, 2003) using the 2σ analytical uncertainty.

asymmetric foliation boudin

mylonitic foliation
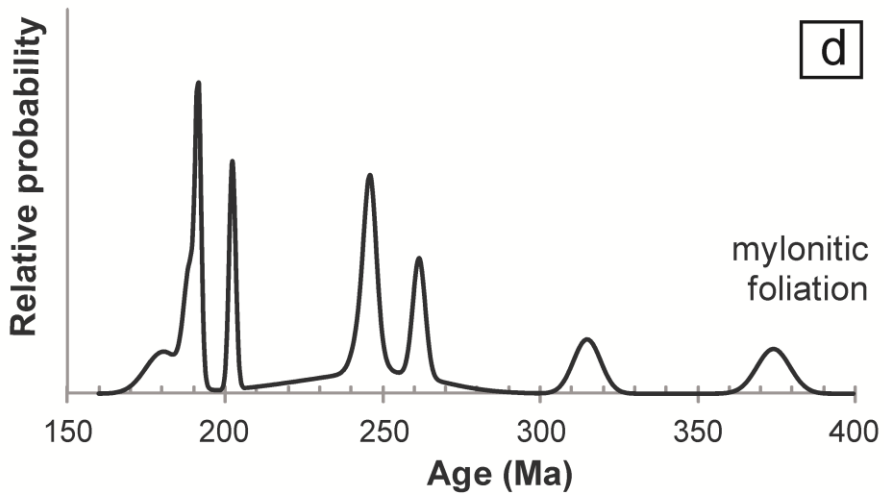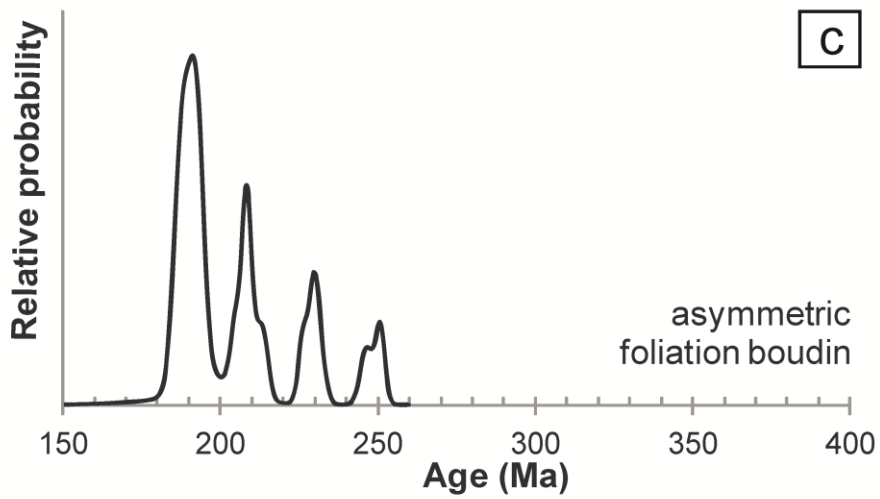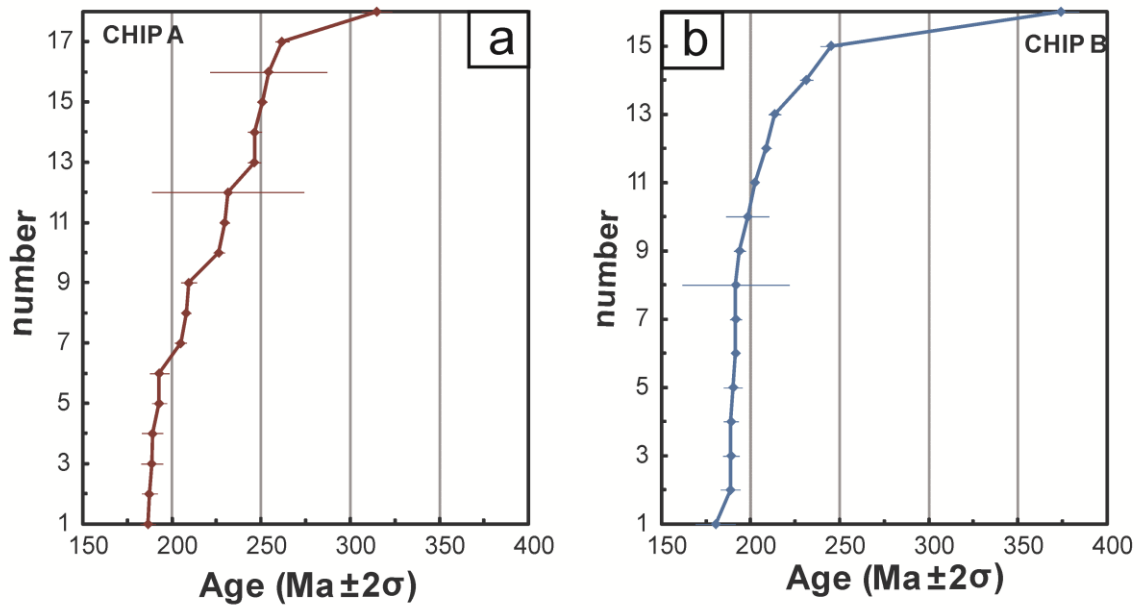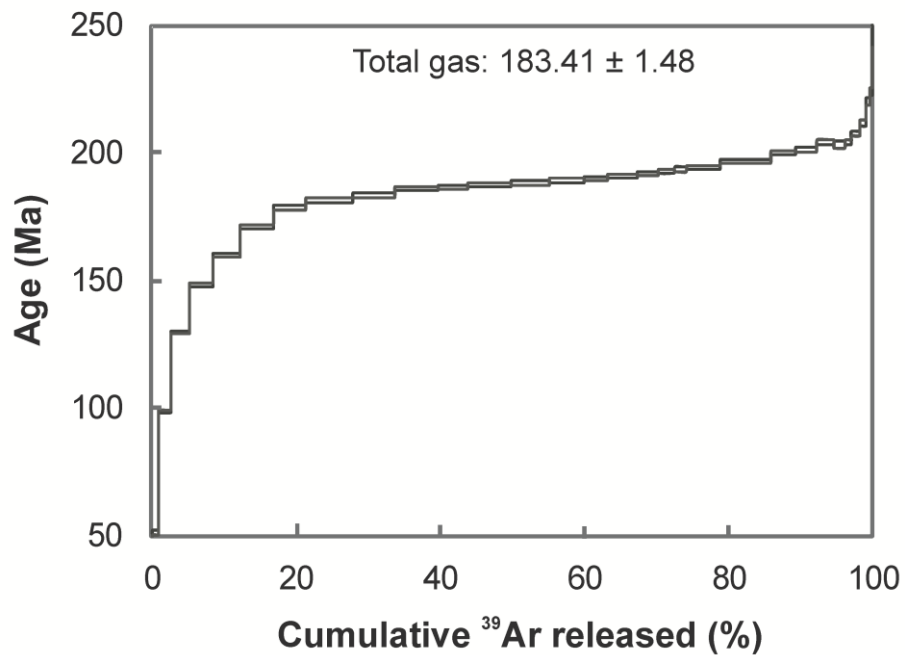
Figure 4.8 Step-heating spectrum in an asymmetric foliation boudin.

4.7 DISCUSSION

4.7.1 Dating asymmetric foliation boudins

In situ ^{40}Ar/^{39}Ar dating of potassic white mica is texturally-controlled, so it is possible to attribute each age to its microstructural position. A comparison of the age distribution in mylonitc foliation and in asymmetric foliation boudins is presented.

Potassic white mica in asymmetric foliation boudins is characterized by four main ages (principal peaks in the relative probability plot in Fig. 4.7c) around 190 Ma, 210 Ma, 230 Ma, 240 Ma. In the asymmetric foliation boudins of chip B younger ages (~190 Ma) are mostly located in the core of the structure, while the rims of the boudin contain older ages (213.4 ± 3.5 Ma, 231.2 ± 3.7 Ma, 208.7 ± 2.9 Ma). Potassic white mica in mylonitic foliation shows four main age peaks around 190 Ma, 210 Ma, 240 Ma, 260 Ma and two subsidiary peaks at 315 Ma, 370 Ma. In particular mylonitic foliation contains the oldest ages (374.0 ± 10.4 Ma, 314.9 ± 8.6 Ma). Thus potassic white mica in mylonitic foliation shows more scattering in age distribution, with probable prekinematic relics. The preservation of older ages occurs within the mylonitic foliation rather than in asymmetric foliation boudins, which, instead, consist in a significant concentration of white mica coeval with the shearing stage.
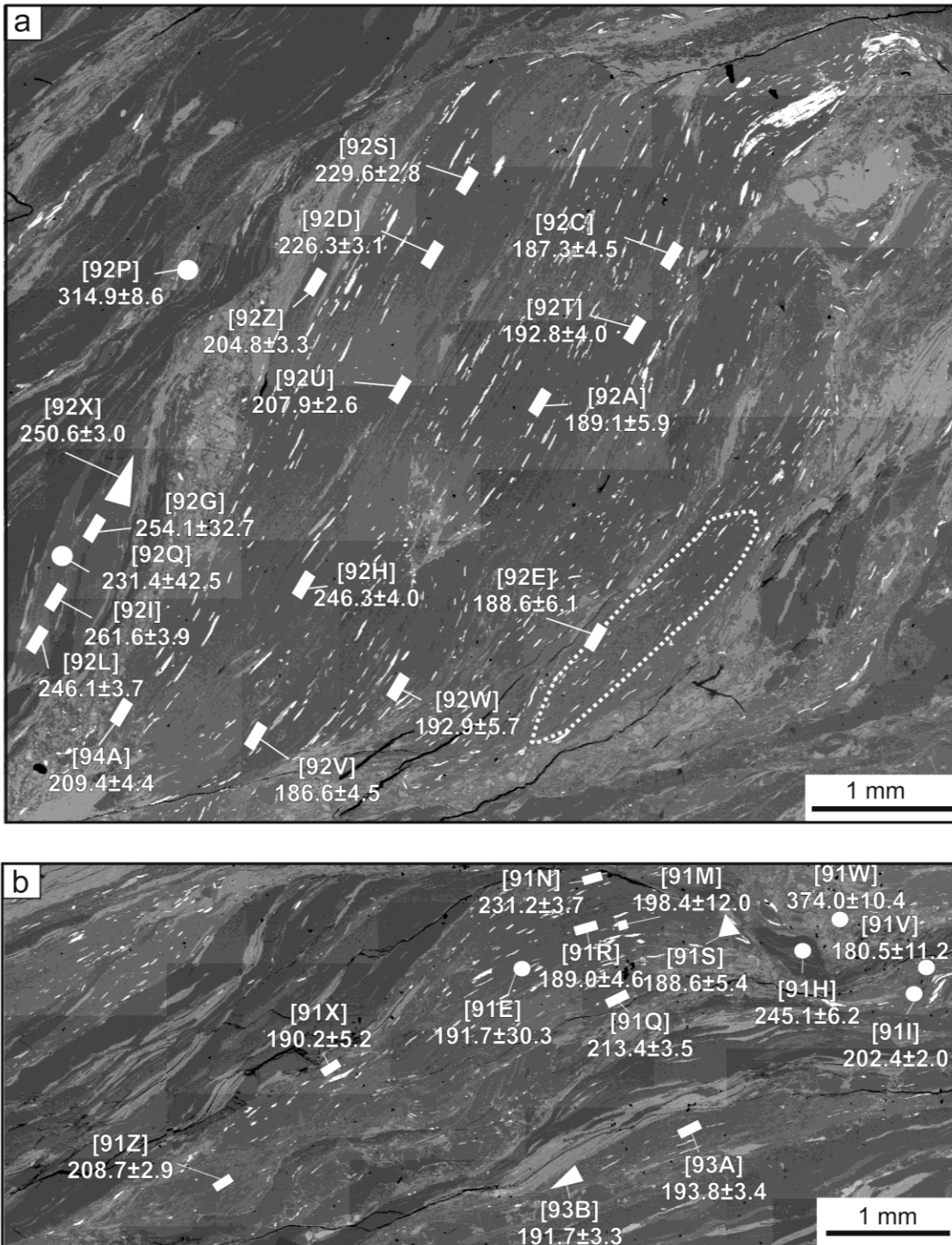
Figure 4.9 BSE images of chip A (a) and chip B (b) with the location of the step-heating area (dotted line), the IR laver spots (circles) and UV laser pits (squares, rectangles and triangles). The correspond ages are reported with the 2σ analytical uncertainty.

4.7.2 Interpretation of the ^{40}Ar-^{39}Ar ages

A complex age record results from the ^{40}Ar-^{39}Ar dating of the ductile shearing microstructures in the mylonitic micaschist of the Cerreto Pass. Asymmetric foliation boudins exhibit compositional and geochronological heterogeneity that is commonly related to local recrystallization of individual potassic white mica grains (Mulch & Costa, 2004). In our case study this is valid also for potassic white mica along the mylonitic foliation.

The staircase-like shape of the step-heating spectrum has been commonly associated to: (i) a partial diffusive loss of radiogenic ^{40}Ar from a single mica population during a thermal event (Kelley & Turner, 1991; Harrison *et al.*, 2005); (ii) mixtures of different generation of micas (West & Lux, 1993); (iii) protracted crystallization (Kirschne *et al.*, 1996). In our case study the step-heating spectrum shows a staircase shape, but with two different slopes: the young ages at low extraction temperatures and the old ages at high extraction temperatures are characterized by a pronounced slope; the intermediate ages (from 178.9 ± 0.8 Ma to 204.6 ± 0.9 Ma) at intermediate extraction temperatures resemble a pseudo-plateau shape with a slight staircase variation. These intermediate ages were obtained for the 78% of the ^{39}Ar released. Thus, we propose two different interpretations for the high-slope and low-slope sectors of the step-heating spectrum. The high-slope sectors may be due to the mixing of argon components for the coexistence of different generation of white mica. The low-slope sector resembles the staircase spectra of Kirschne *et al.* (1996), interpreted as the time span over which mica crystallized and grew. In the Cerreto metapelites, the estimated time of protracted crystallization during ductile deformation is 26 My.

Thus, even if highly-discordant step-heating spectra have occasionally been connected to a partial diffusive loss of radiogenic ^{40}Ar from a single mica population during a thermal event (Kelley *et al.*, 1991; Harrison *et al.*, 2005), the overall staircase shape of the Cerreto spectrum is presumably due to a mixing of different generations of white mica and to a protracted crystallization.

4.7.3 Tectonic implications

The imprints of different recrystallization stages are preserved in the Cerreto micaschist, allowing the identification of some peculiar geochronological signatures (Tab. 4.5).

The oldest *in situ* ages (374 and 315 Ma) are close to the 312, 328, 397 Ma plateau age of the Variscan metamorphism in the amphibolite associated with the micaschist (Molli

et al., 2002), thus they may represent the age of pre-kinematic relics that survived to the shearing deformation. The intermediate ages 210 Ma, 230 Ma, 240 Ma, 260 Ma may be either interpreted as mixed ages or as the record of post-Variscan intracontinental strike-slip tectonics (Massari, 1986; Matte, 2001). Actually, the size of the UV/IR laser spot is bigger (hundreds of μm) than the size of the single muscovite grains (tens to hundreds of μm), so the laser spot can collect the Ar-Ar record of different muscovite generations. On the other hand, exhumation along detachment faults in Permian-Triassic times is also documented in the External Liguride Units representing the transition between the Internal Liguride oceanic domain and the thinned continental margin of the Adria plate (Marroni *et al.*, 1998). In particular, an age of 228 ± 2 Ma ($^{40}Ar/^{39}Ar$ on amphibole) has been ascribed to rift-related cooling along this peri-Tethyan distal continental margin. Furthermore, the sedimentary sequence outcropping in Punta Bianca includes a extensional basin deposit associated with alkaline basalts of Middle-Triassic erupted in a rifting setting (Ricci & Serri, 1975; Martini *et al.*, 1986). Thus, the Permian-Triassic ages obtained for the studied sample may testify the involvement of the Cerreto mylonitc rocks in ductile shear zones that mark the passage from the extension consequent of the collapse of the Variscan chain to the onset of the Tethyan-related rifting.

The younger and most frequent age (190.7 Ma) predates the opening of the Western Tethys in late Jurassic, so it may represent another shearing event in a thinned crust or a thermal event that enhanced the partial loss of radiogenic ^{40}Ar. A first Tethyan-related rifting stage associated with lithosphere stretching has been documented in Western Alps in Lower Jurassic (Eberli & Froitzheim, 1990; Froitzheim & Manatschal, 1996). Occurrences of shearing in Lower Jurassic is documented in the Adriatic rifted margins (Mohn *et al.*, 2010): mafic rocks of a Permian crust sector records the onset of the rifting from 225-200 Ma and exhumation at seafloor between 170 and 140 Ma (Malenco Unit; Müntener *et al.,* 2000; Villa *et al.,* 2000); in the Southern Alps the shearing has been constrained at 182.0 ± 1.6 Ma (Pogallo shear zone; Mulch *et al.,* 2002); extensional shearing in the necking zone of the Adria margin in the East-central Alps occurred at 180-205 Ma from middle crustal depth (Eita shear zone; Mohn *et al.*, 2012); Ar-Ar dating in the Adria distal margin of the Alpine Corsica yielded 187.8 ± 1.4 Ma for the extensional shearing accommodating rift-related crustal thinning (Belli Piani shear zone; Beltrando *et al.*, 2013).

As a whole the geodynamic context of these Adria-derived basement remnants corroborate the thesis of a shearing event at 190 Ma rather than a thermal event.

Table 4.5 Age peaks in the Cerreto micaschist and respective interpretations and references.

Age peaks	Interpretations	References
374 - 315 Ma	Variscan metamorphism	Molli et al., 2002
210 - 260 Ma	post-Variscan intracontinental strike-slip tectonics or mixed ages	Ricci & Serri, 1975; Martini et al., 1986; Massari, 1986; Marroni et al., 1998; Matte, 2001
191 Ma	rift-related shearing	Eberli & Froitzheim, 1990; Froitzheim & Manatschal, 1996; Müntener et al., 2000; Villa et al., 2000; Mulch et al., 2002; Mohn et al., 2010; Mohn et al., 2012; Beltrando et al., 2013

4.7.4 Mica-fish *vs*. foliation-fish. A cautionary note

In the Cerreto mylonitic rocks what seems a mica-fish at low-magnification may be actually a potassic white mica polycrystalline aggregate with a sigmoidal shape. In this respect, this microstructure should not be considered as a mica-fish, but actually as a fish-shaped asymmetric foliation boudin (foliation fish).

Foliation-fish must not be confused with mica-fish. Mica-fish is a large single crystal of mica with a lozenge shape and monoclinic symmetry (Passchier & Trouw, 2005). Differently from foliation-fish, mica-fish is commonly a prekinematic porphyroclast, thus providing information on the earlier phase(s) with respect to the mylonitic stage.

The common assumption that large (apparent single) potassic white mica crystals in mylonite are prekinematic mica-fishes can led to wrong interpretations of potassic white mica-based geothermobarometry and geochronology.

The composition of potassic white mica is commonly used to obtain thermobaric constrains (e.g. compositional isopleths in phase diagrams). In particular the Si content in potassic white mica provides information on the pressure of metamorphism (Massonne & Schreyer; 1987). If the fish-structure involving potassic white mica is interpreted as mica-fish, the *P-T* values indicated by potassic white mica are related to the earlier stages of metamorphic evolution. Instead, if the fish-structure is interpreted

as foliation fish, the *P-T* constrains provided by potassic white mica regard the synkinematic mylonitc stage.

Radiometric ages of potassic white mica separates are in some case interpreted on the basis of the potassic white mica grain size (e.g. Kligfield *et al.*, 1986; West & Lux, 1993): big crystals of potassic white mica are considered prekinematic relics, while fine-grained potassic white mica is commonly associated with the mylonitic foliation development. This is not always true, because the coarse-grained separates might be foliation-fishes. Conversely, fine-grained minerals may belong to pre-kinematic relics. Thus dating mineral separates is not the recommended technique to obtain information about ages in mylonitic rocks.

4.8 CONCLUSIONS

1. In our case study, asymmetric foliation boudin results in a preferential microstructure for obtaining geochronological information about the shearing event because: (i) it shows a more narrow age spectrum, usually related to the shearing stage(s), differently from the mylonitic foliation that may contain prekinematic relics; (ii) white mica in mylonitic foliation is commonly associated with other minerals (e.g. chlorite) that may disturb the analysis; (iii) thanks to its big size, asymmetric foliation boudin is easier to be dated than fine-grained mica along the mylonitic foliation.

2. Pre-mylonitic relics preserve the age of the Variscan metamorphism at 374 and 315 Ma.

3. The main shearing event in the Cerreto micaschist occurred at 400-500°C and 3-5 kbar. The age (190.7 ± 1.3 Ma) testify the involvement of the Northern Apennine basement in the Tethyan-related rifting stage of the Adria margin, widely documented in the Adria-derived Alpine units.

4. Apparent big crystals of white mica in mylonitic rocks are not always prekinematic mica-fishes. They may consist of several fine-grained white-mica grains sinkinematically crystallized during the shearing event.

4.9 REFERENCES

Arslan, A., Passchier, C. W. & Koehn, D., 2008. Foliation boudinage. *Journal of Structural Geology,* **30(3)**, 291-309.

Beltrando, M., Zibra, I., Montanini, A. & Tribuzio, R., 2013. Crustal thinning and exhumation along a fossil magma-poor distal margin preserved in Corsica: A hot rift to drift transition? *Lithos,* **168**, 99-112.

Bernhardt, H.-J, Massonne, H.-J., Reinecke, T., Reinhardt, J. & Willner, A., 1995. Digital element distribution maps, an aid for petrological investigations. Berichte der Deutschen Mineralogischen Gesellschaft, *Beihefte zum European Journal of Mineralogy,* **7**, 28.

Borsi, S., Ferrara, G., Rau, A. & Tongiorgi, M., 1967. Determinazioni col metodo Rb/Sr delle filladi e quarziti listate di Buti (Monti Pisani). *Atti della Società toscana di scienze naturali, Memorie, Serie A,* **73**, 632-646.

Brandelik, A., 2009. CALCMIN – an EXCEL^{TM} Visual Basic application for calculating mineral structural formulae from electron microprobe analyses. *Computers & Geosciences,* **35**, 1540–1551.

Caddick, M. J. & Thompson, A.B., 2008. Quantifying the tectono-metamorphic evolution of pelitic rocks from a wide range of tectonic settings: mineral compositions in equilibrium. *Contributions to Mineralogy and Petrology,* **156**, 177-195.

Coggon, R. &, Holland, T.J.B., 2002. Mixing properties of phengitic micas and revised garnet-phengite thermobarometers. *Journal of Metamorphic Geology,* **20**, 683-696.

Del Moro, A., Puxeddu, M., Radicati di Brozolo, F. & Villa, I.M., 1982. Rb-Sr and K-Ar Ages on Minerals at Temperatures of 3000-400° C from Deep Wells in the Larderello Geothermal Field (Italy). *Contributions to Mineralogy and Petrology,* **81**, 340-349.

Dickin, A.P., 1995. Radiogenic Isotope Geology. Cambridge University Press, Cambridge, UK, pp. 490.

Eberli, G. & Froitzheim, N., 1990. Extensional detachment faulting in the evolution of a Tethys passive continental margin, Eastern Alps, Switzerland. *Geological Society of America Bulletin,* **102**, 1297-1308.

Faure, G., 1986. Principles of isotope geology. Vol. 589. New York, Wiley, pp. 589.

Fossen, H., 2010. Structural geology. Cambridge University Press, pp. 463.

Froitzheim, N. & Manatschal, G., 1996. Kinematics of Jurassic rifting, mantle exhumation, and passive-margin formation in the Austroalpine and Penninic nappes (eastern Switzerland). *Geological Society of America Bulletin,* **108**, 1120-1133.

Goscombe, B.D. & Passchier, C.W., 2003. Asymmetric boudins as shear sense indicators-an assessment from field data. *Journal of Structural Geology,* **25**, 575-589.

Goscombe, B.D., Passchier, C.W. & Hand, M., 2004. Boudinage classification: end-member boudin types and modified boudin structures. *Journal of Structural Geology,* **26**, 739-763.

Hanmer, S., 1986. Asymmetrical pull-aparts and foliation fish as kinematic indicators. *Journal of Structural Geology,* **8**, 111-122.

Harrison, T.M., Grove, M., Lovera, O.M. & Zeitler, P.K., 2005. Continuous thermal histories from closure profiles. In *In Low Temperature Thermochronology: Techniques, Interpretations and Applications, Reviews in Mineralogy and Geochemistry,***58**, 389-409.

Jourdan, F. & Renne, P. R. 2007. Age calibration of the Fish Canyon sanidine ^{40}Ar/^{39}Ar dating standard using primary K-Ar standard. *Geochimica et Cosmochimica Acta,* **71**, 387–402.

Kelley, S.P. & Turner, G., 1991. Laser probe ^{40}Ar-^{39}Ar measurements of loss profiles within individual hornblende grains from the Giants Range Granite, northern Minnesota, USA. *Earth and Planetary Sciences,* **107**, 634-648.

Kirschner, D. L., Cosca, M. A., Masson, H. & Hunziker, J. C., 1996. Staircase ^{40}Ar/^{39}Ar spectra of fine-grained white mica: Timing and duration of deformation and empirical constraints on argon diffusion. *Geology,* **24**, 747-750.

Kligfield, R., Hunziker, J, Dallmeyer, R.D. & Schamel, S. 1986. Dating of deformational phases using K-Ar and ^{40}Ar/^{39}Ar techniques: results from the Northern Apennines. *Journal of Structural Geology,* **8**, 781-798.

Law, R. D., 2014. Deformation thermometry based on quartz c-axis fabrics and recrystallization microstructures: A review. *Journal of Structural Geology,* **66**, 129-161.

Law, R.D., Stahr, D.W., Francsis, M.K., Ashley, K.T., Grasemann, B. & Ahmad, T., 2013. Deformation temperatures and flow vorticities near the base of the Greater

Himalayan Series, Sutlej Valley and Shimla Klippe, NW India. *Journal of Structural Geology,* **54**, 21-53.

Lo Pò, D. & Braga, R., 2014. Influence of ferric iron on phase equilibria in greenschist facies assemblages: the hematite-rich metasedimentary rocks from the Monti Pisani (Northern Apennines). *Journal of Metamorphic Geology,* **32**, 371-387.

Ludwig, K.R., 2003. User's Manual for Isoplot 3.00. A Geochronological Toolkit for Microsoft Excel. Berkeley Geochronology Center. Special Publication No. 4.

Marroni, M., Molli, G., Montanini, A. & Tribuzio, R., 1998, The association of continental crust rocks with ophiolites (Northern Apennines, Italy): Implications for the continent-ocean transition. *Tectonophysics,* **29**, 43-66.

Martini, I. P., Rau, A. & Tongiorgi, M., 1986. Syntectonic sedimentation in a Middle Triassic rift, northern Apennines, Italy. *Sedimentary geology,* **47**, 191-219.

Massari, F., 1986. Some thoughts on the Permo-Triassic evolution of the South Alpine area (Italy). *Memorie della Società Geologica Italiana,* **34**, 179–188.

Massonne, H.-J. & Schreyer, W., 1987. Phengite geobarometry based on the limiting assemblage with K-feldspar, phlogopite, and quartz. *Contributions to Mineralogy and Petrology,* **96**, 212-224.

Matte, P., 2001. The Variscan collage and orogeny (480–290 Ma) and the tectonic definition of the Armorica microplate: a review. *Terra nova,* **13**, 122-128.

McDougall, I. & Harrison, T. M., 1999. Geochronology and Thermochronology by the ^{40}Ar/^{39}Ar Method. Oxford University Press, pp. 269.

Mohn, G., Manatschal, G., Müntener, O., Beltrando, M. & Masini, E., 2010. Unravelling the interaction between tectonic and sedimentary processes during lithospheric thinning in the AlpineTethys margins. *International Journal of Earth Sciences,* **99**, 75–101.

Mohn, G., Manatschal, G., Beltrando, M., Masini, E. & Kusznir, N., 2012. Necking of continental crust in magma-poor rifted margins: Evidence from the fossil Alpine Tethys margins. *Tectonics,* **31**(1).

Molli, G., Montanini, A. & Frank W., 2002. MORB-derived Varisican amphibolites in the Northern Apennine Basement: the Cerreto metamorphic slices (Tuscan-Emilian Apennine, NW Italy). *Ofioliti,* **27**, 17-30.

Mulch, A. & Cosca, M.A., 2004. Recrystallization or cooling ages: in situ UV-laser ^{40}Ar/^{39}Ar geochronology of muscovite in mylonitic rocks. *Journal of the Geological Society,* **161**, 573-582.

Mulch, A., Cosca, M. & Handy, M., 2002. In-situ UV-laser ^{40}Ar/^{39}Ar geochronology of a micaceous mylonite: an example of defect-enhanced argon loss. *Contributions to Mineralogy and Petrology,* **142**, 738-752.

Müntener, O., Hermann, J. & Trommsdorff, V., 2000. Cooling history and exhumation of lower-crustal granulite and upper mantle (Malenco, Eastern Central Alps). *Journal of Petrology* ,**41**, 175-200.

Musumeci, G., Mazzarini, F., Tiepolo, M. & Di Vincenzo, G., 2011. U–Pb and ^{40}Ar–^{39}Ar geochronology of Palaeozoic units in the northern Apennines: determining protolith age and alpine evolution using the Calamita Schist and Ortano Porphyroid. *Geological Journal,* **46**, 288-310.

Passchier, C.W. & Druguet, E., 2002. Numerical modelling of asymmetric boudinage. *Journal of Structural Geology*, **24**, 1789-1803.

Passchier, C.W. & Trouw, R.A.J., 2005. Microtectonics (Second edition). Springer-Verlag, Berlin, pp. 366.

Platt, J. P. & Vissers, R.L.M., 1980. Extensional structures in anisotropic rocks. *Journal of Structural Geology, 2*, 397-410.

Rau, A. & Tongiorgi, M., 1966. Considerazioni preliminari sulla geologia della parte meridionale dei Monti Pisani (versante SW). *Memorie della Società Geologica Italiana*, **5**, 300-314.

Ricci, C.A. & Serri, G., 1975. Evidenza geochimica sulla diversa affinità petrogenetica delle rocce basiche comprese nella serie a facies toscana. *Bollettino Società Geologica Italiana,* **94**, 1187-1198.

Sanchez, G., Rolland, Y., Schneider, J., Corsini, M., Oliot, E., Goncalves, P., Verati, C., Lardeaux, J.M. & Marquer, D., 2011. Dating low-temperature deformation by ^{40}Ar/^{39}Ar on white mica, insights from the Argentera-Mercantour Massif (SW Alps). *Lithos,* **125**, 521-536.

Schiaffino L. & Tongiorgi M., 1962. Stratigrafia del Verrucano dei Monti Pisani. *Atti della Società toscana di scienze naturali, Memorie*, *Serie A*, **69**, 382-446.

Steiger, R.H. & Jäger, E., 1977. Subcommission on Geochronology: Convention on the use of decay constants in geo- and cosmochronology. *Earth and Planetary Science Letters,* **36**, 359–362.

Stipp, M., Stuenitz, H., Heilbronner, R. & Schmid, S. M., 2002. The eastern Tonale fault zone: a 'natural laboratory'for crystal plastic deformation of quartz over a

temperature range from 250 to 700 C. *Journal of Structural Geology,* **24**, 1861-1884.

Vai, G.B. & Martini, I.P., 2001. Anatomy of an Orogen: the Apennines and Adjacent Mediterranean Basins, Kluwer Academic Publishers, pp. 632.

Vernon, R. H., 2004. A practical guide to rock microstructure. Cambridge university press, pp. 594.

Villa, I. M., Hermann, J., Müntener, O. & Trommsdorff, V., 2000. $^{39}Ar-{}^{40}Ar$ dating of multiply zoned amphibole generations (Malenco, Italian Alps). *Contributions to Mineralogy and Petrology,* **140**, 363-381.

West Jr, D. P. & Lux, D. R., 1993. Dating mylonitic deformation by the $^{40}Ar-{}^{39}Ar$ method: An example from the Norumbega Fault Zone, Maine. *Earth and Planetary Science Letters,* **120**, 221-237.

Zwart, H.J. & Calon, T., 1977. Chloritoid crystals from Curaglia; growth during flattening or pushing aside. *Tectonophysics,* **39**, 477-486.

Zwart, H. J., 1962. On the deformation of polymetamorphic mineral associations and its application to the Bosost area (Central Pyrenees). *Geologische Rundschau,* **52**, 38–65.

The Alpine Metamorphism

And The Influence Of Ferric Iron

In The Hematite-Rich Metasedimentary Rocks

From The Pisani Mountains

THE ALPINE METAMORPHISM AND THE INFLUENCE OF FERRIC IRON

IN THE HEMATITE-RICH METASEDIMENTARY ROCKS FROM THE PISANI MOUNTAINS

5.1 INTRODUCTION

In recent years, the study of the metamorphic evolution of metasedimetary rocks has benefited from the introduction of new activity models of minerals containing important minor elements such as Fe^{3+} and Ti (White *et al.*, 2000, 2002, 2007; Diener *et al.*, 2007; Green *et al.*, 2007; Smye *et al.*, 2010). The development of these models has expanded the ability to extract quantitative *P-T* information from metasedimentary rocks modelled in increasingly complex systems, from KFMASHTO (White *et al.*, 2000) to NCKFMASHTO (Diener & Powell, 2010; Boger *et al.*, 2012; Korhonen *et al.*, 2012) and MnNCKFMASHTO (López-Carmona *et al.*, 2013). Although Fe^{3+} is known to have an important control on assemblages, the actual amount of Fe_2O_3 in metasedimentary rocks and minerals is still not able to be quantified accurately. Routine analytical techniques (XRF, EPMA) do not discriminate between FeO and Fe_2O_3. Even when Fe_2O_3 is directly measured in minerals and/or bulk rocks (e.g. by tritation, Mössbauer spectroscopy, synchrotron micro-XANES spectroscopy) its amount is likely to represent an overestimate due to low-temperature oxidation processes, including powder preparation (Diener & Powell, 2010; López-Carmona *et al.*, 2013). Indeed, sample preparation procedures transform part of the Fe^{2+} to Fe^{3+} mainly by contamination, air oxidation and dissolution of the rock powder (Andrade *et al.*, 2002). Milling equipment containing iron or steel may provide an addition of iron to the sample. Besides, the operation of grinding in air provides oxidation of ferrous iron, particularly when the powder is fine and local temperatures are high. Fitton & Gill (1970) demonstrated that only 4 minutes of fine grinding is sufficient to oxidize significantly the powder, with an absolute decrease of FeO by 1 wt. %.

Alternatively, bulk ferric iron can be estimated by using mineral modes and their stoichiometric-based Fe^{3+} calculation, but this method is difficult for some minerals (e.g. mica, amphibole). For example, Fe^{3+} estimation in biotite is uncertain without a complete chemical analysis including H, F and Cl (Braga *et al.,* 2006). Furthermore, other options in dealing with the bulk ferric iron are either to neglect its presence (Braga & Massonne, 2008) or allow a certain amount to stabilize Fe^{3+}-bearing phases in mineral assemblages (e.g., epidote: Braga *et al.*, 2007). Currently, a popular approach is

---

Figure of the previous page: hematite bands in a phyllite from the Pisani Mountains.

This study was published by D. Lo Pò and R. Braga in Journal of Metamorphic Geology , 2014.

to investigate phase relations calculating *P*- or *T-X* pseudosections, where *X* can be assigned to $X\text{Fe}^{3+}$ [$\text{Fe}^{3+}/(\text{Fe}^{3+} + \text{Fe}^{2+})$] (Diener & Powell, 2010) or to $X\text{Fe}_2\text{O}_3$ (e.g.: Phillips *et al.*, 2010; López-Carmona *et al.*, 2013), and to look for correspondence between observations and modelling results.

So far, the effects of Fe_2O_3 have been evaluated in metapelites with mineral associations typical of very high-pressure (López-Carmona *et al.*, 2013) and/or high-temperature conditions (Boger *et al.*, 2012; Korhonen *et al.*, 2012). In the simplified KFMASHTO system, for example, highly oxidized rocks develop garnet- and staurolite-bearing mineral assemblages at higher pressure when compared to the KFMASH system (White *et al.*, 2000). Phase equilibria modelling of high-temperature and high-pressure metapelites in the extended MnNCKFMASHTO system highlights the influence that Fe_2O_3 exerts on phase equilibria (Korhonen *et al.*, 2012; López-Carmona *et al.*, 2013), and on the development of different mineral assemblages in high-grade metapelites with similar bulk-rock composition (Boger *et al.*, 2012). With the exception of the study by White *et al.* (2000) on a theoretical model composition, "normal" greenschist-facies metasedimentary rocks of intermediate pressure with classical high-variance assemblage of chlorite-chloritoid-white mica have never been investigated. One reason might be the notion that chlorite, chloritoid and white mica do not accommodate high amounts of ferric iron, especially at upper greenschist-facies conditions (Hillier & Velde, 1991; Vidal *et al.*, 1999, 2005).

In this paper we present the results of a thermodynamic modelling involving different assumptions on the bulk Fe_2O_3 content, which allowed us to explore the influence of Fe_2O_3 on the development of greenschist-facies assemblages. We show that oxidized hematite-rich metasedimentary rocks from the Variscan basement of the Northern Apennines occurring in the Pisani Mountains (Italy; Fig. 5.1) are better modelled when considering an effective ferric iron content in whole rock that is significantly different from Fe_2O_3 values obtained by titration. The Variscan basement of the Northern Apennines preserves relics of a Carboniferous polyphase metamorphism (Molli *et al.,* 2002; Franceschelli *et al.*, 2004). Its involvement in the Oligocene-Miocene Alpine collision, which is well recorded by HP/LT assemblages in the metasedimentary rocks now overlying the Variscan basement, is not known in detail. The new *P-T* data of this paper suggests that both the Variscan basement and the overlying cover behaved as a coherent tectonic unit during the Oligocene-Miocene collision.

5.2 GEOLOGICAL FRAMEWORK

The Northern Apennines are a thrust and fold belt formed during continental collision between the Corsica-Sardinia (Europe) and Adria (Africa) microplates during the last 30 Ma (Vai & Martini, 2001). The tectonic units are (from top to bottom):

- Liguride Units: ophiolites derived from the Jurassic Ligurian-Piedmontese ocean;
- Tuscan Units: very low-grade metamorphic to non-metamorphic late Triassic-Tertiary sedimentary sequences derived from the Adria crust;
- Tuscan Metamorphic Units: metamorphic sequence belonging to the Adria microplate, consisting of a Variscan pre-Carboniferous basement and Triassic-Oligocene metasedimentary rocks.

In the Northern Apennines the Variscan basement occurs in small and scattered outcrops, which preserve metamorphic and structural Variscan relics and have a strong metamorphic and structural Alpine overprint. The Alpine metamorphism is especially well documented in the Verrucano Formation, a Triassic metasedimentary sequence outcropping from the Alpi Apuane to the Argentario Promontory (the so-called Tuscan metamorphic ridge) and in the Tuscan Archipelago. The Alpine metamorphism is characterized by a first compressional HP-LT phase followed by crustal extension (Franceschelli *et al.*, 1986; Kligfield *et al.*, 1986; Theye *et al.*, 1997; Giorgetti *et al.*, 1998; Jolivet *et al.*, 1998; Franceschelli & Memmi, 1999; Franceschelli *et al.*, 2004). In the first phase (27-20 Ma) SW-NE compressional tectonics produced the main deformation phase (D_1) during wedge thickening and burial of oceanic and continental crust to about 40-55 km depths, with attainment of *P-T* conditions typical of blueschist- to eclogitic-facies metamorphism. The metamorphic peak (6-8 kbar and 420-560 °C) occurred after D_1 and before the second deformational phase (D_2). The D_2 phase (14-12 Ma) is extensional and produced a rapid exhumation triggered by gravitational collapse. *P-T* constraints are 300-370 °C and 3-5 kbar.

5.2.1 The Pisani Mountains

In the Pisani Mountains (Fig. 5.1b), the Variscan basement of the Tuscan Metamorphic Units is known as the Buti Quartzites and Phyllites Formation (Schiaffino & Tongiorgi, 1962; Rau & Tongiorgi, 1966; 1974) and it is found in the cores of Alpine anticlines (Conti *et al.* 1991). It consists of albite-rich quartzites and chlorite-muscovite phyllites. The latter exhibits a banded structure due to the presence of hematite-rich layers. Two

different foliations are recognized: S_1 is the main schistosity delineated by phyllosilicates, partially obliterated by S_2, which is a crenulation schistosity parallel to the axial plane of Alpine anticlines (Rau & Tongiorgi, 1974).

A metasedimentary cover, comprising the metamorphic Triassic silicoclastic succession (Verrucano Formation; Fig. 5.1b) overlies the Variscan basement of the Pisani Mountains. Just a few *P-T* estimates are available from the Verrucano Formation in this area (Franceschelli *et al.*, 1986; Carosi *et al.*, 1993; Montomoli, 2002), while no *P-T* constraints are available for the Variscan basement. Franceschelli *et al.* (1986) proposed two different *P-T* scenarios for the Verrucano Formation, ~ 400 °C and ~ 4-5 kbar or ~ 450 °C and ~ 9-10 kbar. The first one was determined using the phengite geobarometer calibrated by Velde (1965, 1967); the second one, instead, employed the calibration by Massonne (1981). Carosi *et al.* (1993) applied the calcite-dolomite geothermometer to marbles belonging to the metasedimentary cover of the Variscan basement, and obtained maximum temperatures of 380±30 °C. They attributed this temperature to the first Alpine metamorphic-deformational phase. In a fluid inclusion study of Alpine veins in the Verrucano formation, Montomoli (2002) obtained *P-T* conditions of 410 °C and 5 kbar. Because of reequilibration textures in the fluid inclusions, this constraint has to be considered as a retrograde segment of the *P-T* path, rather than the peak conditions (Montomoli, 2002). Thus, during the first Alpine deformational phase the Verrucano Formation probably went to higher pressures than 5-6 kbar.
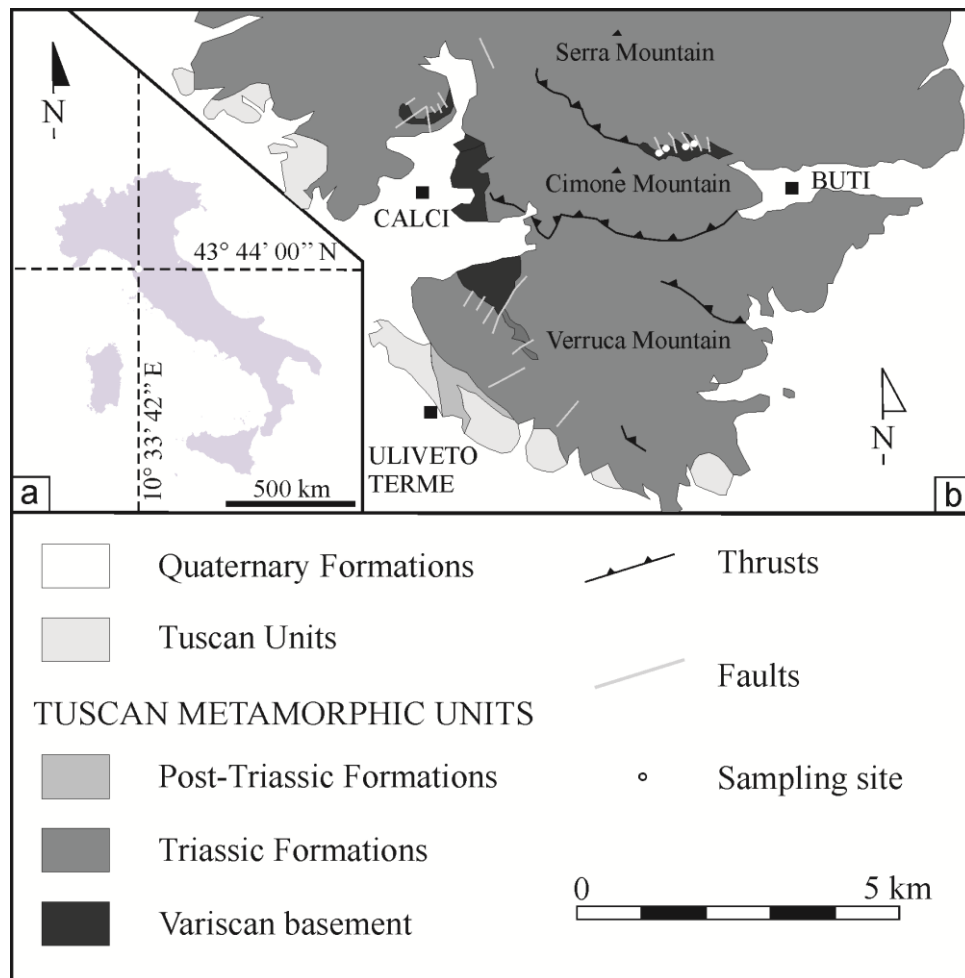
Figure 5.1 Regional geological framework of the study area. (a) Location of the Pisani Mountains in the Northern Apennines; (b) geological map of the Pisani Mountains with the sampling sites (modified from Leoni *et al.*, 2009).

5.3 PETROGRAPHY

The selected hematite-rich rocks, which are representative of the Buti Quartzites and Phyllites Formation, were sampled in the Pisani Mountains from small outcrops near the contact with the Verrucano Formation (Fig. 5.1b). Mineral abbreviations are after Siivola & Schmid (2007).

Five thin sections (MP1, MP2, MP3, MP4, and MP4b) of hematite-rich metasedimentary rocks have been studied in detail. The samples are fine-grained phyllites exhibiting a metamorphic banded structure in hand-specimen, constituted of alternating mm-wide hematite rich- and hematite poor-layers (Fig. 5.2a). In particular MP1 is a fine-grained phyllite with two schistosities, delineated by white mica and hematite. The mineral assemblage consists of white mica, chlorite, quartz and hematite. Rutile, tourmaline, zircon are accessory phases. MP2 and MP3 have the same mineral assemblage as MP1 and only show the first schistosity. MP4b and MP4 contain

chloritoid; mineral modes (vol.%) obtained by point-counting techniques are muscovite (37), quartz (37), chlorite (15), hematite (7) and chloritoid (3), while no biotite and feldspar have been found. Rutile, tourmaline, monazite, apatite, zircon and florencite occur as accessory phases.

A polyphase deformation evolution has been reconstructed for the chloritoid-bearing sample. A first deformation phase (D_1) caused the development of a spaced schistosity (S_1), the main foliation, along which muscovite, chlorite, quartz and hematite crystallized. A second deformation phase (D_2), less pervasive than D_1, caused the folding of S_1 and the formation of a muscovite-chlorite -hematite crenulation schistosity (S_2; Fig. 5.2b). Previous studies interpreted the S_2 as an Alpine structure (Rau & Tongiorgi, 1974; Borsi *et al.*, 1967). A post-kinematic event was responsible for the blastesis of randomly oriented chlorite, hematite, muscovite flakes and chloritoid porphyroblasts occurring as single crystals (up to 500 μm) and rosettes (Fig. 5.2c, d).

Chloritoid porphyroblasts are more abundant in white mica- and chlorite-rich layers rather than in quartz-rich layers. They are poikilitic and contain chlorite, rutile, hematite, quartz, zircon, and florencite inclusions. These inclusions define a helicitic structure (Fig. 5.2e), delineating an internal schistosity continuous and concordant with the external one. Hematite can be considered a major mineral due to its modal quantity (7 vol.%). It occurs as fine-grained aggregates in bands parallel to the main schistosity (Fig. 5.2f) and as single crystals. The sample MP4 was chosen for thermodynamic modelling, because of its chloritoid-bearing assemblage that is useful to retrieve the temperature using the chlorite-chloritoid geothermometer (see Geothermobarometry section).
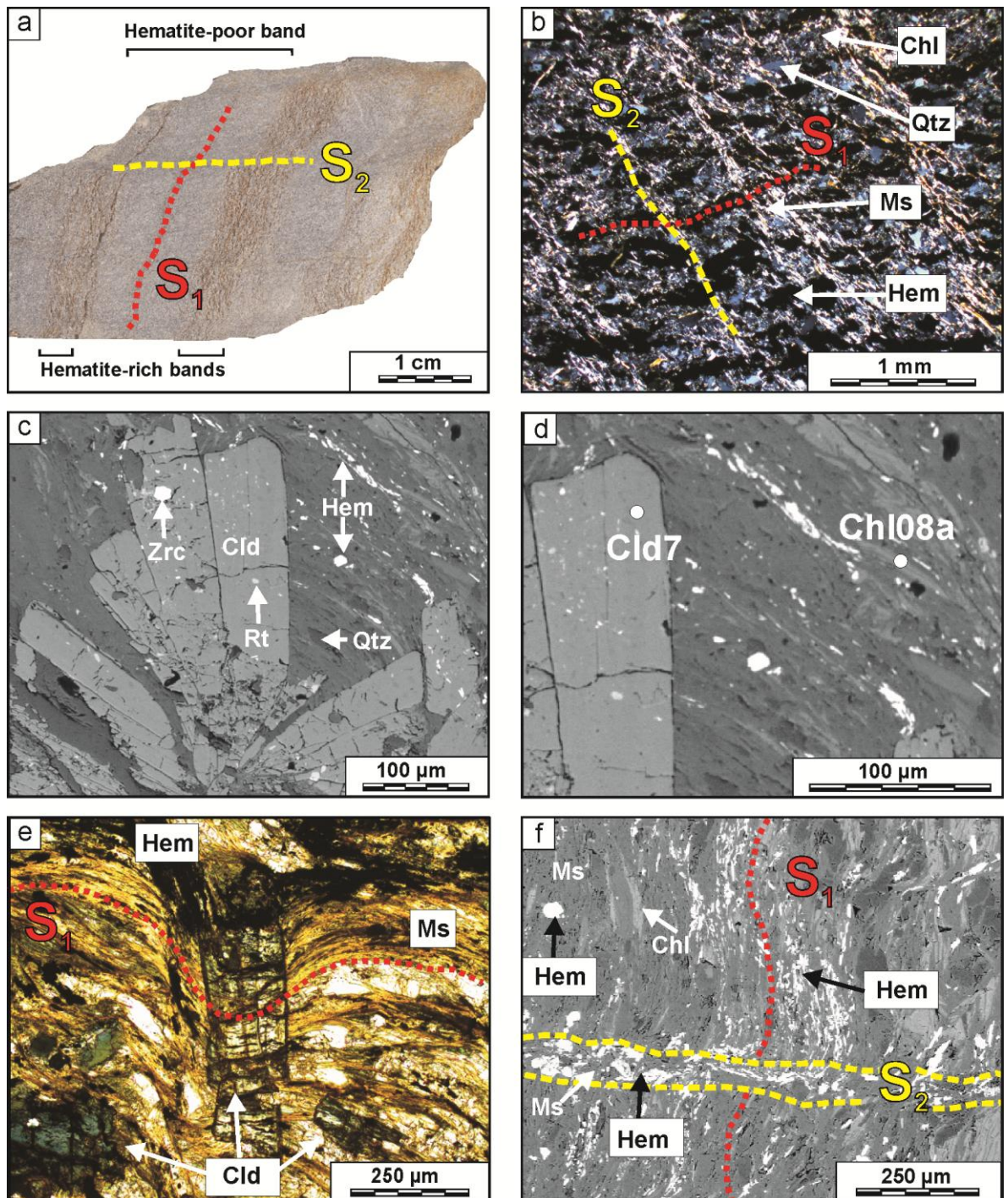
Figure 5.2 Main petrographic and microstructural features of the phyllites of the Buti Formation. (a) Rock slab; (b) crossed polars photomicrograph of the main schistosity (S_1) and the crenulation schistosity (S_2); (c) BSE image showing the chloritoid rosette with zircon and rutile inclusions; (d) enlargment of the previous BSE image showing the location of the analyses of a chlorite-chloritoid pair characterized by equilibrium features; (e) chloritoid porphyroblasts with helicitic structure (photomicrograph with plane polarized light); (f) BSE image showing the hematite bands parallel to S_2 and S_1 and the hematite blasts (Hem_3).

5.4 MINERAL AND WHOLE-ROCK CHEMISTRY

Chemical analyses of potassic white-mica, chlorite and chloritoid in MP4 were obtained with a WDS-CAMECA SX100 electron microprobe (EMP) at the Institut für Mineralogie und Kristallchemie (Universität Stuttgart). Analysis of Na, Mg, Al, Si, K, Ca, Ti, Mn, Fe in white-mica, chlorite and chloritoid was undertaken using an acceleration voltage of 15 kV and a current of 10 nA. For white mica analyses Ba was also measured. Counting times per element were 20 s at the peak and the background. Synthetic and natural minerals and pure oxides were used as standards. The beam diameter was defocused to 5 μm. The PaP correction method was applied. Point analyses were chosen taking into account the microstructural sites. Mineral structural formulae, including Fe^{3+} calculated through stoichiometric constraints, are reported in Tables 5.1, 5.2 and 5.3.

Potassic white-mica is characterised by Si contents ranging from 6.01 to 6.38 apfu (formula based on 22 oxygens; Table 5.1), with Fe^{2+} and Mg are between 0.14-0.36 apfu and 0.05-0.33 apfu. The calculated average Fe^{3+} is 0.03 apfu. Figure 3a, b shows the variation of Si *vs.* Fe^{2+} and Mg in muscovite from different microstructural sites.

Chlorite is invariably a ripidolite characterized by Si content ranging from 2.50 to 2.73 apfu (Fig. 5.3c). The XFe^{2+} ratio ($Fe^{2+}/(Fe^{2+}+Mg)$) shows limited variations (XFe^{2+} = 0.52 - 0.57). On the basis of stoichiometry constraints, no Fe^{3+} was calculated (Table 5.2).

Chloritoid shows only slight chemical variations (Table 5.3). XFe^{2+} is 0.85-0.88, Fe^{3+} and XFe^{3+} are low and 0.04-0.13 apfu and 0.04-0.12 respectively. Mn is 0.01-0.02 apfu.

Figure 5.3 Compositional variations in muscovite and chlorite: Si content *vs.* Fe^{2+} (a); Si content *vs.* Mg (b) in muscovite; (c) Si content *vs.* Fe^{2+} in chlorite.
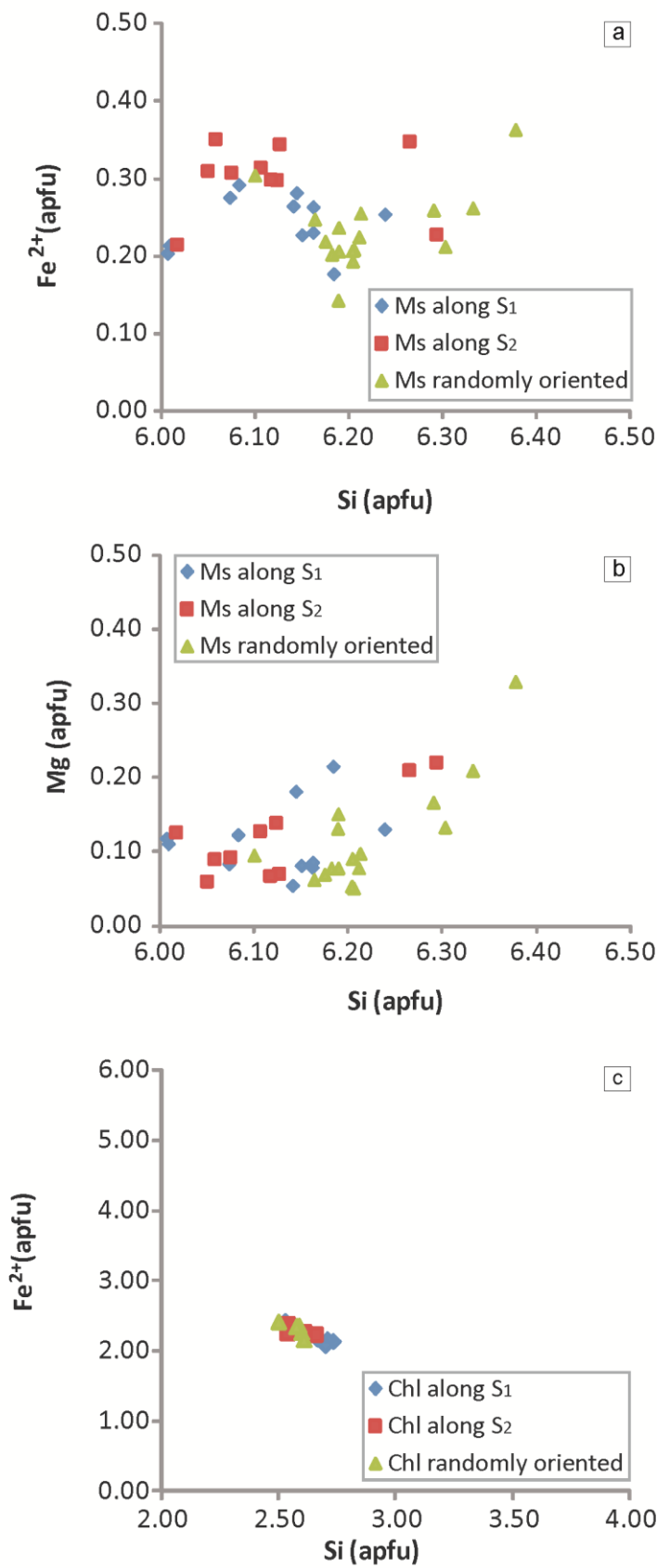
Table 5.1 Microprobe analyses of potassic white mica. *Footnote: s*tructural formulae calculated with CalcMin program (Brandelik, 2008) on the basis of 22 O, assuming 42-(Ca+Ba) valencies and 4 H. Fe^{3+} has been stoichiometric-estimated considering Fe^{3+} = 42–sum of the valencies (Si, Ti, Cr, Al, Mn, Mg, Fe)-Ba- Ca.

K-white mica											
Generation	Kwm_1							Kwm_2			
Analyses	Ms14	Ms39	Ms41	Ms57	Ms58	Ms64		Ms31	Ms33	Ms34	Ms44	Ms45
SiO_2	45.63	47.36	45.90	46.31	46.49	44.66		45.61	45.15	45.69	44.97	44.18
TiO_2	0.05	0.46	0.55	1.81	0.03	0.08		0.08	0.11	0.07	0.15	0.15
Al_2O_3	35.18	35.32	34.38	35.10	35.69	34.12		35.02	34.14	35.42	34.00	34.47
FeO	2.02	1.63	2.52	2.52	2.08	1.81		3.08	2.64	2.68	2.78	2.72
Fe_2O_3	0.00	0.00	0.00	0.00	0.00	3.47		0.00	0.61	0.00	0.93	0.94
MnO	0.01	0.00	0.02	0.00	0.00	0.04		0.04	0.08	0.05	0.02	0.05
MgO	0.41	1.11	0.91	0.43	0.40	0.59		0.36	0.69	0.34	0.64	0.30
CaO	0.09	0.07	0.04	0.06	0.05	0.06		0.04	0.04	0.02	0.13	0.04
Na_2O	1.11	1.41	1.29	1.01	1.62	1.01		1.04	0.86	0.87	1.08	1.16
K_2O	8.54	8.53	8.41	8.95	8.79	8.63		9.43	9.46	9.70	9.04	9.24
BaO	0.08	0.40	0.36	0.19	0.12	0.09		0.17	0.16	0.15	0.13	0.15
Total	93.12	96.27	94.38	96.38	95.26	94.55		94.85	93.94	94.98	93.85	93.39
Si	6.15	6.18	6.14	6.07	6.16	6.01		6.13	6.12	6.12	6.11	6.05
Al^{IV}	1.85	1.82	1.86	1.93	1.84	1.99		1.87	1.88	1.88	1.89	1.95
Al^{VI}	3.74	3.62	3.57	3.50	3.74	3.41		3.67	3.58	3.70	3.54	3.61
Ti	0.01	0.04	0.06	0.18	0.00	0.01		0.01	0.01	0.01	0.02	0.01
Fe^{2+}	0.23	0.18	0.28	0.28	0.23	0.20		0.35	0.30	0.30	0.32	0.31
Fe^{3+}	0.00	0.00	0.00	0.00	0.00	0.35		0.00	0.06	0.00	0.09	0.10
Mn	0.00	0.00	0.00	0.00	0.00	0.00		0.00	0.01	0.01	0.00	0.01
Mg	0.08	0.22	0.18	0.08	0.08	0.12		0.07	0.14	0.07	0.13	0.06
Ca	0.01	0.01	0.01	0.01	0.01	0.01		0.01	0.01	0.00	0.02	0.01
Ba	0.00	0.02	0.02	0.01	0.01	0.00		0.01	0.01	0.01	0.01	0.01
Na	0.29	0.36	0.33	0.26	0.41	0.26		0.27	0.23	0.23	0.28	0.31
K	1.47	1.42	1.44	1.50	1.49	1.48		1.62	1.64	1.66	1.57	1.61

K-white mica											
Generation	Kwm_3										
Point analyses	Ms03	Ms04	Ms07	Ms09	Ms20	Ms21	Ms25	Ms28	Ms29	Ms92	Ms93
SiO_2	46.22	46.12	48.74	47.46	47.37	47.47	47.46	48.12	47.32	46.65	46.43
TiO_2	0.74	0.06	0.03	0.05	0.04	0.28	0.13	0.06	0.24	0.05	0.06
Al_2O_3	34.65	34.71	36.98	36.25	35.43	31.56	34.01	36.52	33.04	35.52	35.12
FeO	1.28	2.00	1.96	1.86	2.33	3.24	2.34	1.92	2.34	1.86	1.73
Fe_2O_3	0.00	0.00	0.00	0.00	0.00	0.00	0.00	0.00	0.00	0.00	0.00
MnO	0.00	0.02	0.03	0.02	0.02	0.00	0.00	0.00	0.00	0.00	0.00
MgO	0.66	0.39	0.27	0.40	0.50	1.65	0.84	0.28	1.05	0.40	0.46
CaO	0.00	0.08	0.07	0.08	0.08	0.01	0.04	0.04	0.06	0.05	0.02
Na_2O	0.60	1.05	0.90	1.87	0.71	0.38	0.96	1.68	0.48	0.89	0.93
K_2O	9.91	8.84	8.97	6.95	8.84	10.49	9.02	7.75	9.88	9.03	8.89
BaO	0.28	0.12	0.12	0.07	0.10	0.12	0.16	0.11	0.16	0.21	0.13
Total	94.34	93.38	98.06	95.00	95.41	95.19	94.96	96.47	94.57	94.66	93.79
Si	6.19	6.21	6.20	6.18	6.21	6.38	6.29	6.20	6.33	6.19	6.20
Al^{IV}	1.81	1.79	1.80	1.82	1.79	1.62	1.71	1.80	1.67	1.81	1.80
Al^{VI}	3.65	3.72	3.75	3.74	3.69	3.37	3.60	3.75	3.54	3.74	3.73
Ti	0.07	0.01	0.00	0.00	0.00	0.03	0.01	0.01	0.02	0.00	0.01
Fe^{2+}	0.14	0.23	0.21	0.20	0.26	0.36	0.26	0.21	0.26	0.21	0.19
Fe^{3+}	0.00	0.00	0.00	0.00	0.00	0.00	0.00	0.00	0.00	0.00	0.00
Mn	0.00	0.00	0.00	0.00	0.00	0.00	0.00	0.00	0.00	0.00	0.00
Mg	0.13	0.08	0.05	0.08	0.10	0.33	0.17	0.05	0.21	0.08	0.09
Ca	0.00	0.01	0.01	0.01	0.01	0.00	0.01	0.00	0.01	0.01	0.00
Ba	0.01	0.01	0.01	0.00	0.00	0.01	0.01	0.01	0.01	0.01	0.01
Na	0.16	0.27	0.22	0.47	0.18	0.10	0.25	0.42	0.12	0.23	0.24
K	1.69	1.52	1.46	1.15	1.48	1.80	1.53	1.27	1.69	1.53	1.52

Table 5.2 Microprobe analyses of chlorite.

Footnote: structural formulae calculated with AX program of T. Holland, on the basis of 14 O. Chlorite is assumed as completely hydrated. Stoichiometric-estimated Fe^{3+}, assuming cation sum equal to 10 for 14 oxygen, is negligible.

Chlorite											
Microstructure	Chl along S_1						Chl along S_2				
Analyses	Chl19	Chl24	Chl31	Chl39	Chl47	Chl48	Chl32	Chl36	Chl37	Chl43	Chl44
SiO_2	23.61	27.05	26.37	24.59	26.15	25.30	25.92	23.06	23.88	24.18	23.90
TiO_2	0.01	0.07	0.04	0.08	0.03	0.01	0.07	0.13	0.21	0.01	0.02
Al_2O_3	23.80	26.27	25.81	24.56	25.90	24.93	25.48	23.46	23.50	24.10	24.41
FeO	27.14	25.36	25.27	25.90	24.13	24.72	26.16	25.92	24.89	26.39	25.48
MnO	0.16	0.10	0.09	0.13	0.11	0.07	0.13	0.09	0.15	0.08	0.15
MgO	12.46	10.72	10.65	12.12	11.04	11.23	11.61	11.77	11.48	12.69	13.00
Total	87.18	89.57	88.23	87.38	87.36	86.26	89.37	84.43	84.11	87.45	86.96
Si	2.53	2.73	2.71	2.59	2.70	2.67	2.66	2.54	2.61	2.56	2.54
Ti	n.c.	0.01	n.c.	0.01	n.c.	n.c.	0.01	0.01	0.02	n.c.	n.c.
Al	3.00	3.13	3.13	3.05	3.15	3.10	3.08	3.04	3.02	3.01	3.06
Fe^{2+}	2.43	2.14	2.17	2.28	2.08	2.18	2.24	2.39	2.27	2.34	2.26
Mn	0.02	0.01	0.01	0.01	0.01	0.01	0.01	0.01	0.01	0.01	0.01
Mg	1.99	1.61	1.63	1.90	1.70	1.76	1.77	1.93	1.87	2.00	2.06
XFe^{2+}	0.55	0.57	0.57	0.55	0.55	0.55	0.56	0.55	0.55	0.54	0.52

Microstructure	Chl randomly oriented					
Analyses	Chl03	Chl04	Chl08a	Chl13	Chl16	Chl18
SiO_2	23.04	24.28	24.18	24.46	23.59	24.03
TiO_2	0.01	0.05	0.03	0.05	n.d.	0.04
Al_2O_3	23.41	23.70	24.19	24.29	23.17	23.48
FeO	26.65	26.52	26.44	25.54	23.44	26.20
MnO	0.09	0.12	0.10	0.04	0.12	0.12
MgO	12.76	12.44	11.88	12.28	12.57	12.61
Total	85.96	87.11	86.82	86.66	82.89	86.48
Si	2.50	2.59	2.58	2.60	2.61	2.58
Ti	n.c.	n.c.	n.c.	n.c.	n.c.	n.c.
Al	3.00	2.98	3.04	3.04	3.02	2.97
Fe^{2+}	2.42	2.36	2.36	2.27	2.17	2.35
Mn	0.01	0.01	0.01	n.c.	0.01	0.01
Mg	2.06	1.98	1.89	1.94	2.07	2.01
XFe^{2+}	0.54	0.54	0.56	0.54	0.51	0.54

Table 5.3 Microprobe analyses of chloritoid.
*Footnote: s*tructural formulae calculated with CalcMin program (Brandelik, 2009) on the basis of 6 O. Chloritoid is assumed as completely hydrated, with 4 H. Fe^{3+} has been stoichiometric-estimated with the following assumption: $Fe^{3+}=(2-Ti-0.5*Al)/0.5$.

Chloritoid									
Analyses	Cld06	Cld07	Cld08	Cld12	Cld14	Cld17	Cld18	Cld22	Cld25
SiO_2	23.23	23.55	22.75	23.24	23.50	23.38	22.33	23.02	23.41
TiO_2	0.03	0.05	0.06	n.d.	0.01	n.d.	0.13	0.02	n.d.
Al_2O_3	39.72	40.66	38.40	39.90	40.15	39.43	37.88	39.72	38.60
Cr_2O_3	0.02	0.01	0.03	0.02	0.02	0.01	0.06	0.02	0.02
FeOtot	25.72	26.02	25.92	27.82	25.47	25.34	27.82	25.47	25.34
MnO	0.39	0.45	0.41	0.42	0.42	0.46	0.38	0.43	0.40
MgO	2.21	2.04	2.41	2.07	2.36	2.10	1.89	2.24	2.21
Total	91.31	92.77	89.96	93.47	91.93	90.71	90.49	90.91	89.97
Si	0.98	0.98	0.98	0.97	0.98	0.99	0.97	0.98	1.00
Ti	n.c.	n.c.	n.c.	n.c.	n.c.	n.c.	n.c.	n.c.	n.c.
Al	1.98	1.99	1.95	1.96	1.98	1.97	1.94	1.99	1.95
Cr	n.c.	n.c.	n.c.	n.c.	n.c.	n.c.	n.c.	n.c.	n.c.
Fe^{3+}	0.06	0.05	0.09	0.10	0.05	0.04	0.13	0.06	0.04
Fe^{2+}	0.85	0.86	0.85	0.87	0.84	0.86	0.88	0.85	0.87
Mn	0.01	0.02	0.01	0.01	0.02	0.02	0.01	0.02	0.01
Mg	0.14	0.13	0.15	0.13	0.15	0.13	0.12	0.14	0.14
XFe^{2+}	0.86	0.87	0.85	0.87	0.85	0.87	0.88	0.86	0.86

Bulk-rock chemistry (Table 5.4) of the hematite-rich phyllite MP4 was obtained through WD-XRF analysis on pressed powder pellets, using a Philips PW1480 spectrometer at the Department of Biological, Geological and Environmental Sciences of Bologna University. Loss on ignition (L.O.I.) was measured with standard gravimetric procedures, after heating the powder at 950 °C for about 12 h.

The FeO content was measured by titration at the Service d'Analyse des Roches et des Mineraux of Nancy. The procedure involves an attack with HF + H_2SO_4 in a teflon beaker on a hot plate and a direct volumetric titration by $K_2Cr_2O_7$ after cooling, and resulted 0.93 ± 0.05 wt. %. The Fe_2O_3 amount content of the rock is 7.00 wt. %.

Whole-rock composition, recalculated excluding L.O.I., was used to classify the protolith, assuming isochemical metamorphism. Normalization diagram of the bulk rock chemistry to PAAS (Post-Archean Australian Shale; Taylor & McLennan, 1985) and to UCC (Upper Continental Crust; McLennan, 2001) indicates depletion in CaO and Na_2O for the MP4 protolith, in agreement with the lack of modal plagioclase and garnet. In

the Fe_2O_3/K_2O *vs.* SiO_2/Al_2O_3 (Herron, 1988) diagram the selected sample plots in the wacke field.

Table 5.4 Whole-rock composition of the hematite-rich metapelite MP4.
Footnote: (a) bulk rock composition of MP4 by XRF; (b) bulk rock composition of MP4 by XRF with FeO by titration and Fe_2O_3 calculated as $[Fe_2O_3^{tot}-(FeO*1.11)]$; (c) compositions used for thermodynamic modelling. $XFe_2O_3 = Fe_2O_3/Fe_2O_3^{tot}$

	XRF (a)	XRF and titration (b)	Thermodynamic modelling (c)		
			MnKNFMASHT system with XRF bulk composition (FeOtot = FeO) (Fig. 5.4)	MnKNFMASHTO system with FeO measured by titration (Fig. 5.5)	MnKNFMASHTO system with Fe_2O_3 estimated by thermodynamic modelling (Fig. 5.8)
	wt. %	wt. %	wt. %	wt. %	wt. %
SiO_2	74.87	74.96	76.80	76.25	76.39
TiO_2	0.42	0.42	0.43	0.43	0.43
Al_2O_3	11.59	11.60	11.89	11.80	11.82
Fe_2O_3	8.03	7.00	-	7.12	5.31
FeO	-	0.93	7.41	0.95	2.59
MnO	0.05	0.05	0.05	0.05	0.05
MgO	0.69	0.69	0.71	0.70	0.70
CaO	0.12	0.12	-	-	-
Na_2O	0.33	0.33	0.34	0.34	0.34
K_2O	2.32	2.32	2.38	2.36	2.36
P_2O_5	0.09	0.09	-	-	-
L.O.I.	1.48	1.48	in excess	in excess	in excess
Total	99.99	100.00	100.01	100.00	99.99
XFe_2O_3		0.87		0.87	0.65

5.5 GEOTHERMOBAROMETRY

5.5.1 Chlorite-chloritoid thermometry

The chlorite-chloritoid Fe/Mg exchange thermometer of Vidal *et al.* (1999) was used to determine the temperature of the post-kinematic event recognized in MP4. This thermometer is suitable because it was empirically calibrated for greenschist- to blueschist-facies conditions (300-550 °C) and pressure does not have to be known. Only pairs of point analyses of coexisting minerals with no reaction and/or disequilibrium structures such as chloritoid overgrown by chlorite or with MnO > 1 wt.% or $(Cr_2O_3+MnO+CaO+Na_2O+K_2O)$ > 2 wt. % were used with this thermometer.

From an initial dataset comprising 30 chlorite analysis and 20 chloritoid analyses, 8 chlorite-chloritoid pairs have been selected because they fully satisfied the equilibrium (Fig. 5.2d) and compositional criteria. The derived temperature is 475 ± 15 °C.

5.5.2 Phase diagram calculations

Thermodynamic modelling (Perple_X, Connolly 1990; Connolly & Petrini, 2002) was performed to reproduce measured mineral compositions and the observed assemblage, represented by randomly oriented muscovite and chlorite ($X\text{Fe}^{2+} = 0.54$), chloritoid ($X\text{Fe}^{2+} = 0.86$), quartz, hematite and rutile. The thermodynamic dataset of Holland & Powell (1998, with the 2002 upgrade) and the compensated Redlich Kwong (CORK) fluid equation of state by Holland & Powell (1991, 1998) were used. SiO_2 and H_2O are in excess. Input compositions are expressed in wt.%. Solid solution models in the MnKNFMASHT system pseudosection with $FeO_{tot} = FeO$ are white-mica (Holland & Powell, 1998), chloritoid (White *et al.*, 2000), garnet (Holland & Powell, 1998), biotite (Tajcmanová *et al.*, 2009), chlorite (Holland *et al.*, 1998), carpholite (Massonne & Willner, 2008), feldspar (Fuhrman & Lindsley, 1988) and ilmenite (ideal ilmenite-geikielite-pyrophanite solid solution; http://www.perplex.ethz.ch/PerpleX_solution_model_glossary.html). In the MnKNFMASHTO system pseudosections the available solution models involving Fe^{3+} end-members for white-mica, chloritoid, carpholite (Smye *et al.*, 2010), garnet (White *et al.*, 2005), biotite (Tajcmanová *et al.*, 2009), hematite and magnetite (Andersen & Lindsley, 1988) were used. There is no solid solution model with Fe^{3+} for chlorite, so the solid solution model by Holland *et al.* (1998) was used. The feldspar model by Fuhrman & Lindsley (1988) was also used. Pure phases are rutile, paragonite kyanite, sillimanite, pyrophyllite and stilpnomelane.

P-T pseudosection in the system MnKNFMASHT with $FeO_{tot} = FeO$

Neglecting ferric iron in the input composition allows us to investigate if the choice of not considering Fe_2O_3 in an obviously Fe_2O_3-bearing rock can reproduce, reasonably enough, the observed mineral assemblage and compositions. The whole-rock XRF composition was assumed to be the equilibrium volume, recalculated excluding Ca and P_2O_5, which are contained in apatite, and L.O.I. According to this procedure $FeO_{tot} = FeO = 7.41$ wt. %. FeO_{tot} was calculated from the conversion of XRF Fe_2O_3. The considered *P-T* range is 4-15 kbar and 300-550 °C respectively. Muscovite and chloritoid are stable in each field of the pseudosection (Fig. 5.4). Garnet is stable above 500 °C and 6 kbar. Biotite is stable at temperatures above 500 °C and pressures below 8 kbar. Carpholite appears at 15 kbar and 300 °C. Rutile breaks down above 425-500 °C, replaced by ilmenite, and appears again at 525 °C and pressures higher than 13 kbar.

In this *P-T* range, the calculated $X\text{Fe}^{2+}$ for chlorite and chloritoid are 0.57-0.85 and 0.84-0.98, respectively. The observed $X\text{Fe}^{2+}$ chlorite composition ($X\text{Fe}^{2+} = 0.54$) is close to the lower end of the calculated range ($X\text{Fe}^{2+} = 0.57$-0.85). The observed chloritoid composition ($X\text{Fe}^{2+}=0.86$) plots in a garnet-bearing field, in disagreement with the observed mineral assemblage. As a consequence the input bulk composition without Fe_2O_3 is inappropriate to reproduce the observed mineral compositions.

Figure 5.4 *P-T* pseudosection with $\text{FeO}_{\text{tot}} = \text{FeO}$

***P-T* pseudosection in the system MnKNFMASHTO with FeO estimated by titration**

A *P-T* pseudosection was performed using the XRF bulk rock composition and FeO and Fe_2O_3 determined by titration (FeO = 0.93 wt. %; Fe_2O_3 = 7.00 wt. %). The pressure and temperature ranges are as in the previous modelling.

Chloritoid is stable in the whole *P-T* range, except at high pressures and low temperatures and low pressures and high temperatures (Fig. 5.5). The garnet stability field occurs below 7 kbar and above 525 °C. Carpholite-out curve is at 350-500 °C, depending on pressure. Hematite and rutile are stable over the entire *P-T* grid, accompanied by magnetite above 500 °C and below 8 kbar.

Calculated chlorite $X\mathrm{Fe}^{2+}$ isopleths are between 0.15 and 0.49, while measured chlorite $X\mathrm{Fe}^{2+}$ = 0.54 is not reproduced. Besides this discrepancy, measured $X\mathrm{Fe}^{2+}$ isopleths of chloritoid plot in fields that include carpholite, which is in disagreement with the observed mineral assemblage.
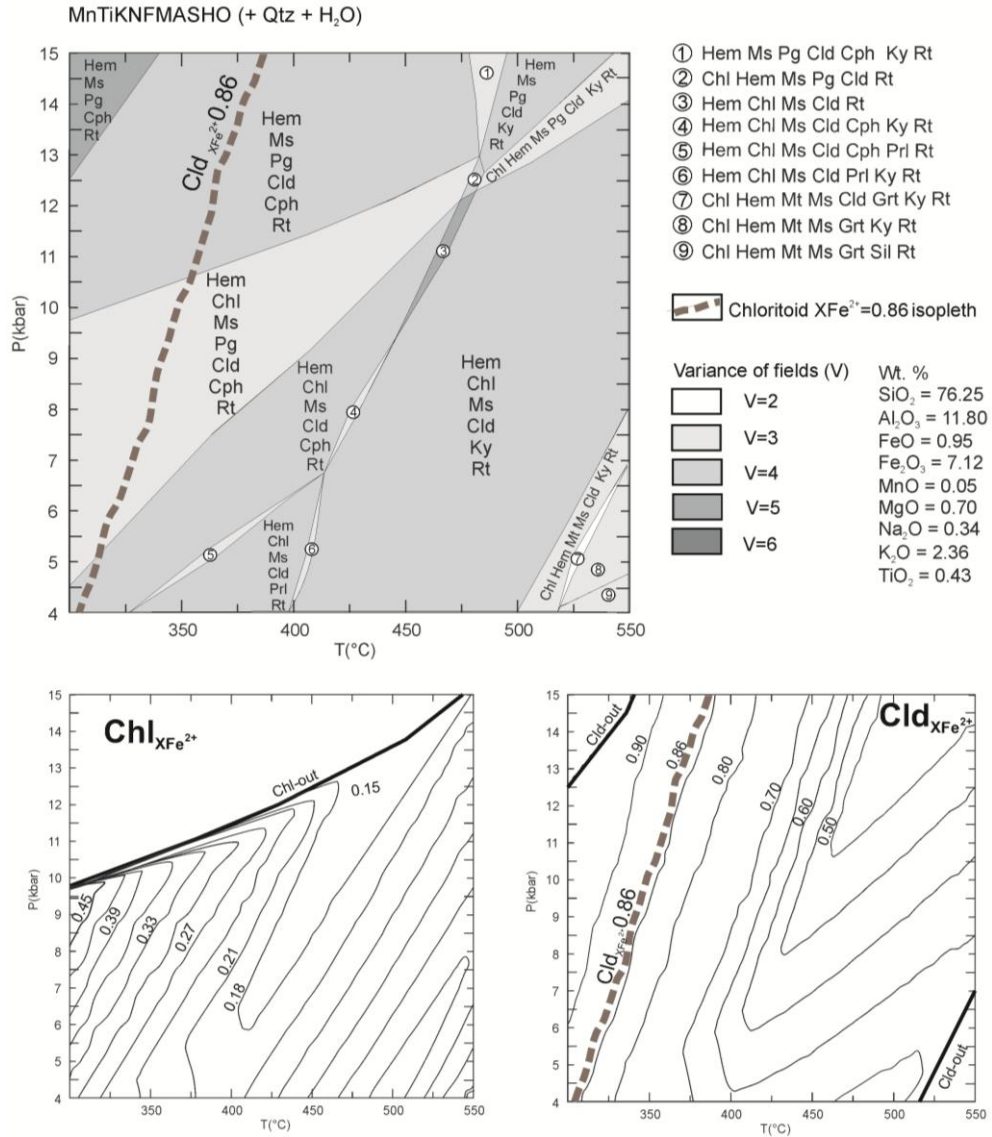
Figure 5.5
P-T pseudosection with FeO determined by titration.

P-X pseudosection in the system MnKNFMASHTO at fixed temperature

In order to calculate the effective Fe_2O_3 content during metamorphism a $P\text{-}XFe_2O_3$ ($XFe_2O_3 = Fe_2O_3/Fe_2O_3{}^{tot}$) pseudosection was performed at a fixed T = 475 °C (Fig. 5.6), derived from the chloritoid-chlorite geothermometer (Vidal *et al.*, 1999). This approach is the same as used by Boger *et al.* (2012) and López-Carmona *et al.* (2013). Stability fields of minerals are reported in Fig. 5.7. Chlorite breaks down at 12 kbar and $XFe_2O_3 = 0.8$, substituted by carpholite. Biotite is stable only at pressures below 3 kbar and in weakly oxidized rocks ($XFe_2O_3 < 0.4$). Chloritoid is present over the full range at $XFe_2O_3 < 0.95$, and is then replaced by garnet, which is stable in extremely oxidized rocks ($XFe_2O_3 > 0.95$).
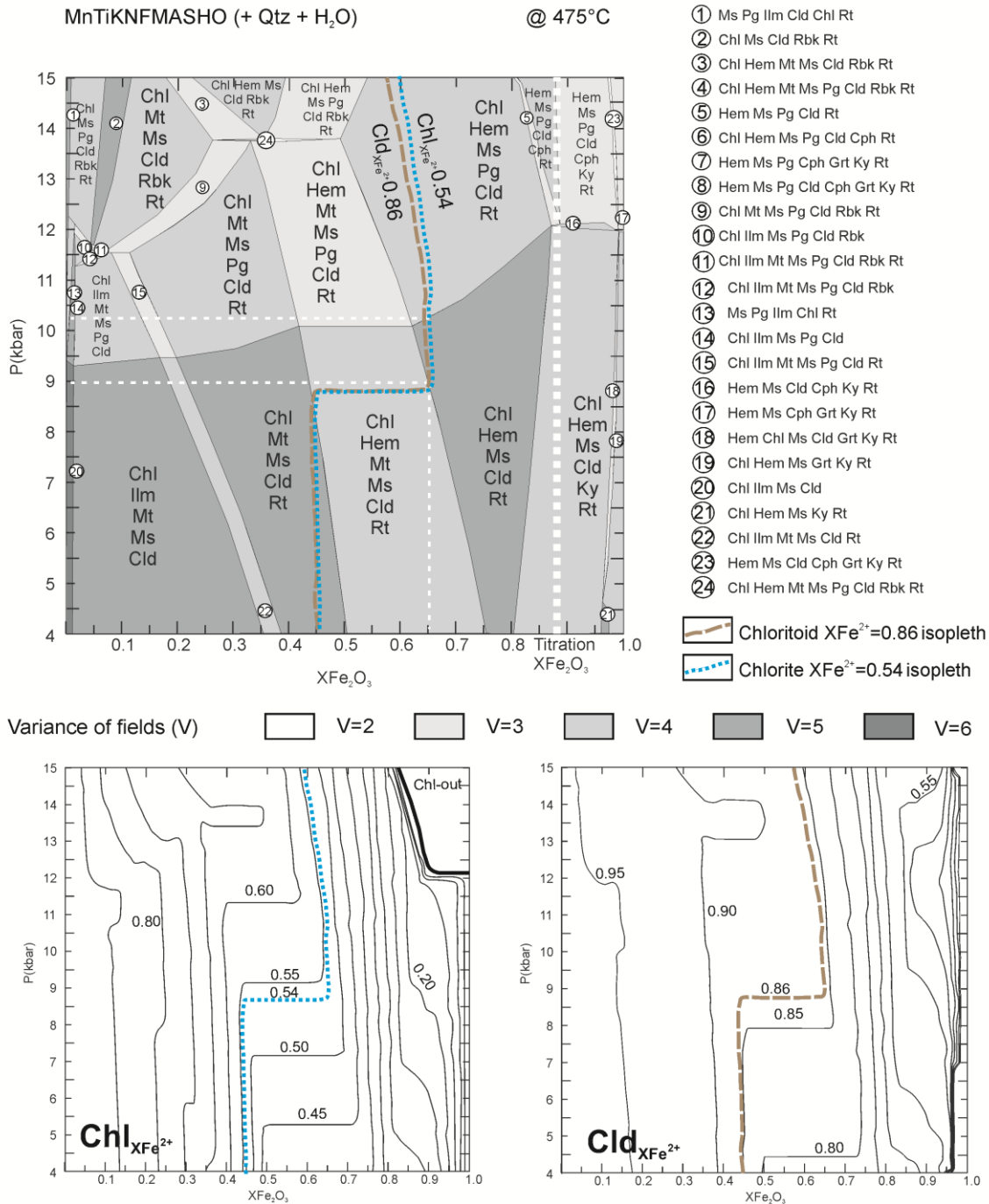
Figure 5.6 *P-X* pseudosection at 475°C.

Ilmenite is stable below 12 kbar and $X\mathrm{Fe_2O_3} < 0.35$. Hematite appears at $X\mathrm{Fe_2O_3} > 0.3$ at pressures of 15 kbar and at $X\mathrm{Fe_2O_3} > 0.5$ in the lower pressure region. Rutile is stable at 10 kbar at $X\mathrm{Fe_2O_3} = 0$, and the pressure of its appearance decreases with increasing $X\mathrm{Fe_2O_3}$. Magnetite is stable in the range of $X\mathrm{Fe_2O_3} = 0.02\text{-}0.75$.

The $P\text{-}X\mathrm{Fe_2O_3}$ field corresponding to the observed mineral assemblage (muscovite + chlorite + chloritoid + quartz + hematite + rutile) is in the range $X\mathrm{Fe_2O_3} = 0.60\text{-}0.85$ and

3-12 kbar, delimitated above 10-12 kbar by paragonite-bearing assemblages, by the magnetite in-curve at $X\mathrm{Fe_2O_3} = 0.60\text{-}0.75$, and by the crystallization of kyanite at $X\mathrm{Fe_2O_3} > 0.8$. Isopleths related to $X\mathrm{Fe}^{2+}$ in chlorite and $X\mathrm{Fe}^{2+}$ in chloritoid intersect in this field at P = 9-10 kbar and $X\mathrm{Fe_2O_3} = 0.65$, equal to FeO = 2.6 wt.% and $\mathrm{Fe_2O_3} = 5.3$ wt.% (effective $\mathrm{Fe_2O_3}$ content).

P-T pseudosection in the system MnKNFMASHTO with the effective $\mathrm{Fe_2O_3}$ content in rock

Considering the bulk $X\mathrm{Fe_2O_3}$ determined from the previously *P-X* pseudosection ($X\mathrm{Fe_2O_3} = 0.65$), a *P-T* pseudosection in the system MnKNFMASHTO was calculated (Fig. 5.8). The field corresponding to the observed mineral assemblage is bounded to high pressure by the paragonite-in, and to high temperature by the magnetite-in curve. The observed mineral assemblage (muscovite + chlorite + chloritoid + quartz + hematite + rutile) and $X\mathrm{Fe}^{2+}$ values ($X\mathrm{Fe}^{2+} = 0.54$ for chlorite and $X\mathrm{Fe}^{2+} = 0.86$ for chloritoid) are successfully reproduced at 475 °C and 9-10 kbar.
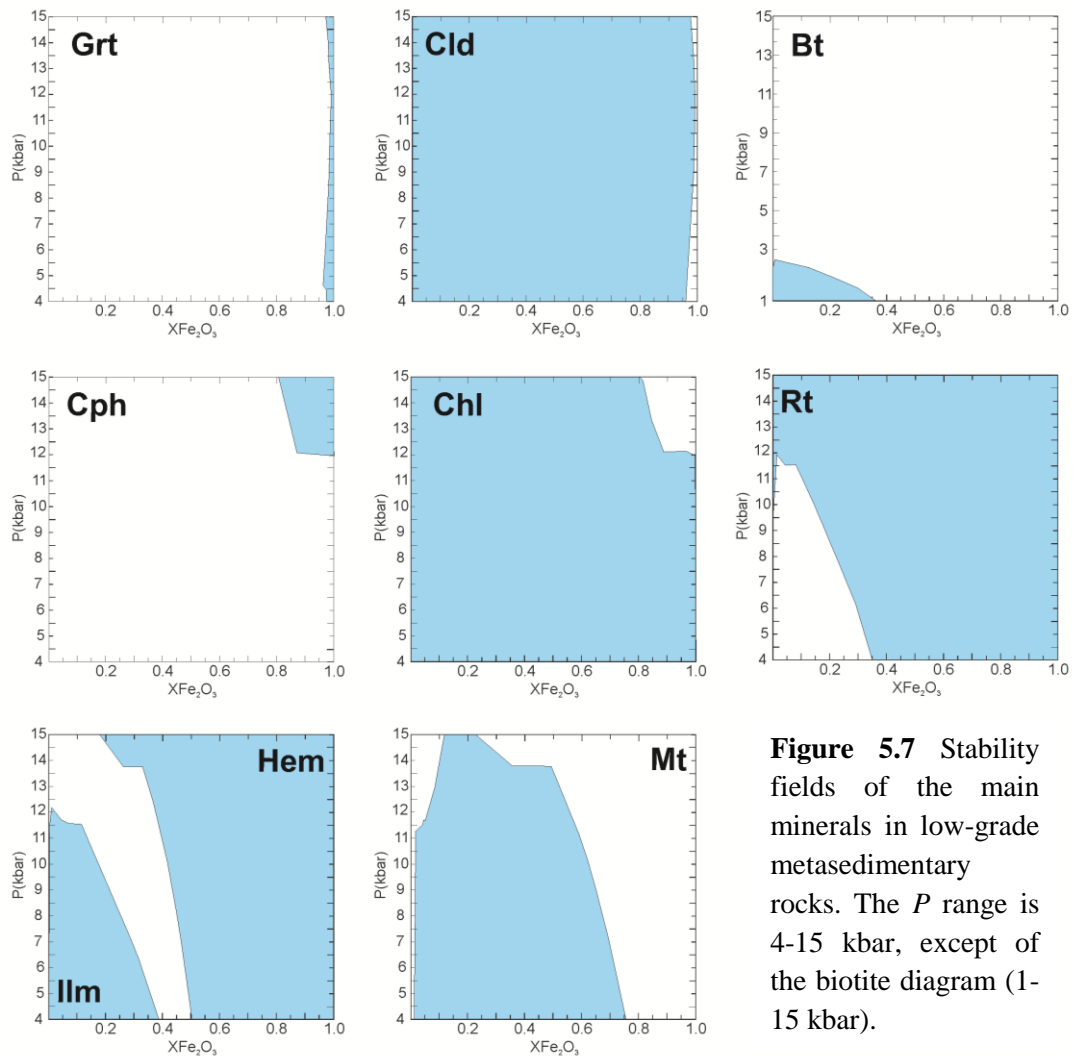
Figure 5.7 Stability fields of the main minerals in low-grade metasedimentary rocks. The *P* range is 4-15 kbar, except of the biotite diagram (1-15 kbar).
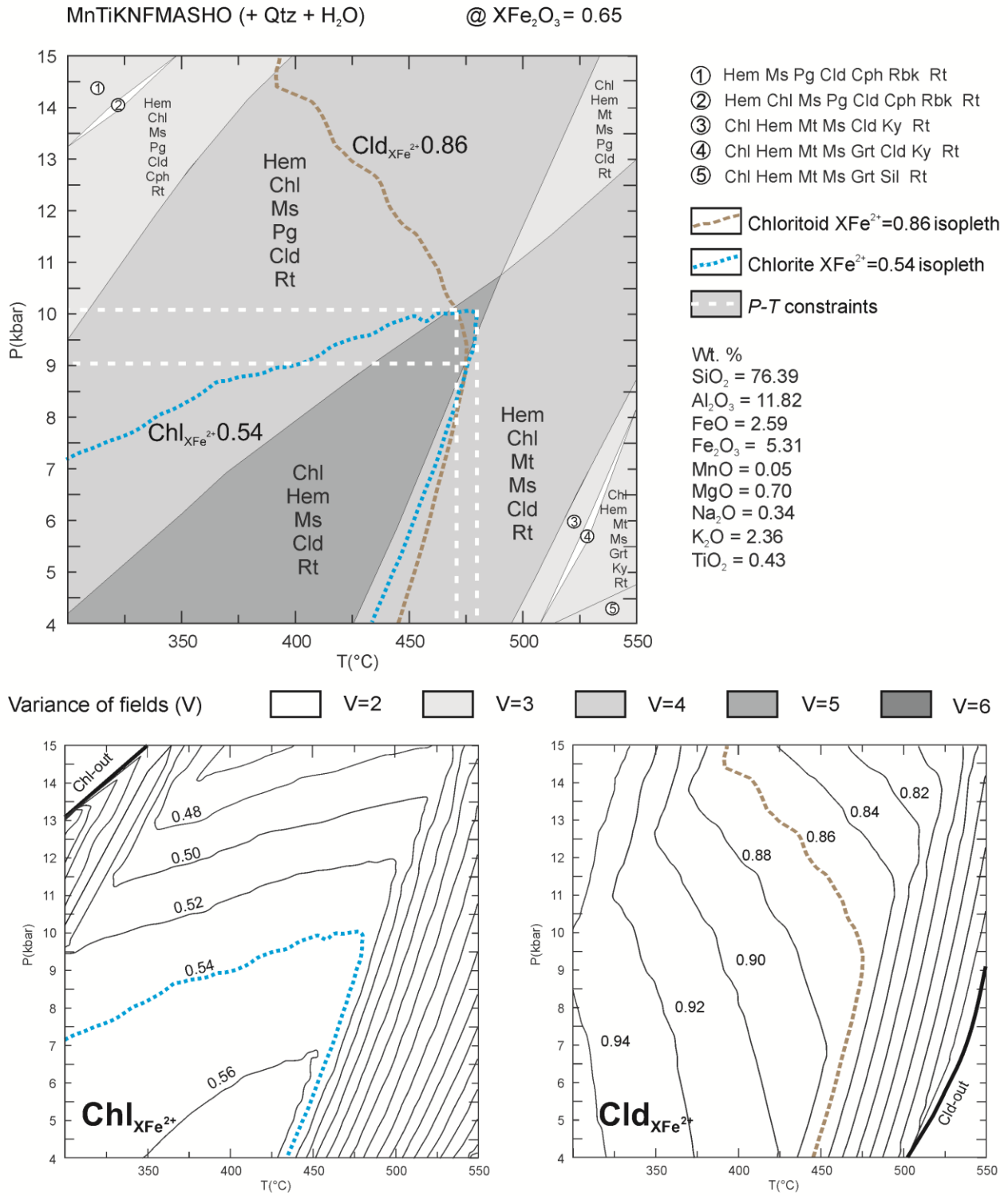
Figure 5.8

P-T pseudosection with the bulk rock chemistry calculated in the previous *P-X* pseudosection.

5.6 DISCUSSION

Calculations of P- or T-XFe$_2$O$_3$ diagrams are good means to evaluate the influence of effective Fe$_2$O$_3$ contents in bulk-rock compositions, thus avoiding an overestimation of the ferric iron due to low-temperature processes and/or sample preparation (Boger *et al.*, 2012, López-Carmona *et al.*, 2013). This approach can provide useful results, but the uncertainties involved in thermodynamic modelling must not be undervalued (Powell & Holland, 2008): the wrong choice of the equilibration volume, the inappropriate assessment of the chemical system, the uncertainties related to the activity–composition (a–x) models are some factors that can introduce significant mistakes in the P-T-XFe$_2$O$_3$ constraints.

Another approach to calculate effective Fe$_2$O$_3$ contents in bulk-rock compositions is to combine phase proportions with measured phase compositions. This method overcomes the problem of oxidation during sample preparation. However, it requires actual determination of Fe^{3+} in minerals, as calculation by stoichiometry can introduce significant errors especially when dealing with mica and amphibole. This problem coupled with the uncertainties related to the determination of the mineral modes may produce a bulk composition that fails to reproduce the mineralogical constraints.

5.6.1 Ferric iron influence on low-grade metasedimentary rocks

The thermodynamic results can be used to examine the behaviour of minerals in low-grade Fe$_2$O$_3$-rich metasedimentary rocks. Figure 9 provides a comparison of two different bulk rock Fe$_2$O$_3$ compositions. The typical greenschist-facies assemblage of white mica + chlorite + chloritoid + quartz develops in Fe$_2$O$_3$-free compositions, with garnet and biotite making an appearance starting from about 500 °C as expected in Al-poor metapelites. Rutile and ilmenite are the dominant Ti-oxides, the latter replacing the former at temperatures towards the greenschist- to amphibolite-facies transition.

In Fe$_2$O$_3$-rich compositions, garnet-bearing assemblages are shifted, especially at intermediate- to high-pressure conditions, towards higher temperatures than in the "all-bulk-iron-as-FeO" case. But it must be noted that the considered MnNKFMASHTO system does not contain Ca, which has the effect of not stabilizing the ugrandite group end-members of garnet. The calculated garnet composition in an XFe$_2$O$_3$=0.65 bulk composition is a spessartine with a low ferric iron content (0.005 apfu) and its mode is very low, around 0.02 vol.%.

Biotite is not stable in the $X\mathrm{Fe_2O_3}$=0.65 bulk composition even at 550 °C, which may be related to the activity-composition model for the $\mathrm{Fe^{3+}}$-bearing end-members of biotite. The thermodynamic modelling of the hematite-rich metasedimentary rock MP4 applied the $\mathrm{Fe^{3+}}$-Ti-biotite model of Tajcmanová et al. (2009), who warned against the use of this extended biotite thermodynamic model in $\mathrm{Fe_2O_3}$-rich compositions. Here, however, the choice of the Ti-$\mathrm{Fe^{3+}}$-biotite model correctly reproduced the observed biotite-free assemblage. The biotite-free assemblage could also be the consequence of a lack of alkali-feldspar that is involved in the production of biotite during prograde chlorite breakdown (chlorite + K-feldspar = muscovite + biotite + quartz + $\mathrm{H_2O}$; Spear, 1993). A further explanation is that hematite acted as a sink for ferric iron and no ferric iron was left for the formation of biotite, which is the major $\mathrm{Fe^{3+}}$ silicate container in metasedimentary rocks (Guidotti & Dyar, 1991). This hypothesis was tested by performing a pseudosection (not shown) in which hematite and magnetite were excluded from the calculation: without these ferric iron phases, biotite occurs in the the mineral assemblages at $X\mathrm{Fe_2O_3}$ contents of 0.65.

Carpholite is another important phase that indicates HP-LT metamorphism in metasedimentary rocks, and its occurrence is long known in the Northern Apennines silicoclastic units of the Triassic Verrucano Formation (Theye et al., 1997). A bulk-rock composition with $X\mathrm{Fe_2O_3} = 0.65$ enlarges the carpholite stability towards lower pressures and higher temperatures conditions. At 300 °C the carpholite-in curve moves from 15 kbar in reduced rock compositions to 10 kbar in oxidized bulk compositions. The minimum pressures for the occurrence of carpholite in $\mathrm{Fe_2O_3}$-rich metasedimentary rocks is close to the minimum pressures of 6-8 kbar estimated for carpholite-bearing metapelitic assemblages (Oberhänsli et al., 2001).

Rutile and hematite are the stable oxides within bulk-rock composition with $X\mathrm{Fe_2O_3} = 0.65$. Magnetite appear above 450 °C at low pressures whereas magnetite-bearing assemblages need temperatures exceeding 500 °C at high pressures.
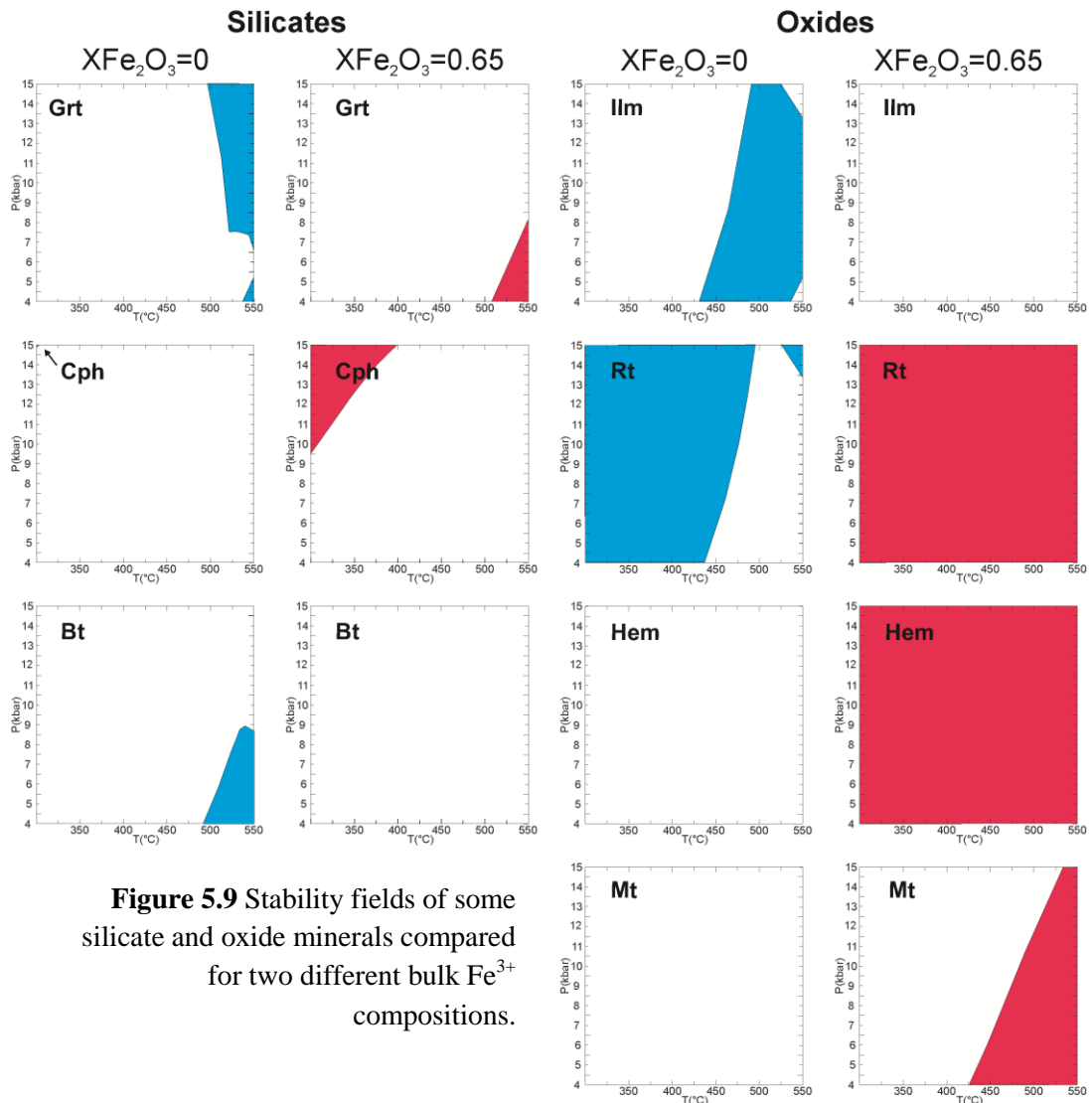
Figure 5.9 Stability fields of some silicate and oxide minerals compared for two different bulk Fe^{3+} compositions.

5.6.2 Geological implications for the Northern Apennines

Many studies devoted to the Triassic Verrucano from the Tuscan Metamorphic Units of the Northern Apennines document HP-LT Oligocene-Miocene metamorphism (Theye *et al.*, 1997; Giorgetti *et al.*, 1998; Jolivet *et al.*, 1998; Franceschelli & Memmi, 1999; Franceschelli *et al.*, 2004). This metamorphic signature, defined by pressures ranging from 8 to 15 kbar and temperatures of 300-560 °C, is associated to subduction and crustal thickening connected to the Corsica-Sardinia and Adria collision (Jolivet *et al.* 1998). In this geodynamic setting, the role of the Variscan basement is generally overlooked, probably because less thermobarometric constraints on its Alpine evolution are available. Our study confirms the involvement of Variscan basement rocks in the Northern Apennine Oligocene-Miocene orogeny (Conti *et al.*, 1991) and helps to clarify the contrasting peak pressure estimates available for the overlying Verrucano of the

Pisani Mountains (4-5 kbar *vs.* 9-10 kbar: Franceschelli *et al.,* 1981). The Alpine peak metamorphism recorded in the Verrucano from Pisani Mountains is similar to the peak *P-T* values (T=300-560 °C; P=8-15 kbar) found elsewhere in the Verrucano cropping out in the Tuscan Archipelago and southern Tuscany. Hence, both the Variscan basement and its sedimentary cover resided at depths of around 25-30 km after the crustal thickening stage, in a collisional tectonic setting characterized by a geotherm of around 50 °C kbar^{-1}.

5.7 CONCLUSIONS

The Pisani Mountains hematite-rich phyllites case study offers the opportunity to achieve *P-T* information by taking into account its effective ferric iron content by *P-X*Fe$_2$O$_3$.

The main results are:

1. Underestimating (or neglegting) ferric iron in oxide-rich phyllites may result in a thermodynamic modelling that reproduces neither the observed mineral assemblage nor the measured mineral compositions. Quantifying Fe$_2$O$_3$ is possible through a *P-T-X*Fe$_2$O$_3$ approach whereas the titration method may overestimate the bulk Fe$_2$O$_3$.

2. The introduction of ferric iron has the effect of increasing the MgO/(MgO+FeO) ratio in bulk rock chemistry and this in turn affects silicate mineral compositions (i.e. chloritoid and chlorite *X*Fe^{2+}) and the Fe–Mg exchange thermobarometry.

3. In Fe$_2$O$_3$-rich (and CaO-poor) bulk compositions garnet and carpholite, two important thermobarometric indicators, occur at higher temperatures than in Fe$_2$O$_3$-poor bulk compositions. Furthermore, carpholite is predicted at lower pressure in the MnNKFMASHTO system than in the MnNKFMASHT system. Our modelling in Fe$_2$O$_3$-rich rocks indicates that the formation of biotite, the typical Fe^{3+}-bearing silicate in metasedimentary rocks, can be controlled by the stability of Fe^{3+}-oxides such as hematite that is the major sink for Fe^{3+} in the present case study. Alternative explanations include the poor knowledge of the activity-composition model for the Fe^{3+}-bearing end-member of biotite, or the lack of precursor K-feldspar. Thus the stability of Fe^{3+}-oxides may have the effect of changing the coexisting silicate mineralogy.

4. Hematite-rich phyllites of the Buti formation (Pisani Mountains, Northern Apennines) reached 475 °C and 9-10 kbar during the metamorphic event

presumably occurring after nappe-stacking in the Alpine continental collision between Adria and Corsica-Sardinia margins. These new *P-T* values agree with the peak pressures recorded by the Verrucano during the Alpine evolution. Hence, both the Variscan basement and its cover behaved as a coherent tectonic unit during the assembly of the Northern Apennines belt.

5.9 REFERENCES

Andersen, D.J. & Lindsley, D.H., 1988. Internally-consistent solution models for Fe-Ti-Mg-Mn oxides – Fe-Ti oxides. *American Mineralogist*, **73**, 714-726.

Boger, S.D., White, R.W. & Schulte, B., 2012. The importance of iron speciation (Fe^{2+}/Fe^{3+}) in determining mineral assemblages: an example from the high-grade aluminous metapelites of south eastern Madagascar. *Journal of Metamorphic Geology*, **30**, 997–1018.

Braga, R., Morten, L. & Zanetti, A., 2006. Origin of a mica megacryst in an alkaline dike from the Veneto Volcanic Province, Italy. *European Journal of Mineralogy*, **18**, 223-231.

Braga, R., Massonne, H.J. & Morten, L., 2007. An early metamorphic stage for the Variscan Ulten Zone gneiss (NE Italy): evidence from mineral inclusions in kyanite. *Mineralogical Magazine*, **71**, 691-702.

Braga, R. & Massonne, H.J., 2008. Mineralogy of inclusions in zircon from high-pressure crustal rocks from the Ulten Zone, Italian Alps. *Periodico di Mineralogia.*, **77**, 43-64.

Brandelik, A., 2008. CALCMIN – an EXCEL^{TM} Visual Basic application for calculating mineral structural formulae from electron microprobe analyses. *Computers & Geosciences*, **35**, 1540–1551.

Connolly, J.A.D., 1990. Multivariable phase diagrams: an algorithm based on generalized thermodynamics. *American Journal of Science*, 290,666–718.

Connolly, J.A.D. & Petrini, K., 2002. An automated strategy for calculation of phase diagram sections and retrieval of rock properties as a function of physical conditions. *Journal of Metamorphic Geology*, **20**, 697–708.

Conti, P., Costantini, A., Decandia, F.A., Elter, F.M., Gattiglio, M., Lazzarotto, A., Meccheri, M., Pandeli, E., Rau, A., Sandrelli, F., Tongiorgi, M. & Di Pisa, A., 1991. Structural frame of the Tuscan Palaeozoic: a review. *Bollettino Societa Geologica Italiana*, **100**, 523–541.

Diener, J.F.A., & Powell, R., 2010. Influence of ferric iron on the stability of mineral assemblages. *Journal of metamorphic Geology*, **28**, 599–613.

Diener, J.F.A., Powell, R., White, R.W. & Holland, T.J.B., 2007. A new thermodynamic model for clino- and orthoamphiboles in the system $Na_2O–CaO–FeO–MgO–Al_2O_3–SiO_2–H_2O–O$. *Journal of Metamorphic Geology*, **25**, 631–656.

Franceschelli, M. & Memmi I., 1999. Zoning of chloritoid from kyanite-facies metapsammites, Alpi Apuane, Italy. *Mineralogical Magazine*, **63**, 105–110.

Franceschelli, M., Leoni, L., Memmi, I. & Puxeddu, M., 1986. Regional distribution of Al-silicates and metamorphic zonation in the low-grade Verrucano metasediments from the Northern Apennines, Italy. *Journal of Metamorphic Geology*, **4**, 309–321.

Franceschelli, M., Gianelli, G., Pandeli, E. & Puxeddu, M., 2004. Variscan and Alpine metamorphic events in the northern Apennines (Italy): a review. *Periodico di Mineralogia*, **73**, 43-56.

Giorgetti, G., Goffé, B., Memmi, I. & Nieto, F., 1998. Metamorphic evolution of Verrucano metasediments in Northern Apennines: new petrological constraints. *European Journal of Mineralogy*, **9**: 859-873.

Green, E.C.R., Holland, T.J.B. & Powell, R., 2007. An order–disorder model for omphacitic pyroxenes in the system jadeite–diopside–hedenbergite–acmite, with applications to eclogitic rocks. *American Mineralogist*, **92**, 1181–1189.

Herron, M.M., 1988. Geochemical classification of terrigenous sands and shales from core and log data. *Journal of Sedimentary Petrology*, **58**, 820–829.

Hillier, S. & Velde, B., 1991. Octahedral occupancy and the chemical composition of diagenetic (low-temperature) chlorites. *Clay Minerals*, **26**, 149-168.

Holland, T.J.B. & Powell, R., 1991. A compensated-Redlich-Kwong (CORK) equation for volumes and fugacities of CO_2 and H_2O in the range 1 bar to 50 kbar and 100–1600 °C. *Contributions to Mineralogy and Petrology*, **109**, 265–273.

Holland, T.J.B. & Powell, R., 1998. An internally consistent thermodynamic data set for phases of petrological interest. *Journal of Metamorphic Geology*, **16**, 309–343.

Holland, T., Baker, J. & Powell, R., 1998. Mixing properties and activity-composition relationships of chlorites in the system MgO-FeO-Al_2O_3-SiO_2-H_2O. *European Journal of Mineralogy* **10**, 395-406.

Jolivet, L., Faccenna, C., Goffè, B., Mattei, M., Rossetti, F., Brunet, C., Storti, F., Funiciello, R., Cadet, J.P., D'Agostino, N. & Parra, T., 1998. Midcrustal shear zones in postorogenic extension: example from the northern Tyrrenian Sea. *Journal of Geophysical Research*, **103**, 12123–12160.

Kligfield, R., Hunziker, J, Dallmeyer, R.D. & Schamel, S. 1986. Dating of deformational phases using K-Ar and $^{40}Ar/^{39}Ar$ techniques: results from the Northern Apennines. *Journal of Structural Geology*, **8**, 781-798.

Korhonen, F.J., Powell, R. & Stout, J.H., 2012. Stability of sapphirine + quartz in the oxidized rocks of the Wilson Lake terrane, Labrador: calculated equilibria in NCKFMASHTO. *Journal of Metamorphic Geology*, **30**, 21–36.

López-Carmona, A., Pitra, P. & Abati, J., 2013. Blueschist-facies metapelites from the Malpica–Tui Unit (NW Iberian Massif): phase equilibria modelling and H_2O and Fe_2O_3 influence in high-pressure assemblages. *Journal of Metamorphic Geology*, **31**, 263–280.

Massonne H.J., 1981. Phengite: eine experimentelle untersuchung ihres druck-temperatur-vertraltens im system K_2O-MgO-Al_2O_3-SiO_2-H_2O. Unpublised thesis, University of Bochum, pp. 211.

McLennan, S.M., 2001. Relationships between the trace element composition of sedimentary rocks and upper continental crust. *Geochemistry, Geophysics, Geosystems*, **2**, 1-24.

Montomoli, C., 2002. Evoluzione termo-barica del Complesso Metamorfico dei Monti Pisani (Appennino Settentrionale) e inclusioni fluide: dati preliminari. *Atti della Società toscana di scienze naturali,. Memorie, Serie A*, **108**, 31-36.

Oberhänsli, R., Partzsch, J., Candan, O. & Cetinkaplan, M., 2001. First occurrence of Fe–Mg carpholite documenting a high-pressure metamorphism in metasediments of the Lycian Nappes, SW Turkey. *International Journal of Earth Sciences*, **89 (4)**, 867–873.

White, R.W., Pomroy, N.E. & Powell, R., 2005. An in-situ metatexite–diatexite transition in upper amphibolite facies rocks from Broken Hill, Australia. *Journal of Metamorphic Geology*, **23**, 579–602.

Rau, A. & M. Tongiorgi, 1966. Considerazioni preliminari sulla geologia della parte meridionale dei Monti Pisani (versante SW). *Memorie della Societa Geologica Italiana*, **5**, 300-314

Rau, A. & Tongiorgi, M., 1974. La geologia dei Monti Pisani a Sud-Est della Valle del Guappero. *Memorie della Società Geologica Italiana*, **13**, 227-408.

Schiaffino L. & Tongiorgi M., 1962. Stratigrafia del Verrucano dei Monti Pisani. *Atti della Società toscana di scienze naturali,. Memorie, Serie A*, **69**, 382-446.

Siivola, J. & Schmid, R.A., 2007. A ystematic nomenclature for metamorphic rocks: 12. List of mineral abbreviations. Recommendations by the IUGS Subcommission on the Systematics of Metamorphic Rocks. *Recommendations*, web version of 01.02.2007.

Smye, A.J., Greenwood, L.V. & Holland, T.J.B., 2010. Garnet–chloritoid–kyanite assemblages: eclogite facies indicators of subduction constraints in orogenic belts. *Journal of Metamorphic Geology*, **28**, 753–768.

Spear, F.S., 1993. Metamorphic phase equilibria and pressure-temperature-time paths. Mineralogical society of America, Washington D.C., pp. 799.

Tajcmanová, L., Connolly, J.A.D, & Cesare, B., 2009. A thermodynamic model for titanium and ferric iron solution in biotite. *Journal of Metamorphic Geology*, **27**, 153-164.

Taylor, S.R. & McLennan, S.M., 1985. The continental crust: its composition and evolution. Blackwell, Oxford, pp. 312.

Theye, T., Reinhardt, J., Goffé, B., Jolivet, L. & Brunet, C. 1997. Ferro and magnesiocarpholite from Mt. Argentario (Italy): first evidence for high-pressure metamorphism of the metasedimentary Verrucano sequence, and significance for P-T path reconstruction. *European Journal of Mineralogy*, **9**, 859-873.

Vidal, O., Goffé, B., Bousquet, R. & Parra, T., 1999. Calibration and testing of an empirical chloritoid-chlorite Mg-Fe exchange thermometer and thermodynamic data for daphnite. *Journal of Metamorphic Geology*, **17**, 25–39.

Vidal, O., Parra, T. & Vieillard, P. 2005. Experimental data on the Tschermak solid solution in Fe-chlorites: application to natural examples and possible role of oxidation. *American Mineralogist*, **90**, 359–370.

White, R.W., Powell, R., Holland, T.J.B. & Worley, B., 2000. The effect of TiO_2 and Fe_2O_3 on metapelitic assemblages at greenschist and amphibolite facies conditions: mineral equilibria calculations in the system K_2O–FeO–MgO–Al_2O_3–SiO_2–H_2O–TiO_2–Fe_2O_3. *Journal of Metamorphic Geology*, **18**, 497–511.

White, R.W., Powell, R. & Clarke, G.L., 2002. The interpretation of reaction textures in Fe–rich metapelitic granulites of the Musgrave Block, central Australia: constraints from mineral equilibria calculations in the system K_2O–FeO–MgO–Al_2O_3–SiO_2–H_2O–TiO_2–Fe_2O_3. *Journal of Metamorphic Geology*, **20**, 41–55.

White, R.W, Powell, R. & Holland, T.J.B., 2007. Progress relating to calculation of partial melting equilibria for metapelites. *Journal of Metamorphic Geology*, **25**, 511–527.

CONCLUSIONS

Chapter 6

CHAPTER 6

CONCLUSIONS

6.1 SUMMARY

The thesis deals with the metamorphic evolution of the Northern Apennines Variscan basement. Only few data (comprising *P-T* estimates obtained through classical thermobarometry) were available for this basement because of (i) complex polymetamorphism (Variscan metamorphism and Alpine overprint); (ii) scarce and rare outcrops, that hamper any regional correlation.

The PhD activity aimed to unravel a complete metamorphic history, including the pre-Alpine stages, the possible correlations with other Variscan basement, the evolution between the Variscan and the Alpine orogenesis, and the Alpine peak conditions.

The study of the Variscan basement of Northern Apennines allowed also to examine some general petrological issues, such as the possibility to combine thermodynamic modelling and microstructural analysis to reconstruct a polyphasic metamorphic evolution, the strategies to link petrology and geochronology, the breakdown reaction of monazite in medium-grade metapelites, the geochronology of mylonitic microstructures, and the influence of ferric iron in greenschist-facies metasediments. The Variscan basement occurrences suitable to investigate the above-mentioned questions were located at the Cerreto Pass, in the Pontremoli area and in the Pisani Mountains. The research was carried out with field work, sampling, petrography and microstructural analysis, determination of the bulk rock- and mineral composition, thermodynamic modelling, classical geothermobarometry, monazite chemical dating, and Ar-Ar dating of muscovite. The thesis has been structured according to a chronological order: Variscan orogeny, post-Variscan evolution, Jurassic shearing and Alpine metamorphism. The results are shown in the following paragraphs.

6.2   PETROLOGICAL FINDINGS

1.   In the Cerreto micaschists the Mg-rich cores within deformed prekinematic potassic white mica record the pre-peak stage. Garnet rim composition is, instead, related to the peak stage. The late paragenesis and the composition of

Figure of the previous page: View of the Northern Apennines from the Cerreto Pass. The mountains in the background are the Apuane Alps.

potassic white mica and chlorite defining the mylonitic foliation provide information about the retrograde shearing stage (chapter 2). Thus, an integrated approach between microstructural analysis and thermodynamic modelling allows to unravel a polyphase *P-T-D* evolution.

2. The application of thermodynamic modelling and U-Th-Pb chemical dating of monazite on micaschists from the Pontremoli well (chapter 3) allowed to investigate the link between monazite age dating and petrology in medium-grade metapelites. Coronitic microstructures of apatite, allanite, epidote around partially dissolved monazite grains are a clear breakdown microstructure. Besides, the high-Th and -U contents in monazite suggests that the monazite was inherited and became unstable undergoing partial or total dissolution. The breakdown reaction of monazite generated apatite + Th-silicate, allanite, and epidote coronae during prograde metamorphism at 500-600°C and 5-7 kbar.

3. Large fish-shaped muscovite crystals in mylonites are not always prekinematic mica-fishes. They can consist of a polycrystalline aggregate of fine-grained muscovite. In this case the fish-shaped microstructure is an asymmetric foliation boudin and muscovite is synkinematic with respect to the mylonitic event (chapter 4). A comparison between the ^{40}Ar-^{39}Ar ages of potassic white mica along the mylonitic foliation and within asymmetric foliation boudins in the Cerreto mylonites reveals that mylonitic foliation provides more scatter ages due to prekinematic relics, while asymmetric foliation boudins ages are related only to the mylonitization. Hence, in our case study, asymmetric foliation boudins is a preferential microstructure for obtaining geochronological information about the shearing event.

4. The long-standing problem of the uncertainties of the bulk FeO/Fe_2O_3 ratio when performing thermodynamic modelling has been tackled in the chapter 5. In the Pisani Mountains hematite-rich phyllites, neglecting the presence of bulk Fe_2O_3 may lead to incorrect *P-T* estimations. Through *P-T-X*Fe_2O_3 phase diagrams it is possible to quantify the amount of ferric iron during metamorphism. This amount can be different from the ferric iron quantity resulting from the titration method, which is related to the present-day ferric iron in bulk-rock composition. The inclusion of Fe^{3+} in thermodynamic modelling increases the whole-rock $MgO/(MgO+FeO)$ ratio, which in turn affects

chloritoid and chlorite XFe^{2+} in chloritoid-bearing phyllites from the Pisani Mountains. The presence of ferric iron in bulk-rock composition influences the stability of the main rock-forming silicates: in Fe_2O_3-rich compositions garnet- and carpholite-in curves shift towards higher temperatures with respect to the Fe_2O_3-free systems. The presence of a ferric-iron oxide (hematite) prevents the formation of biotite from the mineral assemblage even at temperatures approaching 550 °C. Rutile and hematite and magnetite are the stable oxides in ferric iron-rich bulk-rock compositions.

6.3   REGIONAL RECONSTRUCTIONS

The combination of the metamorphic evolution reconstructions for the Cerreto Pass mylonites, the Pontremoli micaschist and the Monti Pisani phyllites allows to depict a long and complex metamorphic history (Figs. 6.1, 6.2).

Carboniferous

The closure of the Rheic Ocean (360 Ma) was followed by the Variscan orogeny with the collision of Gondwana and Laurussia and the formation of Pangea at 300 Ma (Matte, 2001; von Raumer *et al.*, 2009).

In the Cerreto Pass micaschist, the Variscan thickening generated a high-pressure stage occurring at 430-480°C and 11-13.5 kbar. The Variscan peak (600 °C at 9-10 kbar) postdates this stage and was attained at 312-328 Ma (Molli *et al.*, 2002), thanks to correlation with the associated amphibolites.

Some analogy can be established among the tectono-metamorphic Variscan evolution in Northern Apennines and that described for other fragments of the Southern Variscan belt (e.g. Sardinia).

Late Carboniferous- MiddleTriassic

The Late-Carboniferous tectonics dismembered the Variscan chain through intracontinental strike slip shear zones (Arthaud & Matte, 1977; Doglioni 1984; Massari, 1986; Ziegler, 1986; Handy & Zingg, 1991; Rau, 1993; Schmid, 1993; Matte, 2001; Padovano *et al.*, 2012). This tectonic regime is linked to a megashear system affecting the Variscan belt with alternating transpressive and transtensive conditions (Rau, 1990). These megashears caused the displacement of the Sardinian, the Tuscan

and the Calabrian Variscan fragments about 150 km westward away from the "stable" Europe (Rau, 1990 and reference therein).

The Pontremoli metapelites record a metamorphic history younger than 294 ± 5 Ma (U-Th-Pb chemical age on inherited monazite). The replacement of inherited monazite by apatite, allanite and epidote occurred during a prograde evolution at 500-600°C and 5-7 kbar. These metamorphic peak conditions predate a stage characterised by a pressure increase and concomitant cooling to 520°C at 8 kbar, followed by a nearly isothermal cooling to 500°C at 2 kbar. This anticlockwise P-T path is different from the available metamorphic histories of the pre-Mesozoic basement of the Northern Apennines. An Oligocene-Miocene metamorphic history cannot be completely ruled out. However, the comparison with the few adjacent basement slivers and the shape of the P-T path here derived support a post-Variscan stage characterised by transpressive (counterclockwise - T_{max} before P_{max}) to transtensive (near isothermal decompression) tectonics. This reconstruction may be related to the Late Carboniferous-Middle Triassic crustal scale shear zone.

The strike-slip shearing affected probably also the Cerreto mylonites, that show some [40]Ar-[39]Ar age determinations around 210 and 260 Ma.

Late Triassic-Jurassic

Starting from Late Triassic a distensive tectonic regime predominated. The extensional tectonics led to the final separation between the Variscan Sardinia and the Tuscan Variscan basements. The Variscan basement of Northern Apennines became the western divergent margin of the Adria promontory. Along this separation stretching and thinning occurred (Arthaud & Matte, 1977; Rau, 1990). In the meanwhile, tilted and imbricate blocks formed in the Tuscan Adria, such as in the Southern Alps (Schmidt *et al.*, 1987; Handy, 1987). The drifting stage that led to the formation of the Ligurian-Piedmont ocean, a branch of the Western Tethys, occurred in Middle-Late Jurassic.

In this framework the retrograde evolution in the Cerreto mylonites took place. This stage occurred at 190.7 ± 1.3 Ma (Ar/Ar isotopic age of mylonitic muscovite) and was accompanied by a strong ductile deformation at 450-500°C and 6-7.5 kbar (thermodynamic modelling). Thus, the exhumation of the Cerreto mylonites was probably connected with the Ligurian-Piedmont ocean-related rifting stage of the Adria margin.

Cretaceous-Eocene

The convergence between Europe (Corsica-Sardinia) and Africa (Adria) led to the subduction of the Ligurian-Piedmont ocean. Eclogitic- to blueschist-metamorphism affected the Liguride ophiolites at 49-40 Ma (Federico *et al.*, 2004). The Variscan basement of Northern Apennines was not involved in the Alpine collision yet. This is confirmed by the lack of Cretaceous-Eocene geochronological data.

Late Oligocene-Early Miocene

The collision between the Corsica-Sardinia block and the Adria microplate caused the underthrusting of the Adria margin (Vai & Martini, 2001). Some sectors of the Variscan basement were affected by the Alpine metamorphism. The compressional structures of Northern Apennines formed in these times (27 Ma; Kligfield *et al.*, 1986). High-pressure greenschist-facies metamorphism affected the Massa Unit in the Apuane Alps (6-8 kbar and 400-500°C; Molli *et al.*, 200, 2002) and the Buti Formation phyllites from the Pisani Mountains (475 °C and 9-10 kbar; Lo Pò & Braga, 2014).

High-pressure lower-temperature metamorphism (350-420°C and 6-12 kbar) affected, instead, the Tuscan Metamorphic Units in Southern Tuscany, where it is extensively recorded by the Verrucano Group metasediments (Theye *et al.*, 1997; Giorgietti *et al.*, 1998; Jolivet *et al.*, 1998).
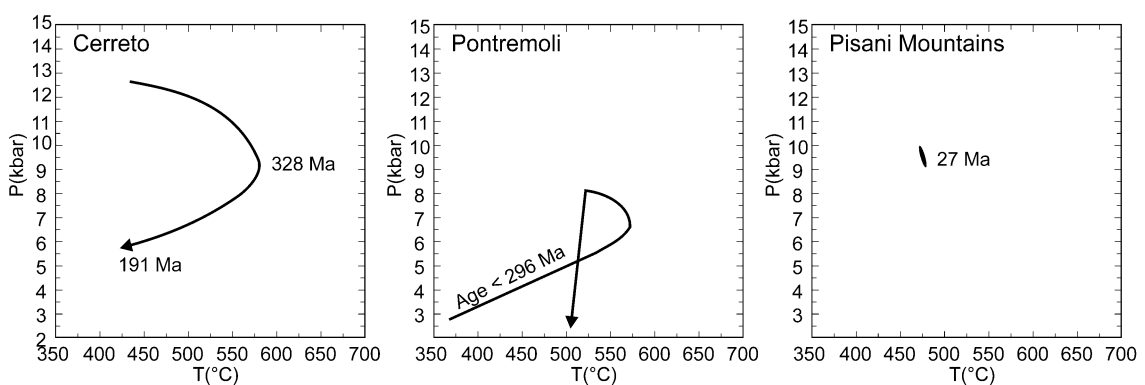
Figure 6.1. *P-T* paths for the Variscan basement determined for the Cerreto Pass, in the Pontremoli well and in the Pisani Mountains.
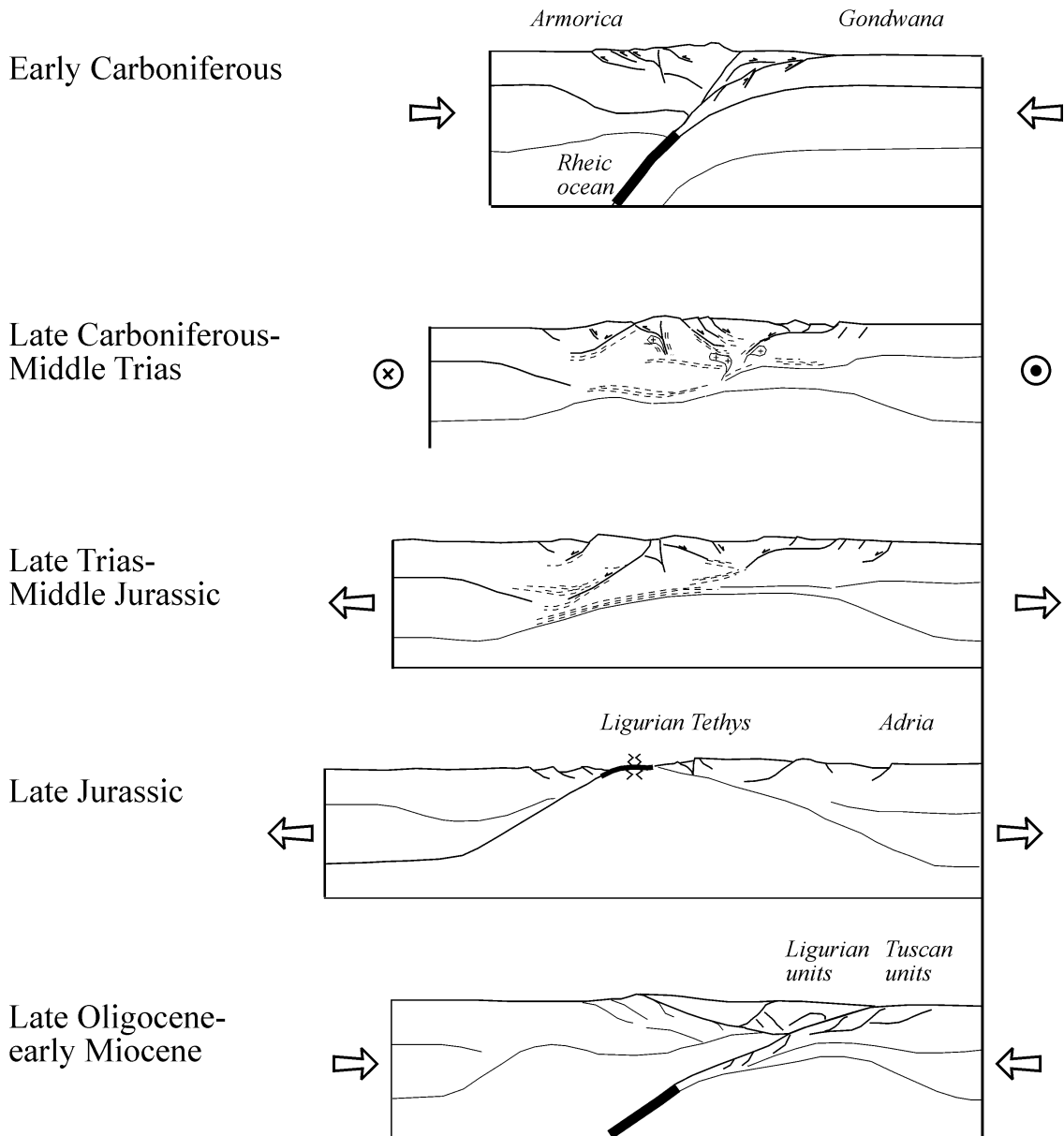
Figure 6.2
Tectonic sketches drawn in collaboration with dr. G. Molli reporting the main events recorded in the Variscan basement of Northern Apennines.

6.3.1 Open questions

Some regional points need to be examined in future researches:

➢ The mafic amphibolites in the Cerreto Pass exhibit a peak metamorphism at 650°C and 8 kbar, calculated using classical geothermobarometry. Our *P-T* estimates from thermodynamic modelling for the associated micaschist is 580-600°C and 9-10 kbar. The differences can be due to the different geothermobarometric methods or, alternatively, these discrepancies are true and need a refinement of the geological interpretations. Thus, it would be interesting to use thermodynamic modelling also for the amphibolites in order to verify if the peak conditions changes.

➢ A debate is still open about the derivation of the Cerreto metamorphic rocks. They have been attributed in the past to the Tuscan domain (Pandeli *et al.*, 2005) or to a more external domain (Umbrian or Padan domain; Reutter *et al.*, 1983; Vai & Cocozza, 1986). A comparative study on the Cerreto micaschist and the Micaschist Complex in the Larderello subsurface is needed to establish if the two belong to the same crustal sector.

➢ The reconstructed metamorphic evolution for the Pontremoli micaschists postdates the chemical monazite age 294 ± 5 Ma. Further dating can more precisely constrain the recognized metamorphic stages. In this respect, Ar-Ar dating on Na-rich muscovite and Mg-rich muscovite may provide information about the age of the thermal peak and of the pressure peak, respectively.

6.4 REFERENCES

Arthaud, F. & Matte, P., 1977. Late Paleozoic strike-slip faulting in southern Europe and northern Africa: Result of a right-lateral shear zone between the Appalachians and the Urals. *Geological Society of America Bulletin,* **88**, 1305-1320.

Doglioni, C., 1984. Tettonica triassica transpressiva nelle Dolomiti. *Giornale di Giologia,* **46**, 47–60.

Federico, L., Capponi, G., Crispini, L. & Scambelluri, M., 2004. Exhumation of alpine high-pressure rocks: insights from petrology of eclogite clasts in the Tertiary Piedmontese basin (Ligurian Alps, Italy). *Lithos,* **74**, 21–40.

Giorgetti, G., Goffe, B., Memmi, I. & Nieto, F., 1998. Metamorphic evolution of Verrucano metasediments in Northern Apennines; new petrological constraints. *European Journal of Mineralogy,* **10**, 1295-1308.

Handy, M.R., 1987. The structure, age and kinematics of the Pogallo fault zone; Southern Alps, northwestern Italy. *Eclogae Geologicae Helvetiae,* **80**, 593–632.

Handy, M.R. & Zingg, A., 1991. The tectonic and rheological evolution of an attenuated cross section of the continental crust: Ivrea crustal section, southern Alps, north-western Italy and southern Switzerland. *Geological Society of America Bulletin,* **103**, 236–253.

Jolivet, L., Faccenna, C., Goffé, B., Mattei, M., Rossetti, F., Brunet, C., Storti, F., Funiciello, R., Cadet, J.P., d'Agostino N. & Parra, T., 1998. Midcrustal shear zones in postorogenic extension: example from the northern Tyrrhenian Sea. *Journal of Geophysical Research: Solid Earth (1978–2012),* **103(B6)**, 12123-12160.

Kligfield, R., Hunziker, J, Dallmeyer, R.D. & Schamel, S. 1986. Dating of deformational phases using K-Ar and ^{40}Ar/^{39}Ar techniques: results from the Northern Apennines. *Journal of Structural Geology*, **8**, 781-798.

Lo Pò, D. & Braga, R., 2014. Influence of ferric iron on phase equilibria in greenschist facies assemblages: the hematite-rich metasedimentary rocks from the Monti Pisani (Northern Apennines). *Journal of Metamorphic Geology,* **32**, 371-387.

Massari, F., 1986. Some thoughts on the Permo-Triassic evolution of the South Alpine area (Italy). *Memorie della Società Geologica Italiana,* **34**, 179–188.

Matte, Ph., 2001. The Variscan collage and orogeny (480-290 Ma) and the tectonic definition of the Armorica microplate: a review. *Terra Nova,* **13**, 112-128.

Molli, G., Montanini, A. & Frank W., 2002. MORB-derived Variscan amphibolites in the Northern Apennine Basement: the Cerreto metamorphic slices (Tuscan-Emilian Apennine, NW Italy). *Ofioliti,* **27**, 17-30.

Padovano, M., Elter, F. M., Pandeli, E. & Franceschelli, M., 2012. The East Variscan Shear Zone: new insights into its role in the Late Carboniferous collision in southern Europe. *International Geology Review,* **54**, 957-970.

Pandeli, E., Gianelli, G. & Morelli, M., 2005. The cristalline units of the middle-upper crust of the Larderello geothermal region (southern Tuscany, Italy): new data for their classification and tectono-metamorphic evolution. *Bollettino della Società Geologica Italiana,* **3**, 139-155.

Rau, A., 1990. Evolution of the Tuscan domain between the Upper Carboniferous and the Middle Triassic: a new hypothesis. *Bollettino della Società Geologica Italiana,* **109**, 231-238.

Rau, A., 1993. Il Paleozoico toscano: da segmento della catena Varisica sud-europea a margine passivo alpidico peri-adriatico. *Memorie della Società Geologica Italiana,* **49**, 325-334.

Reutter, K.J., Teichmuller, M., Teichmuller, R. & Zanzucchi, G., 1983. The coalification patter in the Northern Apennines: paleogeothermic and tectonic significance. *Geologische Rundschau,* **72**, 861-894.

Schmid, S., 1993. Ivrea Zone and adjacent southern Alpine basement. In J.F. von Raumer, F. Neubauer (Eds.), *Pre-Mesozoic Geology in the Alps, Springer*, Berlin, 567-584.

Schmid, S.M., Panozzo, R. & Bauer S., 1987. Simple shear experiments on calcite rocks: rheology and microfabric. *J. Struct. Geol. Journal of Structural Geology,* **9**, 747–778.

Theye, T., Reinhardt, J., Goffe, B., Jolivet, L. & Brunet, C., 1997. Ferro-and magnesiocarpholite from the Monte Argentario (Italy); first evidence for high-pressure metamorphism of the metasedimentary Verrucano sequence, and significance for PT path reconstruction. *European Journal of Mineralogy,* **9**, 859-873.

Vai, G.B. & Martini, I.P., 2001. Anatomy of an Orogen: the Apennines and Adjacent Mediterranean Basins, Kluwer Academic Publishers, pp. 632.

Vai, G.B. & Cocozza, T., 1986. Tentative schematic zonation of the Hercynian chain in Italy. *Bulletin de la Societe Geologique de France,* **8**, 95-116.

von Raumer, J. F., Bussy, F. & Stampfli, G. M., 2009. The Variscan evolution in the External massifs of the Alps and place in their Variscan framework. *Comptes Rendus Geoscience,* **341**, 239-252.

Ziegler, P.A., 1986. Geodynamic model for the Palaeozoic crustal consolidation of Western and Central Europe. *Tectonophysics*, **126**, 303-328.

APPENDIX 1

SAMPLE INFORMATION

SAMPLE	LOCATION	UNIT	LITHOLOGY	OPTICAL MICROSCOPE	SEM EDS	EMP WDS	XRF	GEO THERMOBAROMETRY	GEO CHRONOLOGY
PB8	Punta Bianca	Phyllitic and quartzitic complex	phyllite	x					
PB9	Punta Bianca	Phyllitic and quartzitic complex	phyllite	x			x		
PB9b	Punta Bianca	Phyllitic and quartzitic complex	phyllite	x	x	x	x		
MP1	Pisani Mountains	Phyllitic and quartzitic complex	phyllite	x					
MP2	Pisani Mountains	Phyllitic and quartzitic complex	phyllite	x					
MP3	Pisani Mountains	Phyllitic and quartzitic complex	phyllite	x					
MP4	Pisani Mountains	Phyllitic and quartzitic complex	chloritoid-bearing phyllite	x			x		
MP4b	Pisani Mountains	Phyllitic and quartzitic complex	chloritoid-bearing phyllite	x	x	x	x	x	
CER10a	Cerreto Pass	Micaschist Complex	mylonitic micaschist	x			x		
CER12	Cerreto Pass	Micaschist Complex	mylonitic micaschist	x			x		
CER36-1a	Cerreto Pass	Micaschist Complex	mylonitic micaschist	x			x		
CER8	Cerreto Pass	Micaschist Complex	garnet-bearing mylonitic micaschist	x	x	x	x	x	
CER8 chip	Cerreto Pass	Micaschist Complex	garnet-bearing mylonitic micaschist			x			
CER9	Cerreto Pass	Micaschist Complex	mylonitic micaschist	x			x		
CER41-3	Cerreto Pass	Micaschist Complex	garnet-bearing amphibolite	x			x		
CER40-7	Cerreto Pass	Micaschist Complex	amphibolite	x			x		
PC1	Cerreto Pass	Micaschist Complex	garnet-bearing mylonitic micaschist	x					
PC1b	Cerreto Pass	Micaschist Complex	garnet-bearing mylonitic micaschist	x	x		x	x	

189

SAMPLE	LOCATION	UNIT	LITHOLOGY	OPTICAL MICROSCOPE	SEM EDS	EMP WDS	XRF	GEO THERMOBAROMETRY	GEO CHRONOLOGY
PC1 chip	Cerreto Pass	Micaschist Complex	garnet-bearing mylonitic micaschist				x		
PC2	Cerreto Pass	Micaschist Complex	garnet-bearing mylonitic micaschist	x					
PC2b	Cerreto Pass	Micaschist Complex	garnet-bearing mylonitic micaschist	x	x				
PC4	Cerreto Pass	Micaschist Complex	garnet-bearing mylonitic micaschist	x					
PC5	Cerreto Pass	Micaschist Complex	ultramylonite	x					
PC6	Cerreto Pass	Micaschist Complex	mylonitic biotite-micaschist	x					
PC7b	Cerreto Pass	Micaschist Complex	mylonitic biotite-micaschist	x					
PC11	Cerreto Pass	Micaschist Complex	mylonitic micaschist	x					
PC12	Cerreto Pass	Micaschist Complex	mylonitic biotite-micaschist	x					
PC13	Cerreto Pass	Micaschist Complex	ultramylonite	x					
PC14	Cerreto Pass	Micaschist Complex	mylonitic biotite-micaschist	x					
PC15	Cerreto Pass	Micaschist Complex	mylonitic micaschist	x					
PC16	Cerreto Pass	Micaschist Complex	mylonitic micaschist	x					
PC17	Cerreto Pass	Micaschist Complex	mylonitic biotite-micaschist	x					
PC18	Cerreto Pass	Micaschist Complex	mylonitic micaschist	x					
PC19	Cerreto Pass	Micaschist Complex	green amphibole-amphibolite	x					
PC20	Cerreto Pass	Micaschist Complex	ultramylonite	x					
PC21	Cerreto Pass	Micaschist Complex	mylonitic micaschist	x	x				
PC22	Cerreto Pass	Micaschist Complex	mylonitic micaschist	x	x				
PC23	Cerreto Pass	Micaschist Complex	garnet-bearing mylonitic micaschist	x	x	x	x	x	

SAMPLE	LOCATION	UNIT	LITHOLOGY	OPTICAL MICROSCOPE	SEM EDS	EMP WDS	XRF	GEO THERMOBAROMETRY	GEO CHRONOLOGY
PC23 chip	Cerreto Pass	Micaschist Complex	garnet-bearing mylonitic micaschist			x			x
PC24	Cerreto Pass	Micaschist Complex	garnet-bearing mylonitic micaschist	x	x				
PC24b	Cerreto Pass	Micaschist Complex	garnet-bearing mylonitic micaschist	x					
PC25	Cerreto Pass	Micaschist Complex	mylonitic micaschist	x					
3118	Pontremoli 1 well	Micaschist Complex	phyllite	x					
AG7	Pontremoli 1 well	Micaschist Complex	garnet-bearing micaschist	x	x		x		
Pontremoli 8	Pontremoli 1 well	Micaschist Complex	garnet-bearing micaschist	x	x				
Pontremoli a	Pontremoli 1 well	Micaschist Complex	phyllite	x					
AG6a	Pontremoli 1 well	Micaschist Complex	phyllite	x					
AG6	Pontremoli 1 well	Micaschist Complex	phyllite	x			x		
AG6 chip	Pontremoli 1 well	Micaschist Complex	phyllite			x			
Pontremoli 7	Pontremoli 1 well	Micaschist Complex	garnet-bearing micaschist	x	x	x		x	x
AG8	Pontremoli 1 well	Micaschist Complex	garnet-bearing micaschist	x	x				
AP1	Apuane Alps	Phyllitic and quartzitic complex	phyllite	x	x	x	x		
AP2	Apuane Alps	Phyllitic and quartzitic complex	phyllite	x	x		x		
AP3	Apuane Alps	Phyllitic and quartzitic complex	porphyric schist	x	x		x		
AP4	Apuane Alps	Phyllitic and quartzitic complex	porphyroid	x	x		x		
AP5	Apuane Alps	Phyllitic and quartzitic complex	metabasite	x	x		x		
AP6	Apuane Alps	Phyllitic and quartzitic complex	phyllite	x	x		x		
AP7	Apuane Alps	Phyllitic and quartzitic complex	phyllite	x	x		x		

The complete bulk-rock and mineral composition dataset can be requested sending a mail to deborah.lopo@unibo.it.

APPENDIX 2

EMP COMPOSITION AND AGE OF MONAZITE

Sample	Pontremoli7						
Location	Pontremoli 1 well						
Analysis	Mnz01_01	Mnz01_04	Mnz04_01	Mnz02_05	Mnz04_04	Mnz01_11	Mnz01_01a
SiO_2	0.66	1.56	0.58	0.72	0.40	1.46	0.78
P_2O_5	29.07	29.72	29.34	29.40	28.13	29.99	27.44
SO_3	0.04	0.02	0.03	0.02	0.02	0.04	0.03
CaO	1.53	2.54	1.54	1.33	4.41	1.50	1.52
Y_2O_3	0.07	0.16	0.05	0.03	0.15	0.09	0.09
La_2O_3	13.72	10.00	14.56	15.31	13.62	13.53	14.01
Ce_2O_3	27.73	24.96	28.64	29.41	29.20	26.55	27.83
Pr_2O_3	3.01	2.50	3.05	3.06	2.24	2.96	2.93
Nd_2O_3	11.98	11.00	11.95	11.59	12.21	11.53	11.82
Sm_2O_3	2.17	1.66	2.11	1.60	0.86	1.93	2.01
Gd_2O_3	1.66	0.97	1.54	0.84	1.60	1.27	1.53
Dy_2O_3	0.23	0.22	0.20	0.12	0.00	0.19	0.25
PbO	0.13	0.05	0.10	0.09	0.02	0.08	0.12
ThO_2	8.20	10.35	6.89	7.32	3.15	10.93	8.26
UO_2	0.45	0.29	0.42	0.38	0.45	0.26	0.49
Tot	100.65	96.00	100.99	101.22	96.46	102.31	99.11
Si	0.026	0.061	0.023	0.028	0.016	0.056	0.032
P	0.969	0.989	0.972	0.971	0.958	0.968	0.945
S	0.001	0.001	0.001	0.001	0.001	0.001	0.001
Ca	0.064	0.107	0.065	0.056	0.190	0.061	0.066
Y	0.002	0.003	0.001	0.001	0.003	0.002	0.002
La	0.199	0.145	0.210	0.220	0.202	0.190	0.210
Ce	0.400	0.359	0.410	0.420	0.430	0.371	0.415
Pr	0.043	0.036	0.043	0.044	0.033	0.041	0.043
Nd	0.169	0.155	0.167	0.161	0.175	0.157	0.172
Sm	0.030	0.022	0.028	0.022	0.012	0.025	0.028
Gd	0.022	0.013	0.020	0.011	0.021	0.016	0.021
Dy	0.003	0.003	0.003	0.002	0.000	0.002	0.003
Pb	0.001	0.001	0.001	0.001	0.000	0.001	0.001
Th	0.074	0.093	0.061	0.065	0.029	0.095	0.076
U	0.004	0.003	0.004	0.003	0.004	0.002	0.004
AGE	311.21	103.61	289.59	247.70	91.75	170.42	292.17
statistical error	6.51	4.80	7.21	0.25	10.68	4.99	6.24

Sample	Pontremoli7					
Location	Pontremoli 1 well					
Analysis	Mnz01_02a	Mnz01_04a	Mnz01_05a	Mnz01_06a	Mnz01_07a	Mnz01_08a
SiO_2	0.81	0.80	0.79	0.87	0.96	0.91
P_2O_5	27.30	26.28	26.75	30.17	29.76	29.80
SO_3	0.02	0.04	0.03	0.03	0.03	0.06
CaO	1.58	1.78	1.80	1.75	1.86	1.88
Y_2O_3	0.09	0.08	0.05	0.06	0.06	0.05
La_2O_3	13.42	13.72	13.37	13.39	13.36	13.84
Ce_2O_3	27.53	26.80	26.66	26.88	26.87	26.70
Pr_2O_3	2.65	2.79	2.94	2.95	2.94	2.93
Nd_2O_3	11.48	11.12	11.55	11.80	11.65	11.33
Sm_2O_3	2.05	1.97	2.11	2.11	2.05	2.04
Gd_2O_3	1.57	1.50	1.50	1.53	1.53	1.46
Dy_2O_3	0.27	0.21	0.21	0.22	0.21	0.21
PbO	0.13	0.14	0.13	0.14	0.15	0.15
ThO_2	9.08	9.62	9.62	9.86	10.24	10.17
UO_2	0.48	0.50	0.50	0.47	0.50	0.52
Tot	98.46	97.35	98.02	102.24	102.18	102.05
Si	0.033	0.033	0.033	0.033	0.037	0.035
P	0.946	0.931	0.937	0.979	0.970	0.972
S	0.001	0.001	0.001	0.001	0.001	0.002
Ca	0.069	0.080	0.080	0.072	0.077	0.077
Y	0.002	0.002	0.001	0.001	0.001	0.001
La	0.203	0.212	0.204	0.189	0.190	0.197
Ce	0.413	0.411	0.404	0.377	0.379	0.376
Pr	0.040	0.043	0.044	0.041	0.041	0.041
Nd	0.168	0.166	0.171	0.161	0.160	0.156
Sm	0.029	0.028	0.030	0.028	0.027	0.027
Gd	0.021	0.021	0.021	0.019	0.020	0.019
Dy	0.004	0.003	0.003	0.003	0.003	0.003
Pb	0.001	0.002	0.001	0.001	0.002	0.002
Th	0.085	0.092	0.091	0.086	0.090	0.089
U	0.004	0.005	0.005	0.004	0.004	0.004
AGE	293.63	288.20	281.49	294.97	295.74	293.88
statistical error	5.88	5.58	5.70	5.66	5.51	5.49

Sample	Pontremoli7					
Location	Pontremoli 1 well					
Analysis	Mnz01_09a	Mnz02_01a	Mnz02_03a	Mnz02_04a	Mnz02_05a	Mnz02_06a
SiO_2	0.88	0.81	0.81	0.58	0.63	0.75
P_2O_5	30.10	30.00	29.48	29.98	30.33	27.16
SO_3	0.03	0.03	0.03	0.03	0.02	0.04
CaO	1.70	1.36	1.60	1.47	1.51	1.25
Y_2O_3	0.07	0.06	0.05	0.01	0.03	0.06
La_2O_3	13.73	14.81	14.10	15.39	14.86	14.12
Ce_2O_3	27.40	28.06	28.69	29.16	28.70	27.71
Pr_2O_3	3.01	3.10	3.04	3.04	3.06	2.73
Nd_2O_3	11.97	12.00	12.36	11.63	11.87	11.83
Sm_2O_3	2.12	2.07	2.07	1.54	1.90	1.98
Gd_2O_3	1.47	1.50	1.41	0.79	1.18	1.43
Dy_2O_3	0.21	0.20	0.20	0.11	0.17	0.28
PbO	0.11	0.10	0.11	0.11	0.12	0.13
ThO_2	9.49	6.66	8.26	7.44	7.69	7.08
UO_2	0.40	0.30	0.31	0.42	0.47	0.48
Tot	102.72	101.05	102.54	101.70	102.55	97.03
Si	0.034	0.031	0.031	0.022	0.024	0.031
P	0.975	0.981	0.965	0.981	0.982	0.952
S	0.001	0.001	0.001	0.001	0.001	0.001
Ca	0.070	0.056	0.066	0.061	0.062	0.056
Y	0.002	0.001	0.001	0.000	0.001	0.001
La	0.194	0.211	0.201	0.219	0.210	0.215
Ce	0.384	0.397	0.406	0.412	0.402	0.420
Pr	0.042	0.044	0.043	0.043	0.043	0.041
Nd	0.164	0.166	0.171	0.161	0.162	0.175
Sm	0.028	0.027	0.028	0.021	0.025	0.028
Gd	0.019	0.019	0.018	0.010	0.015	0.020
Dy	0.003	0.002	0.002	0.001	0.002	0.004
Pb	0.001	0.001	0.001	0.001	0.001	0.001
Th	0.083	0.059	0.073	0.065	0.067	0.067
U	0.003	0.003	0.003	0.004	0.004	0.004
AGE	248.71	296.20	274.78	292.51	311.87	362.33
statistical error	5.64	7.68	6.50	6.81	6.69	7.19

Sample	Pontremoli7					
Location	Pontremoli 1 well					
Analysis	Mnz02_09a	Mnz03_06a	Mnz04_01a	Mnz04_03a	Mnz04_04a	Mnz04_05a
SiO_2	0.71	1.42	0.54	0.52	0.49	0.55
P_2O_5	29.96	27.93	30.10	30.75	30.51	26.70
SO_3	0.02	0.03	0.03	0.03	0.02	0.01
CaO	1.42	1.15	1.57	1.50	1.40	1.82
Y_2O_3	0.04	0.40	0.06	0.09	0.09	0.09
La_2O_3	15.14	14.39	14.86	14.77	14.69	14.51
Ce_2O_3	29.34	29.72	29.14	28.94	29.02	28.95
Pr_2O_3	3.08	3.26	3.13	3.08	3.09	3.06
Nd_2O_3	11.50	13.23	12.08	12.05	12.19	12.26
Sm_2O_3	1.50	2.19	2.15	2.13	2.15	2.04
Gd_2O_3	0.86	1.32	1.60	1.60	1.59	1.40
Dy_2O_3	0.10	0.38	0.21	0.24	0.27	0.26
PbO	0.09	0.04	0.10	0.09	0.09	0.07
ThO_2	7.69	4.30	6.66	6.24	5.87	5.29
UO_2	0.39	0.04	0.43	0.42	0.43	0.33
Tot	101.84	99.82	102.65	102.45	101.88	97.33
Si	0.027	0.057	0.021	0.020	0.019	0.023
P	0.978	0.939	0.978	0.991	0.990	0.939
S	0.001	0.001	0.001	0.001	0.001	0.000
Ca	0.059	0.049	0.064	0.061	0.057	0.081
Y	0.001	0.008	0.001	0.002	0.002	0.002
La	0.215	0.211	0.210	0.207	0.208	0.222
Ce	0.414	0.432	0.409	0.403	0.407	0.440
Pr	0.043	0.047	0.044	0.043	0.043	0.046
Nd	0.158	0.188	0.166	0.164	0.167	0.182
Sm	0.020	0.030	0.028	0.028	0.028	0.029
Gd	0.011	0.017	0.020	0.020	0.020	0.019
Dy	0.001	0.005	0.003	0.003	0.003	0.003
Pb	0.001	0.000	0.001	0.001	0.001	0.001
Th	0.067	0.039	0.058	0.054	0.051	0.050
U	0.003	0.000	0.004	0.004	0.004	0.003
AGE	249.86	189.74	293.63	291.96	307.32	277.90
statistical error	6.50	11.96	7.35	7.70	8.01	8.67

Sample	Pontremoli7			
Location	Pontremoli 1 well			
Analysis	Mnz04_06a	Mnz04_07a	Mnz04_08a	Mnz04_02a
SiO_2	0.52	0.50	0.48	0.61
P_2O_5	30.68	30.77	30.44	29.96
SO_3	0.02	0.01	0.03	0.04
CaO	1.50	1.58	1.58	1.67
Y_2O_3	0.10	0.10	0.10	0.05
La_2O_3	14.48	14.67	14.89	14.97
Ce_2O_3	29.13	29.10	29.58	29.20
Pr_2O_3	3.16	3.20	3.16	3.10
Nd_2O_3	12.17	12.26	12.44	12.33
Sm_2O_3	2.12	2.14	2.15	2.14
Gd_2O_3	1.55	1.55	1.57	1.57
Dy_2O_3	0.25	0.27	0.26	0.20
PbO	0.09	0.10	0.09	0.11
ThO_2	5.99	5.76	5.60	7.01
UO_2	0.40	0.43	0.43	0.42
Tot	102.16	102.43	102.80	103.38
Si	0.020	0.019	0.018	0.023
P	0.991	0.991	0.983	0.970
S	0.001	0.000	0.001	0.001
Ca	0.061	0.064	0.064	0.068
Y	0.002	0.002	0.002	0.001
La	0.204	0.206	0.209	0.211
Ce	0.407	0.405	0.413	0.409
Pr	0.044	0.044	0.044	0.043
Nd	0.166	0.167	0.169	0.168
Sm	0.028	0.028	0.028	0.028
Gd	0.020	0.020	0.020	0.020
Dy	0.003	0.003	0.003	0.002
Pb	0.001	0.001	0.001	0.001
Th	0.052	0.050	0.049	0.061
U	0.003	0.004	0.004	0.004
AGE	295.57	315.43	301.51	311.04
statistical error	7.99	8.18	8.27	33.11

LIST OF FIGURES

Chapter 1

A TIME TRAVEL THROUGH

THE EVOLUTION OF THE VARISCAN BASEMENT OF NORTHERN APENNINES

Chapter 2

INSIGHTS INTO THE VARISCAN OROGENY:

THE TECTONO-METAMORPHIC EVOLUTION OF THE CERRETO MICASCHIST

Chapter 3

A NEW *P-T-t* PATH FOR THE POST-VARISCAN HISTORY:

LINKING MONAZITE AND GARNET IN THE PONTREMOLI METAPELITES

Chapter 4

DATING THE MYLONITIC STAGE IN THE CERRETO VARISCAN BASEMENT:

AR/AR LASER ANALYSIS OF POTASSIC WHITE MICA IN

ASYMMETRIC FOLIATION BOUDINS

Chapter 5

THE ALPINE METAMORPHISM AND THE INFLUENCE OF FERRIC IRON IN THE HEMATITE-RICH METASEDIMENTARY ROCKS FROM THE PISANI MOUNTAINS

Chapter 6

CONCLUSIONS

LIST OF TABLES

Chapter 2

INSIGHTS INTO THE VARISCAN OROGENY:

THE TECTONO-METAMORPHIC EVOLUTION OF THE CERRETO MICASCHIST

Chapter 3

A NEW *P-T-t* PATH FOR THE POST-VARISCAN HISTORY:

LINKING MONAZITE AND GARNET IN THE PONTREMOLI METAPELITES

Chapter 4

DATING THE MYLONITIC STAGE IN THE CERRETO VARISCAN BASEMENT:

AR/AR LASER ANALYSIS OF POTASSIC WHITE MICA IN

ASYMMETRIC FOLIATION BOUDINS

Chapter 5

THE ALPINE METAMORPHISM AND THE INFLUENCE OF FERRIC IRON IN THE HEMATITE-RICH METASEDIMENTARY ROCKS FROM THE PISANI MOUNTAINS
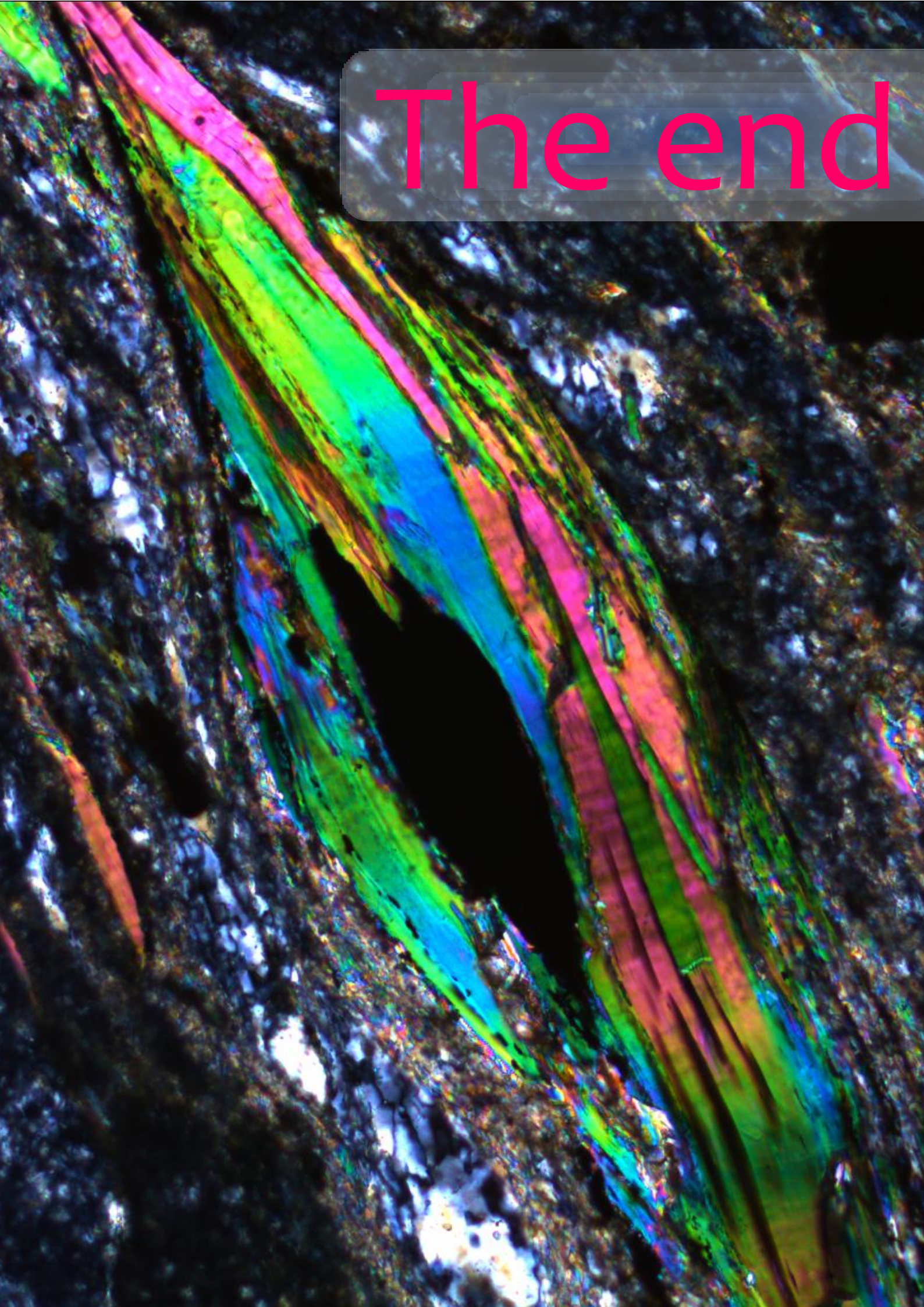
ACKNOWLEDGMENTS

CURRICULUM VITAE

Deborah Lo Pò was born on 11th November 1987 in Messina, Italy. She grew up in a small town near the sea, Furci Siculo (Italy). She attended the Secondary School at "Liceo Scientifico C. Caminiti" from 2001 to 2006. Then she studied Geological Sciences at the University of Catania (Italy). She got the Bachelor Degree and the Master Degree with final grade of 110/110 cum laude. In 2012 she moved to Bologna to start the PhD in Earth Sciences. This thesis is the result of the PhD activity.

The end